Transport Phenomena in Direct Methanol Fuel Cells:

Modelling and Experimental studies

VÂNIA SOFIA BROCHADO DE OLIVEIRA

Dissertation presented for the Doctor of Philosophy degree

in Chemical And Biological Engineering

at the Faculty of Engineering, University of Porto, Portugal

This thesis was supervised by

Doctor Alexandra Maria Pinheiro da Silva Ferreira Rodrigues Pinto, Departamento de Engenharia Química, Faculdade de Engenharia da Universidade do Porto

Cento de Estudos de Fenómenos de Transporte

Departamento de Engenharia Química

Faculdade de Engenharia

Universidade do Porto

August, 2009

Abstract

The main goal of this thesis was the experimental and modelling study of an active feed Direct Methanol Fuel Cell (DMFC) working close to ambient conditions. Bearing in mind that the passive DMFC systems emerge as a solution for portable applications, the study was extended for passive feed DMFCs.

A steady state, one dimensional model accounting for coupled heat and mass transfer processes along with the electrochemical reactions occurring in the fuel cell was developed both for the active and passive feed DMFC. These simplified models using low CPU and rapidly implemented reproduce with satisfactory accuracy experimental data.

An experimental set-up to determine the cell polarization and power curves was implemented. «In-house» developed active and passive feed DMFCs with 25 cm^2 of active area were designed. A detailed experimental characterization of the active DMFC working close to room temperature is provided as well as some results with the passive cell.

The experimental polarization and power density curves were successfully compared with the model predictions and when it was possible, the results were explained under the light of the model predictions for oxygen concentration profiles and for methanol and water crossover. Both models were also validated with published data.

The effect of operating conditions (such as methanol feed concentration and fuel and air flow rates) and of design parameters (active area, diffusion layer materials and thickness, catalyst loading and membrane thickness) on the fuel cell performance was evaluated. Particular attention was devoted to the influence of these parameters on methanol and water crossover. The models predict the correct trends of the effect of the different parameters on these two cross flows and consequently on cell performance.

The influence of different anode and cathode flow field designs on the active feed DMFC was also studied.

The developed models were intensively used to set-up optimized conditions leading to enhanced performances both for active and passive DMFCs. Tailored Membrane Electrode Assemblies (MEAs) with different structures and combinations of membrane thicknesses, diffusion layers and catalyst loadings were designed and tested in order to select optimal working conditions with high methanol concentrations and relatively low

water and methanol crossover levels, situation with increased interest in portable applications.
The results reported in this work are relevant for the design, optimization and operation of both active and passive Direct Methanol Fuel Cell systems.

Keywords: Direct methanol fuel cell, Modelling, Heat and mass transfer, Methanol crossover, Water crossover, High methanol concentrations, Tailored MEAs

Resumo

O presente trabalho teve como objectivo o estudo experimental e de modelação de uma célula de combustível com injecção directa e activa de metanol operando em condições próximas das ambientais. Tendo em conta a importância crescente dos sistemas com alimentação directa e passiva de metanol como solução para as aplicações portáteis devido à sua simplicidade, optou-se por estender o estudo a células de metanol com alimentação passiva.

No decurso do trabalho, foi desenvolvido um modelo matemático quer para a célula activa quer passiva, em estado estacionário e a uma dimensão incorporando o transporte de calor e massa bem como as reacções electroquímicas que ocorrem no ânodo e no cátodo da célula de combustível. Estes modelos simplificados, com baixo tempo de CPU e de rápida implementação reproduzem satisfatoriamente os dados experimentais obtidos.

Foi desenvolvida neste estudo uma instalação experimental (incluindo uma estação de medida para células com injecção directa de metanol e um sistema de controlo de temperatura) para a determinação experimental das curvas de polarização e de potência. Várias células com uma área activa de 25 cm^2 foram concebidas e construídas ao longo do trabalho. Apresenta-se um estudo experimental detalhado para a célula activa e alguns resultados para a célula passiva.

As curvas de polarização e de potência experimentais foram comparadas com sucesso com as previsões dos modelos e sempre que possível os resultados foram explicados à luz das previsões para os perfis de concentração do oxigénio e para o atravessamento de metanol e de água através da membrana. Ambos os modelos foram também validados com dados da literatura.

O efeito das condições de operação (tais como a concentração de metanol na alimentação ao ânodo e os caudais de solução de metanol e ar), bem como de parâmetros de configuração (área activa, materiais que constituem as camadas de difusão e espessura da membrana polimérica), no desempenho da célula activa e passiva foi estudado detalhadamente. Dedicou-se particular atenção à influência dos diferentes parâmetros no atravessamento de metanol e de água através da membrana que condicionam a eficiência da célula de combustível.

A influência da geometria dos canais distribuidores do combustível e oxidante na eficiência da célula foi igualmente estudada.

Os modelos desenvolvidos foram intensivamente utilizados para estabelecer condições de operação optimizadas que conduzem ao desenvolvimento de células (e pilhas) com melhores desempenhos, tanto em sistemas de alimentação activa como passiva. Foram propostas e testadas diferentes MEAs (conjuntos de membrana, camadas catalíticas e camadas de difusão) com diferentes configurações, originando desempenhos optimizados que permitem operar com elevadas concentrações de metanol, mantendo-se em níveis relativamente baixos os fluxos de metanol e água através da membrana. Estas condições de operação são de extremo interesse em aplicações portáteis das pilhas de metanol directo.

Os resultados obtidos nesta tese são de relevância e utilidade significativas para o design e construção de novas DMFCs, para a optimização de condições de operação e para a validação de modelos matemáticos.

Palavras-chave: Célula de Combustível de Metanol Directo, Modelação, Transporte de Calor e Massa, Atravessamento de Metanol, Atravessamento de Água, Concentrações Elevadas de Metanol, MEAs

Resumé

L'objectif de cette thèse est l'étude expérimentale et de modélisation d'une pîle à combustible à utilisation directe et active du méthanol (Direct Methanol Fuel Cells: DMFC) fonctionnant en conditions proches de la température ambiante. Une fois que l'importance des systhèmes avec alimentation passive de méthanol comme une solution d'interêt pour les applications portables, est de plus en plus haute, on a décidé d'étudier aussi les piles de méthanol passives.

On a dévelopé um modèle mathématique pour la pile active et pour la pile passive en régime permanent, à une dimension, qui intègre le transfert de chaleur et masse bien comme les réactions electrochimiques de l'anode et du cathode. Ces modèles simplifiés avec un temps de CPU baisse et de mise en oeuvre rapide, reproduisent convenablement les données expérimentales.

Une instalation éxpérimentale a été mise en œuvre dans ce travail pour obtenir les courbes courant-tension et de puissance. Différentes piles DMFC avec un surface active de 25 cm^2 ont été conçues et construites pendant le déroulement du travail. Un étude experimentale détaillée pour la pile d'alimentation active est présenté bien comme quelques résultats obtenus avec la célule passive

Les courbes expérimentales courant-tension et de puissance ont été comparées avec les prévisions des modèles et, si possible les résultats ont été expliqués par rapport aux prévisions des profiles de concentration d'oxygène et de l'écoulement du méthanol et de l'eau à travers la membrane échangeuse de protons. Les deux modèles ont aussi été validés avec des données expérimentales trouvées dans la littérature.

L'effet des conditions d'opération (concentration de méthanol et débits de méthanol et air) et de plusieurs paramètres de configuration (surface active, matériaux qui constituent les couches de diffusion et épaisseur de la membrane échangeuse de protons) dans la performance de la pile active et passive á été étudié en détail. On a dévoué une attention particulière à l'étude de l'influence des différents paramètres dans l'écoulement de méthanol et eau qui passent à travers la membrane et qui influencent le fonctionnement et performance de la pile.

L'influence de la géométrie des canaux de distribution de méthanol et air dans la performance de la pile a été également étudiée.

Les modèles développés on été utilisés pour établir des conditions d'opération optimisées qui conduisent au développement de piles avec meilleures performances, autant en systèmes d'alimentation active que passive. Différentes MEAs (groupe membrane, couches catalytiques et couches de diffusion) avec différentes configurations et résultant en performances optimisées qui permettent de travailler avec hautes concentrations de méthanol et qui maintiennent le cross-over de méthanol et eau dans des niveaux basses, on été proposées. Ces conditions d'opération sont d'extrême importance dans les applications portables des DMFC.

Les résultats présentés dans ce travail sont déterminants pour de design et construction de nouvelles piles DMFC, pour l'optimisation de conditions d'opération et pour la validation de travaux de simulation numérique en ce type de piles à combustible.

Mots Clés: Pile à combustible à utilisation directe du méthanol, Modélisation, Transfert de Chaleur et Masse, Méthanol cross-over, Cross-over de l'Eau, Hautes Concentrations de Méthanol, MEAs

To Bruno, mother, father, Ana and

to the memory of a Great man, my grandfather, Pinto

Acknowledgements

This may be the most difficult part… since I am not, for sure, the best person in finding the right words concerning the acknowledgments to my family and friends. I would like to say that during these four years, I had the opportunity to meet so many wonderful persons and I am grateful to all of them.

To **Bruno,** my marvellous husband, who always supported and believed in me. His love, patience, help and understanding during these years have been determinant for the development of my work and for the concretization of my dream. For everything we have shared, my deepest gratitude and love. Without your support everything would be more difficult.

To my **Mother** and **Father** who have always supported me and made sacrifices for giving me all possible advantages in my life. They always have been and will be my inspiration. For all your love I will give you all my love.

To **Ana**, my lovely sister, for all the friendship and love and for being the best gift that I have received from my parents. You are simple the best!!!

Most important, I am grateful to my supervisor Dr. **Alexandra Pinto**, for believing in me and for giving me the opportunity to do this interesting PhD. For your supervision, support and friendship during these four years. It was a pleasure to work with you and find out the amazing person you are. Your enthusiasm and knowledge is enormous and inspires everyone that works with you.

I would like to thank to Prof. **Fernando Martins** for his help in the simulation studies.

I also, want to thank to all my friends from **E319**, **João**, **Herney**, **Sofia**, **Klara**, **Filipa**, **Joana**, **Daniela**, **Marta, Pedro**, **Tiago**, **Renato**, in Faculty of Engineering in Oporto University (FEUP).

Particularly, to you **Daniela** for your support, friendship and help during these four years. I wish you all the luck for your PhD and I hope we can work together in the future. I believe that you will make it!!!

To, **Joana**, **Marta**, **Sofia** and **Eliana**, for your support, friendship, help and good advices during these years. I will never forget you!!!

I would like to thank the partial support of “Fundação para a Ciência e Tecnologia (FCT)” through project POCTI/EQU/47054/2002 is gratefully acknowledged. POCI (FEDER) also supported this work via CEFT. I also like to thank FCT the financial support of my scholarship, ref. SFRH/BD/18681/2004, making this thesis possible and the concretization of my dream.

Finally, to all the people who made this thesis possible.

List of publications

1. Oliveira, V.B, Falcão, D.S., Rangel, C.M. and Pinto, A.M.F.R., A comparative study of approaches to direct methanol fuel cells modelling, International Journal of Hydrogen Energy 32 (2007) 415-424.
2. Oliveira, V.B, Falcão, D.S., Rangel, C.M. and Pinto, A.M.F.R., Heat and mass transfer effects in a direct methanol fuel cell: A 1D model, International Journal of Hydrogen Energy, Vol. 33, Issue 17, July 2008 3818-3828.
3. Oliveira, V.B, Rangel, C.M. and Pinto, A.M.F.R., Modelling and experimental studies on a Direct Methanol Fuel Cell working under low methanol crossover and high methanol concentrations, International Journal of Hydrogen Energy 34 (2009) 6443-6451.
4. Oliveira, V.B, Rangel, C.M. and Pinto, A.M.F.R., Water management in direct Methanol Fuel Cells, International Journal of Hydrogen Energy (2009), doi:10.1016/j.ijhydene.2009.07.111
5. Oliveira, V.B, Rangel, C.M. and Pinto, A.M.F.R., Performance of a Direct Methanol Fuel Cell operating near ambient conditions, submitted to Journal of Fuel Cell Science and Technology.
6. Oliveira, V.B, Rangel, C.M. and Pinto, A.M.F.R., Effect of anode and cathode flow field design on the performance of a direct methanol fuel cell, submitted to Chemical Engineering Journal.
7. Oliveira, V.B, Rangel, C.M. and Pinto, A.M.F.R., One-dimensional and non-isothermal model for a passive DMFC, submitted to International Journal of Heat and Mass Transfer.
8. Oliveira, V.B, Rangel, C.M. and Pinto, A.M.F.R., Water management in a passive DMFC, submitted to Journal of Power Sources.

Table of Contents

Chapter 1 1
1. INTRODUCTION 1
1.1. Fuel cells 1
1.2. Fuel cells in society 2
1.3. History of fuel cells 4
1.4. Fuel cell description 6
1.5. Fuel cell types 8
1.5.1. Polymer Electrolyte Membrane Fuel Cell (PEMFC) 9
1.5.2. Direct Methanol Fuel Cell (DMFC) 9
1.5.3. Alkaline Fuel Cell (AFC) 10
1.5.4. Phosphoric Acid Fuel Cell (PAFC) 11
1.5.5. Molten Carbonate Fuel Cell (MCFC) 11
1.5.6. Solid Oxide Fuel Cell (SOFC) 12
1.6. Advantages and disadvantages 13
1.7. Applications 15
1.7.1. Transportation 15
1.7.2. Stationary power 16
1.7.3. Portable power 17
Chapter 2 19
2. DIRECT METHANOL FUEL CELLS: STATE-OF-THE-ART 19
2.1. Introduction 19
2.2. Operating principle of the DMFC 20
2.3. Fundamentals of a DMFC 22
2.3.1. Cell components 22
2.3.2. Thermodynamics and polarization curve 25
2.3.3. Methanol oxidation and oxygen reduction kinetics 28
2.4. Two-phase flow phenomena 33
2.4.1. Gaseous carbon dioxide in anode 33
2.4.2. Liquid water transport in the cathode 37
2.5. Mass transport phenomena 38
2.5.1. Methanol crossover 38

2.5.2. Water management 47
2.6. Single cell performance – Polarization behaviour 50
2.6.1. Operating conditions 51
2.6.1.1. Methanol concentration 51
2.6.1.2. Fuel cell temperature 52
2.6.1.3. Methanol and air flow rate 52
2.6.1.4. Air pressure 53
2.6.2. Configuration parameters 53
2.6.2.1. Flow field design 53
2.6.2.2. Catalyst loading 56
2.6.2.3. Diffusion Layers 58
2.7. Mathematical Modelling 59
2.7.1. Analytical models 60
2.7.2. Semi-empirical models 62
2.7.3. Mechanistic models 63
2.8. Passive DMFC 66
2.9. Applications 72
2.10. Summary and Scope of the present work 74
Chapter 3 77
3. MODEL FORMULATION FOR AN ACTIVE FEED DMFC 77
3.1. General model structure 77
3.2. Model assumptions 79
3.3. Governing equations and Boundary conditions – Anode and Cathode 80
3.3.1. Mass transport 80
3.3.2. Heat transport 85
3.4. Cell performance 89
3.5. Analytical solutions 90
3.5.1. Mass transport 90
3.5.2. Heat transport 94
3.6. Results and discussion 97
3.7. Concluding remarks 105
Chapter 4 107
4. EXPERIMENTAL SETUP FOR AN ACTIVE FEED DMFC 107
4.1. Fuel cell design 107

4.1.1. End Plates 109
4.1.2. Insulating Plates 109
4.1.3. Connector plates 110
4.1.4. Monopolar plates 110
4.1.5. Membrane Electrode Assembly (MEA) 112
4.1.6. Diffusion layers 112
4.2. Methanol Test Kit Testing Unit 114
4.2.1. Methanol handling system 116
4.2.2. Gas handling system 118
4.2.3. Loadbank system 119
4.3. Fuel cell heater control system 121
4.4. Experimental procedure 121
Chapter 5 123
5. EXPERIMENTAL AND MODELLING STUDIES OF AN ACTIVE FEED DMFC 123
5.1. Results and Discussion 124
5.1.1. Effect of diffusion layers 125
5.1.2. Effect of operating conditions 127
5.1.2.1. Effect of methanol concentration 128
5.1.2.2. Effect of fuel cell temperature 133
5.1.2.3. Effect of methanol flow rate 138
5.1.2.4. Effect of air flow rate 143
5.1.3. Effect of design parameters 147
5.1.3.1. Effect of anode diffusion layer material 147
5.1.3.2. Effect of cathode diffusion layer material 154
5.1.3.3. Effect of membrane thickness 160
5.1.3.4. Effect of Catalyst loading 167
5.1.3.5. Effect of anode flow field 175
5.1.3.6. Cathode flow field 180
5.1.4. Tailored MEAs (Membrane Electrode Assemblies) 185
5.2. Concluding remarks 189
Chapter 6 193
6. PASSIVE FEED DIRECT METHANOL FUEL CELL 193
6.1. Model Formulation for a passive feed DMFC 194

6.1.1. General model structure 194
6.1.2. Model assumptions 195
6.1.3. Governing equations and Boundary conditions 196
6.1.3.1. Mass transport 196
6.1.3.2. Heat transport 202
6.1.4. Cell performance 205
6.1.5. Analytical solutions - Mass transport 206
6.2. Experimental Setup for a passive feed DMFC 211
6.2.1. Fuel cell design 211
6.2.1.1. End Plates 213
6.2.1.2. Insulating Plates 214
6.2.1.3. Connector plates 215
6.2.1.4. Membrane Electrode Assembly (MEA) and diffusion layers 215
6.2.2. Methanol Test Kit Testing Unit 216
6.2.3. Experimental procedure 216
6.3. Experimental and Modelling studies for a passive feed DMFC 216
6.3.1. Results and Discussion 216
6.3.1.1. Model validation 217
6.3.1.2. Water Management in a Passive DMFC – model simulations 225
6.3.1.3. Tailored MEAs 234
6.3.1.4. Active feed DMFC vs. Passive feed DMFC 236
6.3.2. Concluding remarks 238
Chapter 7 241
7. CONCLUSIONS AND SUGGESTIONS FOR FUTURE WORK 241
7.1 Conclusions 241
7.2 Suggestions for future work 244
Chapter 8 245
8. References 245
Appendix A: Uncertainty analysis 263
Appendix B: Physical Properties and Parameters 271
Appendix C: Experimental Results of an active feed DMFC 285

List of Figures

Figure 1.1 – Schematic representation of a fuel cell generating electricity from a fuel. 1

Figure 1.2 – Schematic representation of hydrogen economy. 4

Figure 1.3 – Cross section of general fuel cell. 6

Figure 1.4 – Schematic representation of fuel cell polarization curve. 8

Figure 1.5 – Examples of fuel cell applications (Courtesy of Honda, Ballard, Samsung, Shell, Jadoo, Motorola, Suzuki, Company's XX25, Pearl Hydrogen, Yamaha, DaimlerChrysler and Plug Power Inc.) 15

Figure 2.1 – Operating principle of a DMFC. 20

Figure 2.2 – Schematic representation of a direct methanol fuel cell MEA. 22

Figure 2.3 – Schematic representation of the Nafion chemical structure. 23

Figure 2.4 – Anode catalyst layer (a) and cathode catalyst layer (b) microstructures, taken from reference [1]. 24

Figure 2.5 – Micrographs of commercially available carbon paper (a) and carbon cloth (b), taken from reference [1]. 25

Figure 2.6 – Schematic representation of a typical DMFC polarization curve. 27

Figure 2.7 – A photograph of a transparent DMFC, taken from reference [37]. 35

Figure 2.8 – Bubble behaviour on the anode side using hydrophobic carbon paper (a) and hydrophilic carbon cloth (b), taken from reference [37]. 35

Figure 2.9 – Water drop behaviour on the cathode side using carbon paper (a) and ELAT carbon cloth (b), taken from reference [37]. 38

Figure 2.10 – Representation of the most commonly used DMFC flow fields. 54

Figure 2.11 – DMFC model categorization based on areas of investigation. 60

Figure 2.12 – Schematic representation of conventional design of a passive DMFC. 68

Figure 2.13 – Direct Methanol Fuel Cell applications (Courtesy Toshiba, Samsung, Motorola, Suzuki, Company's XX25, Yamaha, DaimlerChrysler, DoCoMo and Fujitsu, Intermec, Panasonic, Volkswagen). 73

Figure 3.1 – Schematic representation of a DMFC. 78

Figure 3.2 – Predicted methanol concentration profiles in the cell for different current densities. Operating conditions: temperature 70 ºC, pressure 1 atm, q^{AF} = 0.33 cm^3/s and q^{CF} = 1.67 cm^3/s. 98

Figure 3.3 – Model prediction for methanol crossover for different methanol feed concentrations. Operating conditions: temperature 70 ºC, pressure 1 atm, q^{AF} = 0.33 cm^3/s and q^{CF} = 1.67 cm^3/s. 99

Figure 3.4 – Predicted water concentration distribution in the cell at different current densities: (a) anode and membrane and (b) cathode. Operating conditions: methanol concentration 0.5M, temperature 70 ºC, pressure 1 atm, q^{AF} = 0.33 cm^3/s and q^{CF} = 1.67 cm^3/s. 100

Figure 3.5 – Model predictions of the net water transport coefficient for different methanol concentrations. Operating conditions: temperature 70 ºC, pressure 1 atm, q^{AF} = 0.33 cm^3/s and q^{CF} = 1.67 cm^3/s. 101

Figure 3.6 – Influence of methanol concentration on the net water transport coefficient at different current densities. Operating conditions: temperature 70 ºC, pressure 1 atm, q^{AF} = 0.33 cm^3/s and q^{CF} = 1.67 cm^3/s. 102

Figure 3.7 – Prediction for the temperature distribution in the cell at different current densities. Operating conditions: methanol concentration 0.5M, pressure 1 atm, q^{AF} = 0.33 cm^3/s and q^{CF} = 1.67 cm^3/s. 103

Figure 3.8 – Comparison of the presented model predictions and the model developed by Brenda *et al.*; dots: experimental data from [120], lines: model predictions. Operating conditions: methanol concentration 0.1M, temperature 70 ºC, pressure 1 atm, q^{AF} = 0.33 cm^3/s and q^{CF} = 1.67 cm^3/s. 104

Figure 3.9 – Comparison of the model predictions of polarization curves for different methanol concentrations; dots: experimental data from [120], lines: model predictions. Operating conditions: temperature 70 ºC, pressure 1 atm, q^{AF} = 0.33 cm^3/s and q^{CF} = 1.67 cm^3/s. 105

Figure 4.1 – 3D CAD drawing of the active feed DMFC. 108

Figure 4.2 – Photograph of an «in-house» designed DMFC. 109

Figure 4.3 – Photograph of an end plate (aluminium) 109

Figure 4.4 – Photograph of an isolating plate (rubber). 110

Figure 4.5 – Photograph of a connector plate. 110

Figure 4.6 – Photograph of a Membrane Electrode Assembly (MEA) 112

Figure 4.7 – Photograph of Diffusion layers. 113

Figure 4.8 – Photograph of experimental setup. 114

Figure 4.9 – Schematic diagram of the experimental set-up. 115

Figure 4.10 – Schematic diagram of the methanol handling system. 117

Figure 4.11 – MTK software panel with methanol control option. 118

Figure 4.12 – Schematic diagram of the gas handling system. 119

Figure 4.13 – MTK software panel with air control option. 119

Figure 4.14 – MTK software panel with electronic load option. 120

Figure 4.15 – Photograph of a fuel cell with heater resistance. 121

Figure 4.16 – Photograph of the front panel of the digital controller. 121

Figure 5.1 – Influence of gas diffusion layers on a) cell performance and b) power density for different methanol concentrations. Operating conditions: methanol flow rate 8 ml/min, air flow rate 3.6 l/min and fuel cell temperature 20ºC. Gas diffusion layers materials: carbon cloth at the anode and ELAT (E-TEK) at the cathode.....126

Figure 5.2 – Influence of gas diffusion layers on a) cell performance and b) power density for different methanol concentrations. Operating conditions: methanol flow rate 3 ml/min, air flow rate 3.6 l/min and fuel cell temperature 20ºC. Gas diffusion layers materials: carbon cloth at the anode and ELAT (E-TEK) at the cathode.....127

Figure 5.3 – Effect of methanol concentration on a) cell performance and b) power density. Operating conditions: methanol flow rate 8 ml/min, air flow rate 3.6 l/min and fuel cell temperature 20ºC. 130

Figure 5.4 – Model predictions for the methanol crossover for different methanol feed concentrations. Operating conditions: methanol flow rate 8 ml/min, air flow rate 3.6 l/min and fuel cell temperature 20ºC.....131

Figure 5.5 – Comparison of model predictions on cell performance and power density; dots: experimental data, lines: model predictions. Operating conditions: methanol flow rate 8 ml/min, air flow rate 3.6 l/min and fuel cell temperature 20ºC. 132

Figure 5.6 – Model prediction for net water transport coefficient for different methanol feed concentrations. Operating conditions: methanol flow rate 8 ml/min, air flow rate 3.6 l/min and fuel cell temperature 20ºC.....133

Figure 5.7 – Effect of fuel cell temperature on a) cell performance and b) power density. Operating conditions: methanol flow rate 8 ml/min, air flow rate 3.6 l/min and methanol concentration 0.75M.....135

Figure 5.8 – Model predictions for the anode overpotential for different fuel cell temperatures. Operating conditions: methanol flow rate 8 ml/min, air flow rate 3.6 l/min and methanol concentration 0.75M. 136

Figure 5.9 – Model predictions for the cathode overpotential for different fuel cell temperatures. Operating conditions: methanol flow rate 8 ml/min, air flow rate 3.6 l/min and methanol concentration 0.75M. 136

Figure 5.10 – Model predictions for the methanol crossover for different methanol feed concentrations. Operating conditions: methanol flow rate 8 ml/min, air flow rate 3.6 l/min and methanol concentration 0.75M. 137

Figure 5.11 – Model predictions for net water transport coefficient for different fuel cell temperatures. Operating conditions: methanol flow rate 8 ml/min and air flow rate 3.6 l/min, methanol concentration 0.75M..... 137

Figure 5.12 – Comparison of model predictions on cell performance and power density; dots: experimental data, lines: model predictions. Operating conditions: methanol concentration 0.75M, methanol flow rate 8 ml/min and air flow rate 3.6 l/min..... 138

Figure 5.13 – Effect of methanol flow rate on a) cell performance and b) power density. Operating conditions: methanol concentration 0.75M, fuel cell temperature 20ºC and air flow rate 3.6 l/min..... 139

Figure 5.14 – Predicted methanol concentration profiles in the anode catalyst layer (thickness 0.0023 cm) for different methanol flow rates. Operating conditions: methanol concentration 0.75M, air flow rate 3.6 l/min and a current density of 0.03 A/cm^2..... 140

Figure 5.15 – Model predictions for the methanol crossover for different methanol flow rates. Operating conditions: air flow rate 3.6 l/min, methanol concentration 0.75M and fuel cell temperature 20ºC..... 141

Figure 5.16 – Model predictions for net water transport coefficient for different methanol flow rates. Operating conditions: air flow rate 3.6 l/min, methanol concentration 0.75M and fuel cell temperature 20ºC..... 142

Figure 5.17 – Comparison of model predictions on cell performance and power density; dots: experimental data, lines: model predictions. Operating conditions: methanol concentration 0.75M, fuel cell temperature 20ºC and air flow rate 3.6 l/min. 142

Figure 5.18 – Effect of air flow rate on a) cell performance and b) power density. Operating conditions: methanol concentration 0.75M, fuel cell temperature 20ºC, methanol flow rate 8 ml/min..... 144

Figure 5.19 – Predicted oxygen concentration profile in the cathode catalyst layer (thickness 0.0023 cm) for different air flow rates. Operating conditions: methanol concentration 0.75M, methanol flow rate 8 ml/min a current density of 0.03 A/cm^2. 145

Figure 5.20 – Model prediction for net water transport coefficient for different air flow rates. Operating conditions: methanol flow rate 8 ml/min, methanol concentration 0.75M and fuel cell temperature 20ºC..... 146

Figure 5.21 – Comparison of model predictions on cell performance and power density; dots: experimental data, lines: model predictions. Operating conditions: methanol concentration 0.75M, fuel cell temperature 20ºC and methanol flow rate 8 ml/min..... 146

Figure 5.22 – Effect of anode diffusion layer material on a) cell performance and b) power density. Operating conditions: methanol concentration 0.75M, air flow rate 3.6 l/min and fuel cell temperature 20ºC. Design parameters: Nafion 117 and ELAT (E-TEK) at the cathode gas diffusion layer. 149

Figure 5.23 – Predicted methanol concentration profile in the anode catalyst layer (thickness 0.0023 cm) for different anode gas diffusion layer materials. Operating conditions: methanol concentration 0.75M, methanol flow rate 3 ml/min, air flow rate 3.6 l/min and fuel cell temperature 20ºC. Design parameters: Nafion 117 and ELAT (E-TEK) at the cathode gas diffusion layer. 150

Figure 5.24 – Comparison of model predictions on a) cell performance and b) power density; dots: experimental data, lines: model predictions. Operating conditions: methanol concentration 0.75M and 5M, methanol flow rate 3 ml/min and air flow rate 3.6 l/min. Design parameters: Nafion 117 and ELAT (E-TEK) at the cathode gas diffusion layer.....151

Figure 5.25 – Model predictions for the methanol crossover for different anode gas diffusion layer materials. Operating conditions: methanol concentration 5M, methanol flow rate 3 ml/min, air flow rate 3.6 l/min and fuel cell temperature 20ºC. Design parameters: Nafion 117 and ELAT (E-TEK) at the cathode gas diffusion layer.....152

Figure 5.26 – Model predictions for net water transport coefficient for different anode gas diffusion layer materials. Operating conditions: methanol concentration 5M, methanol flow rate 3 ml/min, air flow rate 3.6 l/min and fuel cell temperature 20ºC. Design parameters: Nafion 117 and ELAT (E-TEK) at the cathode gas diffusion layer. 153

Figure 5.27 – Effect of anode diffusion layer material on a) cell performance and b) power density. Operating conditions: methanol concentration 0.75M, methanol flow rate 8 ml/min and air flow rate 3.6 l/min. Design parameters: Nafion 117 and ELAT (E-TEK) at the cathode gas diffusion layer. 154

Figure 5.28 – Effect of cathode diffusion layer material on a) cell performance and b) power density. Operating conditions: methanol concentration 0.75M, methanol flow rate 8 ml/min and cell temperature 20ºC. Design parameters: Nafion117 and carbon cloth as anode gas diffusion layer. 156

Figure 5.29 – Comparison of model predictions on a) cell performance and b) power density; dots: experimental data, lines: model predictions. Operating conditions: methanol concentration 0.75M and 5M, methanol flow rate 3 ml/min and air flow rate 3.6 l/min. Design parameters: Nafion 117 and carbon cloth as anode gas diffusion layer. 157

Figure 5.30 – Predicted oxygen concentration profile in the cathode catalyst layer (thickness 0.0023 cm) for different cathode gas diffusion layer materials. Operating conditions: methanol concentration 5M, methanol flow rate 3 ml/min, air flow rate 3.6 l/min and fuel cell temperature 20ºC. Design parameters: Nafion 117 and carbon cloth as anode gas diffusion layer.....158

Figure 5.31 – Model predictions for net water transport coefficient for different cathode gas diffusion layer materials. Operating conditions: methanol concentration 5M, methanol flow rate 3 ml/min, air flow rate 3.6 l/min and fuel cell temperature 20ºC. Design parameters: Nafion 117 and carbon cloth as anode gas diffusion layer. 159

Figure 5.32 – Effect of cathode diffusion layer material on a) cell performance and b) power density. Operating conditions: methanol concentration 0.75M, methanol flow rate 8 ml/min and air flow rate 3.6 l/min. Design parameters: Nafion 117 and carbon cloth as anode gas diffusion layer. 160

Figure 5.33 – Effect of membrane thickness on a) cell performance and b) power density. Operating conditions: methanol concentration 0.75M, air flow rate 3.6 l/min and cell temperature 20ºC..... 162

Figure 5.34 – Model predictions for the methanol crossover for different membrane thicknesses. Operating conditions: methanol concentration 0.75M and 5M, methanol flow rate 3 ml/min, air flow rate 3.6 l/min and fuel cell temperature 20ºC. 163

Figure 5.35 – Effect of membrane thickness on a) cell performance and b) power density. Operating conditions: air flow rate 3.6 l/min, methanol flow rate 3 ml/min and cell temperature 20ºC..... 164

Figure 5.36 – Model predictions for the net water transport coefficient for different membrane thicknesses. Operating conditions: methanol concentration 0.75M and 5M, methanol flow rate 3 ml/min, air flow rate 3.6 l/min and fuel cell temperature 20ºC..... 165

Figure 5.37 – Effect of membrane thickness on a) cell performance and b) power density. Operating conditions: methanol concentration 0.75M, methanol flow rate 8 ml/min and air flow rate 3.6 l/min. 166

Figure 5.38 – Comparison of model predictions on a) cell performance and b) power density; dots: experimental data, lines: model predictions. Operating conditions: methanol concentration 0.75M and 5M, methanol flow rate 3 ml/min and air flow rate 3.6 l/min. 167

Figure 5.39 – Effect of catalyst loading on a) cell performance and b) power density. Operating conditions: methanol concentration 0.75M, air flow rate 3.6 l/min and cell temperature 20ºC. Design parameters: catalyst loading SL (4 mg/cm^2) and HL (8 mg/cm^2). 169

Figure 5.40 – Model predictions for the anode overpotential for different catalyst loadings. Operating conditions: methanol flow rate 3 ml/min, air flow rate 3.6 l/min and methanol concentration 0.75M. Design parameters: catalyst loading SL (4 mg/cm^2) and HL (8 mg/cm^2). 170

Figure 5.41 – Model predictions for the cathode overpotential for different catalyst loadings. Operating conditions: methanol flow rate 3 ml/min, air flow rate 3.6 l/min and methanol concentration 0.75M. Design parameters: catalyst loading SL (4 mg/cm^2) and HL (8 mg/cm^2). 170

Figure 5.42 – Effect of catalyst loading on a) cell performance and b) power density. Operating conditions: air flow rate 3.6 l/min, methanol flow rate 3 ml/min and cell temperature 20ºC. Design parameters: catalyst loading SL (4 mg/cm^2) and HL (8 mg/cm^2). 171

Figure 5.43 – Model predictions for the methanol crossover for different catalyst loadings. Operating conditions: methanol concentration 0.75M and 5M, methanol flow rate 3 ml/min, air flow rate 3.6 l/min and fuel cell temperature 20ºC. Design parameters: catalyst loading SL (4 mg/cm^2) and HL (8 mg/cm^2)..... 172

Figure 5.44 – Model predictions for the net water transport coefficient for different catalyst loadings. Operating conditions: methanol concentration 0.75M and 5M, methanol flow rate 3 ml/min, air flow rate 3.6 l/min and fuel cell temperature 20ºC. Design parameters: catalyst loading SL (4 mg/cm^2) and HL (8 mg/cm^2).....173

Figure 5.45 – Effect of catalyst loading on a) cell performance and b) power density. Operating conditions: methanol concentration 0.75M, methanol flow rate 8 ml/min and air flow rate 3.6 l/min. Design parameters: catalyst loading SL (4 mg/cm^2) and HL (8 mg/cm^2).....174

Figure 5.46 – Comparison of model predictions on a) cell performance and b) power density; dots: experimental data, lines: model predictions. Operating conditions: methanol concentration 0.75M and 5M, methanol flow rate 3 ml/min and air flow rate 3.6 l/min. Design parameters: catalyst loading SL (4 mg/cm^2) and HL (8 mg/cm^2).....175

Figure 5.47 – Effect of anode flow field design on a) cell performance and b) power density. Operating conditions: methanol concentration 0.75M, air flow rate 3.6 l/min and cell temperature 20ºC. 177

Figure 5.48 – Effect of anode flow field design on a) cell performance and b) power density. Operating conditions: air flow rate 3.6 l/min, methanol flow rate 3 ml/min and cell temperature 20ºC. 178

Figure 5.49 – Effect of anode flow field design on a) cell performance and b) power density. Operating conditions: methanol concentration 0.75M, methanol flow rate 8 ml/min and air flow rate 3.6 l/min. 180

Figure 5.50 – Effect of cathode flow field design on a) cell performance and b) power density. Operating conditions: methanol concentration 0.75M, methanol flow rate 8 ml/min and cell temperature 20ºC. 182

Figure 5.51 – Effect of cathode flow field design on a) cell performance and b) power density. Operating conditions: air flow rate 3.6 l/min, methanol flow rate 3 ml/min and cell temperature 20ºC. 183

Figure 5.52 – Effect of cathode flow field design on a) cell performance and b) power density. Operating conditions: methanol concentration 0.75M, methanol flow rate 8 ml/min and air flow rate 3.6 l/min. 185

Figure 5.53 – Comparison of model predictions on cell performance and power density; dots: experimental data, lines: model predictions. Operating conditions: methanol concentration 5M, methanol flow rate 3 ml/min, air flow rate 3.6 l/min and fuel cell temperature 20ºC.....187

Figure 5.54 – Model prediction for the methanol crossover for different MEAs. Operating conditions: Operating conditions: methanol concentration 5M, methanol flow rate 3 ml/min, air flow rate 3.6 l/min and fuel cell temperature 20ºC. 188

Figure 5.55 – Model prediction for the net water transport coefficient for different MEAs. Operating conditions: methanol concentration 5M, methanol flow rate 3 ml/min, air flow rate 3.6 l/min and fuel cell temperature 20ºC. 189

Figure 6.1 – Schematic representation of a passive DMFC. 194

Figure 6.2 – 3D CAD drawing of the passive feed DMFC.. 212

Figure 6.3 – Photograph of an «in-house» designed passive feed DMFC. 213

Figure 6.4 – Anode end plate (acrylic) (a) photograph, (b) 3D CAD drawing. 214

Figure 6.5 – Cathode end plate (acrylic) (a) photograph, (b) 3D CAD drawing. 214

Figure 6.6 – Photograph of the isolating plates. 214

Figure 6.7 – Photograph of the connector plates. 215

Figure 6.8 – Comparison of the model predictions of a) polarization curves and b) power for different methanol concentrations; dots: experimental data, lines: model predictions. 218

Figure 6.9 – Comparison of the model predictions of a) polarization curves and b) power for different methanol concentrations; dots: experimental data, lines: model predictions. 219

Figure 6.10 – Comparison of the model predictions for different 1M and 3M methanol concentrations; dots: experimental published data [160], lines: model predictions. 220

Figure 6.11 – Model prediction for methanol crossover for different methanol feed concentrations. 221

Figure 6.12 – Predicted methanol concentration profiles in the cell for different current densities. Operating conditions: methanol concentration 3M. 222

Figure 6.13 – Predicted water concentration distribution in the cell at different current densities. Operating conditions: methanol concentration 3M. 222

Figure 6.14 – Model predictions of the net water transport coefficient, α, for different methanol concentrations. 223

Figure 6.15 – Influence of methanol concentration on the net water transport coefficient at different current densities. 224

Figure 6.16 – Prediction for the temperature distribution in the cell at different current densities. Operating conditions: methanol concentration 3M. 225

Figure 6.17 – Influence of methanol concentration on net water transport coefficient. 226

Figure 6.18 – Influence of anode gas diffusion layer structure on a) fuel cell performance and b) net water transport coefficient. Operating conditions: methanol concentration 5M. 228

Figure 6.19 – Influence of cathode gas diffusion layer structure on a) fuel cell performance and b) net water transport coefficient. Operating conditions: methanol concentration 5M. 229

Figure 6.20 – Influence of anode catalyst layer loadings on a) fuel cell performance and b) net water transport coefficient. Operating conditions: methanol concentration 5M. 231

Figure 6.21 – Influence of cathode catalyst layer loadings on a) fuel cell performance and b) net water transport coefficient. Operating conditions: methanol concentration 5M. 232

Figure 6.22 – Influence of MEA thickness on a) fuel cell performance and b) net water transport coefficient. Operating conditions: methanol concentration 5M. 234

Figure 6.23 – Influence of MEA properties on a) fuel cell performance and b) net water transport coefficient for commercial Nafion 117 and tailored Nafion 212. Operating conditions: methanol concentration 5M. 236

Figure 6.24 – Comparison of the experimental results, for a) polarization curves and b) power, with different reactants feeding. Structural parameters: Nafion 115. Structural parameters: anode and cathode diffusion layer 30% wet-proofed carbon cloth type A, anode catalyst loading 4mg/cm^2 Pt/Ru, cathode catalyst loading 4mg/cm^2 Pt. Operating conditions: temperature 20ºC, methanol flow rate 3 ml/min and air flow rate 3.6 l/min. 238

Figure C.1 – Effect of methanol concentration on a) cell performance. Operating conditions: methanol flow rate 8 ml/min and air flow rate 3.6 l/min. 286

Figure C.2 – Effect of methanol concentration on a) cell performance. Operating conditions: methanol flow rate 3 ml/min and air flow rate 3.6 l/min. 286

Figure C.3 – Effect of methanol concentration on a) cell performance. Operating conditions: methanol flow rate 3 ml/min and air flow rate 1 l/min. 287

Figure C.4 – Effect of fuel cell temperature on a) cell performance. Operating conditions: methanol flow rate 8 ml/min and air flow rate 3.6 l/min. 288

Figure C.5 – Effect of fuel cell temperature on a) cell performance. Operating conditions: methanol flow rate 3 ml/min and air flow rate 3.6 l/min. 288

Figure C.6 – Effect of fuel cell temperature on a) cell performance. Operating conditions: methanol flow rate 3 ml/min and air flow rate 1 l/min. 289

Figure C.7 – Effect of methanol flow rate on a) cell performance. Operating conditions: methanol concentration 0.25M and air flow rate 3.6 l/min. 290

Figure C.8– Effect of methanol flow rate on a) cell performance. Operating conditions: methanol concentration 0.75M and air flow rate 3.6 l/min. 290

Figure C.9 – Effect of methanol flow rate on a) cell performance. Operating conditions: methanol concentration 0.75M and air flow rate 1 l/min. 291

Figure C.10 – Effect of air flow rate on a) cell performance. Operating conditions: methanol concentration 0.25M and methanol flow rate 8 ml/min. 292

Figure C.11 – Effect of air flow rate on a) cell performance. Operating conditions: methanol concentration 0.75M and methanol flow rate 8 ml/min. 292

Figure C.12 – Effect of air flow rate on a) cell performance. Operating conditions: methanol concentration 0.75M and methanol flow rate 3 ml/min. 293

Figure C.13– Effect of anode diffusion layer material on a) cell performance. Operating conditions: methanol concentration 0.75M, air flow rate 3.6 l/min and cell temperature 20ºC. Design parameters: Nafion117. 294

Figure C.14 – Effect of anode diffusion layer material on a) cell performance. Operating conditions: methanol concentration 0.75M, methanol flow rate 8 ml/min and cell temperature 20ºC. Design parameters: Nafion117. 295

Figure C.15 – Effect of anode diffusion layer material on a) cell performance. Operating conditions: methanol flow rate 3 ml/min, air flow rate 3.6 l/min and cell temperature 20ºC. Design parameters: Nafion117. 295

Figure C.16 – Effect of anode diffusion layer material on a) cell performance. Operating conditions: methanol concentration 0.75M, methanol flow rate 8 ml/min and air flow rate 3.6 l/min. Design parameters: Nafion117. 296

Figure C.17 – Effect of anode diffusion layer material on a) cell performance. Operating conditions: methanol concentration 0.75M, air flow rate 3.6 l/min and cell temperature 60ºC. Design parameters: Nafion117. 296

Figure C.18 – Effect of anode diffusion layer material on a) cell performance. Operating conditions: methanol concentration 0.75M, methanol flow rate 3 ml/min and cell temperature 60ºC. Design parameters: Nafion117. 297

Figure C.19 – Effect of anode diffusion layer material on a) cell performance. Operating conditions: methanol concentration 2M, air flow rate 3.6 l/min and cell temperature 20ºC. Design parameters: Nafion117. 297

Figure C.20 – Effect of anode diffusion layer material on a) cell performance. Operating conditions: methanol concentration 2M, methanol flow rate 3 ml/min and cell temperature 20ºC. Design parameters: Nafion117. 298

Figure C.21 – Effect of anode diffusion layer material on a) cell performance. Operating conditions: methanol concentration 0.75M, air flow rate 3.6 l/min and cell temperature 20ºC. Design parameters: Nafion212. 298

Figure C.22 – Effect of anode diffusion layer material on a) cell performance. Operating conditions: methanol concentration 0.75M, methanol flow rate 8 ml/min and cell temperature 20ºC. Design parameters: Nafion212. 299

Figure C.23 – Effect of anode diffusion layer material on a) cell performance. Operating conditions: methanol flow rate 3 ml/min, air flow rate 3.6 l/min and cell temperature 20ºC. Design parameters: Nafion117.....299

Figure C.24 – Effect of anode diffusion layer material on a) cell performance. Operating conditions: methanol concentration 0.75M, methanol flow rate 8 ml/min and air flow rate 3.6 l/min. Design parameters: Nafion212.....300

Figure C.25 – Effect of anode diffusion layer material on a) cell performance. Operating conditions: methanol concentration 0.75M, air flow rate 3.6 l/min and cell temperature 60ºC. Design parameters: Nafion212.....300

Figure C.26– Effect of anode diffusion layer material on a) cell performance. Operating conditions: methanol concentration 0.75M, methanol flow rate 3 ml/min and cell temperature 60ºC. Design parameters: Nafion212.....301

Figure C.27 – Effect of anode diffusion layer material on a) cell performance. Operating conditions: methanol concentration 2M, air flow rate 3.6 l/min and cell temperature 20ºC. Design parameters: Nafion212.....301

Figure C.28 – Effect of anode diffusion layer material on a) cell performance. Operating conditions: methanol concentration 2M, methanol flow rate 3 ml/min and cell temperature 20ºC. Design parameters: Nafion212.....302

Figure C.29 – Effect of cathode diffusion layer material on a) cell performance. Operating conditions: methanol concentration 0.75M, air flow rate 3.6 l/min and cell temperature 20ºC. Design parameters: Nafion117.....303

Figure C.30 – Effect of cathode diffusion layer material on a) cell performance. Operating conditions: methanol concentration 0.75M, methanol flow rate 8 ml/min and cell temperature 20ºC. Design parameters: Nafion117.....303

Figure C.31 – Effect of cathode diffusion layer material on a) cell performance. Operating conditions: air flow rate 3.6 l/min, methanol flow rate 3 ml/min and cell temperature 20ºC. Design parameters: Nafion117.....304

Figure C.32 – Effect of cathode diffusion layer material on a) cell performance. Operating conditions: methanol concentration 0.75M, methanol flow rate 8 ml/min and air flow rate 3.6 l/min. Design parameters: Nafion117.....304

Figure C.33 – Effect of cathode diffusion layer material on a) cell performance. Operating conditions: methanol concentration 0.75M, air flow rate 3.6 l/min and cell temperature 60ºC. Design parameters: Nafion117.....305

Figure C.34 – Effect of cathode diffusion layer material on a) cell performance. Operating conditions: methanol concentration 0.75M, methanol flow rate 3 ml/min and cell temperature 60ºC. Design parameters: Nafion117.....305

Figure C.35 – Effect of cathode diffusion layer material on a) cell performance. Operating conditions: methanol concentration 2M, air flow rate 3.6 l/min and cell temperature 20ºC. Design parameters: Nafion117. 306

Figure C.36 – Effect of cathode diffusion layer material on a) cell performance. Operating conditions: methanol concentration 2M, methanol flow rate 3 ml/min and cell temperature 20ºC. Design parameters: Nafion117. 306

Figure C.37 – Effect of cathode diffusion layer material on a) cell performance. Operating conditions: methanol concentration 0.75M, air flow rate 3.6 l/min and cell temperature 20ºC. Design parameters: Nafion212. 307

Figure C.38 – Effect of cathode diffusion layer material on a) cell performance. Operating conditions: methanol concentration 0.75M, methanol flow rate 8 ml/min and cell temperature 20ºC. Design parameters: Nafion212. 307

Figure C.39 – Effect of cathode diffusion layer material on a) cell performance. Operating conditions: air flow rate 3.6 l/min, methanol flow rate 3 ml/min and cell temperature 20ºC. Design parameters: Nafion212. 308

Figure C.40 – Effect of cathode diffusion layer material on a) cell performance and b) power. Operating conditions: methanol concentration 0.75M, methanol flow rate 8 ml/min and air flow rate 3.6 l/min. Design parameters: Nafion212. 308

Figure C.41 – Effect of cathode diffusion layer material on a) cell performance and b) power. Operating conditions: methanol concentration 0.75M, air flow rate 3.6 l/min and cell temperature 60ºC. Design parameters: Nafion212. 309

Figure C.42 – Effect of cathode diffusion layer material on a) cell performance and b) power. Operating conditions: methanol concentration 0.75M, methanol flow rate 3 ml/min and cell temperature 60ºC. Design parameters: Nafion212. 309

Figure C.43 – Effect of cathode diffusion layer material on a) cell performance and b) power. Operating conditions: methanol concentration 2M, air flow rate 3.6 l/min and cell temperature 20ºC. Design parameters: Nafion212. 310

Figure C.44 – Effect of cathode diffusion layer material on a) cell performance and b) power. Operating conditions: methanol concentration 2M, methanol flow rate 3 ml/min and cell temperature 20ºC. Design parameters: Nafion212. 310

Figure C.45 – Effect of membrane thickness on a) cell performance and b) power. Operating conditions: methanol concentration 0.75M, air flow rate 3.6 l/min and cell temperature 20ºC. 311

Figure C.46 – Effect of membrane thickness on a) cell performance and b) power. Operating conditions: methanol concentration 0.75M, methanol flow rate 8 ml/min and cell temperature 20ºC. 312

Figure C.47 – Effect of membrane thickness on a) cell performance and b) power. Operating conditions: air flow rate 3.6 l/min, methanol flow rate 3 ml/min and cell temperature 20ºC. 312

Figure C.48 – Effect of membrane thickness on a) cell performance and b) power. Operating conditions: methanol concentration 0.75M, methanol flow rate 8 ml/min and air flow rate 3.6 l/min. 313

Figure C.49 – Effect of membrane thickness on a) cell performance and b) power. Operating conditions: methanol concentration 0.75M, air flow rate 3.6 l/min and cell temperature 60ºC. 313

Figure C.50 – Effect of membrane thickness on a) cell performance and b) power. Operating conditions: methanol concentration 0.75M, methanol flow rate 3 ml/min and cell temperature 60ºC. 314

Figure C.51 – Effect of membrane thickness on a) cell performance and b) power. Operating conditions: methanol concentration 2M, air flow rate 3.6 l/min and cell temperature 20ºC. 314

Figure C.52 – Effect of membrane thickness on a) cell performance and b) power. Operating conditions: methanol concentration 2M, methanol flow rate 3 ml/min and cell temperature 20ºC. 315

Figure C.53 – Effect of catalyst loading on a) cell performance and b) power. Operating conditions: methanol concentration 0.75M, air flow rate 3.6 l/min and cell temperature 20ºC. 316

Figure C.54– Effect of catalyst loading on a) cell performance and b) power. Operating conditions: methanol concentration 0.75M, methanol flow rate 8 ml/min and cell temperature 20ºC. 316

Figure C.55 – Effect of catalyst loading on a) cell performance and b) power. Operating conditions: air flow rate 3.6 l/min, methanol flow rate 3 ml/min and cell temperature 20ºC. 317

Figure C.56 – Effect of catalyst loading on a) cell performance and b) power. Operating conditions: methanol concentration 0.75M, methanol flow rate 8 ml/min and air flow rate 3.6 l/min. 317

Figure C.57 – Effect of catalyst loading on a) cell performance and b) power. Operating conditions: methanol concentration 0.75M, air flow rate 3.6 l/min and cell temperature 60ºC. 318

Figure C.58 – Effect of catalyst loading on a) cell performance and b) power. Operating conditions: methanol concentration 0.75M, methanol flow rate 3 ml/min and cell temperature 60ºC. 318

Figure C.59 – Effect of catalyst loading on a) cell performance and b) power. Operating conditions: methanol concentration 2M, air flow rate 3.6 l/min and cell temperature 20ºC. 319

Figure C.60 – Effect of catalyst loading on a) cell performance and b) power. Operating conditions: methanol concentration 2M, methanol flow rate 3 ml/min and cell temperature 20ºC. 319

Figure C.61 – Effect of anode flow field design on a) cell performance and b) power. Operating conditions: methanol concentration 0.75M, air flow rate 3.6 l/min and cell temperature 20ºC. 320

Figure C.62 – Effect of anode flow field design on a) cell performance and b) power. Operating conditions: methanol concentration 0.75M, methanol flow rate 8 ml/min and cell temperature 20ºC. 321

Figure C.63 – Effect of anode flow field design on a) cell performance and b) power. Operating conditions: air flow rate 3.6 l/min, methanol flow rate 3 ml/min and cell temperature 20ºC. 321

Figure C.64 – Effect of anode flow field design on a) cell performance and b) power. Operating conditions: methanol concentration 0.75M, methanol flow rate 8 ml/min and air flow rate 3.6 l/min. 322

Figure C.65 – Effect of anode flow field design on a) cell performance and b) power. Operating conditions: methanol concentration 0.75M, air flow rate 3.6 l/min and cell temperature 60ºC. 322

Figure C.66 – Effect of anode flow field design on a) cell performance and b) power. Operating conditions: methanol concentration 0.75M, methanol flow rate 3 ml/min and cell temperature 60ºC. 323

Figure C.67 – Effect of anode flow field design on a) cell performance and b) power. Operating conditions: methanol concentration 2M, air flow rate 3.6 l/min and cell temperature 20ºC. 323

Figure C.68 – Effect of anode flow field design on a) cell performance and b) power. Operating conditions: methanol concentration 2M, methanol flow rate 3 ml/min and cell temperature 20ºC. 324

Figure C.69 – Effect of cathode flow field design on a) cell performance and b) power. Operating conditions: methanol concentration 0.75M, air flow rate 3.6 l/min and cell temperature 20ºC. 325

Figure C.70 – Effect of cathode flow field design on a) cell performance and b) power. Operating conditions: methanol concentration 0.75M, methanol flow rate 8 ml/min and cell temperature 20ºC. 325

Figure C.71 – Effect of cathode flow field design on a) cell performance and b) power. Operating conditions: air flow rate 3.6 l/min, methanol flow rate 3 ml/min and cell temperature 20ºC. 326

Figure C.72 – Effect of cathode flow field design on a) cell performance and b) power. Operating conditions: methanol concentration 0.75M, methanol flow rate 8 ml/min and air flow rate 3.6 l/min. 326

Figure C.73 – Effect of cathode flow field design on a) cell performance and b) power. Operating conditions: methanol concentration 0.75M, air flow rate 3.6 l/min and cell temperature 60ºC. 327

Figure C.74 – Effect of cathode flow field design on a) cell performance and b) power. Operating conditions: methanol concentration 0.75M, methanol flow rate 3 ml/min and cell temperature 60ºC 327

Figure C.75 – Effect of cathode flow field design on a) cell performance and b) power. Operating conditions: methanol concentration 2M, air flow rate 3.6 l/min and cell temperature 20ºC. 328

Figure C.76 – Effect of cathode flow field design on a) cell performance and b) power. Operating conditions: methanol concentration 2M, methanol flow rate 3 ml/min and cell temperature 20ºC. 328

List of Tables

Table 1.1 – Major characteristics of different fuel cell types.....8

Table 2.1 – Comparison of different flow fields used in DMFCs.....56

Table 3.1 – Values for the parameters used in the model equations. 96

Table 3.2 – Comparison between model predictions, for the net water transport coefficient, and experimental data from Liu *et al.* [175] and absolute deviation for 60 ºC, Nafion212 at 0.15 A/cm^2. 103

Table 4.1 – Different elements of a fuel cell.....108

Table 4.2 – Different flow field designs used. 111

Table 4.3 – Specifications of MTK [179]. 116

Table 5.1 – Set of DMFC characteristics used to analyse the effect of the operating conditions on the cell performance.....128

Table 5.2 – Set of operating conditions used to analyse the effect of methanol concentration on the cell performance. 128

Table 5.3 – Set of operating conditions used to analyse the effect of cell temperature on the cell performance. 133

Table 5.4 – Set of operating conditions used to analyse the effect of methanol flow rate on the cell performance. 138

Table 5.5 – Set of operating conditions used to analyse the effect of air flow rate on the cell performance. 143

Table 5.6 – Set of operating conditions used to analyse the effect of design parameters on the cell performance. 147

Table 5.7 – Structural characteristics of the common materials used as gas diffusion layers [177, 178].....148

Table 6.1 – Values for the parameters used in the model equations. 210

Table 6.2 – Different elements of the passive feed DMFC.....213

Table A.1 – Values of parameters and uncertainties regarding the methanol concentration for the active feed DMFC.....264

Table A.2 – Values of parameters and uncertainties regarding the methanol concentration for the passive feed DMFC. 265

Table A.3 – Values of parameters and uncertainties regarding the air flow rate. 266

Table A.4 – Values of parameters and uncertainties regarding the current. 267

Table A.5 – Values of parameters and uncertainties regarding the potential. 268

Table A.6 – Values of parameters and uncertainties regarding the fuel cell power. 269

Table A.7 – Values of parameters and uncertainties regarding the fuel cell temperature. 269

Table A.8 – Values of parameters and uncertainties regarding the methanol solution temperature. 270

Table B.1 – Densities 271

Table B.2 – Specific Heat 272

Table B.3 – Thermal conductivities 273

Table B.4 – Standard enthalpies of formation 273

Table B.5 – Standard Gibbs free energy 274

Table B.6 – Viscosities 274

Table B.7 – Liquid molar volumes 275

Table B.8 – Parachors values 275

Table B.9 – Diffusion volumes 275

Table B.10 – Tortuosity 276

Table B.11 – Porosities of the common materials used as gas diffusion layers. 278

Table C.1 – Set of operating conditions used to analyse the effect of methanol concentration on the cell performance. 285

Table C.2 – Set of operating conditions used to analyse the effect of cell temperature on the cell performance. 287

Table C.3 – Set of operating conditions used to analyse the effect of methanol flow rate on the cell performance. 289

Table C.4 – Set of operating conditions used to analyse the effect of air flow rate on the cell performance. 291

Table C.5 – Set of operating conditions used to analyse the effect of design parameters on the cell performance. 293

Table C.6 – Set of design parameters used to analyse the effect of the diffusion layer material on the cell performance. 294

Table C.7 – Set of design parameters used to analyse the effect of the diffusion layer material on the cell performance. 302

Table C.8 – Set of design parameters used to analyse the effect of the membrane thickness on the cell performance. 311

Table C.9 – Set of design parameters used to analyse the effect of the catalyst loading on the cell performance. 315

Table C.10 – Set of design parameters used to analyse the effect of the anode flow field on the cell performance. 320

Table C.11 – Set of design parameters used to analyse the effect of the cathode flow field on the cell performance. 324

Nomenclature

a	specific surface area of the anode, cm^{-1}
A^S	total surface area of the channels, cm^2
A_a	active area, cm^2
A_1	total area without the holes, cm^2
A_{holes}	total area of the holes, cm^2
C	concentration, mol/cm^3
$C_{O_2,ref}$	reference concentration of oxygen, mol/cm^3
Cp	specific heat, J/(molK)
$\partial E / \partial T$	rate of change of electromotive force, V/K
D	diffusion coefficient, cm^2/s
D^{eff}	effective diffusion coefficient, cm^2/s
E_{Cell}	thermodynamic equilibrium potential, V
e	width of the channel, cm
F	Faraday´s constant, 96500 C/mol
G	Gibbs free energy, J/mol
g	gravitational acceleration, cm^2/s
H	enthalpy of reaction, J/mol
h_{mass}	mass transfer coefficient, cm/s
h_{heat}	heat transfer coefficient, $W/(cm^2K)$
I_{Cell}	cell current density, A/cm^2
I_{CH_3OH}	leakage current density due to methanol crossover, A/cm^2
$I_{0,ref}^{CH_3OH}$	exchange current density of methanol, A/cm^2
$I_{0,ref}^{O_2}$	exchange current density of oxygen, A/cm^2
j_A	volumetric current density, A/cm^3
k	constant in the rate expression (2.21)
K_{2-9}	partition coefficients
K	thermal conductivity, W/(cmK)
L	length of the active area, cm

n	number of electrons
$n_{channels}$	number of channels
n_d	electro-osmotic drag coefficient of water
N	molar flux, mol/(cm^{2}s)
P_{air}	pressure of air in cathode, atm
q	flow rate, cm^3/s
Q^{AC}	heat generated in AC, W/cm^2
Q^{CC}	heat generated in CC, W/cm^2
Q^{AF}	heat transfer to the anode stream, W/cm^2
Q^{CF}	heat transfer to the cathode stream, W/cm^2
Q	heat transfer, W/cm^2
R	ideal law gas constant, 8.314 J/(molK)
R_{Cell}	internal resistance of the fuel cell, cm^2/S
R_{cond}	conduction resistance, K/W
R_{conv}	convection resistance, K/W
R_{total}	total thermal resistance, K/W
T	temperature, K
U_{CH_3OH}	thermodynamic equilibrium potential of methanol oxidation, V
U_{O_2}	thermodynamic equilibrium potential of oxygen oxidation, V
V	volume, ml or l
V_{Cell}	cell voltage, V
w	length of the channels, cm
W_{actual}	actual electric work, W
$W_{maximum}$	maximum work, W
x_{CH_3OH}	mole fraction of methanol, mol/mol
x	coordinate direction normal across the cell, cm
Y	parameter

Greek

Δ	variation
α	net water transport coefficient
α_A	anodic transfer coefficient
α_C	cathodic transfer coefficient
β	coefficient of volume expansion, 1/K
δ	thickness, cm or uncertainty (Appendix A)
ε	porosity
η	overpotential, V or total energy efficiency (eq. 2.8)
η_{fuel}	fuel efficiency
η_{rev}	thermodynamic efficiency
$\eta_{voltaic}$	voltaic efficiency
κ	ionic conductivity of the membrane, S/cm
λ	constant in the rate expression, mol/cm^3
μ	dynamic viscosity, g/(cms)
ν	kinematic viscosity, cm^2/s
ρ	density, g/cm^3
υ_{O_2}	stoichiometric coefficients of oxygen in the cathode reaction
υ_{H_2O}	stoichiometric coefficients of water in the cathode reaction
υ_{cross,O_2}	stoichiometric coefficients of oxygen in the undesired cathode
υ_{cross,H_2O}	stoichiometric coefficients of water in the undesired cathode
ξ_{CH_3OH}	electro-osmotic drag coefficient of methanol

Subscripts

A	anode
air	air
C	cathode
Cell	fuel cell
CH_3OH	methanol
fin	fin

final	final
i	species i
initial	initial
j	species j
H_2O	water
O_2	oxygen

Superscripts

0	feed conditions
AAP	anode aluminum/acrylic plate
ACP	anode copper plate
AC	anode catalyst layer
AD	anode diffusion layer
AF	anode flow channel
ARP	anode rubber plate
CAP	cathode aluminum/acrylic plate
CC	cathode catalyst layer
CCP	cathode copper plate
CD	cathode diffusion plate
CF	cathode flow channel
CRP	cathode rubber plate
G	graphite
l	plate l
M	membrane
t	plate t

Acronyms

1D	One dimension
2D	Two dimensions
3D	Three dimensions
AAP	Anode Aluminum Plate
AC	Anode Catalyst
ACP	Anode Copper Plate
AD	Anode Diffusion
AF	Anode Compartment or Anode Flow Channel
AFC	Alkaline Fuel Cell
ARP	Anode Rubber Plate
BPPO	Bromomenthylated poly(2,6-dimethyl-1,4-phennylene oxide)
CAD	Computer Aided Design
CAP	Cathode Aluminum Plate
CC	Cathode Catalyst
CCP	Cathode Copper Plate
CD	Cathode diffusion
CEFT	Centro de estudos de Fenómenos de Transporte
CF	Cathode Compartment or Cathode Flow Channel
CFD	Computational Fluid Dynamics
CRP	Cathode Rubber Plate
CS	Crosslinked Chitosan
CSTR	Continuous Stirred Tank Reactor
DFC	Direct Fuel Cell
DMFC	Direct Methanol Fuel Cell
DPS	Diphenylsilicate
FCT	Fundação para a Ciência e a Tecnologia
FEDER	Fundo Europeu de Desenvolvimento Regional
FEUP	Faculdade de Engenharia da Universidade do Porto
GDL	Gas Diffusion Layer
GE	General Electric
HL	High Loading

LB	Loadbank
LDH	Layered Double Hydroxides
MCFC	Molten Carbonate Fuel Cell
MEA	Membrane Electrode Assemblies
MFC	Mass Flow controller
MFF	Mixed Flow Field
MHS	Methanol Handling System
MMT	Montmorillonite
MP	Micropump
MPL	Microporous Layer
MSFF	Multi Serpentine Flow Field
MTK	Methanol Test Kit
NASA	National Aeronautics and Space Administration
PAFC	Phosphoric Acid Fuel Cell
PBI	Phosphoric Acid-doped Polybenzimidazole
PEM	Polymer Electrolyte Membrane
PEMFC	Polymer Electrolyte Membrane Fuel Cell
PF	Pore-Filling
PFF	Parallel Flow Field
POP	Sulphonate substituted Polyoxiphenylenes
PTFE	Polytretrafluoroethylene (Teflon)
SFF	Single Serpentine Flow Field
SL	Standard loading
SOFC	Solid Oxide Fuel Cell
SPEEK	Sulfonated poly(etheretherketone)
SPI	Sulfonated Polyimide
TC	Thermocouple

Motivation, objectives and thesis layout

Fuel cells are extensively being studied today because of their potential as an alternate energy converter for a wide range of applications. Fuel cells have unique technological attributes: efficiency, absence of moving parts and very low emissions. In particular, the proton-exchange membrane (PEM) fuel cells (FCs) are today in the focus of interest as one of the most promising developments in power converters. Among the different types of PEMFCs the Direct Methanol Fuel Cells (DMFCs) are being investigated with a high degree of motivation as portable power sources due to their higher power density, instant recharging and smaller size than batteries. Representing the market segment closest to achieve widespread use by consumers, the small power Direct Methanol Fuel Cells (in particular the micro DMFCs) will probably induce them to believe and accept the fuel cells as an emerging technology, contributing in this way for an energetic paradigm shift.

The main motivation of the present work was to intensively study small power direct methanol fuel cells operating close to ambient conditions bearing in mind the portable applications of this type of fuel cells. An integrated approach was followed toward DMFC optimization: the development of a mathematical model incorporating the main transfer processes as well as the electrochemical reactions, to validate the model and in a last step to use the model to set–up optimized conditions leading to enhanced fuel cell performances.

This PhD thesis results from the work carried out at CEFT (Centro de Estudos de Fenómenos de Transporte) in the Chemical Engineering Department of Faculty of Engineering in Oporto University (FEUP), throughout the period between February 2005 and August 2009.

The initial goals of this work were the modelling and experimental studies on an «in-house» active feed direct methanol fuel cell (DMFC). Based on recent state-of-the-art, concerning the DMFC development, it was verified that the passive feed DMFC systems were, probably, the first to be commercialized. In this way, work with a designed passive feed DMFC was also developed.

This thesis is organized in seven principal Chapters. The first Chapter considers a general introduction concerning the fuel cells, with a systematic description of the different fuel cell types.

Chapter 2 is devoted to the description of the direct methanol fuel cells and to the review of the state-of-the-art focused in experimental and modelling studies. The advances in new materials and new designs for DMFCs in order to achieve the best fuel cell performance are described. Recent work and advances in passive DMFCs are also presented.

The Chapters 3, 4 and 5, are devoted to the active feed direct methanol fuel cell. In Chapter 3, the developed mathematical model for an active feed DMFC is presented. The general model structure, the major model assumptions and the governing equations and boundary conditions concerning the mass and the heat transport are described.

In Chapter 4 the experimental setup and experimental procedure as well as the active feed fuel cell design are provided.

In Chapter 5, the experimental results obtained with the designed active feed DMFC are presented as well as the model predictions for the polarization and power density curves.

In Chapter 6 the results of the study of a designed passive feed direct methanol fuel cell are presented: model development, experimental setup, experimental results and cell optimization.

Finally, the main conclusions of the present work are summarized and lines of possible future work are suggested in Chapter 7.

CHAPTER 1

1. INTRODUCTION

In this Chapter, basic elements involved in Fuel Cells systems are described. A brief explanation of the importance of fuel cells in our society and a historic perspective of fuel cells is also, provided. A brief overview of the different fuel cell types, major characteristics and advantages and disadvantages is presented as well as, market perspectives for fuel cells.

1.1. Fuel cells

A fuel cell is an electrochemical device that continuously converts chemical energy into electric energy as long as fuel and oxidant are supplied (Fig. 1.1). Fuel cells therefore have similarities both to batteries and to engines. With batteries, fuel cells share the electrochemical nature of power generation process and with engines, they share the continuously work consuming a fuel of some type. A fuel cell operates quietly and efficiently and when hydrogen is used as fuel it generates only power and water a so-called zero emission engine. A difference between a fuel cell and a battery is that a fuel cell generates by-products and the system is required to manage those. A battery also generates some heat but at a much lower rate that usually does not require any special or additional equipment.

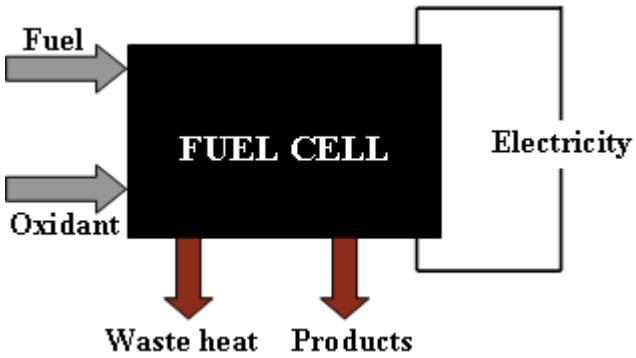

Figure 1.1 – Schematic representation of a fuel cell generating electricity from a fuel.

A fuel cell can convert over than 90% of the chemical energy of a fuel into electricity. Typical reactants for fuel cells are hydrogen and oxygen, however neither of them has to be in its pure form. Hydrogen may be present either in a mixture with other gases, such as carbon dioxide, nitrogen and carbon monoxide, or in hydrocarbons such as natural gas and methane, or even in liquid hydrocarbons such as methanol. Ambient air contains enough oxygen to be used as oxidant in fuel cells.

1.2. Fuel cells in society

There are two major problems with using fossil fuels, which meet about 80% of the world energy demand. The first problem is that they are limited in amount and sooner will be depleted. This means that there will be a disparity between demand and availability of fossil fuels. The second problem is that fossil fuels, coal, oil and natural gas are causing serious environmental problems, such as consumption and pollution of water, air pollution, ozone layer depletion, climate change melting of ice, creation of toxic wastes, damages in plants and animal life and global warming. Using nuclear fuels as an alternative, poses serious safety risks due to the amount of radiation contained in their products. Renewable energy resources emerge as a solution for this global issue.

Renewable energy resources can provide many immediate environmental benefits by avoiding the impacts caused by using fossil fuels as energy sources and risks and can help conserve fossil resources for future generations. Of course, renewable energy also has environmental impacts. For example, biomass plants produce some emissions, and fuel can be harvested at unsustainable rates. Wind farms change the landscape, and some have harmed birds. Hydroprojects, if their impacts are not mitigated, can greatly affect wildlife and ecosystems. However, these impacts are generally much smaller and more localized than those of fossil and nuclear fuels. Care must nevertheless be taken to mitigate them. Despite the advantages of using renewable energy these sources are insufficient to produce the amount of world energy demanded which has been growing exponentially. As a result fuel cells appear as an efficiently and environmentally friendly solution and a complement to renewable energy. Fuel cells can provide increased efficiency, greater scaling flexibility, reduced emissions and other advantages compared to conventional power technologies.

Early in the 1970s Hydrogen Energy System had been proposed as a solution for the problems caused by using fossil fuels to produce energy. Since then, during the last quarter of last century, through research and development work in universities and research laboratories around the world, foundations of the Hydrogen Energy System have been established.

Hydrogen is an excellent energy carrier with many unique properties. It is the lightest, most efficient and cleanest fuel. Through electrochemical processes, the hydrogen can be converted to electricity in fuel cells with higher efficiencies than conversion of fossil fuels to mechanical energy in internal combustion engines or to electrical energy in thermal power plants. This unique property of hydrogen has made hydrogen fuel cells the power plant of choice for car companies and power plants companies. It is possible that during the next years fuel cells can replace the heat engines as hydrogen replaces fossil fuels. However, the feasibility of hydrogen as energy carrier depends on price advantage, production costs, transport, logistic and storage.

The concept of hydrogen economy is not new, many scientist in the beginning of the 20th century described the production, storage and application possibilities of hydrogen. As shown schematically in Fig. 1.2, hydrogen fuel cells are coupled with electrolysers and renewable energy technologies to provide a completely closed-loop, pollution free energy economy. When the sun is shining or the wind is blowing, the electricity produced from solar and wind energy would be used to power cities directly while production extra hydrogen on the side via electrolysis. Anytime the wind stops or night falls, however, the fuel cells could be dispatched to provide on-demand power by converting the stored hydrogen into electricity. While the hydrogen economy does not become a reality, it is important to realize that fuel cells have found, and will continue to find niche applications. These applications should continue to drive forward progress for decades to come.

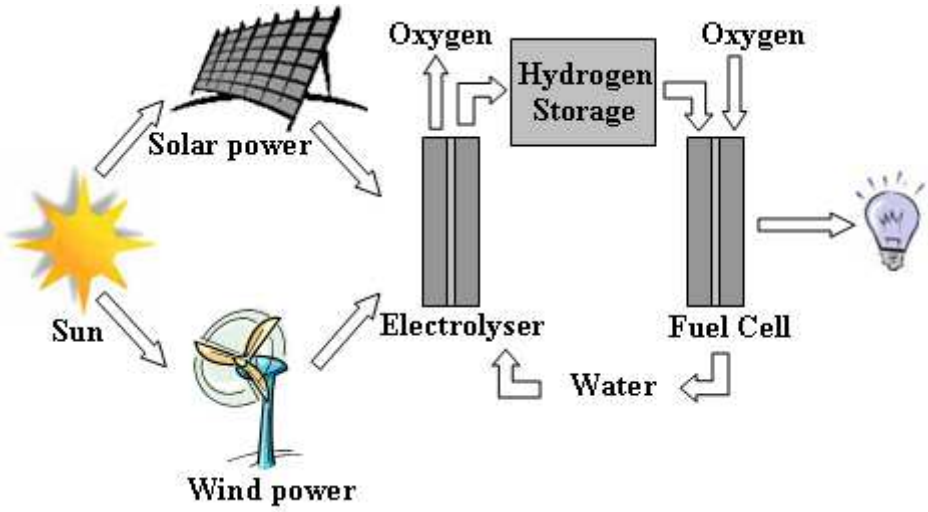

Figure 1.2 – Schematic representation of hydrogen economy.

1.3. History of fuel cells

Fuel cells are really not new! Sir William Robert Grove developed the first fuel cell in England in 1838. Grove believed that if he did the reverse of the electrolysis process (use electricity to split water into hydrogen and oxygen) he would be capable to produce electricity and water. He enclosed two platinum strips in separate sealed bottles. One bottle containing hydrogen and the other oxygen. When these bottles were immersed in dilute sulphuric acid, a current began to flow between the two electrodes and water was formed in the gas bottles. To increase the voltage produced, Grove linked several of these devices in series and produced what he referred to as a "gas battery"- the first fuel cell.

In 1889, Ludwig Mond and his assistant Carl Langer attempted to build the first practical device using air and industrial coal gas. Friedrich Wilhelm Ostwald, a founder of the field of physical chemistry, provided much of the theoretical understanding of how fuel cells operate. In 1893, he experimentally determined the interconnected roles of the various components of the fuel cell: electrodes, electrolyte, oxidizing and reducing agents, anions, and cations. Grove had speculated that the action in his gas battery occurred at the point of contact between electrode, gas, and electrolyte, but did not explain further. Ostwald, drawing on his pioneering work in relating physical properties and chemical reactions, solved the puzzle of Grove's gas battery. His exploration of the underlying chemistry of fuel cells laid the groundwork for later fuel cell researchers.

Scientists and engineers soon learned that they would have to overcome many hurdles if this new technology was to be commercialized. By the end of the nineteen century, the internal combustion engine was emerging and the widespread exploitation of fossil fuels sent the fuel cell the way of scientific curiosity.

Francis Thomas Bacon wrote a major Chapter in the fuel cell story. In 1932, he resurrected the machine developed by Mond and Langer and implemented a number of modifications to the original design. He replaced the platinum electrodes by less expensive nickel gauze. He also substituted the sulphuric acid electrolyte for alkali potassium hydroxide, a substance less corrosive to the electrodes. This device, which he named the "Bacon Cell," was in essence the first alkaline fuel cell. After 27 years Bacon produced a truly workable fuel cell. In 1959, Bacon demonstrated a machine capable of producing 5 kW of power, enough to power a welding machine.

In 1955 a scientist working at General Electric (GE) modified the original fuel cell design. Willard Thomas Grubb used a sulphonated polystyrene ion-exchange membrane as the electrolyte. Three years later another GE chemist, Leonard Niedrach, devised a way of depositing platinum onto this membrane, which ultimately became known as the "Grubb-Niedrach fuel cell." GE and NASA developed this technology together resulting in its use on the Gemini space project. This was the first commercial use of a fuel cell.

In the early 1960s, aircraft engine manufacturer Pratt & Whitney licensed the Bacon patents for the Alkaline Fuel Cell. With the goal of reducing the weight and designing a longer-lasting fuel cell than the GE PEM design, Pratt & Whitney improved the original Bacon design. As a result, Pratt & Whitney won a contract from NASA to supply these fuel cells to the Apollo spacecraft. Alkali cells have ever since been used on most subsequent manned United States space missions, including those of the Space Shuttle.

The oil embargos of 1973 and 1979 helped to push along the research effort of the fuel cell as the United States Government was looking for a way to become less dependent on petroleum imports. A number of companies and government organizations began serious research into overcoming the obstacles to widespread commercialization of fuel cells. Throughout the 1970s and 1980s, a large research effort was devoted to developing the materials needed, identifying the optimum fuel source and drastically reducing the cost of this technology. During the 1980s, fuel cell technology began to be tested by utilities and automobile manufacturers. Technical breakthroughs during the decade included the development of the first marketable fuel cell powered vehicle in 1993 by the Canadian company, Ballard.

1.4. Fuel cell description

Fuel cells work via an electrochemical reaction that converts the chemical energy stored in a fuel directly into electricity. This conversion involves an energy transfer step, where the energy from the fuel source is passed along to the electrons constituting the electric current. This transfer has a finite rate and must occur at an interface or reaction surface. It is clear that the amount of electricity produced depends on the amount of reaction surface area or interfacial area available for the energy transfer. Larger surface areas lead to larger currents. To provide large reaction surfaces, fuel cells are made into thin planar structures and the electrodes used are highly porous. One side is provisioned with fuel (anode side) and the other with oxidant (cathode side). A thin electrolyte layer separates the fuel and the oxidant electrodes and ensures that the two half reactions occur isolated from each other.

There are a variety of types of fuel cells which utilize different electrochemical reactions but the general process is always the same. Figure 1.3 shows a cross sectional view of a general fuel cell illustrating the major steps in electricity generation.

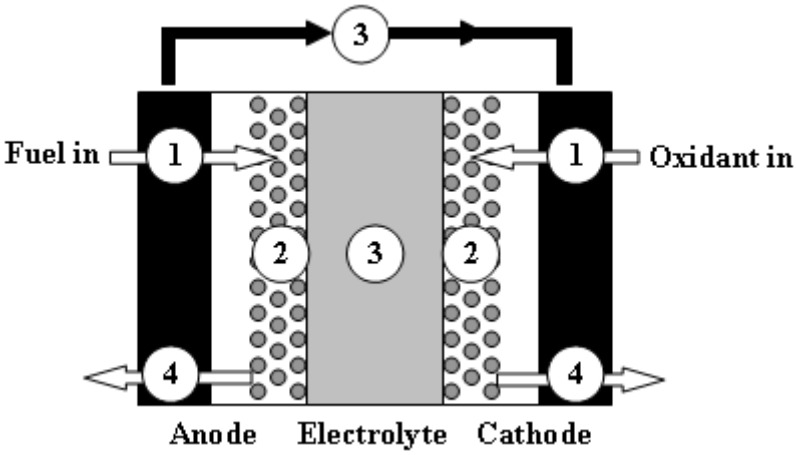

Figure 1.3 – Cross section of general fuel cell.

In step 1 the reactants, fuel and oxidant, are delivered into the fuel cell. Although this step seems to be a simple one, it can be quite complex, because for a fuel cell to produce electricity it must be continually supplied with fuel and oxidant and when operated at high current densities the demand for reactants is very high. The delivery of reactants is more efficient using flow field plates which have many fine channels or

grooves to carry the gas flow and distribute it over the surface of the fuel cell. The shape, size and pattern flow channels can influence the performance of the fuel cell.

In step 2 the electrochemical reactions take place at the electrodes. The current generated by the fuel cell is directly related to how fast the electrochemical reactions proceed. Fast electrochemical reactions result in a high current output from the fuel cell. To increase the speed and efficiency of the electrochemical reactions, catalysts are used.

The electrochemical reactions occurring in the previous step either produce or consume ions and electrons. The ions and electrons produced in one electrode must be consumed at the other one. In step 3 the ions are conducted through the electrolyte and electrons through the external circuit. In addition to electricity, all fuel cell reactions will generate at least one product and heat. If these products are not removed they will accumulate over time preventing the new fuel and oxidant from being able to react. In step 4 the products formed in the electrochemical reactions are removed from the fuel cell.

An ideal fuel cell would supply any amount of current while maintaining a constant voltage determined by thermodynamics. In real fuel cells, however, the actual voltage output is less than the ideal thermodynamically predicted voltage due to irreversible losses. There are three major types of losses (activation, ohmic and mass transport region) each of these associated with one of the basic steps mentioned above. Each type of losses can be the predominant loss factor depending on the cell voltage and current density. The activation loss is due to electrochemical reaction since the reactions take more energy to catalyze than in the ideal case. The activation barrier is the major factor contributing to inefficiency when operating a cell at high voltage and low current density. In the middle of operating range the predominant loss is the Ohmic loss and is due to ionic and electronic conduction. At very high current densities, the major loss is the concentration loss due to mass transport. An example of a fuel cell polarization curve with the three losses is provided in Fig. 1.4.

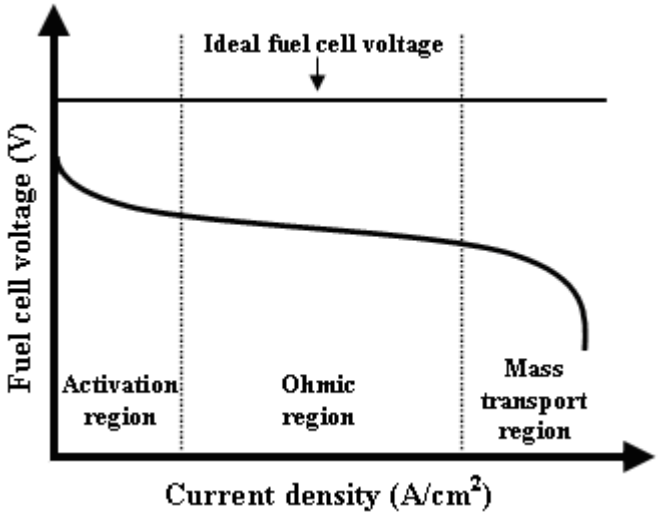

Figure 1.4 – Schematic representation of fuel cell polarization curve.

1.5. Fuel cell types

Fuel cells are classified by their electrolyte material. At the present time, there are several types of fuel cells that are being developed for different applications. While all different fuel cells types are based upon the same underlying electrochemical principles, they all operate at different range of temperature, incorporate different materials and often differ in their fuel tolerance and performance characteristics, as shown in Table 1.1.

Table 1.1 – Major characteristics of different fuel cell types.

Fuel cell type	Electrolyte	Charge carrier	Operating temperature	Fuel compatibility
PEMFC	Polymer membrane	H^+	20-80ºC	Hydrogen
DMFC	Polymer membrane	H^+	20-80ºC	Methanol
AFC	Liquid potassium hydroxide	OH^-	60-220ºC	Hydrogen
PAFC	Liquid phosphoric acid	H^+	200ºC	Hydrogen
MCFC	Molten carbonate	CO_3^{2-}	650ºC	Hydrogen and Methane
SOFC	Ceramic	O^{2-}	600-1000ºC	Hydrogen, Methane and Carbon monoxide

1.5.1. Polymer Electrolyte Membrane Fuel Cell (PEMFC)

Polymer Electrolyte Membrane fuel cells use a polymer membrane as the electrolyte. This polymer is permeable to protons who are the ionic charge carriers. The fuel used in this type of fuel cells is hydrogen and the oxidant pure oxygen or from the air. At the anode, the hydrogen molecule is split into hydrogen ions (protons) and electrons. The protons pass through the electrolyte to the cathode while the electrons flow through an external circuit and produce electric power. Oxygen is supplied to the cathode and combines with the electrons and the protons to produce water. The reactions at the electrodes are as follows:

Anode reaction: $H_2 \rightarrow 2H^+ + 2e^-$ (1.1)

Cathode reaction: $\frac{1}{2}O_2 + 2H^+ + 2e^- \rightarrow H_2O$ (1.2)

Overall reaction: $H_2 + \frac{1}{2}O_2 \rightarrow H_2O$ (1.3)

Compared to other types of fuel cells, PEMFCs generate more power for a given volume or weight of fuel cell making them compact and lightweight. The operation temperature is less than 100ºC, which allows rapid star-up. Since this type of fuel cells uses a solid material as electrolyte, the sealing of the anode and cathode gases is simpler and therefore less expensive to manufacture. The solid electrolyte has fewer problems with corrosion thus leading to a longer cell and stack life. Due to their advantages PEMFCs are believed to be the best type of fuel cell as the vehicular power source to replace the Otto and Diesel internal combustion engines.

1.5.2. Direct Methanol Fuel Cell (DMFC)

Direct methanol fuel cell is similar to the PEMFC since the electrolyte is a polymer and the charge carrier is the hydrogen ion (proton). However the DMFC draws hydrogen from liquid methanol eliminating the need of a reformer. In this point of work no further

information is given about DMFC since Chapter 2 is devoted to an extensive explanation of this type of fuel cell.

1.5.3. Alkaline Fuel Cell (AFC)

Alkaline fuel cells use an electrolyte that is an aqueous solution of potassium hydroxide (KOH) retained in a porous stabilized matrix. The concentration of the solution can be varied with the fuel cell operating temperature, which ranges from 65 to 220ºC. The charge carrier for an AFC is the hydroxyl ion (HO^-) that passes through the electrolyte from the cathode to the anode where it reacts with hydrogen to produce water and electrons. Water formed at the anode migrates back to the cathode to regenerate hydroxyl ions. The reactions in this type of fuel cell produce electricity and heat. The reactions that take place on the anode and cathode side are:

Anode reaction: $H_2 + 2OH^- \rightarrow 2H_2O + 2e^-$ (1.4)

Cathode reaction: $\frac{1}{2}O_2 + H_2O + 2e^- \rightarrow 2OH^-$ (1.5)

Overall reaction: $H_2 + \frac{1}{2}O_2 \rightarrow H_2O$ (1.6)

Alkaline fuel cells are one of the most developed technologies and, as referred above, have been used since the mid-1960s by NASA in the Apollo and Space Shuttle programs.

AFCs are the cheapest fuel cells to manufacture because the catalyst that is required at the electrodes can be any of a number of different materials that are relatively inexpensive compared to the catalysts required for other types of fuel cells. Their sensitivity to poisoning, which requires use of pure or cleansed hydrogen and oxygen, is an insuperable obstacle at the present time. Conversely, AFCs operate at relatively low temperatures and are among the most efficient fuel cells, characteristics that would enable a quick starting power source and high fuel efficiency, respectively.

1.5.4. Phosphoric Acid Fuel Cell (PAFC)

The Phosphoric Acid Fuel Cells (PAFCs) use as electrolyte the phosphoric acid that can approach high concentrations. The ionic conductivity of phosphoric acid is low at low temperatures, so PAFCs are operated at higher temperature ranges.

The charge carrier in this type of fuel cell is the hydrogen ion (proton). Similar to the PEMFC, the hydrogen introduced at the anode is split into its protons and electrons. The protons migrate through the electrolyte and combine with the oxygen, usually from air, at the cathode to form water. The electrons are routed through an external circuit where they can perform useful work. These reactions produce electricity and heat as by product. The reactions that take place at the anode and cathode side are:

Anode reaction: $H_2 \rightarrow 2H^+ + 2e^-$ (1.7)

Cathode reaction: $\frac{1}{2}O_2 + 2H^+ + 2e^- \rightarrow H_2O$ (1.8)

Overall reaction: $H_2 + \frac{1}{2}O_2 \rightarrow H_2O$ (1.9)

The high efficiency of the PAFC when operated in cogeneration mode is one advantage of this fuel cell type. In addition, CO_2 (carbon dioxide) does not affect the electrolyte or cell performance and can therefore be easily operated with reformed fossil fuel. Simple construction, low electrolyte volatility and long-term stability are additional advantages. Such characteristics have made the PAFC a good candidate for early stationary applications.

1.5.5. Molten Carbonate Fuel Cell (MCFC)

Molten Carbonate Fuel Cells (MCFCs) work quite differently from other fuel cells since they use an electrolyte composed of a molten mixture of carbonate salts. The two mixtures that can be used are lithium carbonate and potassium carbonate. To melt the carbonate salts and achieve high ion mobility through the electrolyte, the MCFCs operate at high temperatures.

When heated these salts melt and become conductive to carbonate ions (CO_3^{2-}). These ions flow from the cathode to the anode where they combine with hydrogen to give water, carbon dioxide and electrons. These electrons pass through an external circuit back to the cathode, generating electricity and heat. The reactions that take place on the anode and cathode side are as follows:

Anode reaction: $CO_3^{2-} + H_2 \rightarrow H_2O + CO_2 + 2e^-$ (1.10)

Cathode reaction: $CO_2 + \frac{1}{2}O_2 + 2e^- \rightarrow CO_3^{2-}$ (1.11)

Overall reaction: $H_2 + \frac{1}{2}O_2 \rightarrow H_2O$ (1.12)

The Molten Carbonate Fuel Cell (MCFC) is in the class of high temperature fuel cells. At the higher operating temperature, fuel reforming of natural gas can occur internally, eliminating the need for an external fuel processor. Additional advantages include the ability to use standard materials for construction, such as stainless steel sheet, and allow the use of nickel-based catalysts on the electrodes. The by-product heat, from an MCFC, can be used to generate high pressure steam that can be used in many industrial and commercial applications. However, the high temperature requires significant time to reach operating conditions and responds slowly to changing power demands. These characteristics make MCFCs more suitable for constant power applications. The carbonate electrolyte can also cause electrode corrosion problems. Furthermore, since CO_2 is consumed at the cathode and transferred to the anode, introduction of CO_2 and its control in air stream becomes an important issue for achieving optimum performance.

1.5.6. Solid Oxide Fuel Cell (SOFC)

The Solid Oxide Fuel Cell (SOFC) is currently the highest temperature fuel cell in development. To operate at such high temperatures, the electrolyte is a thin, solid ceramic material (solid oxide) that is conductive to oxygen ions (O^{2-}), the charge carrier in the SOFC. At the cathode, the oxygen molecules from the air are split into oxygen

ions with the addition of four electrons. The oxygen ions are conducted through the electrolyte and combine with hydrogen at the anode, releasing four electrons. The electrons travel an external circuit providing electric power and producing heat.

Anode reaction: $2H_2 + 2O^{2-} \rightarrow 2H_2O + 4e^-$ (1.13)

Cathode reaction: $O_2 + 4e^- \rightarrow 2O^{2-}$ (1.14)

Overall reaction: $2H_2 + O_2 \rightarrow 2H_2O$ (1.15)

The high temperature operation of the SOFC enables them to tolerate relatively impure fuels, such as those obtained from the gasification of coal or gases from industrial process and other sources. However, the high temperatures require more expensive materials of construction and result in a significant time required to reach operating temperature and a slow answer to changes in electricity demand.
The SOFCs are, therefore, considered to be a leading candidate for high power applications including industrial and large-scale central electricity generating stations.

1.6. Advantages and disadvantages

Fuel cells are a very promising energy technology with several possible applications due to their many attractive properties when compared with conventional energy conversion technologies, namely:

- Low Emissions – Fuel cells operating on hydrogen generate zero emissions since the only products are water and unused air. If methanol is used instead of hydrogen, some emissions are generated, including carbon dioxide. Although these emissions are much lower than those of comparable conventional energy conversion technologies.
- High efficiency – Since fuel cells do not use combustion, their efficiency is not linked to their maximum operating temperature. As a result, the efficiency of the power conversion step (the actual electrochemical reaction as opposed to the

actual combustion reaction) can be significantly higher than that of thermal engines.

- Refuelling time – Fuel cell systems do not require recharging. Rather, fuel cell systems must be refuelled, which is faster than charging a battery and can provide greater range depending on the size of the storage tank.
- No moving parts and long life – Since fuel cells does not have any moving parts, it may be expected to exhibit a long life.
- Modular – fuel cells are modular so more power may be generated simply by adding more cells. Mass produced fuel cells may be significantly less expensive than traditional power plants.
- Size and weight – fuel cells may be made in a variety of sizes which makes them useful in a variety of applications, from powering electronic devices to powering entire buildings.

Despite their numerous advantages fuel cells presented some disadvantages:

- Hydrogen – Hydrogen which is of such benefit environmentally when used in a fuel cell, is also its greatest liability because it is difficult to manufacture and store. Current manufacturing processes are expensive and energy intensive, and often derive ultimately from fossil fuels.
- Contaminants sensitivity – Fuel cells require relatively pure fuel, free of specific contaminants. These contaminants can deactivate the fuel cell catalyst effectively destroying its ability to operate.
- High cost catalyst – Fuel cells suitable for automotive applications typically require the use of a platinum catalyst to promote the power generation reaction and platinum is a rare and expensive metal.
- New technology – Fuel cells are an emerging technology. So the reductions in cost, weight and size along with increases in reliability and lifetime are needed.

1.7. Applications

As the understanding and technology for fuel cells grow, and the concern over world petroleum reserves and the environmental impact of its combustion increases, fuel cells emerge as one of the possible solutions to provide clean energy production. Since fuel cells can be stacked to increase energy output depending on the demand, they have a wide range of uses. There are three main sectors of applications where fuel cells could play an important role in the future: transportation, stationary power, and portable power (Fig. 1.5).

Figure 1.5 – Examples of fuel cell applications (Courtesy of Honda, Ballard, Samsung, Shell, Jadoo, Motorola, Suzuki, Company's XX25, Pearl Hydrogen, Yamaha, DaimlerChrysler and Plug Power Inc.)

1.7.1. Transportation

A key commercial application of fuel cells is to possibly replace the internal combustion engine in transportation applications. A great deal of excitement and potential lies in the market opportunity for fuel cell vehicles. Today, all of the major automobile manufacturers and several related companies are developing prototype fuel cell vehicles

to investigate this possibility. Some of the companies involved in the area are DaimlerChrysler, Ford, General Motors, Honda, Hyundai, Mazda, Mitsubishi Motors, Nissan, PSA Peugeot, Citroen, Renault and Toyota Motor Corporation. There are many vehicles in various stages of demonstration and development. Since Ballard revealed the world's first fuel cell bus in 1993, approximately twenty five fuel cell buses have been built and operated worldwide. Fuel cells can also be used in trucks, scooters, bicycles, utility vehicles (wheel chair), golf carts, airplanes, space shuttles, space orbiters and locomotives. In the shipping area, development work is underway in the area of propulsion as well as auxiliary power for cruise ships, powered barges, ferry boats, offshore supply boats, push-tow boats, oceangoing tugs, submersibles, and even submarine tankers. Fuel cells have also been suggested for use as power sources for ports, offshore oil platforms, underwater facilities, and for refrigeration on containerships. For transportation applications of fuel cells, one of the most important developments involves fuel handling and fuel processing. For example, the proton exchange membrane fuel cell (PEMFC), which is considered to be the primary candidate for transportation propulsion applications, needs a pure, clean hydrogen fuel. Therefore, stringent requirements must be placed on the processing of transportation fuels like gasoline and methanol to eliminate compounds that could poison the cells. The development of compact, efficient, cost-effective, high purity, hydrogen producing reformer technology is a key requirement. An alternative strategy to relieve the need for on-board reformation of liquid transportation fuels is the storage and direct use of hydrogen. This approach will require significant advances in the storage of hydrogen using metal hydrides, carbon nano-tubes, or crash-worthy, high pressure hydrogen tank technology. A significant development of the hydrogen supply infrastructure would be needed as well.

1.7.2. Stationary power

Fuel cells could potentially produce electricity for homes, commercial, institutions, and industry through stationary power plants. Sizes range from 1 kilowatt to several megawatts (enough to power institutions or factories). Some fuel cell developers for stationary applications are Avista Labs (PEMFC), Ebara Ballard (PEMFC), Fuel Cell Energy (MCFC), Fuel Cell Technologies (SOFC), GE Microgen (PEMFC), General

Motors (PEMFC), H Power (PEMFC), Idatech (PEMFC), Matsushita Electric Industrial Co Ltd (PEMFC), Nuvera (PEMFC), Plug Power, Inc. (PEMFC) and UTC Fuel Cells (PAFC, PEMFC). In residential applications, small fuel cell power plants could be installed for the production of both electricity and heat or hot water for homes utilization. Industrial applications refering to general group of large-scale applications that typically incorporate multiple buildings include universities and colleges, prisons, government or military facilities. In these applications, the ability to generate electricity and heat onsite has multiple benefits including the utilization of heat for air cooling, laundry facilities, cafeteria facilities, preheating water for onsite boilers. Commercial application refers to applications that are connected to a business. Examples include an apartment building or complex, an office building, strip mall or a hotel. Stationary power applications of fuel cells will require the development of low-cost, reliable, and efficient power inverter and grid interface technology. Power inversion is required to convert the direct current power produced ordinarily by the fuel cell stack into the alternating current on the utility grid. Also, control technology is needed to achieve reliable and cost-effective operation of fuel cells and to produce high-quality power. The balance of plant considerations such as pumps, valves, piping, controls, and power electronics require advancement in reliability, cost, and optimization for fuel cell applications.

1.7.3. Portable power

Fuel cells will change the telecommunication world, powering cellular phones, laptops and palm pilots hours longer than batteries. Companies have already demonstrated fuel cells that can power cell phones for 30 days without recharging and laptops for 20 hours. Other applications for fuel cells include pagers, video recorders, portable power tools, and low power remote devices such as hearing aids, smoke detectors, burglar alarms, hotel locks and meter readers. Most of the portable applications have used PEMFC although nowadays the Direct Methanol Fuel Cells is an area of intense research and development. Some companies involved in the area of portable fuel cells are Casio, Direct Methanol Fuel Cell Corporation, Hitachi, MTI Micro Fuel Cells, Motorola, Panasonic, Samsung Advanced Institute of Technology, Sanyo, Smart Fuel Cells and Toshiba.

CHAPTER 2

2. DIRECT METHANOL FUEL CELLS: STATE-OF-THE-ART

This Chapter starts with a brief introduction recalling the Direct Methanol Fuel Cell Technology. Then the basic fundamentals of an active feed DMFC and of a passive feed DMFC are presented. An intensive review on the recent work done in active and passive DMFC experimental and modelling studies is described. Finally examples of DMFC applications are reported.

The contents of this Chapter were partially published in Oliveira, V.B, Falcão, D.S., Rangel, C.M. and Pinto, A.M.F.R., "A comparative study of approaches to direct methanol fuel cells modelling", International Journal of Hydrogen Energy, Vol. 32, Issue 3, March 2007 415-424.

2.1. Introduction

Within the last years, the interest in fuel cells of all types has increased dramatically, due to high efficiencies, nonexistence of gaseous pollutants (sulphur dioxide and various nitrogen oxides), simplicity and absence of moving parts leading to the conclusion that a one possible alternative for internal combustion engines was found. Particular attention was devoted to the polymer electrolyte membrane fuel cells (PEMFCs). Hydrogen emerges as the best fuel for the cell in terms of operating the fuel cell itself, although the production, storage and distribution of this fuel are complex issues. Alternatively, the direct fuel cells (DFCs) which use fuels (in liquid or vapour form) directly without a reforming step have gained increasing importance. The most commonly used liquid fuels in direct fuel cells are methanol, ethanol and formic acid. Although hydrogen can be used as a direct fuel, these liquid fuels usually have much higher volumetric energy density and are much easier to store, transport and distribute. DFCs usually have a compact design and potentially can offer up to 10 times the energy density of rechargeable batteries. In addition, DFCs can be designed to operate at ambient temperature, which significantly reduces thermal management challenges for small systems. These advantages make the technology attractive to the rapid growing

need for portable power sources which should include micro and small DFCs. The major disadvantages of using direct fuel cells are the slow anode kinetics arising from a multi-step fuel oxidation process at the anode, and the fuel crossover from the anode to the cathode. The crossover not only lowers the fuel utilization, but also degrades the cathode performance and generates extra heat. The slow anode kinetics results in higher anodic overpotentials. Among different fuel options, methanol is an attractive one because it is a liquid at room temperature, has limited toxicity, high energy density, is easy to handle, relatively easy to distribute and has low cost since it can be generated from natural gas, coal, or biomass. Due to its important characteristics, the direct methanol fuel cells (DMFCs) have received in the last years the most extensive attention and efforts compared to other types of fuel cells.

2.2. Operating principle of the DMFC

A direct methanol fuel cell (DMFC) is an electrochemical cell that generates electricity based on the oxidation of methanol and reduction of oxygen using a polymer membrane as the electrolyte. This polymer is permeable to protons who are the ionic charge carrier. Figure 2.1 shows schematically a typical direct methanol fuel cell, comprising an anode flow channel (AF), an anode diffusion layer (AD), an anode catalyst layer (AC), a membrane (M), a cathode catalyst layer (CC), a cathode diffusion layer (CD) and a cathode flow channel (CF).

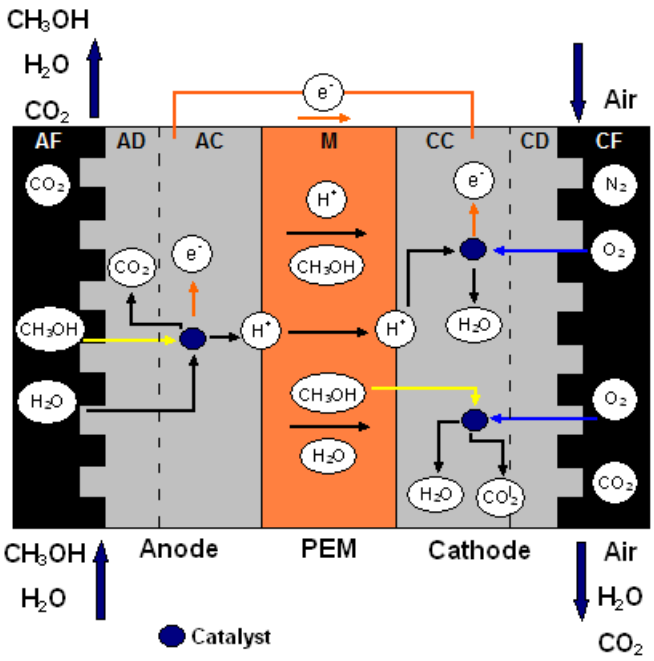

Figure 2.1 – Operating principle of a DMFC.

The heart of a DMFC is the membrane electrode assembly (MEA) formed by sandwiching a polymer electrolyte membrane (PEM) between an anode and a cathode. Upon hydration the PEM shows good proton conductivity. On both sides of the membrane the catalyst layers where the reactions take place and on each side of these, two diffusion layers are put to provide the current collection and to optimize distribution of the different species toward the catalyst layers. Finally, on both sides of the MEA, graphite plates with flow channels distribute the aqueous methanol solution and the gas feed.

Methanol or aqueous methanol solution is fed to the DMFC anode compartment (AF), either in liquid or vapour phase. The reactant diffuses through the anode diffusion layer (AD) towards the anode catalyst layer (AC) where it is converted to carbon dioxide, protons and electrons. The oxidation reaction occurring at the anode catalyst layer is given by:

$$CH_3OH + H_2O \rightarrow CO_2 + 6H^+ + 6e^- \tag{2.1}$$

The carbon dioxide generated from the oxidation reaction emerges from the anode baking layer as bubbles and is removed via the out flowing aqueous methanol, as the membrane is almost impermeable of gases. The protons and electrons are transported, respectively, through the membrane and through the external circuit to the cathode side.

Simultaneously, air is fed to the cathode compartment (CF) and the oxygen is transported through the cathode diffusion layer (CD) towards the cathode catalyst layer (CC). Here the oxygen combines with the electrons and protons to form water. The reduction reaction taking place on the cathode is given by:

$$O_2 + 4H^+ + 4e^- \rightarrow 2H_2O \tag{2.2}$$

The water produced moves counter-currently toward the cathode flow channel via the cathode diffusion and catalyst layers and also under some operating conditions, by back diffusion toward the anode.

The two electrochemical reactions occurring at each side are combined to form an overall reaction as:

$$CH_3OH + \frac{3}{2}O_2 \rightarrow CO_2 + 2H_2O \tag{2.3}$$

The operation temperature of a DMFC is less than 100ºC, which allows rapid start-up.

2.3. Fundamentals of a DMFC

The present section deals with the fundamental transport processes of methanol, water and heat, essential in DMFCs. The basic transport phenomena, along with electrochemical kinetics are critical to address the four technical challenges in a DMFC: i) low rate of methanol oxidation kinetics on the anode, ii) methanol crossover through the membrane, iii) water management and iv) heat management.

2.3.1. Cell components

As referred, the heart of a DMFC is the membrane electrode assembly (MEA). A schematic representation of a direct methanol fuel cell MEA is shown in Fig. 2.2, consisting of:

- a diffusion layer (AD) and a catalyst layer (AC) at the anode side;
- a polymer electrolyte membrane (M);
- a catalyst layer (CC) and a diffusion layer (CD) at the cathode side.

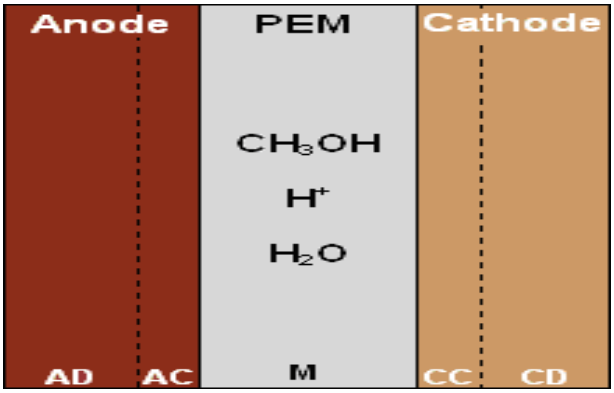

Figure 2.2 – Schematic representation of a direct methanol fuel cell MEA.

The most important component of a PEM fuel cell, specifically a DMFC, is the polymer electrolyte membrane (PEM) which must have a relatively high proton conductivity, must be a barrier to the mixing of fuel and reactant gases and must be chemically and mechanically stable in the fuel cell environment. Typically, the membranes for DMFCs

are made of perfluorocarbon-sulfonic acid ionomer which results from the combination of tetrafluorethylene with perfluorosulfonate monomers. The perfluorinated sulfonic acid membranes were developed by DuPont and sold under the commercial name of Nafion. Figure 2.3 shows the chemical structure of a Nafion membrane.

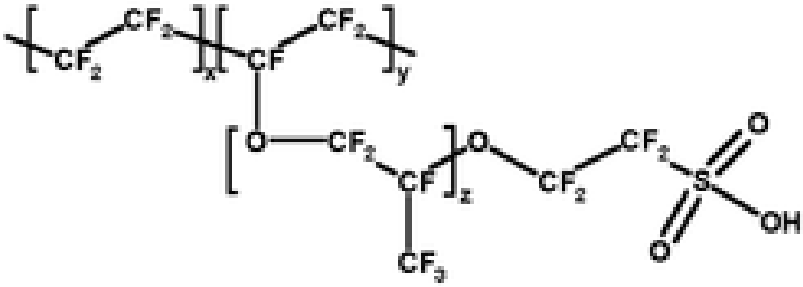

Figure 2.3 – Schematic representation of the Nafion chemical structure.

The SO_3H (sulfonic acid) group is ionically bonded and so the end of the chain is an SO_3^- ion with H^+ ion. This is the reason why this structure is called ionomer. The groups SO_3^- are responsible for creating hydrophilic regions, thus absorbing relatively large amounts of water. The H^+ ions movement within the well hydrated regions makes these materials proton conductive. Nafion membranes are available in several thicknesses and are marked with a letter N, followed by a 3 or 4 digit number. The last one or two digits represent the membrane thickness in mills, for example N117 has 7 mills (0.178 mm).

As already referred, on either side of the membrane are placed the anode and cathode catalyst layer. In the reactions occurring in a DMFC, gaseous and liquid reactants, electrons and protons are presented. The reactions take place in a portion of the catalyst surface where all three species have access. Electrons travel through electrically conductive solids, protons through ionomer and the reactants through the voids. Therefore the electrode must be porous to allow the reactants to travel to the reaction sites. At the same time the products formed in the electrochemical reactions must be effectively removed to allow the reactants access.

The most common used catalysts in DMFCs are Pt/Ru on the anode side and Pt on the cathode side. The microstructure of the catalyst layer is very important for the kinetics of the electrochemical reaction and for the diffusion of species. Figure 2.4 shows an example of the microstructures of the DMFC anode and cathode, respectively, where high surface areas for electrochemical reactions are clearly visible.

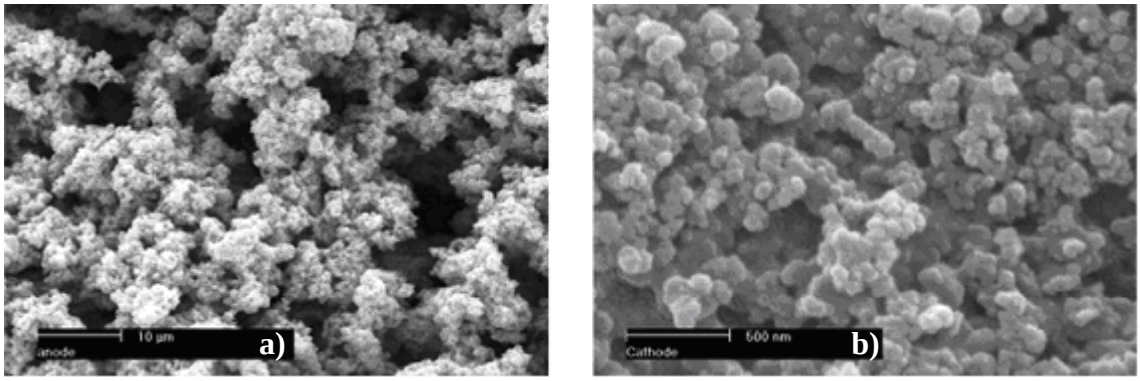

Figure 2.4 – Anode catalyst layer (a) and cathode catalyst layer (b) microstructures, taken from reference [1].

The layers between the catalyst layer and the flow field plate are called, as already referred, diffusion layers. These layers do not participate directly in the electrochemical reactions but have the following important functions:

- allow the access of reactants to the catalyst active area;
- provide the removal of the products from the catalyst layer;
- electrically connect the catalyst layer to the flow field plate;
- allow heat removal;
- provide mechanical support to the MEA, preventing it from sagging into the flow field channels.

According to these functions the required properties of the diffusion layers are the follow:

- sufficiently porous to allow flow of both reactants and products;
- electrically and thermally conductive;
- the porous facing the catalyst layer must not be too big since the catalyst layer is made of discrete small particles;
- sufficiently rigid to support the delicate MEA, but must have some flexibility to maintain good electrical contacts.

These requirements are best met by carbon fibber based materials such as carbon fibber papers and woven carbon fabrics or cloths, shown in Fig. 2.5. Two structural parameters of the diffusion layer affect the fuel cell performance: i) the tortuosity, which influences

the species transport and ii) the surface properties, the wettability and roughness, controlling the droplet/bubble attachment or coverage on the diffusion layer surface. Carbon cloth is more porous and less tortuous than carbon paper, although carbon paper has excellent electronic conductivity. Diffusion media are generally made hydrophobic to avoid flooding in their bulk since the hydrophobic character allows the excess water in the cathode catalyst layer to be expelled from the cell. To fulfill these goals, typically, the gas diffusion layers are PTFE (polytetrafluoroethylene) treated. Although, the anode diffusion layer of a DMFC should be hydrophilic to facilitate the mass transfer of the dilute methanol solution to the anode. One approach to transform the anode diffusion layer more hydrophilic is to partially fill the pores of the carbon porous media with certain metal oxide compounds (for example: aluminum oxide or niobium oxide).

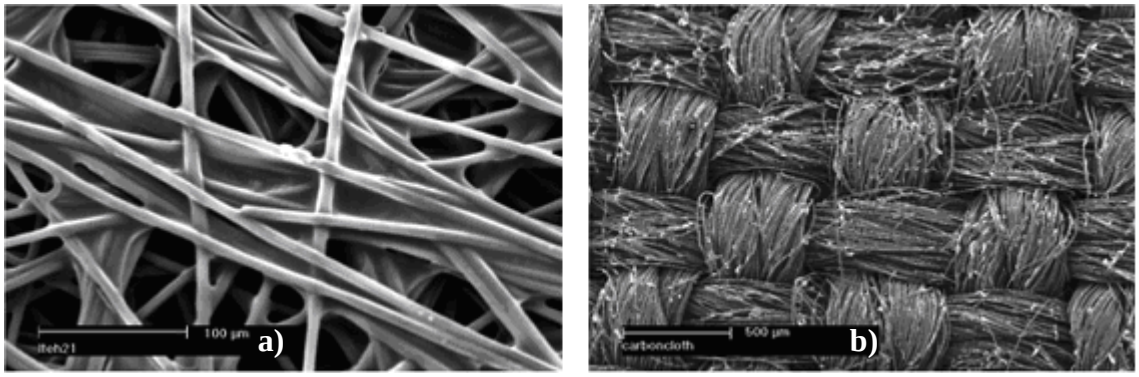

Figure 2.5 – Micrographs of commercially available carbon paper (a) and carbon cloth (b), taken from reference [1].

2.3.2. Thermodynamics and polarization curve

The thermodynamic equilibrium potential of a DMFC can be calculated as follows [1]:

$$\Delta E = -\frac{\Delta G}{nF} = -\frac{\Delta H - T\Delta S}{nF} \tag{2.4}$$

where n represents the number of electrons involved (equal to 6), F is the Farady constant, the ΔG, ΔH and ΔS values at 25ºC and 1 atm are, respectively, -704 kJ/kg, -727 kJ/kg and -77 kJ/kgK. For the liquid feed DMFC the thermodynamic cell potential is 1.21 V.

The thermodynamic efficiency of a fuel cell is defined as the ratio of maximum possible electrical work to the total chemical energy:

$$\eta_{rev} = \frac{\Delta G}{\Delta H} \times 100 = -\frac{nF\Delta E}{\Delta H} \times 100 \tag{2.5}$$

The theoretical thermodynamic efficiency of DMFC reaches 97% at 25ºC. However the real energy efficiency is much lower after accounting for the inherent losses in a fuel cell: voltage and fuel losses. The voltaic efficiency is defined as the ratio of the actual electric work and the maximum possible work and can be written as:

$$\eta_{voltaic} = \frac{W_{actual}}{W_{\max imum}} \times 100 = \frac{-nFE_{Cell}}{\Delta G} \times 100 = \frac{-nFE_{Cell}}{-nF\Delta E} \times 100 = \frac{E_{Cell}}{\Delta E} \times 100 \tag{2.6}$$

where E_{Cell} is the cell voltage at a current of I. If the cell is running at 0.5 V, then the voltaic efficiency is 41%. This low efficiency is caused by substantial overpotentials existed in the anode and cathode of a DMFC.

The fuel efficiency, due to methanol crossover, is defined as:

$$\eta_{fuel} = \frac{I_{Cell}}{I_{cell} + I_{CH_3OH}} \times 100 \tag{2.7}$$

where I_{Cell} is the cell current and I_{CH_3OH} is the current caused by methanol crossover.

The total electric energy efficiency of a DMFC is given by:

$$\eta = \eta_{fuel} \times \eta_{voltaic} \times \eta_{rev} \tag{2.8}$$

The energy efficiency of the PEMFC is relatively higher due to its negligible fuel crossover and overpotential for hydrogen oxidation on the anode. In order to achieve higher energy efficiency in DMFC it is necessary to control the methanol crossover.

The waste heat produced in the DMFC is given by:

$$Q = \frac{I_{Cell} \times E_{Cell}}{\eta} - I_{Cell} \times E_{Cell} = \frac{-\Delta H \left(I_{Cell} + I_{CH_3PH} \right)}{nF} - I_{Cell} \times E_{Cell} \tag{2.9}$$

where the first term, on the right hand side, represents the chemical energy of methanol consumed power generation and by crossover and the second the electric energy generated.

As was mentioned before the thermodynamic equilibrium cell potential for a DMFC is 1.21 V, although the real open circuit voltage is much lower than this, largely due to the methanol crossover. Figure 2.6 shows a polarization curve (voltage (V) vs. current density (A/cm^2)) of a typical DMFC.

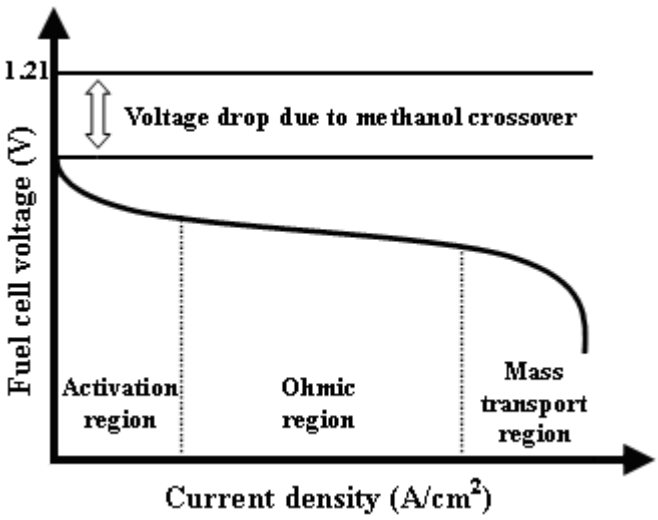

Figure 2.6 – Schematic representation of a typical DMFC polarization curve.

The activation region or kinetic control region is dictated by slow methanol oxidation kinetics at the anode as well as slow oxygen reduction kinetics at the cathode. The area where the cell voltage decreases nearly linearly is recognized as the ohmic control region. As the membrane in DMFC is usually well hydrated, the voltage loss in this region is minimal. The last part of the curve is referred to as the mass transport control region, where either methanol transport on the anode side results in a mass transport limiting current, or the oxygen supply at the cathode becomes a limiting step.

2.3.3. Methanol oxidation and oxygen reduction kinetics

Combined with the methanol crossover, slow anode kinetics lead to a decreasing power density, which in a DMFC is three to four times lower than in a hydrogen fuel cell. While the anodic oxidation of hydrogen is a well understood fast reaction, the anodic methanol oxidation is more complex. Although the thermodynamic characteristics are similar to the hydrogen reaction, the methanol electro-oxidation reaction is a slower process and involves the transfer of six electrons to the electrode for complete oxidation to carbon dioxide.

Many studies on the oxidation of small organic molecules at low temperatures have been carried out [2-13]. Most of these studies have been carried out in a half-cell configuration and on smooth electrode surfaces, in order to establish the best electrocatalyst composition. These investigations were combined with spectroscopic techniques in order to elucidate the oxidation mechanism and to investigate the irreversibly adsorbed species on the electrode surface. During these studies, it was concluded that almost all electro-oxidation reactions involving low molecular weight organic molecules, such as CO (carbon monoxide) and CH_3OH (methanol), require the presence of Pt-based (Platinum based) materials displaying a high enough stability and activity to be attractive as catalysts. A second common aspect to these molecules is that all these electro-oxidation reactions give rise to the formation of strongly adsorbed CO species in linear or bridge-bonded form.

As was mentioned before, the electro-oxidation of methanol to carbon dioxide requires the transfer of six electrons, but it is highly unlikely that these electrons will transfer simultaneously. It is also unlikely that partial electron transfer will lead to the formation of a range of stable solution intermediates. Clearly, there must be surface adsorbed species present on the surface of the platinum electrocatalyst across its useful potential range, and it is these species which are responsible for the poor catalytic activity of platinum towards methanol electro-oxidation. The assumed mechanisms for methanol oxidation on Pt based catalyst were reviewed by Parsons *et al.* [13] and can be divided in two major steps: i) adsorption of methanol followed by several steps of dehydrogenation/deprotonation and ii) dissociation of water to provide oxygen that allows the adsorbed carbon containing intermediates to generate carbon dioxide. A scheme for the first step is given by [14]:

$$CH_3OH + Pt \rightarrow PtCH_2OH + H^+ + 1e^- \tag{2.10}$$

$$CH_2OH + Pt \rightarrow PtCHOH + H^+ + 1e^- \tag{2.11}$$

$$CHOH + Pt \rightarrow PtCHO + H^+ + 1e^- \tag{2.12}$$

A surface rearrangement of methanol oxidation intermediates gives carbon monoxide as follows:

$$PtCHO \rightarrow Pt - C \equiv O + H^+ + 1e^- \tag{2.13}$$

In the absence of promoting element, water discharge occurs at high anodic overpotentials on Pt with the formation of adsorbed OH species:

$$Pt + H_2O \rightarrow PtOH + H^+ + 1e^- \tag{2.14}$$

Finally the reaction that produces carbon dioxide:

$$PtOH + PtCO \rightarrow 2Pt + CO_2 + H^+ + 1e^- \tag{2.15}$$

On a pure Pt surface, the dissociative chemisorption of water on Pt is the rate determining step at low voltages, precisely in the potential region which is of technical interest [15]. As a result, an active catalyst for methanol oxidation should give rise to water discharging at low potentials, to unstable CO chemisorption and should also catalyze the oxidation of carbon monoxide. The additions of secondary materials that can combine with platinum are seen as a mean to improve the electrocatalytic behavior of electrodes, either by minimizing the poisoning reaction or by enhancing the main oxidation reaction. Some of the advanced materials that have been developed display enhanced activities and the most likely possible explanations for this are: i) the metal modifies the electronic properties of the catalyst, weakening the chemical bond between platinum and the surface intermediate and ii) the second element increases OH adsorption on the catalyst surface, at lower overpotentials, and decreases the adsorption strength of the poisoning species.

Much research efforts are being rendered on catalysts to find one which can avoid the poisoning effect of the CO species [16, 17]. One of the most important and most

investigated secondary materials is Ruthenium (Ru). A bimetallic alloy consisting of Pt and Ru supported on carbon has thus far been one of the major research interests on catalyst for direct methanol fuel cells. Other materials such as Sn (Tin), Os (Osmium), W (Tungsten), Mo (Molybdenum) and other metals have also been investigated for methanol oxidation and CO poisoning [18-23] and have been found to have a promoting effect on the catalytic activity for methanol oxidation. For all these species it was found that the determining factor for promotion is the formation of adsorbed oxygen containing species, which is needed for the oxidation of intermediate adsorbates, on the secondary metal at potentials lower than for platinum.

According to the mechanism mentioned above it is accepted that Pt sites in Pt/Ru alloys are involved in both the methanol dehydrogenation step and in the strong chemisorption of methanol residues. At low electrode potentials, water discharging occurs on Ru sites with the formation of Ru-OH groups at the catalyst surface:

$$Ru + H_2O \rightarrow RuOH + H^+ + 1e^- \tag{2.16}$$

Finally the reaction producing carbon dioxide:

$$RuOH + PtCO \rightarrow Ru + Pt + CO_2 + H^+ + 1e^- \tag{2.17}$$

The nature of the catalyst support, catalyst particle size and the atomic ratio between platinum (Pt) and ruthenium (Ru) are important factors that affect the anode catalyst performance. Arico *et al.* [24] and Ren *et al.* [25] found that thinner support layers and even unsupported catalyst lead to better performances. The authors also found that smaller particles and higher surface areas are beneficial for the process. Contrarily, the atomic ratio between platinum and ruthenium seems to have a lower influence. For higher operating temperatures, the optimal performance has been found with atomic ratios in the region of 1:1. For lower temperatures a higher relative platinum content seems to be beneficial.

As was mentioned and explained before, most of the studies conclude that the reaction can proceed according to multiple mechanisms. However, it is commonly accepted that the more significant reactions are the adsorption of methanol and the oxidation of

carbon monoxide adsorbed. So the following reaction mechanism, similar to the one used by Meyers *et al.* [26], was used in the present work.

$$CH_3OH + Pt \rightarrow \left(CH_3OH \right)_{ads} \tag{2.18}$$

$$\left(CH_3OH\right)_{ads} \rightarrow \left(CO\right)_{ads} + 4H^+ + 4e^- \tag{2.19}$$

$$\left(CO\right)_{ads} + H_2O \rightarrow CO_2 + 2H^+ + 2e^- \tag{2.20}$$

This mechanism does not segregate the electrochemical oxidation of water reaction from the electrochemical oxidation of carbon monoxide. This assumption does not change the kinetic expression appreciably and is applicable for Pt/Ru catalyst where the oxidation of water on Ru occurs much faster than the oxidation of carbon monoxide.

The kinetic expression used to described the methanol oxidation reaction is taken from Meyers *et al.* [26] as

$$I_{Cell} = \int a I_{0,ref}^{CH_3OH} \frac{k C_{CH_3OH}^{AC}}{C_{CH_3OH}^{AC} + \lambda \exp\left(\frac{\alpha_A \eta_A F}{RT_{AC}}\right)} \exp\left(\frac{\alpha_A \eta_A F}{RT_{AC}}\right) dx \tag{2.21}$$

where I_{Cell} is the cell current density, a is the specific surface area of the anode, $I_{0,ref}^{CH_3OH}$ is the exchange current density of methanol, k and λ are constants in the rate expression, $C_{CH_3OH}^{AC}$ is the methanol concentration at the anode catalyst layer, α_A is the anodic transfer coefficient, η_A is the anode overpotential, T_{AC} is the temperature on the anode catalyst layer and R is the ideal law gas constant.

At the cathode, the reduction of oxygen to water usually takes place on platinum catalysts, pure or supported in carbon black. Although these catalysts are the most widely used in low temperature fuel cells, due to their intrinsic activity and stability, there is still great interest in the development of more active, selective and less expensive electrocatalysts for the cathode reaction. However, there are a few options that can be investigated to reduce the costs and to improve the electrocatalytic activity of Pt, especially in the presence of methanol crossover. One of them is to increase Pt utilization, this can be achieved either by increasing its dispersion on carbon and the

interfacial region with the electrolyte. Another successful approach to enhance the electrocatalysis of O_2 (oxygen) reduction is by alloying Pt with transition metals. This enhancement in electrocatalytic activity has been interpreted in different ways, and several studies have been conducted to make an in depth analysis of the surface properties of the proposed alloy combinations [27-30].

The oxygen electrochemical reaction has been largely examined in the last years accompanying the development of PEMFCs [31, 32]. In this type of fuel cells the oxygen reduction reaction is much lower than the anodic hydrogen oxidation, therefore it is very important to optimize the cathodic reaction. Contrarily, in the DMFCs the anodic methanol oxidation is much slower that the cathodic oxygen reduction being the first one assumed as the rate determining step under most operating conditions.

In the DMFC, a second reaction takes place at the cathode platinum catalyst, the methanol oxidation reaction, arising from the methanol crossing trough the membrane from the anode to the cathode side. So, methanol oxidation and oxygen reduction compete for the same sites producing a mixed potential which reduces the cell potential. Although all reaction intermediates of the methanol oxidation can be found on the catalyst layer, none of them is found in the cathode exhaust gas of a DMFC. This is due to the fact that the oxygen stoichiometry is usually very high allowing a full oxidation of methanol to carbon dioxide. To achieve better performances in a DMFC, a significant reduction in the methanol crossover is desired. This can be achieved using membrane materials less permeable to methanol, optimizing methanol feeding strategies (possible dynamic feedings) or using low methanol feed concentrations. Another possibility is to use different cathode catalyst materials or promoting elements for oxygen reduction which simultaneously hinders the methanol chemisorption while still maintaining the proper catalyst characteristics (structure and particle size).

The oxygen reduction reaction on the DMFC cathode is described using Tafel equation taking in account the mixed potential:

$$I_{Cell} + I_{CH_3OH} = I_{0,ref}^{O_2} \frac{C_{O_2}^{CC}}{C_{O_2,ref}^{CC}} \exp\left(\frac{\alpha_C \eta_C F}{RT_{CC}} \right) \tag{2.22}$$

where I_{CH_3OH} is the leakage current density due to the oxidation of methanol that crosses the membrane, I_{Cell} is the cell current density, $I_{0,ref}^{O_2}$ is the exchange current

density of oxygen, $C_{O_2}^{CC}$ is the oxygen concentration on the cathode catalyst layer, $C_{O_2,ref}^{CC}$ is the reference concentration of oxygen, α_C is the cathodic transfer coefficient, η_C is the cathode overpotential and T_{CC} is the temperature on the cathode catalyst layer.

2.4. Two-phase flow phenomena

To ensure continuity and stabilization of the electrochemical reaction in an operating DMFC, the carbon dioxide gas and the liquid water must be removed rapidly and efficiently to allow fresh fuel and oxygen to arrive at the catalyst layers. At the anode and cathode, carbon dioxide gas and liquid water can adhere to the surface of the diffusion layer and block the pores, which in turns hinder the diffusion of fuel and oxidant to the catalyst layers. This can lead to a severe cell performance loss. Hence, investigation on the two-phase flow will serve as a guide for the improvement of the performance of DMFC [33-46].

Flow visualization is an effective way to investigate quantitatively and qualitatively the dynamic behaviour of carbon dioxide gas bubbles in the anode channels and liquid water bubbles in the cathode of an operating DMFC. Although the number of papers published on DMFC has grown, few research works have been reported in visualization experiments due to its difficulty of implementation.

2.4.1. Gaseous carbon dioxide in anode

On the anode side of a DMFC, carbon dioxide is produced as a result of the methanol oxidation reaction. If the carbon dioxide cannot be removed efficiently from the surface of the gas diffusion layer (AD) it remains covering this surface and consequently induce a decrease of the effective mass transfer area. In addition, flow blockage results, particularly in channels of small dimensions as required for micro or compact portable DMFCs. Therefore, gas management on the anode side is an important and critical issue in DMFC design. Argyropoulos *et al.* [33, 34] were perhaps among the first to observe the two-phase flow pattern in the anode of a DMFC. They used acrylic cells and a high speed video camera for visually investigate the carbon dioxide gas evolution process inside an operating DMFC environment. The effect of operating conditions on the gas management using different gas diffusion layers (carbon cloth and carbon paper), flow

channel designs, cell sizes and exhaust manifold configurations was studied. The visualization studies showed that carbon paper has a relatively low ability to gas removal. Increasing the methanol solution inlet flow rate was beneficial for gas removal. Increasing the current density leads to a higher gas production and in the formation of gas slugs, especially for low flow rates, which can block the channels and lower the cell performance. The new flow channels design, proposed by the authors, based on a heat exchanger concept was more effective for gas management and gave a more uniform flow distribution in the channels than a simple parallel flow channel. This study was, however, undertaken under low cell performance. A few years later, Nordlund *et al.* [35] developed a visual DMFC, comprising a transparent anode and a cathode endplate with an integrated heat exchanger and a picture analysis methodology. They took the data analysis a step further, since they presented a methodology to acquire good visual data and to perform a high-quality and time effective analysis. In particular, they demonstrated how a visual cell in combination with digital video recordings and picture analysis can be used to give valuable insight into two-phase flow in the anode of a DMFC. Bewer *et al.* [36] developed a new method to analyse the interaction of the flow distribution and the bubble generation in an aqueous medium. The method is based on the decomposition of hydrogen peroxide solution to oxygen and water in aqueous media at the presence of a catalyst. By using an appropriate hydrogen peroxide concentration, the gas evolution rate can be set to the same order of magnitude as in real DMFC. This method can simulate the bubble formation in the anode compartment of a DMFC without any electrical current. The current density to be simulated can be adjusted by an appropriate setting of the hydrogen peroxide concentration independently of ohmic losses. As no current conducting parts are needed, the whole cell can be made of a transparent material (perspex) to ensure a complete visibility of the flow. The cell has a simple modular design in which different manifold and flow fields can be tested. Lu *et al.* [37] developed a carefully designed transparent DMFC to visualize, in situ, the bubble flow in the anode of a DMFC. Figure 2.7 shows a picture of the transparent fuel cell used in their work.

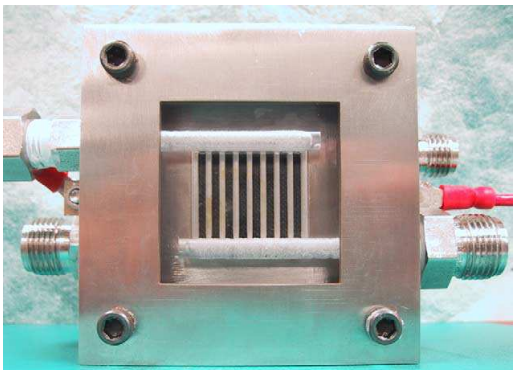

Figure 2.7 – A photograph of a transparent DMFC, taken from reference [37].

Normally, the transparent cells used in the visualization studies are constructed with a pair of stainless steel plates mated with a polycarbonate plate, forming a window to allow direct observation of flow behaviour. The polycarbonate plate is concave in design while the stainless steel plate had a matching convex pattern to avoid flow leakage. The channels are machined through the stainless steel plate and the surface that contacts with the MEA are coated with Cr (Chromium) and Au (Gold) to minimize the contact resistance.

They used two types of MEAs based on Nafion 112 to investigate the effects of the backing pore structure and wettability on cell polarization and two-phase flow dynamics. One employed hydrophobic carbon paper backing material and the other hydrophilic carbon cloth. For the hydrophobic carbon paper they observed that carbon dioxide bubbles nucleate at certain locations and form large and discrete bubble slugs in the channel (see Fig. 2.8, a)). For the hydrophilic carbon cloth it was shown that bubbles are produced more uniformly and of smaller size (see Fig. 2.8, b)).

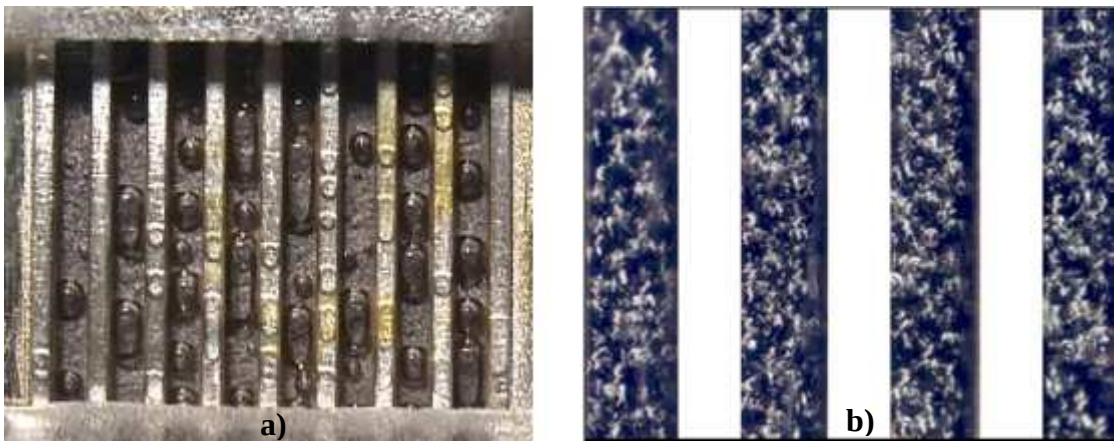

Figure 2.8 – Bubble behaviour on the anode side using hydrophobic carbon paper (a) and hydrophilic carbon cloth (b), taken from reference [37].

Yang *et al.* [38, 39] used a transparent DMFC to investigate experimentally the effect of the single serpentine (SFF) and parallel flow fields (PFF) on the cell performance and on carbon dioxide bubble behaviour. They found that the DMFCs equipped with SFFs leads to better performances than those with PFFs. It was also found that gas bubbles blocked the flow channels in the PFF at low methanol solution flow rates and high current densities. Since fuel cells with PFFs had poor performance they focused their work on studying the effects of various SFF design parameters, including open ratio and channel length, on cell performance.

More recently, Liao *et al.* [40] presented a study where a transparent DMFC was constructed to visualize the two-phase flow of aqueous methanol solution and carbon dioxide bubbles by using a high-speed video camera. The dynamic behaviour of carbon dioxide gas bubbles including emergence, growth, coalescence and removal was recorded in situ, and polarization curves were obtained to provide a fundamental understanding of the relationship between the behaviour of carbon dioxide gas bubbles and the cell performance. A series of parametric studies, including aqueous methanol solution flow rate, temperature, concentration and cell pressure difference between the anode and the cathode was presented in order to evaluate the effects of these parameters on carbon dioxide gas bubbles behaviour and on cell performance. It was observed that gas bubbles first emerge around the corner on the porous diffusion layer and the channel ribs and formed large gas slugs by growth and coalescence in the channel. The cell performance was improved with increasing aqueous methanol flow rates, feed temperature, feed concentration and pressure gradient between the anode and cathode.

Experimental observation in a small DMFC test cell done by Lundin *et al.* [41] indicated that the rate of bubble formation can be reduced by increasing the fuel flow because more liquid is available for the carbon dioxide to dissolve in. The authors also found that potassium hydroxide and lithium hydroxide added to the fuel eliminate in situ carbon dioxide gas formation at low concentrations, because of the consequent greatly increased solubility. They presented a model that explains the rate of carbon dioxide gas formation at the anode of a DMFC including a function of the cells output current, operating temperature, operating pressure, fuel flow rate, and the solubility of carbon dioxide in fuel solution, which is also a strong function of temperature.

A better understanding of the basic transport phenomena of carbon dioxide on the anode side achieved through combined flow visualization studies and transport simulations is essential to overcome this challenge and to inspire new design concepts.

2.4.2. Liquid water transport in the cathode

Another important aspect of the DMFC is the possibility of water flooding at the cathode pores and channel structure due to water transport through the membrane and to the water production by the cathode reaction. The formation of water within the cathode catalyst layer and its transport through the cathode diffusion layer add another mass transport resistance for oxygen on its flow towards the reaction zone, and therefore reduces the limiting cell current with respect to the cathodic reactions. The importance of flooding at the cathode side in PEMFCs has been emphasized in literature [42-44]. Similarly, water flooding on the cathode side of a DMFC was identified as a critical issue by Mench *et al.* [45]. A proper water level of water at the cathode side is necessary to hydrate the polymer membrane, increasing in this way the proton conductivity. However, a too large amount of water in the cathode side leads to water flooding at the pores decreasing the cathode performance. In order to accurately predict critical operation conditions to avoid flooding, visualization of the cathode side is essential to yield fundamental physics behind the flooding occurrence. As described above, Lu *et al.* [37] developed a carefully designed transparent DMFC (Fig. 2.7) to visualize, in situ, the bubble flow in the anode of a DMFC and the cathode flooding. The authors used two types of gas diffusion layers (GDLs), carbon paper and ELAT carbon cloth (formed of carbon cloth type A and treated with Pt on one side). Flow visualization of cathode flooding indicates that more water droplets appear upon the carbon paper GDL surface than upon the single-side ELAT GDL, due mainly to the higher hydrophobicity of the latter material at elevated temperatures, as shown in Fig. 2.9.

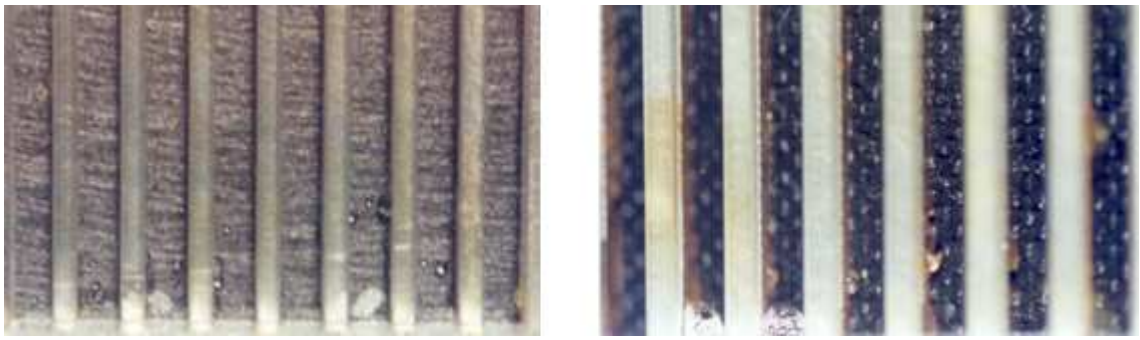

a) b)

Figure 2.9 – Water drop behaviour on the cathode side using carbon paper (a) and ELAT carbon cloth (b), taken from reference [37].

Chen *et al.* [46] presented simplified models that are based on macroscopic force balances and droplet-geometry approximations for predicting the onset of instability leading to removal of water droplets at the diffusion layer / flow channel interface. They carried out visualization experiments to observe the formation, growth, and removal or instability of the water droplets at the selected interface of a simulated polymer electrolyte fuel cell cathode.

In spite of these studies, much remains to be understood on the fundamental process of flooding occurrence and its relation with the backing layer material.

2.5. Mass transport phenomena

2.5.1. Methanol crossover

In Direct Methanol Fuel Cells, methanol crossover occurs due to the inability of the Nafion membranes to prevent methanol from permeating its polymer structure. Diffusion and electro-osmotic drag are the prime driving forces for methanol transport through the membrane. As already referred, the methanol that reaches cathode side reacts with the platinum catalyst sites on the cathode, leading to a mixed potential, which causes a decrease in cell voltage. Methanol reaching the cathode also results in decreased fuel efficiency thus lowering the energy density of the system. In order to improve the performance of the DMFC it is necessary to eliminate or reduce the loss of fuel across the membrane. In this section special attention is given in showing the

studies found in the literature on the methanol crossover and its influence on the performance of a DMFC. Some possible solutions to solve this problem are presented.

There are a few experimental methods to determine the methanol crossover from the anode to the cathode side. Verbrugge [47] measured the methanol diffusivity of Nafion equilibrated with sulphuric acid at room temperature by using a radioactive tracer method. Kauranen and Skou [48] developed an approach for the measurement of the permeability of methanol in proton exchange membranes equilibrated with a supporting liquid electrolyte at elevated temperatures. The time responses of anodic peak currents on two working electrodes allowed the estimation of the permeability of a Nafion 117 perfluorosulfate membrane. Tricoli *et al.* [49] studied the proton conductivities and methanol crossover rate in two commercially available, partially fluorinated membranes. The methanol crossover rate was monitored by measuring the steady state current at the cathode when methanol was introduced into the anode. Hikita *et al.* [50] determined the methanol crossover rates by continuously measuring the concentration of methanol, carbon monoxide and carbon dioxide in the exhaust gas of the cathode.

A common method to measure the methanol crossover in a DMFC is the analysis of the carbon dioxide content of the cathode exhaust. However it is necessary to point out that during the operation of a DMFC a large amount of carbon dioxide is produced in the anodic reaction and some of this can diffuse partially to the cathode side. In this case the amount of carbon dioxide present in the cathode exhaust is a contribution of the carbon dioxide resulting from the methanol crossover oxidation at the cathode side and of the carbon dioxide that passes through the membrane to the cathode side. In their work, Dohle *et al.* [51] describe a method to separate the two contributions under real DMFC operating conditions and clearly define the amount of carbon dioxide due to methanol oxidation on the cathode side. Ramya and Dhathathreyan [52] directly measured methanol flux rates across Nafion membranes by an electrochemical method, like cyclic voltammetry and chronoamperometry. The membrane permeability was measured by this technique for various methanol concentrations. The authors found that the permeability of methanol is dependent on the concentration of methanol, the permeability increases with an increase on the methanol concentration.

The need to evaluate methanol crossover by an easier and faster method than conventional carbon dioxide analysis method has become significant. A potentiometric method has been reported by Munichandraiah *et al.* [53], showing that the slope (dE/dt), of E_{Cell} versus t (time) curve, is proportional to the crossover rate. Methanol crossover

rate has been calculated from the time required to reach the equilibrium concentration of methanol on either side of the polymer electrolyte membrane.

Jiang and Chu [54] estimated the amount of methanol crossover more accurately with a method of gravimetric determination of barium carbonate to analyse the amount of carbon dioxide. The equivalent current of methanol crossover was calculated from the discharge current of the fuel cell and the sum of dry barium carbonate precipitate collected at the anode and the cathode exhaust. With the method proposed by the authors, the common experimental deviation of measuring methanol crossover caused by carbon dioxide permeation through the polymeric electrolyte membrane can be corrected. In the work presented by Kin *et al.* [55], the methanol crossover rate of PEM and the efficiency of DMFC were estimated by measuring the transient voltage and the current at the DMFC when methanol was introduced into the anode. The proposed method simply yields an estimate of the methanol crossover rate of PEM and the efficiency of a DMFC and does not require fitting analyses. Han and Liu [56] determined the methanol crossover rate in a DMFC by measuring the carbon dioxide concentration at the cathode exit in real time, at different inlet methanol concentrations and various operating conditions. Park *et al.* [57] presented a practical way of characterizing the mass transport phenomena of membrane electrode assemblies (MEAs) through mass balance research in DMFC systems. This method could be used to measure methanol utilization efficiency, the water transport coefficient and the methanol to electricity conversion rate of a MEA in DMFCs. The research on the DMFC MEA design was performed with the aim of reducing methanol and water crossover maintaining high power characteristics. By varying material properties, the critical design parameters were identified for high methanol utilization improving power density through systematic experiments.

Due to the impact of methanol crossover on the DMFC performance, its effects have been studied in the literature under various operating conditions, such as, methanol concentration, cathode air pressure, temperature, fuel flow rate, membrane thickness and equivalent weight and catalyst morphology.

In their work, Kauranen and Skou [48] studied the influence of the temperature in methanol permeability and found an increase of the crossover rate with temperature. Ravikumar and Shukla [58] found that in despite of the fact that the increase in temperature increases the methanol crossover, the increase of temperature also leads to an improvement of cell performance, since the ohmic resistance and polarization

reduce. The authors also found that the cathode electrode performance is significantly lowered at higher methanol concentration leading to a decrease in cell performance, since higher methanol concentrations result in higher rates of methanol transport through the membrane.

In their work, Cruickshank and Scott [59] studied the effects of methanol concentration and oxygen pressure in cell performance and found that higher methanol concentrations lead to a lower cell performance and attributed this to the fuel crossover phenomena. They also found that pressurising the oxygen reduced the methanol crossover leading to higher methanol concentrations. Küver and Vielstich [60] studied the effects of methanol concentration, fuel cell temperature and catalyst loading in cell performance. A new catalyst support was found showing a good performance with a smaller noble metal loading. Scott *et al.* [61] investigated the effect of cell temperature, air cathode pressure and methanol concentration on the power performance on a small-scale DMFC. Higher power densities were achieved at higher temperatures and cathode air pressures. They concluded that the selection of methanol concentration, to obtain maximum power density, depends upon the current density. Gurau and Smotkin [62] measured the methanol crossover by gas chromatography as a function of temperature, fuel flow rate and methanol concentration. Gogel *et al.* [63] presented investigations to determine the dependence of the performance of direct methanol fuel cells and the methanol crossover rate on the operating conditions, on the structure of the electrodes and on the noble metal loading. It was shown that performance and methanol permeation depend strongly on cell temperature and cathode air flow. Also, methanol permeation can be reduced significantly by varying the anode structure, but the changed electrode structure also leads to somewhat lower power densities. The metal loading was varied at the anode and cathode, affecting the cell performance. Furthermore, the differences between supported and unsupported catalysts were compared. They also, discussed the optimum conditions for the DMFC operation considering the various important factors. Du *et al.* [64] developed a half-cell consisting of a normal direct methanol fuel cell (DMFC) cathode and a membrane contacting with an electrolyte solution to investigate the effect of methanol crossover on the cathode behaviour. Open circuit potentials, cyclic voltammetry profiles, polarization curves and electrochemical impedance spectroscopy, resulting from the oxygen reduction reaction with/without the effect of methanol oxidation reaction, were measured. The steady-state results confirmed that the presence of methanol at the cathode led to a significant poisoning

effect on the oxygen reduction reaction, especially when the DMFC operates at higher methanol concentrations and discharges at lower potentials. Ramya and Dhathathreyan [65] investigated the methanol permeability when the membrane was processed at a high temperature. Their work took into consideration the conductivity of the membrane and the methanol permeability studied as a function of processing temperature for the membrane. Reduced methanol permeability was observed when the membranes were processed at temperatures much above the glass transition temperature but below the degradation temperature of the membranes. The permeability of methanol decreased despite of the thickness of the membrane on processing. Recently, Park *et al.* [57] performed parametric investigations to reveal the effects of operating conditions of fuel cell systems such as methanol concentration, fuel/air stoichiometry, operating current, and cell temperature. The methanol utilization efficiency and methanol to electricity conversion rate were strongly affected by temperature, current density, methanol concentration, and the stoichiometry of fuel and air.

As the fuel crossover causes considerable cell voltage losses in the DMFC, different approaches to minimise or eliminate methanol crossover have been carried out from different points of view. An alternative is the membrane technology trying to obtain a new methanol-impermeably polymer electrolyte [66-85].

Pu *et al.* [66] studied a composite electrolyte where a film of a methanol impermeable protonic conductor, such as a metal hybrid, was sandwiched between proton permeable electronic insulators, such as Nafion. They studied different electrolyte systems where membrane was Nafion 115 with a metal hybrid Pd (Palladium), and the influence of interfaces modification with Pt via various techniques. The results obtained showed that the methanol crossover was smaller than in the Nafion polymer and that the higher performance was obtained with the system (N/Pt/Pd/Pt/N), where N is the Nafion 115 membrane, treated by palladization and followed by platinization using electrochemical methods common to the preparation of hydrogen reference electrodes.

Wainright *et al.* [67] studied the conductivity, water content and methanol vapour permeability of the phosphoric acid-doped polybenzimidazole (PBI). Experimental results confirmed the low methanol crossover in a PEM fuel cell employing a doped polybenyimidazole membrane. One year later, Wang *et al.* [68] used the same membranes and studied the methanol crossover and the performance of a DMFC. They observed that the methanol crossover rate increased with a decrease in the water methanol ratio in the anode feed stream. These authors, however, found that methanol

crossover increased with increasing current density and decreased when temperature increased. They present in their work, the influence of increasing different operating parameters in the methanol crossover and in the performance of DMFCs using acid doped PBI membranes.

Küver and Kamloth [69] studied the methanol crossover in substituted and crosslinked POP membranes (sulphonate substituted polyoxiphenylenes) using differential electrochemical mass spectrometry. They compared the results with those obtained with different commercial membranes and it was found that the superiority of POP membranes was evident, with respect to methanol permeation, and especially attractive since the POP film was only 0.2 to 0.3 mm thick.

In his work, Tricoly [70] investigated the influence of doping poly(perfluorosulfonated acid) membranes with cessium in several degrees on the methanol permeability at room temperature and found that the membrane permeability can be drastically reduced by an appropriate doping cessium ions.

Choi *et al.* [71] reported a new method for reducing methanol crossover by a plasma etching and palladium-sputtering on the Nafion membrane surface. The plasma etching of Nafion membrane increases the roughness of the membrane surface and decreases the methanol permeability. The sputtering of palladium on the plasma-etched membrane was found to further decrease the methanol crossover.

Hobson *et al.* [72] introduced a thin barrier layer of PBI at the Nafion 117 surface by screen printing and a reduction on methanol permeability was shown whilst maintaining proton conductivity at a level comparable to that of the parent material. Uchida *et al.* [73] presented a new polymer electrolyte membrane where platinum nanocrystals were highly dispersed in a Nafion 117 film to catalyse the oxidation of the methanol crossover with oxygen. An increase in the cathode potential was observed resulting from the reduced amount of methanol reaching the cathode.

In order to reduce the methanol crossover from the anode to the cathode side in direct methanol fuel cells (DMFC), Yang *et al.* [74] fabricated and characterized multilayered membranes containing a thin layer of sulfonated poly(etheretherketone) (SPEEK) with different sulfonation levels and thickness and two outer layers of recast Nafion. With a comparable polarization loss in DMFC, the multilayered membranes show a significant reduction in methanol crossover compared to the native Nafion membranes since, the thin middle layer of SPEEK blocks the methanol permeation effectively without adversely increasing the cell resistance significantly.

Bettelheim *et al.* [75] report a study consisting on the use of tetra(orthoaminophenyl)porphyrin as the methanol barrier when electropolymerized on a direct methanol fuel cell cathode. Using an electrochemical quartz cristal microbalance and atomic force microscopy techniques the authors showed a reduction on methanol permeability.

Lee *et al.* [76] incorporated layered double hydroxides (LDH) into polyelectrolyte membranes in order to investigate the electrochemical reaction processes affected by transport rates of methanol and protons in direct methanol fuel cell applications. Depending on different ion exchange capacities and its LDH compositions, the polyelectrolyte membranes gave different methanol diffusion coefficients and proton conductivities. Decreasing the methanol diffusion coefficient, the open circuit voltage increased and the overall performance of DMFC was improved by incorporating LDH nanoparticles.

In their work, Tang *et al.* [77] prepared multi-layer self-assembly Nafion membranes (MLSA Nafion membranes) by alternately assembling charged Pd particles and Nafion ionomers onto Nafion membranes. The drastic decrease of methanol crossover demonstrated the feasibility of the proposed process, especially if 3 double layer of Pt particles and Nafion ionomers was self-assembled. In this condition, slightly adverse effects on the proton conductivity of the original Nafion membrane occurred but the methanol crossover had a considerable decrease.

Mu *et al.* [78] prepared charged Au nanoparticles by refluxing a solution of hydrogen tetrachloroaurate trihydrate and protective cationic agents in ethanol/water. The charged Au nanoparticles were self-assembled onto the Nafion 212 membrane surface as methanol barriers. All the self-assembled PEMs had higher performance than original Nafion 212 membrane and had higher performances due to the decrease of the methanol permeation current density and acceptable membrane area resistances.

Liang *et al.* [79] synthesized organically modified silicate microparticles, known as diphenylsilicate (DPS), and showed that the synthesized DPS has a nano-layered microstructure. The authors utilized this material as filler for fabricating Nafion/DPS composite membranes for mitigating the problem of methanol crossover in direct methanol fuel cells. The DMFC performance tests demonstrated that the use of the Nafion/DPS composite membranes resulted in a lower rate of methanol crossover, higher open-circuit voltage and better cell performance than the pure Nafion membrane, especially when working with a higher methanol concentration.

Jung *et al.* [80] examined methanol crossover through Pt/Ru/Nafion composite membranes for the direct methanol fuel cell. The composite membrane was characterized by inductively coupled plasma-mass spectroscopy and thermo-gravimetric analysis. The methanol permeability and proton conductivity of the composite membranes were measured by gas chromatography and impedance spectroscopy, respectively. The proton conductivity of the composite membrane decreased with increasing number of Pt/Ru particles embedded in the pure Nafion membrane, while the level of methanol permeation was retarded. The Pt/Ru particles embedded in the Nafion membrane act as a barrier against methanol crossover by the chemical oxidation of methanol on embedded Pt/Ru particles and by reducing the proton conduction pathway.

Higuchi *et al.* [81] developed novel cross-linked sulfonated polyimide (c-SPI) membrane as an electrolyte for direct methanol fuel cells (DMFCs). The cross-linked SPI (c-SPI) was found to exhibit fairly low methanol permeation rate with sufficiently high proton conductivity as the electrolyte membrane for DMFCs.

Yamauchi *et al.* [82] compared the performance of the membrane electrode assembly for direct methanol fuel cells (DMFCs) composed of a pore-filling polymer electrolyte membrane (PF membrane) with that composed of a commercial Nafion 117 membrane. The use of a PF membrane allows the application of a highly concentrated methanol solution as a fuel without decreasing either the DMFC performance or the energy density. In addition, the reduction of methanol crossover in the MEA using the PF membrane allows a lower amount of cathode catalyst to be used, and the low electro-osmosis of the PF membrane decreases the flow rate of the cathode gas without flooding, which also generates a more compact DMFC system.

Gosalawit *et al.* [83] proposed Nafion and Montmorillonite (MMT) functionalized with Krytox nanocomposite membrane (Krytox–MMT–Nafion) for DMFC applications. When compared with normal Nafion membranes the new membrane shows a reduction on methanol crossover rate.

Zhong *et al.* [84] focused their work on the modification of sulfonated poly(etheretherketone) (SPEEK) by coating a crosslinked chitosan (CS) layer on the surface of SPEEK membrane, in order to decrease the methanol crossover. In comparison to the pure SPEEK and Nafion 117 membranes, the composite membranes showed significantly stronger methanol barrier property.

Wu *et al.* [85] developed a series of proton-conducting membranes for direct methanol fuel cell (DMFC) applications via sulfonation of bromomethylated poly(2,6-dimethyl-

1,4-phenylene oxide) (BPPO) base membranes. Besides the low manufacture cost, the membranes exhibited an excellent control on methanol crossover and swelling, and a sound balance with high proton conductivities.

Since the methanol crossover is one of the major problems in DMFC, it is interesting to have simple models that describe this phenomenon to check the new membrane materials reducing time and experimental work. In the last years some work has been done in order to develop models that can describe and estimate the methanol flux across the membrane in DMFC [59, 86, 87].

Cruickshank and Scott [59] presented a simplified model to describe the methanol permeation from the anode to the cathode side, through Nafion 117 membranes. The model was also used to predict the DMFC cell voltage characteristics depending on some key parameters obtained from measuring the permeation rates of methanol and water across the membrane.

Barragán and Heinzel [86] described a simple model to easily estimate the methanol diffusion coefficient through the membrane of a DMFC from open circuit voltage measurements using Nafion membranes as electrolyte.

In their work, Sandhu *et al.* [87] developed a direct methanol fuel cell (DMFC) mass flux model to predict the fluid phase superficial velocity, methanol and water molar fluxes, and the chemical species (methanol and water) dimensionless concentration profiles in the polymer electrolyte membrane, Nafion 117, of a DMFC. They concluded that the methanol crossover flux decreases with a decrease in the methanol concentration at the anode side. This decrease in the methanol concentration at the anode side of the DMFC can result from a low concentration of methanol in the fuel fed to the anode channel or from a higher reaction rate at a higher temperature resulting in a higher current density.

Despite of the work done in understanding the methanol crossover phenomena, this mechanism is still unclear. Some correlations are used based on the assumption that methanol is dragged by the protons like water is dragged by the protons. More work is needed to clarify this issue.

The investigations found in literature show that methanol is readily transported across Nafion membranes and in order to minimize the effects of methanol crossover, alternative membrane materials have been sought. Nafion membranes still are the most

usually used as solid polymer electrolyte in DMFCs, since they are commercially available and have lower costs when compared to new ones.

An alternative to new membrane technology, in order to minimize the methanol crossover rate, is to improve the activity of methanol electro-oxidation catalysts, to use different catalyst loadings and to employed different diffusion layers materials with different thicknesses. This approach was followed in the present work.

2.5.2. Water management

In order to compete with traditional batteries, the most important requirement of a portable DMFC system must be a higher energy density. Recent studies [87-96] indicate that the water management is a critical challenge for DMFCs to accomplish the desirable energy levels. The amount and disposition of water within the fuel cell strongly affects efficiency and reliability. As was described in the last section, another important challenge to overcome in DMFC that employ Nafion membranes is the methanol crossover, which results in a fuel loss and decrease the overall cell voltage due to a mixed potential at the cathode. To solve this problem, the anode fuel solution should be very dilute, requiring a large amount of water to be carried in the system and thereby reducing the energy content of fuel mixture. The presence of a large amount of water floods the cathode and reduces its performance. So, an important engineering issue is to remove water from the cathode to avoid severe flooding and subsequently supply water to the anode to make up water loss due to water crossover through the membrane. Low water flux through the membrane is desirable for DMFCs, as the anode does not require an excessive amount of water replenishment and the cathode is less susceptible to severe flooding.

Formally, the water flux through the membrane, caused by diffusion and electro-osmosis, can be quantified in terms of net a water transfer coefficient (α–alfa value). The ideal value of this net water transfer coefficient is a negative value [90], which means that no water is necessary from the anode feed and the water needed to oxidize methanol comes from the water produced at the cathode side.

Izenson and Hill [88] presented the basic design relationships that govern the water balance in a PEM fuel cell. Specific calculations were presented, based on data from hydrogen/air and direct methanol fuel cells and they showed how the water balance

operating point depends on the cell operating parameters and on the sensitivity to design conditions.

Lu *et al.* [89] reported a novel DMFC design based on a cathode gas-diffusion layer coated with a microporous layer to build up the hydraulic pressure on the cathode side and on a thin membrane, Nafion 112, to promote water back-flow under this difference in hydraulic pressure. Such MEAs exhibit extraordinarily low water flux through the polymer membrane. The importance of the experimental work reported by the authors is the fact that commercially available Nafion membranes and MEA materials were used and the cell operated with ambient air without pressurization.

Sandhu *et al.* [87] developed a mass flux model to predict the fluid phase superficial velocity, methanol and water molar fluxes, and the chemical species (methanol and water) dimensionless concentration profiles in the polymer electrolyte membrane, Nafion 117, of a DMFC. This model can be used to generate the numerical data as a function of different variables, such as the pressure difference across the membrane, methanol concentration, temperature, and position in the membrane.

In their work, Liu *et al.* [90] described a new MEA design intended to achieve, simultaneously, low water crossover, low methanol crossover and high power density. They performed extensive experimental parametric studies to elucidate the effects of material properties, MEA fabrication processes and operating conditions. They observed that the important material properties are the membrane thickness and structure of the cathode gas diffusion media. The authors suggest that the key operating parameters are the methanol crossover and the cathode stoichiometry, cell temperature and current density.

Liu and Wang [91] based on a 3D two-phase model numerically investigated an interfacial liquid coverage model applied at the interface between the cathode backing layer and flow channel and its effects on the net water transport coefficient distribution in a DMFC were explored under typical operating conditions for portable applications. The authors showed that interfacial liquid coverage has a profound effect on the net water transport coefficient through the membrane by affecting water diffusion and hydraulic permeation.

Shi *et al.* [92] analyzed water transport phenomenon in PEM and the mechanism of occurrence and development of a two-phase countercurrent flow with corresponding transport phenomenon in the PEM. A one-dimensional steady state model of heat and mass transfer in porous media system with internal volumetric ohmic heating was

developed and simulated numerically to analyze water transport characteristics in the PEM.

Xu and Zhao [93] proposed a measurement method enabling an in situ determination of the water-crossover flux through the membrane in a DMFC. With this method the authors investigated the effects of various design and geometric parameters as well as operating conditions, such as the properties of cathode gas diffusion layer, membrane thickness, cell current density, cell temperature, feed methanol concentration, and oxygen flow rate, etc., on the water crossover through the membrane in a DMFC.

The water transport and the degree of cathode flooding in DMFCs appear to be significantly different from those occurring in PEFCs. Therefore, it is critical to optimize the cathode microporous (MPL) for DMFCs such that the anode water loss can be reduced and the cell performance can be upgraded. In their work, Xu et al [94] experimentally investigated the effects of both the PTFE loading in the cathode backing layer as well as in the microporous layer (MPL) and the carbon loading in the MPL on both water transport and cell performance. The experimental data showed that with the presence of a hydrophobic MPL in the cathode backing layer, the water-crossover flux through the membrane decreased slightly with an increase in the PTFE loading in the backing layer. However, a higher PTFE loading in the backing layer not only lowered cell performance, but also resulted in an unstable discharging process. It was found that the PTFE loading in the MPL had a small effect on the water crossover flux, but its effect on cell performance was substantial. The experimental results further showed that increasing the carbon loading in the MPL significantly lowered the water-crossover flux, but a too high carbon loading would decrease the cell performance as the result of the increased oxygen transport resistance [94]. The most common GDLs commercially available do not have MPL layers.

Xu *et al.* [95] developed a one-dimensional, isothermal two-phase mass transport model to investigate the water transport through the MEA. The liquid and gas two-phase mass transport in the porous anode and cathode was formulated based on classical multiphase flow theory in porous media. At the anode and cathode catalyst layers, the simultaneous three-phase (liquid and vapour in pores as well as dissolved phase in the electrolyte) water transport was considered and the phase exchange of water was modelled with finite-rate interfacial exchanges between different phases. This model enables quantification of the water flux corresponding to each of the three water transport mechanisms through the membrane, such as diffusion, electro-osmotic drag, and

convection. This model allows the numerical investigation of the effects of MEA design parameters on the water crossover and cell performance under various operating conditions.

Liu *et al.* [96] experimentally studied various anode diffusion media to reduce the water crossover in a DMFC. A two-phase water transport model was also employed to theoretically study the effects of those structures on water transport and saturation level in a DMFC anode. It was found that wettability of the anode microporous layer (MPL) has a dramatic effect on water crossover or on the water transport coefficient (α) through the membrane. Under different current densities, the MEA with a hydrophobic anode MPL had consistently low α values, several times smaller than those with a hydrophilic MPL or without an anode MPL. A modelling study of anode water transport revealed that the liquid saturation in the anode was significantly lowered with the increase of the anode MPL contact angle, which was thus identified as a key parameter to minimize water crossover in a DMFC.

The literature review concerning the water management in a DMFC indicates that some efforts have been made for studying water transport through Nafion type of membranes used in DMFCs. However, most of previous studies have generally been limited to the cases without taking account the effects of MEA design and geometric parameters as well as operating conditions. A general understanding of water crossover through the membrane that is integrated with the MEA for DMFCs is far less understood. In order to evaluate the water transport effect on DMFCs performance it is necessary to use different MEAs structures, with different membrane thicknesses, diffusion layers materials and thicknesses and catalyst layers properties. The development of mathematical model describing the water transport is, also, fundamental to better evaluate its effects on fuel cell performance.

2.6. Single cell performance – Polarization behaviour

The direct methanol fuel cell is a multiphase system involving simultaneous mass, charge and energy transfer. All these processes are intimately coupled, resulting in a need to search for optimal cell design, such as flow field design, and operating conditions (cell temperature, methanol concentration, cathode pressure and methanol

and air flow rate). A good understanding of this complex, interacting phenomena is thus essential and can most likely be achieved through a combined mathematical modelling and detailed experimental approach.

2.6.1. Operating conditions

An understanding of the interdependence of the operating conditions emerges as an important role in optimizing the performance of a DMFC. In fact, some work had been done in order to achieve optimal performances [97-105].

2.6.1.1. Methanol concentration

The effect of the methanol concentration on the DMFC performance generally reflects two phenomena. Increases on the methanol concentration lead to an increase on the coverage of the electrocatalyst sites by methanolic species, but also increase the concentration gradient between the anode and cathode side with a consequent increase in the crossover through the Nafion membrane. This requires a delicate balance among the effects of methanol oxidation kinetics and methanol crossover in order to enhance the performance of a DMFC. Another point that should be accounted for is the fact that the polarization behaviour in the mass transfer region is directly related to the methanol concentration, so an increase in the limiting current density is achieved with an increase in methanol concentration. Generally, almost all the experimental studies reported in literature [97, 99, 100, 104, 105] showed that there is a general increase in the limiting current with increase in concentration whilst at low current densities higher methanol concentrations cause a reduction in voltage at a fixed current density. As previously referred, the open-circuit voltage is much lower than the thermodynamic equilibrium cell voltage as a result of methanol crossover. At low current densities and high feed methanol concentrations the cell performance is lower. This is due to the fact that higher methanol concentrations result in higher values of methanol crossover. At the cathode side, methanol reacts with the oxygen to form a mixed potential. Hence, a higher methanol concentration leads to a higher mixed potential, causing thereby a lower cell performance. It is also reported in literature that the best performance is achieved with 1 to 2M methanol concentration, since usually methanol concentrations higher than these values generate higher values of methanol crossover.

2.6.1.2. Fuel cell temperature

Most of the experimental studies were performed with high temperatures [97-105] because higher temperatures lead to an increase in cell performance, since the electrochemical kinetics at the anode and cathode is favoured by increasing temperature. However, higher cell temperatures also have negative effects: the rate of methanol crossover and the water loss from the anode to the cathode increase with temperature and the membrane stability and the oxygen partial pressure decrease with temperature. The effective influence of the cell temperature is, in this way, a result of both positive effect of temperature on the electrode kinetics and the combined negative effects.

The increase of temperature also increases the open-circuit voltage and reduces the activation overvoltage according to the Arrhenius relation, thus resulting in a higher performance. However, if the operation temperature is similar to the boiling temperature of the solution, the cell performance decreases, since small bubbles of the vapour formed in the catalyst layer and diffusion layer may obstruct the fuel transport [99,103].

2.6.1.3. Methanol and air flow rate

Efficient removal of carbon dioxide gas bubbles and liquid water produced on the anode and cathode side, respectively, must be maintained to allow reactants to reach catalyst sites. Removal of carbon dioxide slugs and prevention of cathode “flooding” can be attained by increasing flow rates. However, increasing flow rates requires more pumping power. A very high flow rate at the cathode will dry out the polymer membrane, decreasing proton conductivity and hence cell performance.

According to several experimental studies [98, 99, 104, 105], the cell voltage and power slightly increases with the anode flow rate up to a certain value, after which a gradual decrease in the limiting current is seen as the flow rate increases. This is due to the fact that an increase in the anode flow rate is, under certain conditions, accompanied by an increase in the static pressure in the flow field. A higher static pressure tends to increase the methanol crossover towards the cathode, leading to a decrease in the cell performance [105].

The cell performance and cell power also increase with the air flow rate up to a certain value. From this optimum value on, any further increase on the air flow rate has no significant impact on the cell performance and power. When the cell is operating under

lower air flow rate the oxygen concentration decreases along the cathode flow channels resulting in lower cell voltage and power. When the air flow rate is high enough, any further increase will only slightly change the oxygen concentration profile, with a negligible effect on the cell performance [103, 104].

2.6.1.4. Air pressure

In most experimental studies performed in the last years [98-100, 102] high pressure operation was chosen in order to achieve a high performance. A reduction in the air pressure in the cathode of a DMFC will reduce cell performance due to a reduction in the cathode potential, which may be accentuated by the effect of methanol crossover from the cathode. The crossover of methanol can be, slightly reduced by a high cathode air pressure. However, some works [103, 105] suggested a high performance even at atmospheric pressure by optimizing the structures and compositions of the electrodes. This less severe condition is favourable especially for portable applications.

2.6.2. Configuration parameters

To improve the levels of performance in DMFCs there are an increased interest in reducing mass transport limitations, reduction of the kinetic and ohmic limitations. In this regard, some work has been done in order to improve the design of the reactant flow fields [39, 98, 99, 103, 106, 107], the catalyst loading [63, 99, 103] and the characteristics of the backing layer in terms of composition and thickness [63, 94, 98, 108, 109].

2.6.2.1. Flow field design

Once the reactants enter the cell, they must be distributed over the entire active area. This is typically accomplished through a flow field, which may be in a form of channels covering the entire area in some pattern or porous structures. The main task of these is to guarantee distribution of fuel and oxidant over the reaction surface area as well as the removal of products from the cell. Different types of flow fields for DMFCs have been presented in the literature [39, 98, 99, 103, 106, 107]. The most commonly used are parallel, serpentine, spot (or grid), and interdigitated channels as shown in Fig. 2.10.

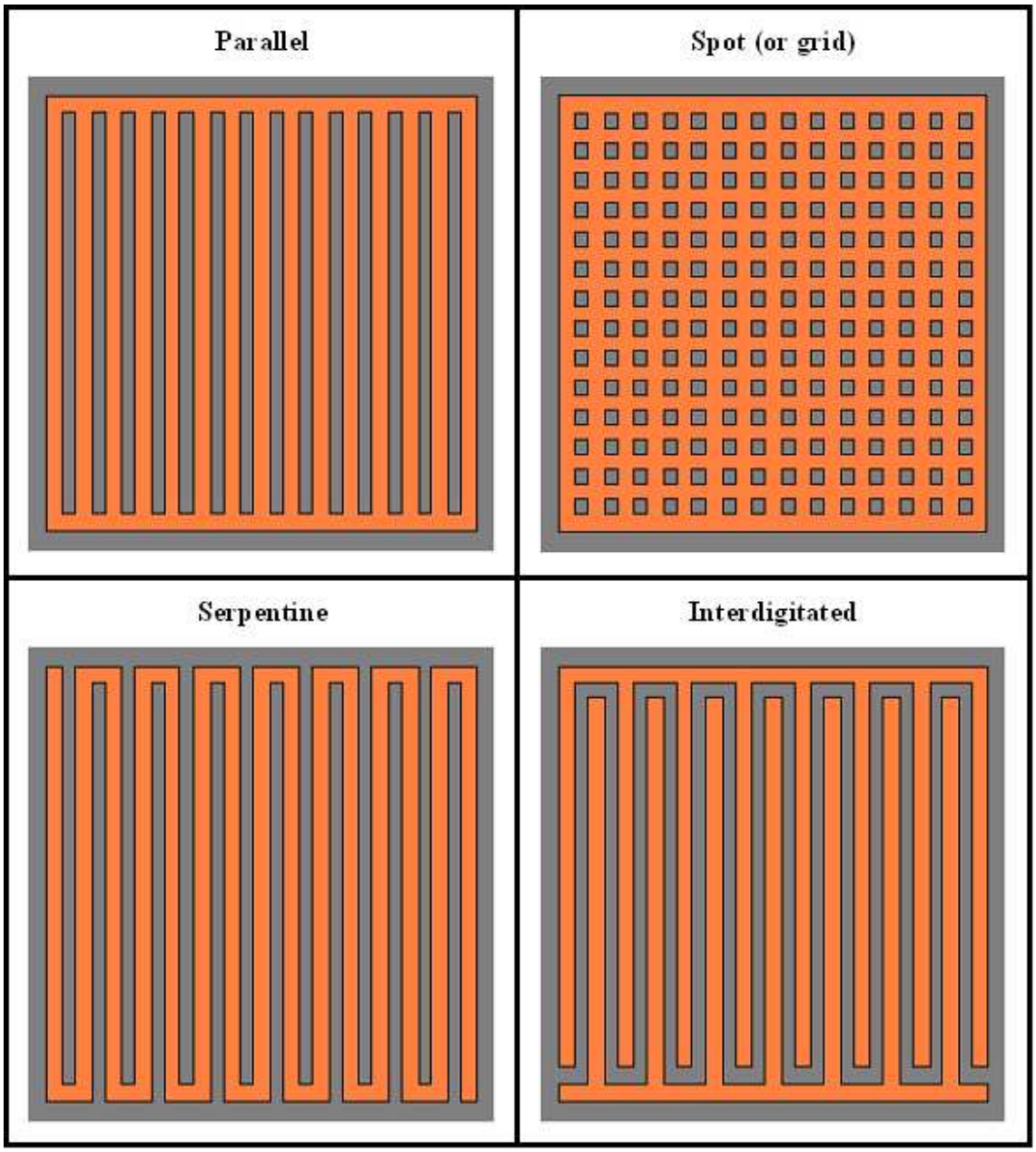

Figure 2.10 – Representation of the most commonly used DMFC flow fields.

The flow field most widely employed in direct methanol fuel cells is based on the serpentine configuration. In such a configuration, the reactant is constrained to flow in a zigzag way along parallel channels which are machined in a graphite plate. In general, different flow field designs have advantages and disadvantages associated with their application. Proper selection of flow fields with respect to the DMFCs operational and application conditions can help to achieve cost and performance goals.

The parallel and the spot flow field design generally give comparable performance, although at higher current densities, a higher cell voltage at the same current densities is

obtained when the cell uses the parallel design [98]. This may be partly due to an increased cell resistance resulting from a reduced contact with the MEA in the spot design. The results also suggest that the mass transfer limiting current for methanol oxidation was reached earlier in the spot design. Although the use of a spot design shows good results there are certain practical limitations with this design, such as, the fabrication which is more difficult and thus more expensive. Under operation there is a risk of puncturing of the MEA which occurs more frequently if the spots are not precisely aligned on the cathode and anode sides.

In the serpentine flow field the reactant is constrained to flow along parallel channels and the reactant molecules have access to the catalytic sites through diffusion across the diffusion/backing layers. In the interdigitated design the reactant is forced to enter into the electrode pores and exit from them under a pressure gradient. In this way the flow is no more governed by a diffusion mechanism but becomes a forced-convection mechanism. According to Aricò *et al.* [106] the interdigitated flow field significantly enhances mass transport and membrane humidification, in a DMFC, allowing higher maximum power outputs compared to the serpentine flow field. The DMFC equipped with serpentine flow field showed however lower methanol crossover, higher fuel utilization and a slightly large efficiency at low current densities. When comparing the serpentine and parallel flow field the results presented in the literature [39,107] showed that a DMFC equipped with the serpentine flow field showed better performance than those with the parallel flow field. It is also been found that gas bubbles blocked the flow channels in the parallel flow field at lower methanol flow rates and higher current densities. This phenomenon was never found in the serpentine flow field conditions tested in the work done by Yang *et al.* [39]. Since the serpentine flow field exhibited a better performance than the parallel flow field they focused their studied on the effects of the open ratio and channel length of the serpentine flow field on the cell performance and pressure drop. The studies indicated that the open ratio and flow channel length have important effects on the cell performance and pressure drop. When designing a serpentine flow field, caution has to be taken to ensure an optimal open ratio and flow channel length.

A comparison of these different flow fields, in terms of advantages and disadvantages is given in Table 2.1.

Table 2.1 – Comparison of different flow fields used in DMFCs

Flow field	Advantages	Disadvantages	References
Parallel	Low pressure drops	Inhomogeneous reactant distribution and difficult product removal	[39,98,107]
Spot	Similar to parallel flow field	Similar to parallel flow field and high cell resistance due to a reduced contact to the MEA	[98]
Serpentine	Helpful to remove reaction products and to enhance two-phase mass transport	High pressure drops between the inlet and outlet	[39,107]
Interdigitated	Enhanced mass transport and membrane humidification	High methanol crossover and high pressure difference required between channels	[106]

2.6.2.2. Catalyst loading

As was mentioned in section 2.3.3, the common catalyst layers used in DMFC are made by Pt/Ru on the anode side and Pt on the cathode side. In order to achieve high power densities in a DMFC, some work has been done in order to evaluate the influence of the anode and cathode catalyst loading on the cell performance [63, 99, 103]. There are also some reports in literature on supported, normally carbon-supported and unsupported catalyst compositions [63].

It should be noted that there are two essential properties of the electrode that may be affected when changing the catalyst loading: electronic conductivity and electrode thickness.

According to references [63, 99, 103] the cell performance increases with the Pt/Ru loading up to a certain value, after which any further increase on loading has a slightly reduction on the cell performance. At low current densities the activation overvoltage is

a major portion in the total overvoltage at the anode, so the increase in the Pt/Ru loading reduces the activation overvoltage at the anode, increasing the cell performance. With the increasing Pt/Ru the thickness of the catalyst layer increases and therefore the mass transfer resistance through this layer becomes greater. In spite of this, the cell performance increases with the metal loading because the thicker anode catalyst layer creates a higher resistance to methanol transport thereby controlling the rate of methanol reaching the membrane and reducing the methanol crossover. This reduction leads to a reduction of the parasite current formed, due to the oxidation of methanol at the cathode side and consequently the cell performance increases. At high current densities and with a loading above a critical value, the cell performance decreases, suggesting that the concentration overvoltage caused by the mass transfer of methanol through the thicker catalyst layer at the anode significantly increases.

On the cathode side a reduction on the noble metal loading leads to a decrease in the cell performance [63]. The reduction of the cathode catalyst layer leads to a reduction on active surface area, an increase on resistivity and consequently a decrease in electronic conductivity. An increase on the catalyst loading also causes an increase in electrode thickness. A thicker electrode conducts to a higher mass transport resistance but, on the other hand, may also be advantageous at the cathode, since mixed potential formation may be avoided to some extent. In a thicker electrode not all the catalyst particles may be reached by the permeated methanol flux, so more active sites are free for oxygen reduction reaction.

With carbon supported materials the loading can be reduced without a decrease of the electronic conductivity of the electrode. However, the use of carbon supported catalyst with a much lower bulk density is associated with a higher thickness of the active layer which is an important parameter for the cell performance. A thicker electrode may lead to a higher mass transport resistance of methanol leading to a decrease of the fuel cell performance. On the other hand, this resistance may be also an advantage at the cathode side since mixed potential formation may be avoided in some extend. So, the use of carbon supported catalysts and their optimization in the electrode structure has the potential to significantly reduce metal loading which will contribute to the cost reduction in DMFCs [63].

2.6.2.3. Diffusion Layers

The operation of the DMFC requires that the methanol has good access to the anode while the carbon dioxide gas generated is able to move away freely from the catalyst sites on the catalyst surface. Ideally, these flows should be isolated such that discrete paths for gas flow and for liquid flow exist, rather than a two phase flow with gas bubbles moving against a liquid flow, induced by the anode reaction and the electro-osmotic transport of water and methanol. The simplest way to approach this ideal is to make the carbon surface hydrophobic adding Teflon to the diffusion layer. The cathode of the DMFC may be similarly affected by possible problems of flooding, but in comparison to the anode this is a less critical issue. Some work has been done in order to explore the effect of Teflon (PTFE) content on the cell performance [63, 94, 98, 108, 109]. According to the work developed in this area, the DMFCs using untreated anode diffusion layers produce the poorest performance. The PTFE content decreases the methanol crossover leading to an increase in the open circuit voltage and the cell performance. The presence of PTFE, also, increases the internal resistance of the cell which leads to a decrease of the cell performance for PTFE contents above 30% [98,108].

In their work, Xu *et al.* [94] used carbon paper as anode diffusion layer and studied the effect of the anode diffusion layer thickness on the cell performance. The increase in carbon paper thickness leads to an increase on the cell performance and the carbon paper with the medium thickness (Toray-090 (TGPH090), 0.26 mm) gave the best performance in the entire current density region. At low current densities, a further increase in carbon paper thickness (TGPH120, 0.35 mm) leads to a cell performance similar as that for TGPH090, while at high current densities the cell performance dropped rapidly. The experimental results presented by the authors shown that when a too thin carbon paper was used the voltages generated by the fuel cell were low in the entire current density region. On the other hand, when a too thick carbon paper was used, the fuel cell yielded a low limiting current density. Therefore, it can be concluded that exists an optimal carbon paper thickness that results in the best performance.

Thicker gas diffusion layers lead to lower methanol concentration at the anode catalyst layer surface, since the diffusion path is longer. As the current density is dependent on the methanol surface concentration, lower performances are obtained for thicker anodes. However thicker gas diffusion layers limits, also, the amount of methanol that crosses

the membrane leading to an increase in fuel cell performance. More work should be done in order to evaluate these two opposite effects on DMFC performance.

The power and cell voltage of the DMFC has been considerably increased in the last years, but it must be further increased by improving the anode catalyst activity and the electrode structure. Similarly, the air stoichiometry was significantly reduced, but it is still too high for practical systems in terms of energy losses for air management. High flow rates are required to remove the large amounts of water and methanol diffusing through the membrane in particular for high methanol concentrations and high values of current densities. Therefore, the development of a specific membrane electrode assembly by changing the catalyst layer loading, gas diffusion layer properties and membrane thickness, with a low methanol and water crossover, will be the key issue for development a reasonable DMFC system. These parameters could increase the cell voltage and reduce the air stoichiometry necessary for portable applications.

2.7. Mathematical Modelling

Fuel cell modelling has received much attention over the last decade in an attempt to better understand the phenomena occurring within the cell. Different types of approaches are available in literature [110], [111]. Analytical models are an adequate tool to understand the effect of basic variables on fuel cell performance. Many simplifying assumptions are made concerning variable profiles within the cell to develop an approximate analytical voltage versus current density correlation. Semi-empirical models allow designers and engineers to predict the fuel cell performance as a function of different operating conditions (such as pressure, temperature or fuel concentration) using simple empirical equations. Mechanistic models are transport models using differential and algebraic equations whose derivation is based in the electro-chemistry and physics governing the phenomena taking place in the cell. These equations are numerically solved by different methods. These models while involving extensive calculations, accurately predict the flux and concentration of multiple species in the cell. Mechanistic or theoretical models can be subcategorized as multi-domain (sets of equations for each region of the DMFC) or single-domain (or unified) models (all the regions of interest are combined in a unique domain).

Single fuel cell models aim to describe quantitatively interactions among the several physical and electrochemical phenomena occurring along the different layers and may be classified in one of the three types enounced (analytical, semi-empirical and mechanistic). Figure 2.11 categorizes the thirty nine models reviewed according to the features studied (dimension, polarization, transport phenomena, thermal effects, concentration effects, catalyst utilization, flow channels geometry, methanol crossover, two phase flow effects, dynamic effects and fuel cell stacks).

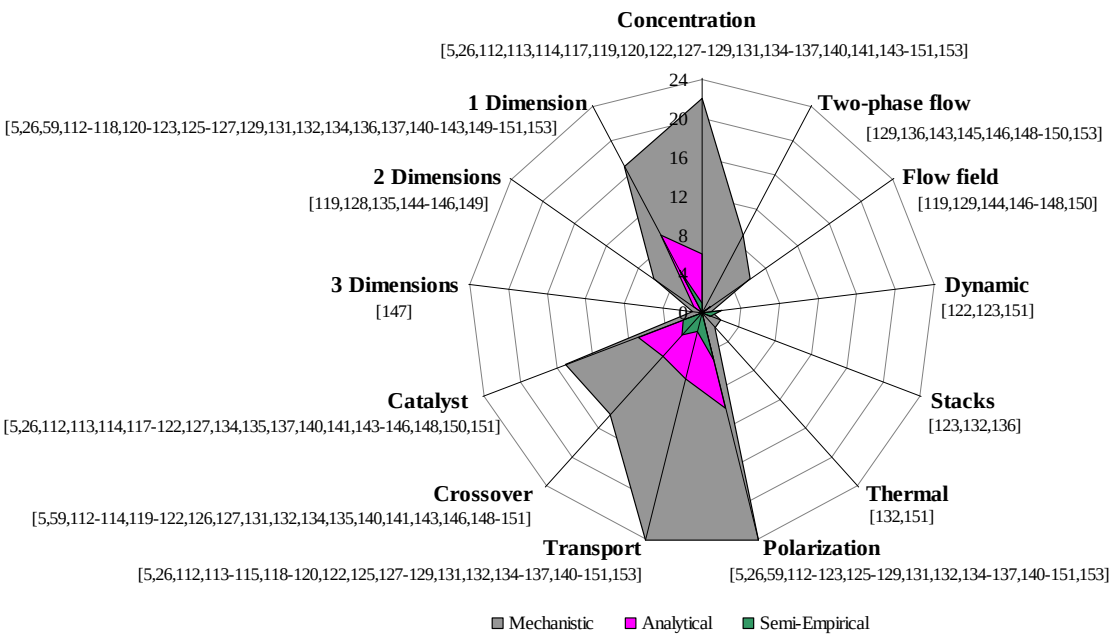

Figure 2.11 – DMFC model categorization based on areas of investigation.

2.7.1. Analytical models

Models described in references [59, 112-120] are examples of analytical modeling. They all rely on many simplifying assumptions, but most of them have the merit of predicting voltage losses for simple designs and they can be useful for rapid calculations in these systems. Some of these models are not «purely» analytical since they incorporate one or more empirical correlations.

Scott *et al.* [112] developed a simple model to evaluate cell performance describing mass transport in the porous electrode structures and the potential and concentration distributions in the electrode regions. The model also incorporates the influence of

methanol crossover from anode to cathode based on a combination of diffusion, electro-osmotic drag and pressure.

Cruickshank and Scott [59] present a simplified model to predict the DMFC cell voltage characteristics depending on some key parameters obtained from measured permeation rates of methanol and water through Nafion 117 membranes.

Sundmacher and Scott [113] developed a steady state, isothermal cell model accounting for the essential mass transfer and charge transport processes in the different fuel cell layers.

Kulikovsky [114-116] has reported analytical models but employing a semi-empirical approach to account for the limiting current behavior. The general expression for the voltage-current curve is based on exact solution for the catalyst layer reaction and includes the over potential due to transport limitation in diffusion backing layer and the one due to methanol crossover. Some of the model parameters are obtained by fitting experimental data.

Scott and Argyropoulos [117, 118] presented a one-dimensional model to predict the current and potential distribution in a porous electrode of a DMFC which accounts for internal limitations of mass transport. Some difficulties arise when one tries to implement this model since the results obtained by the authors can not be reproduced. There is an error on the model development (equation 33 of reference [118]) as was pointed out by Kulikovsky [152].

Guo and Ma [119] reported a two-dimensional analytical model to describe electrochemical reactions on the anode and cathode and main transport phenomena in the fuel cell including methanol crossover, diffusion of reactants in porous media layers and fluid flow in the reactants distributor. In fact, the model is one-dimensional since the authors neglect the transport in the channel direction (y – direction in Fig. 2.1). This simple model was in agreement with the experimental data reported (T=90°C, methanol concentration in the range 0.125M to 0.625M especially for current densities higher than 0.01 A/cm^2). This model was in the present study tested out of these operation conditions and the discrepancy between predictions and experimental is higher namely for low values of current densities, relatively low values of temperature and high methanol concentration.

Garcia *et al.* [120] provided a very interesting model accounting for the kinetics of the multi-step methanol oxidation reaction at the anode, the diffusion and crossover of methanol and the mixed potential of the oxygen on the cathode due to methanol

crossover. Some of the kinetic and diffusional parameters are estimated by adjusting the model to experimental data. This model has the merit of being rapidly implemented and therefore it is suitable for inclusion in real-time system level DMFC calculations. This «semi-analytical» model was selected for a more deep study in the next section.

2.7.2. Semi-empirical models

Most empirical performance models combine theoretically differential and algebraic equations with empirical determined correlations. The great advantage of these models is their simple structure and the small computational effort to perform calculations. However the estimated parameters from the experimental data are normally specific to certain types of cell and valid for a limited range of operating conditions. The models are very useful to perform quick predictions for existing designs but fail to predict innovative ones.

The number of semi-empirical models developed for DMFCs is limited [121-126].

Kauranen and Skou [121] reported a model describing both the oxygen reduction and the methanol oxidation in the cathode of a DMFC and concluded that the oxygen reduction current is reduced in the presence of methanol oxidation due to surface poisoning.

Sundmacher *et al.* [122] observed that pulsed methanol feeding could achieve a significant increase of the time averaged cell voltage and a considerable reduction of the methanol consumption in the fuel cell. The model was able of describing quantitatively the behavior of the cell.

Simouglou *et al.* [123, 124] developed an empirical model using statistical methods and providing one step-ahead predictions of the dynamic voltage response from measurements of cell voltage and current density for the fuel cell that the authors designed in order to fit the model.

Argyropoulos *et al.* [125] presented a model to predict the cell voltage versus current density for a liquid feed DMFC. The model is based on a semi-empirical approach in which methanol oxidation and oxygen reduction kinetics are combined with effective mass transport coefficients for the fuel cell electrodes. The implementation of this simple model presents some difficulties since the obtained results are not in accordance with those of the authors. For example the effect of temperature in the polarization

curve is unexpected since an increase in temperature leads to a decrease in the cell voltage for a given current density.

Dohle and Wipperman [126] developed a model to predict polarization curves and the permeability of methanol trough a DMFC based on a set of parameters adjusted from experiments performed in a wide range of operating conditions.

This semi-empirical model was selected for a more profound study in the next section.

2.7.3. Mechanistic models

The mechanistic models account for the detailed fundamental phenomena such as heat, momentum, multi-component mass transport and electrochemical processes. Since the pioneering woks of Scott *et al.* [127] and Kulikovsky *et al.* [128] considerable effort has been devoted to the development of mechanistic models for DMFCs.

Most of the mechanistic models developed for DMFCs were solved using the multi-domain approach. In the past three or four years with the introduction of CFD methods to fuel cell modelling the single-domain approach begun to be used [147]. The single-domain approach is appropriate to be used in multidimensional modelling since in this case there is no need of using the internal boundary conditions or continuity condition at each interface which could become cumbersome in 2D or 3D dimensions. The single-domain approach lends therefore to be implemented in commercial CFD codes.

Most of the developed models are one-dimensional, analysing the different phenomena across the fuel cell. More recently, various two-dimensional models [135, 144, 145, 148] have been developed. In a 2D model based on current conservation equations, Kulikovski [135] concluded that, near the fuel channel, transport of methanol is determined mainly by a pressure gradient. In the active layers and in the membrane diffusion transport dominates. “Shaded” zones, where there is a lack of methanol appear in front of the current collectors.

Krewer *et al.* [147] presented a 3D model but only concerning the anode of a DMFC. The authors studied the residence time behaviour and concentration distribution in a simplified rhomboidal anode flow bed. The simulation results compared well with experimental results.

The electrochemical reactions taking place at a DMFC are exothermic. Heat can be also produced by irreversibilities in the cell (ohmic or activation losses). Heat removal is a critical issue for fuel cells. Depending on whether the temperature profile is simulated

or not, fuel cell models can be categorized as isothermal or non-isothermal. Argyropoulos *et al.* [132] developed a thermal energy one-dimensional mechanistic model for a DMFC stack based on the differential thermal energy equation. The model allows the assessment of the effect of operating parameters such as fuel and oxidant inlet temperature, flowrate, pressure and current density and also of some design parameters (active area, material properties and geometry) in the cell temperature along the stack. Recently, Shultz and Sundmacher [151] developed a non-isothermal, one-dimensional, dynamic model using the multi-domain approach. In this model, mass transport within the different porous structures of the DMFC was described using the generalised Stefan-Maxwell equations. For the membrane, an activity model based on the Flory-Huggins approach is used accounting for swelling phenomena, non-idealities and phase equilibria between the pore liquid inside the PEM and the fluids inside both of the catalysts layers. The model showed good agreement to experimental data obtained by the authors, concerning methanol crossover and steady state current-voltage characteristics.

The performance of fuel cell strongly depends on the flow field effects directly related to a non-uniform flow distribution in both the flow field plates. The main factors that influence the flow distribution are the hydraulic resistance, the flow field plate design and the temperature profiles. Some of the mechanistic reviewed models have incorporated flow field effects [26, 127, 129, 137, 144, 146, 147, 148]. Argyropoulos *et al.* [129] investigated the pressure drop in the anode and cathode flow fields. They established an equation to determine the pressure drop of the two-phase flow.

Until now there is no reported study on a single model accounting for both flow and temperature distribution and also only simple geometries of the flow field plate have been considered.

In the early stages of fuel cell modelling (and DMFC modelling) only single phase flow was considered. Dohle *et al.* [134] developed a one dimensional model for a vapour fed DMFC. Kulikovski et al [128, 135] extended their hydrogen fuel cell model to both the vapour fed and liquid fed DMFC. In all of these models only one phase was considered. Recently several works have been devoted to the study of two-phase flows in fuel cells [127, 129, 131, 136, 145, 146, 148, 149, 150, 153]. Among these, Wang and Wang [146] is the most comprehensive two-phase flow model for direct methanol fuel cells. In addition to the anode and cathode electrochemical reactions the model considers convection and diffusion of both gas and liquid phases in the backing layers and flow

channels. This model using the multi-domain approach fully accounts for the mixed potential effect of methanol oxidation at the cathode as a result of methanol crossover. The model was solved numerically using CFD. One of the main contributions of this work is the two-phase flow modelling of the anode. The authors considered that the gas phase at the anode is saturated with water and methanol and the liquid phase is saturated with CO_2. The gas phase concentration of the three species and the carbon dioxide concentration in the liquid phase can be determined by thermodynamic equilibrium relationships.

Current two-phase models assume that both the liquid and gas phases are continuous. However there is no visualization evidence of this picture. Experimental studies are needed to visualize the evolution process of two-phase flow both in the anode and the cathode flow channels to further develop mathematical models.

A significant number of the DMFC mechanistic models incorporate the influence of methanol crossover. Some of these models such as Dohle *et al.* [134] and Kulikovsky *et al.* [128, 135] consider that the methanol crossing the membrane is completely consumed in the cathode catalyst layer. Wang and Wang [146] considered the complete oxidation of methanol at the cathode and assumed that the current density for methanol crossover is dictated by the crossover flux. The authors concluded in their work that the methanol crossover is driven diffusion, convection caused by pressure gradient and electro-osmosis. The three contributions occur differently under different operating conditions. Methanol transport is dominated by molecular diffusion at zero and small current densities. At high current densities the methanol crossover flux becomes small and both diffusion and electro-osmosis contribute to the crossover. The mechanism of methanol transport trough the membrane is unclear. Some correlations are used based on the assumption that methanol is dragged by the proton like water is dragged by the protons. More work is needed to clarify this issue.

Analytical, semi-empirical and mechanistic models for direct methanol fuel cells have been reviewed. In spite of the modelling work on DMFCs developed in the past few years, a number of unresolved issues demand for intensive research. One of the most important areas to investigate is the numerical modelling of two-phase flows (both in the anode and the cathode) and also parallel experimental studies on visualization of these phenomena. Improved and validated mechanistic models namely using the single-domain approach are required to enable better design of fuel cells. Some of the simpler

models (either analytical or semi-empirical) can be used under some conditions. The validity of semi-empirical models is limited to a narrow corridor of operating conditions. Semi-empirical models give quick predictions for existing designs but fail to predict innovative ones. Analytical models predict voltage losses for simple designs and they can be useful for rapid calculations in these systems.

In addition, much effort should be directed towards the development of a coupled model for methanol, water and heat transport processes simultaneously in a DMFC. Such models are extremely useful for the discovery of unique design and operation regimes of the DMFC system for portable application, where the high energy density entails using highly concentrated methanol (preferably pure methanol), maintaining low water and methanol crossover, and improving high-voltage performance.

2.8. Passive DMFC

Energy needs for portable electronics are rising rapidly in the past few years due to the increasing functionalities of portable devices, especially cell phones. Nowadays the cell phones incorporate graphics and games, internet service, instant messaging and are helpful even to find a restaurant or museum. Conventional batteries are soon becoming inadequate for the increasing power and complexity of portable electronics and computers. The lifetime of portable devices is still limited to how long they can operate as truly portable by the quantity of energy that can be stored within the batteries. Fuel cell systems and particularly direct methanol fuel cell (DMFC) are being considered as a possible solution to replace the current battery as the dominant power provider for portable application. The passive and particularly the micro-DMFC are capable of replacing the conventional batteries, due to their high energy density and inherent simplicity of operation with methanol as the liquid fuel. This system is smaller, better, less costly, environmentally safer and much more efficient and can be used either in the plane, train, and car or in remote areas where there is no electricity. The refuelling of the passive DMFC is fast and the fuel can last several months. The product is cost competitive due to the large market size and economies of scale.

The fuel and oxidant can be supplied to a DMFC in an active and a passive way. Active systems use extra components such as a pump or blower, a fan for cooling, reactant and product control, which allows the operation of a DMFC at favourable conditions with

respect to temperature, pressure, concentration and flow rate. As was described before, this improves flow mass transport and electrochemical activity, therefore higher current density and power can be achieved. This type of system supply has greater costs and lower system energy density so, it is better suited for large fuel cells. Passive systems use natural capillary forces, diffusion, convection (air breathing) and evaporation to achieve all processes without any additional power consumption. They usually operate at low current densities resulting in reduced cooling loads, less water management issue, less heat production and lower required fuel delivery rate. Therefore, by using a well designed compact architecture, a passive system is more suitable for portable power sources.

The passive fuel cell system must be made small and compact for portable applications, and each application has different power, voltage and geometric design requirements. Significant effort for future commercialization has to be put in developing systems that can achieve the optimum balance of cost, efficiency, reliability and durability. However, miniaturization is not a simple scaling down of the larger system. Furthermore, each component of the fuel cell must be redesigned with an eye towards miniaturization.

As was mentioned before, in the passive feed system the fuel pump and air blower are eliminated. The fuel is supplied to the anode from a fuel reservoir built in the anode and the air to the cathode, normally by natural convection (Fig. 2.12). However, this simple design causes lower system performance due to the difficulty in getting a continuous and homogeneous supply of reactants to the anode and cathode. The lack of flowing force to remove the bubbles that constantly build up from the formation of carbon dioxide, in the anode reaction, will also hinder further oxidation of fuel at the anode surface. At the cathode, water droplet tends to build up and block the active surface, thus reducing the oxygen supply.

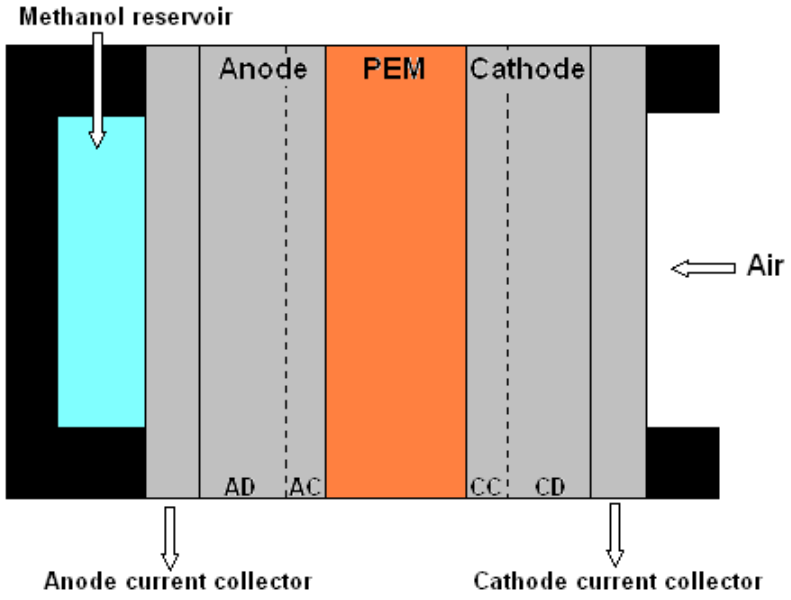

Figure 2.12 – Schematic representation of conventional design of a passive DMFC.

System control associated with water and methanol management adds considerable complexity to passive DMFC systems, particularly those being developed for portable applications. It is desirable to recycle the water produced at cathode to anode for dilution of fuel, but there is very little information disclosed by established fuel cell manufacturers on their advanced prototypes.

In a passive DMFC, the anode suffers from high activation overpotentials due to the slow kinetics of methanol oxidation reaction. This negative effect limits the rate of electrode reactions, which reduces the cell voltage and severely affects the voltage efficiency of the system. In practice, methanol oxidation at anode is promoted most effectively by platinum-based electro-catalyst. A passive DMFC generally needs higher loading of catalyst due to the slow kinetics of methanol electro oxidation reaction and severe methanol crossover to the cathode side. Unfortunately, the noble metal used as catalyst in this type of fuel cells is high in cost, and this tends to discourage the progress commercialization of portable DMFCs.

The most important challenges to overcome in passive systems are the methanol crossover rate and the thermal and water management.

Methanol crossover in passive DMFC is a fundamental problem to overcome in order to stimulate the development of this system. High concentration of methanol provides a higher achievable energy density, but it also causes severe methanol crossover through the membrane and results in a mixed potential at the cathode generating, therefore, a low cell performance. As already referred, methanol crossover has two negative

consequences: self-discharge of methanol, which provides additional heat instead of electricity, and drastic reduction of the cathode voltage. Other important factor is the temperature rise in the cell due to the oxidation the methanol at the cathode that releases heat. Moreover, the actual practical electrochemical energy recoverable from a passive DMFC system is much lower than the theoretical value, since from the total energy involved a small percentage can be expected as electricity, while the rest is converted into heat. The heat produced has to be dissipated, or else the accumulated heat in the system might be a strong disadvantage for compact portable systems.

Some work has been done in order to evaluate the effect of methanol concentration, methanol crossover and the heat and water management on the cell performance [154-161].

The passive feed systems have lower power densities, also, due to the inability to handle the excess water evolved at the cathode and crossed from the anode. The presence of a large amount of water floods the cathode and reduces its performance. So, a very important engineering issue is to remove water from the cathode to avoid severe flooding and subsequently supply water to the anode to make up water loss due to water crossover through the membrane. As already referred in section 2.5.2, the water flux through the membrane, caused by diffusion and electro-osmosis, can be quantified in terms of a net water transport coefficient (α value). The ideal value of this net water transport coefficient is a negative value, which means that no water is needed from the anode and the water needed to oxidize methanol comes from the water produced on the cathode side. The magnitude and spatial distribution of the net water transport coefficient are very important for the design of innovative water management strategies in DMFCs, but with particular interest in micro DMFCs. Some studies on water management for a passive feed DMFC have been performed [162-165].

Kim *et al.* [162] propose a new MEA structure to effectively reduce the methanol crossover by adopting a composite membrane. The structure was carefully designed to enhance water back diffusion through the membrane by using diffusion layers with hydrophilic nano-particles developed by the authors. Both novel structure and conventional structure were built and tested, and the results were compared to evaluate the effectiveness of the new structure. The water back diffusion was measured and the novel MEA proposed showed an impressive improvement compared with the conventional structure.

Song *et al.* [163] studied the water crossover behaviour in air-breathing DMFC with varying structural variables of membrane electrode assembly, such as the existence of a microporous layer in the cathode diffusion layer, hydrophobicity of the cathode backing layer, and membrane thickness. They observed that water crossover from anode to cathode was lowered by the introduction of the microporous layer in the cathode backing layer, the reduction of hydrophobicity of the cathode backing layer and the reduction of the membrane thickness. They also found that the methanol crossover was lowered when reducing water crossover. The MEA designed for low water crossover revealed improved stability under continuous operation.

In their work, Jewett *et al.* [164] examined the effects of the membrane thickness, water management system, air management system and gas diffusion electrodes on the water balance coefficient (this coefficient relates the amount of water used per methanol used in mole quantities), fuel utilization efficiency, energy efficiency and power density. When the water balance coefficient is equal to zero, the system is losing 2 mol of water for every 1 mol of methanol consumed (the net product of 2 mol created by the reaction), which is water neutral operation. This is the ideal state for the cell to operate in. When the water balance coefficient is negative, there is an excess amount of water being lost or consumed, more than 2 mol of water used per mole of methanol used. When the water balance coefficient is positive, there is an excess amount of water being retained by the system, less than 2 mol of water used per mole of methanol used. This is the goal at which an external supply of water is not required. The authors used two different membranes, Nafion 117 and Nafion 112 and they found that Nafion 117 cells had grater water balance coefficients, higher fuel utilization efficiency and greater energy efficiency.

Scharfer *et al.* [165] presented the measurement of the concentration profiles of water and methanol in Nafion membranes by means of confocal Raman spectroscopy with high spatial resolution. The experimental results showed that the measurement technique is suited to investigate the water and methanol transport within fuel cell membranes. They verified the influence of the air flow rate, the temperature and the methanol concentration solution on the concentration profiles of water and methanol using Nafion membranes. They found that the methanol concentration profiles changed with the air flow rate, with temperature and, as expected, were dependent on the methanol concentration. The water concentration profiles showed a dependency on the

air flow rate and almost no dependency on the temperature and on the methanol concentration.

Despite the number of modelling studies in DMFCs only a few simulate passive DMFCs [166-169] and only two of them take into account thermal effects [166, 169].

Since thermal management is a key issue in the portable DMFC system it is important to develop new models accounting for this effect and that can be a simple computer-aided tool to the design and optimization of passive direct methanol fuel cells.

Chen *et al.* [166] presented a one-dimensional model to describe a passive liquid-feed direct methanol fuel cell combining the effects of heat and mass transfer. The model provides the temperature profile along the different layers of a passive DMFC.

More recently, Chen *et al.* [169] presented a two-dimensional two-phase thermal model for passive direct methanol fuel cells (DMFC). The inherently coupled heat and mass transport, along with the electrochemical reactions occurring in the passive DMFC are modelled based on the unsaturated flow theory in porous media. The model is solved numerically using a home-written computer code to investigate the effects of various operating and geometric design parameters, including methanol concentration as well as the open ratio and channel and rib width of the current collectors, on the cell performance.

These two models [166, 169] have the disadvantages of considering the catalyst layers as interfaces, so it is not possible to obtain the temperature and concentration profiles in these layers, and the authors assumed that the anode side is well insulated so no heat is lost from the anode side. This assumption may be very unrealistic in a passive DMFC working in a portable system.

As was discussed above, many challenges exist for passive DMFC systems. Low water crossover, low methanol crossover and high power densities are essential requirements of a direct methanol fuel cell for portable applications. It is extremely important to develop new MEAs designs intended to achieve all three goals simultaneously. Extensive parametric studies should be performed to elucidate the effects of material properties, MEA fabrication processes and operating conditions in passive feed systems. It is, also, crucial to develop new models accounting for the effects of coupled heat and mass transfer, along with the electrochemical reactions, preferably consisting of a simple computer-aided tool to the design and optimization of passive direct methanol fuel cells. Further research and development in this area could significantly

improve power and energy density, efficiency, cost and reliability for DMFC portable applications.

2.9. Applications

The direct methanol fuel cells (DMFCs) can be used in everything that uses a battery, like mobile phones, laptops or CD players. Like the other types of fuel cells, DMFC technology is a great source of clean alternative energy and has the advantage of using a liquid fuel eliminating the need of fuel reformer, high operation pressures and temperatures and of lowering the system size and weight.

The opportunities and demand for direct methanol fuel cells in stationary applications are also extraordinary. More than 2500 fuel cell systems have been installed all over the world providing primary or backup power. Producing immediate stationary, decentralized power by using direct methanol fuel cell technology for every electrical need can reduce energy costs by 20% to 40% over conventional energy service. Direct methanol fuel cells are ideal for power generation, either connected to the electric grid to provide supplemental power and backup assurance for critical areas, or installed as a grid-independent generator for on-site service in areas that are inaccessible by power lines. DMFCs generators can be used to provide hot water or space heating for a residential. These types of fuel cells are, also, being incorporated into buses, trains, scooters and golf carts. Luxury liners and tankers, yachts and fishing boats can power themselves across the oceans using DMFCs having on-board power for personal comforts without the dreadful noise and fumes of combustion generators. Furthermore, the use of methanol, a biodegradable fuel, will rescue our oceans from the pollution caused by the dumping of other fuels.

Possibly the most wide uses for direct methanol fuel cells are in the area of portable power since this technology will change the telecommuting world, powering laptops and palm pilots hours longer than batteries and allowing up to a month of talk time on a mobile phone. Other applications for DMFC fuel cells include pagers, video recorders, portable power tools, and low power remote devices such as hearing aids, smoke detectors, burglar alarms, hotel locks and meter readers (Fig. 2.13).

Figure 2.13 – Direct Methanol Fuel Cell applications (Courtesy Toshiba, Samsung, Motorola, Suzuki, Company's XX25, Yamaha, DaimlerChrysler, DoCoMo and Fujitsu, Intermec, Panasonic, Volkswagen).

2.10. Summary and Scope of the present work

The fundamental transport processes of methanol, water and heat occurring in DMFCs have been reviewed, along with a summary of recent DMFC models and experimental studies. Significant challenges still exist before a DMFC can be ready to commercialization and compete with the traditional batteries. A better understanding of the basic transport phenomena achieved through combined flow visualization studies and transport simulations is essential to overcome these challenges and to encourage new design concepts. Material problems remain as an issue in DMFC research and development, but in this area (membrane and catalyst properties) already notable efforts are made by various groups and companies.

Some effort is being directed towards the development of DMFC mathematical models describing the transport phenomena occurring in the DMFC, although only a few models describe all the inside phenomena processes. In general, these models account for the effects of the two-phase flow and multicomponent transport in channels and porous regions (backing layers, catalyst layers, and membrane) along with the electrochemical reaction presented in a DMFC. They also included the mixed potential effect of methanol oxidation at the cathode as a result of methanol crossover and can be solved numerically using CFD (Computational Fluid Dynamics). These models can be used to investigate the effects of various operating and structural parameters on cell performance, however the practical usefulness of CFD models is relatively low (computing times, for example, are still prohibitive). It is necessary to developed “old fashioned” analytical and semi-empirical models (using applied mathematical techniques and computing power) to obtain useful, reduced models. Despite all the work done in DMFC modelling, there is still the need for reliable mathematical models of complete fuel cells coupling, simultaneously, methanol, water and heat transport processes in a DMFC. Such models are helpful for the discovery of new cell designs and operation regimes of the DMFC system. One of the objectives of the present work is the development of a model considering the effects of coupled heat and mass transfer, along with the electrochemical reactions occurring in an active and passive feeding DMFC. The model should be used to predict the methanol, oxygen, carbon dioxide and water concentration profiles in the anode, cathode and membrane as well as to estimate the methanol and water crossover and the temperature profile across the cell. The model, describing the active feed DMFC, should allow the assessment of the effect of

operating parameters (such as methanol and oxygen feed concentration, flow-rate and current density) and the design parameters (channel geometry, active area and material properties) on the temperature and concentration profiles along the cell and consequently on the cell performance. The model for the passive feed DMFC should, also, allow the assessment of the effect of methanol concentration and material properties on the temperature and concentration profiles along the cell and on the cell performance. To further understand the physical and chemical phenomena occurring inside the DMFC, steady-state experiments were carried out and were used to validate the developed models. The models were, also, used to provide suitable operating ranges adequate to different applications for different operating conditions and variable MEA structures.

There is a lack of work published on DMFCs operating at atmospheric pressure and low temperatures and these less severe conditions are favourable especially for portable applications. It is also a main objective of this to work study the effect of operating conditions, such as methanol feed concentration, methanol and air flow rate, and the effect of configuration parameters, such as gas diffusion media, catalyst loading, membrane thickness, and flow field designs on the cell performance of an active feed DMFC at ambient conditions (atmospheric pressure and ambient temperature).

CHAPTER 3

3. MODEL FORMULATION FOR AN ACTIVE FEED DMFC

The necessity of formulation of adequate mathematical models is based on the need to reach a deeper understanding of internal processes (reactions, mass transport, heat transport) which can not be observed directly in experiments or the possibility to apply mathematical optimisation methods to obtain hints as to where further technical improvements may be required or beneficial, and, finally, for the development of optimal control and operating strategies.

In this chapter the development of a semi-analytical one-dimensional model considering the effects of coupled heat and mass transfer, along with the electrochemical reactions occurring in an active feeding DMFC are presented. The main objective is to produce a simplified model describing the main heat and mass transfer effects in a DMFC reproducing with satisfactory accuracy experimental data.

The contents of this Chapter were partially published in Oliveira, V.B, Falcão, D.S., Rangel, C.M. and Pinto, A.M.F.R., "Heat and mass transfer effects in a direct methanol fuel cell: A 1D model", International Journal of Hydrogen Energy, Vol. 33, Issue 17, July 2008, 3818-3828.

3.1. General model structure

A schematic representation of an active-feed direct methanol fuel cell, with all the layers considered in the model, is shown in Fig. 3.1, consisting of

- an aluminium plate (AAP), a rubber plate (ARP), a copper plate (ACP), a graphite plate with flow channels (AF), a diffusion layer (AD) and a catalyst layer (AC) at the anode side;
- a polymer electrolyte membrane (M);

- a catalyst layer (CC), a diffusion layer (CD), a graphite plate with flow channels (CF), a copper plate (CCP), a rubber plate (CRP) and an aluminium plate (CAP) at the cathode side.

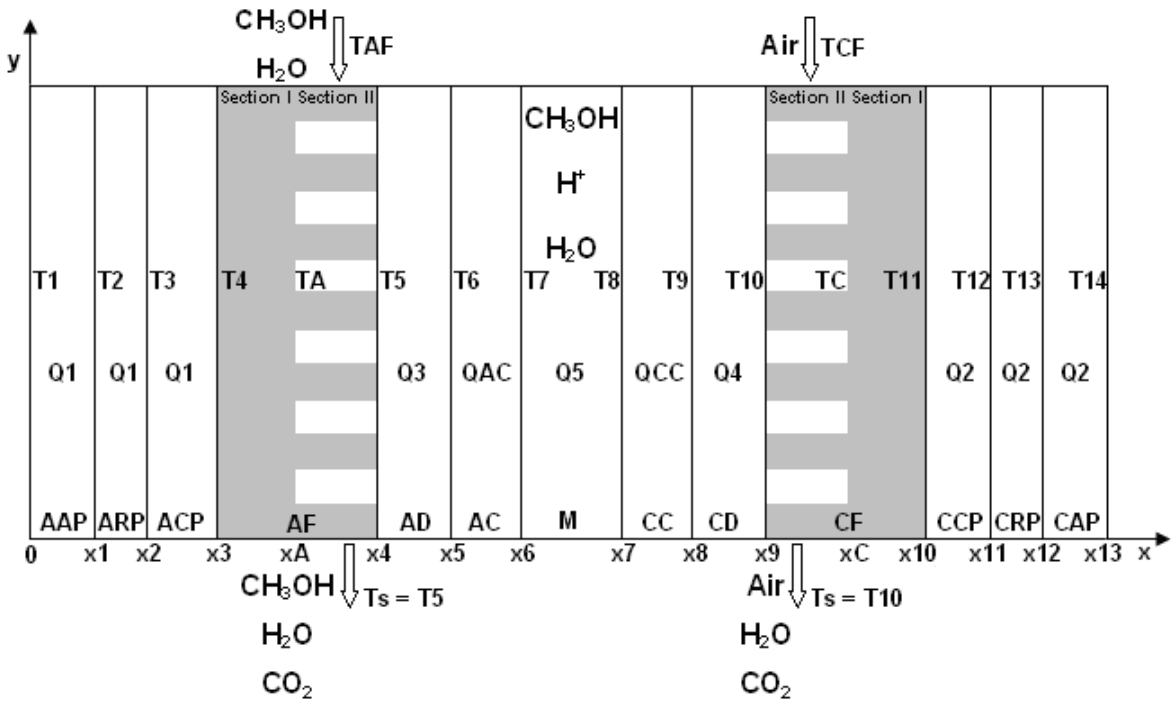

Figure 3.1 – Schematic representation of a DMFC

In an active-feed DMFC the fuel, methanol or an aqueous methanol solution, is supplied to the reaction zone by a liquid pump and the oxidant, air, by a mass flow controller. From the AD through the AC and from the AC through the M, methanol solution is transported primarily by diffusion. In a similar way the transport of oxygen on the CD and CC is enhanced by diffusion. After the electrochemical reaction of methanol oxidation, which takes place in the AC, the carbon dioxide produced moves countercurrently toward the AF via the AD and AC. At sufficiently high current densities carbon dioxide emerges in the form of gas bubbles from the surface of the AC. In the CC, oxygen reacts with protons and electrons generating water. The water produced in CC moves counter-currently toward the CF via the CD and CC and also under some operating conditions, by back diffusion toward the anode.

3.2. Model assumptions

The direct methanol fuel cell is a multiphase system involving simultaneous mass, charge and energy transfer. To make this complex system simpler it is here prescribed as a one-dimensional transport (along the x direction) with the following simplifications and assumptions:

- the fuel cell is assumed to operate under steady-state conditions;
- the transport of heat and mass through the gas diffusion and catalyst layers is assumed to be a diffusion-predominated process and the convection effect is negligible;
- mass transport in the diffusion layers and membrane is described using effective Fick models;
- the thermal energy model is based on the differential thermal energy conservation equation (Fourier's law);
- pressure gradient across the layers is negligible;
- only the liquid phase is considered in the anode side, so carbon dioxide remains dissolved in solution;
- gaseous methanol and water are considered in the cathode;
- solutions are considered ideal and dilute;
- local equilibrium at interfaces is represented by partition functions;
- the catalyst layers are assumed to be a macro-homogeneous porous electrode so reactions in these layers are modelled as a homogeneous reaction;
- anode kinetics is described by step mechanism, with a rate expression similar to the used by Meyers *et al.* [26];
- the anodic and cathodic overpotentials are constant through the catalyst layers;
- cathode kinetics is described by Tafel equation;

- methanol and water transport through the membrane is assumed to be due to the combined effect of the concentration gradient between the anode and the cathode and the electro-osmosis force;
- the anode and cathode flow channels are treated as a continuous stirred tank reactor (CSTR). Accordingly, the composition and temperature inside the flow channels are uniform and equal to their values at the channel outlet;
- the heat generation by electrochemical reactions occurring in the catalyst layers is considered;
- when compared with the heat generated by electrochemical reactions and overpotential, the heat released by Joule Effects is ignored;
- the contact thermal resistance between the graphite plates and the gas diffusion layers is negligible;
- the anode and the cathode streams are acting as heat transfer fluids so they remove heat from the cell at their outlet temperatures;
- the temperatures of the external walls of the cell (T_1 and T_{14} in Fig. 3.1) are known;
- the heat flux generated in the catalyst layers is assumed to be constant.

3.3. Governing equations and Boundary conditions – Anode and Cathode

3.3.1. Mass transport

<u>Anode reaction:</u>

$$\textit{Methanol oxidation}:\ CH_3OH + H_2O \rightarrow CO_2 + 6H^+ + 6e^- \tag{3.1}$$

<u>Cathode reaction:</u>

$$\textit{Oxygen reduction}:\ O_2 + 4H^+ + 4e^- \rightarrow 2H_2O \tag{3.2}$$

$$\textit{Methanol oxidation}:\ CH_3OH + \frac{3}{2}O_2 \rightarrow CO_2 + 2H_2O \tag{3.3}$$

The anode flow channels are treated as a continuous stirred tank reactor (CSTR), so the methanol and water flux are described by

$$N_j = \frac{q^{AF}}{A^S}\left(C_j^0 - C_j^{AF}\right) \tag{3.4}$$

where j represents methanol or water and

$$A^S = n_{channels} \times e \times w \tag{3.5}$$

where $n_{channels}$ is the channel number and e and w are the width and length of the channels, respectively.

In the anode diffusion and catalyst layer, the methanol and water flux are related to the concentration gradient by assuming Fickian diffusion [171] with an effective diffusivity $D_j^{eff,AD}$ in the AD and $D_j^{eff,AC}$ in the AC. The methanol and water flux can be determined from:

$$N_j = -D_j^{eff,AD}\frac{dC_j^{AD}}{dx}, \ j \text{ represents methanol or water} \tag{3.6}$$

and

$$N_j = -D_j^{eff,AC}\frac{dC_j^{AC}}{dx}, \ j \text{ represents methanol or water} \tag{3.7}$$

The concentration at the AF/AD and AD/AC interfaces is given by assuming local equilibrium with a partition coefficient K_4 and K_5, respectively. The boundary conditions for Eq. (3.6) and (3.7) are (see Fig. 3.1)

$$At\ x = x_4: \quad C_j^{AD} = K_4 C_j^{AF}, \ j \text{ represents methanol or water} \tag{3.8}$$

$$At\ x = x_5: \quad C_j^{AC} = C_{5,j}^{AC} = K_5 C_j^{AD}, \ j \text{ represents methanol or water} \tag{3.9}$$

$$At\ x = x_6: \quad C_j^{AC} = C_{6,j}^{AC}, \ j \text{ represents methanol or water} \tag{3.10}$$

In fuel cells, all the fluxes can be related to a single characteristic flux, the current density or charge flux of the fuel cell. In the DMFC, the methanol flux is related to the current density and the permeation flux of methanol through the membrane, ($N^{M}_{CH_3OH}$), by:

$$N_{CH_3OH} = \frac{I_{Cell}}{6F} + N^{M}_{CH_3OH} \tag{3.11}$$

At the anode side, the water flux is related to the current density and to the net water transport coefficient, α (defined as the ratio of the net water flux though the membrane from the anode to the cathode normalized by protonic flux), by:

$$N_{H_2O} = \frac{I_{Cell}}{6F}(\alpha + 1) \tag{3.12}$$

The transport of methanol and water through the membrane is assumed to be due to the combined effect of the concentration gradient and the electro-osmosis force. The fluxes can be determined from:

$$N^{M}_{CH_3OH} = -D^{eff,M}_{CH_3OH}\frac{dC^{M}_{CH_3OH}}{dx} + \xi_{CH_3OH}\frac{I_{Cell}}{F} \tag{3.13}$$

$$N^{M}_{H_2O} = \alpha\frac{I_{Cell}}{6F} = -D^{eff,M}_{H_2O}\frac{dC^{M}_{H_2O}}{dx} + n_d\frac{I_{Cell}}{F} \tag{3.14}$$

The electro-osmotic drag (ξ_{CH_3OH}, n_d), in equations (3.13) and (3.14), is defined as the number of methanol or water molecules dragged by the hydrogen ions moving through the membrane.

The net water transport coefficient, α, can be calculated using the equation (3.14).

The concentration at the AC/membrane interface is given by assuming local equilibrium with a partition coefficient K_6. The boundary conditions for the integration of equations (3.13) and (3.14) is given by

$$At\ x = x_6: \quad C^{M}_{j} = K_6 C^{AC}_{6,j}\ ,\ j \text{ represents methanol or water} \tag{3.15}$$

In the cathode catalyst layer, the methanol, water and oxygen flux are related to the concentration gradient by assuming Fickian diffusion [171] with an effective diffusivity $D_j^{eff,CC}$. The flux can be determined from:

$$N_j = -D_j^{eff,CC} \frac{dC_j^{CC}}{dx}, \text{ } j \text{ represents methanol, water or oxygen} \tag{3.16}$$

It is here considered that the entire methanol crossing the membrane reacts at the cathode catalyst layer so the concentration at the CC/CD interface is zero**.** It is assumed that there is no oxygen crossover, so the oxygen concentration in CC/M interface is zero. The concentration of water and methanol at the membrane/CC interface and the concentration of water and oxygen at the CC/CD interface are given by assuming local equilibrium with a partition coefficient K_7 and K_8, respectively. The boundary conditions for Eq. (3.16) are:

$$At\ x = x_7: \quad C_j^{CC} = C_{7,j}^{CC} = K_7 C_{7,j}^{M}, \text{ } j \text{ represents methanol or water and } C_{7,O_2}^{CC} = 0 \tag{3.17}$$

$$At\ x = x_8: \quad C_{CH_3OH}^{CC} \cong 0, C_{H_2O}^{CC} = C_{8,H_2O}^{CC} \text{ and } C_{O_2}^{CC} = C_{8,O_2}^{CC} \tag{3.18}$$

At the cathode catalyst layer, the oxygen reacts with the electrons and protons to produce water. However, part of oxygen fed is consumed due to methanol crossover to form an internal current and a mixed potential. Therefore the oxygen flux is related to the current density and the permeation flux of methanol through the membrane by

$$N_{O_2} = \upsilon_{O_2} \frac{I_{Cell}}{4F} + \upsilon_{cross,O_2} N_{CH_3OH}^{M} \tag{3.19}$$

where

$\upsilon_{O_2} = 1$ and $\upsilon_{cross,O_2} = 3/2$

At the cathode side, the water flux is related to the water production from the oxygen reduction reaction and methanol crossover oxidation and to the net water flux transported from the anode to the cathode by:

$$N_{H_2O} = \upsilon_{H_2O} \frac{I_{Cell}}{4F} + \upsilon_{cross,H_2O} N^{M}_{CH_3OH} + N^{M}_{H_2O} \tag{3.20}$$

where

$\upsilon_{H_2O} = 2$, $\upsilon_{cross,H_2O} = 2$

In the cathode diffusion layer the oxygen and water flux are related to the concentration gradient by

$$N_i = -D_i^{eff,CD} \frac{dC_i^{CD}}{dx} \text{, } i \text{ represents oxygen or water vapour} \tag{3.21}$$

where $D_i^{eff,CD}$ is the effective diffusion coefficient of oxygen and water in the CD.

The concentration at the CF/CD and CD/CC interfaces is given by assuming local equilibrium with a partition coefficient K_9 and K_8. The boundary conditions for Eq. (3.21) are

$$At\ x = x_8 : \quad C_i^{CD} = K_{8,i} C_{8,i}^{CC} \tag{3.22}$$

$$At\ x = x_9 : \quad C_i^{CF} = K_{9,i} C_i^{CD} \tag{3.23}$$

Like at the anode side, the cathode flow channels are treated as a continuous stirred tank reactor (CSTR), so the oxygen and water vapour flux are described by

$$N_i = \frac{q^{CF}}{A^S} \left(C_i^0 - C_i^{CF} \right) \tag{3.24}$$

where i represents oxygen or water vapour and

$$A^S = n_{channels} \times e \times w \tag{3.25}$$

If dry air is fed to the cathode, the water vapour feed concentration ($C^0_{H_2O}$) is zero.

To account for the effect of methanol crossover on the cathode overpotential it is assumed that the methanol crossing the membrane completely reacts electrochemically at the cathode. In this way the internal current (I_{CH_3OH}) due to methanol oxidation can be written as

$$I_{CH_3OH} = 6FN^{M}_{CH_3OH} \tag{3.26}$$

where the methanol flux in the membrane ($N^{M}_{CH_3OH}$) is obtained from Eq. (3.13).

The volumetric current density expression for methanol oxidation is taken from Meyers et al [26] as

$$j_A = aI^{CH_3OH}_{0,ref} \frac{kC^{AC}_{CH_3OH}}{C^{AC}_{CH_3OH} + \lambda \exp\left(\frac{\alpha_A \eta_A F}{RT_{AC}}\right)} \exp\left(\frac{\alpha_A \eta_A F}{RT_{AC}}\right) \tag{3.27}$$

The current density is related to the volumetric current density using the following equation

$$I_{Cell} = \int_{x_5}^{x_6} j_A \, dx = \int_{x_5}^{x_6} aI^{CH_3OH}_{0,ref} \frac{kC^{AC}_{CH_3OH}}{C^{AC}_{CH_3OH} + \lambda \exp\left(\frac{\alpha_A \eta_A F}{RT_{AC}}\right)} \exp\left(\frac{\alpha_A \eta_A F}{RT_{AC}}\right) dx \tag{3.28}$$

Equation (3.28) is used to calculate the anode overpotential for a given I_{Cell}, assuming η_A as constant in the anode catalyst layer AC.

At the cathode, the electrochemical reaction is modelled using Tafel equation for the oxygen reduction taking in account the mixed potential. The cathode overpotential can then be determined from:

$$I_{Cell} + I_{CH_3OH} = I^{O_2}_{0,ref} \frac{C^{CC}_{O_2}}{C^{CC}_{O_2,ref}} \exp\left(\frac{\alpha_C \eta_C F}{RT_{CC}}\right) \tag{3.29}$$

3.3.2. Heat transport

Based on the simplifications and assumptions described previously the following overall heat transfer equation can be proposed (see Fig. 3.1):

$$Q^{AC} + Q^{CC} = Q_1 + Q_2 + Q^{AF} + Q^{CF} \tag{3.30}$$

where Q^{AF} and Q^{CF} represent the heat transferred to the anode and cathode stream. The total heat generated in the DMFC is equal to the heat losses to the surrounding environment at the anode and cathode side plus the heat removed by the anode and cathode fuel streams.

Complementarly, the following heat transfer balances can be written:

$$Q_1 = Q_3 - Q^{AF} \tag{3.31}$$

$$Q_2 = Q_4 - Q^{CF} \tag{3.32}$$

$$Q_5 = Q^{AC} - Q_3 \tag{3.33}$$

$$Q_4 = Q^{CC} + Q_5 \tag{3.34}$$

The energy balance for the anode and cathode streams, considering a steady-flow system with one inlet and one outlet, where the changes in kinetic and potential energies are negligible and there is no work interaction, are, respectively,

$$Q^{AF} = \frac{q^{AF}\rho^{AF}Cp^{AF}}{A^S}\left(T_5 - T_{AF}\right) \tag{3.35}$$

$$Q^{CF} = \frac{q^{CF}\rho^{CF}Cp^{CF}}{A^S}\left(T_{10} - T_{CF}\right) \tag{3.36}$$

where ρ^{AF} and ρ^{CF} are the densities of the anode and cathode streams and Cp^{AF} and Cp^{CF} the specific heats for anode and cathode streams, respectively.

At the anode, heat generated by the electrochemical reaction in the AC is given by

$$Q^{AC} = I_{Cell}\eta_A - I_{Cell}\left(\frac{\Delta H_A - \Delta G_A}{6F}\right) \tag{3.37}$$

In this equation the first term represents the heat due to the activation and mass transfer overpotentials at the anode and the second term represents the entropy change of the anodic electrochemical reaction, with ΔH_A denoting the anodic reaction enthalpy and ΔG_A the Gibbs free energy. This equation can be rewritten as:

$$Q^{AC} = I_{Cell}\eta_A - \beta_1 - \beta_2\left(T_{AC} - 298\right) \tag{3.38}$$

where

$$\beta_1 = \frac{I_{Cell}}{6F}\left(\Delta H_A^0 - \Delta G_A^0\right), \tag{3.39}$$

$$\beta_2 = \frac{I_{Cell}}{6F}\left(Cp_{CO_2} - Cp_{CH_3OH} - Cp_{H_2O}\right) \tag{3.40}$$

and

$$T_{AC} = \frac{T_6 + T_7}{2} \tag{3.41}$$

In a similar way, the heat generated at the CC, can be determined from

$$Q^{CC} = (I_{Cell} + I_{CH_3OH})\eta_C - I_{Cell}\left(\frac{\Delta H_C - \Delta G_C}{4F}\right) \tag{3.42}$$

where the first term represents the heat due to the activation and mass transfer overpotentials and mixed potential caused by methanol crossover through the cathode and the second term represents the entropy change of the cathodic electrochemical reaction, with ΔH_C denoting the cathodic reaction enthalpy and ΔG_C, the Gibbs free energy. This equation can be rewritten as

$$Q_{CC} = \left(I_{Cell} + I_{CH_3OH}\right)\eta_C - \beta_3 - \beta_4\left(T_{CC} - 298\right) \tag{3.43}$$

where

$$\beta_3 = \frac{I_{Cell}}{4F}\left(\Delta H_C^0 - \Delta G_C^0\right), \tag{3.44}$$

$$\beta_4 = \frac{I_{Cell}}{4F}\left(2Cp_{H_2O} - Cp_{O_2}\right) \tag{3.45}$$

and

$$T_{CC} = \frac{T_8 + T_9}{2} \tag{3.46}$$

In the anode aluminium, rubber and copper plates and diffusion layer the heat flux Q_1 and Q_3 can be related to the temperature gradient across each layer, using the Fourier's law, as

$$Q = -K^{l} \frac{dT}{dx} \tag{3.47}$$

where *l* represents AAP, ARP, ACP or AD

At the cathode side, the heat fluxes Q_2, Q_4 and Q_5 can be related to the temperature gradient across the CAP, CRP, CCP, CD and M layers as

$$Q = -K^{t} \frac{dT}{dx} \tag{3.48}$$

where *t* represents CAP, CRP, CCP, CD or M.

Anode and Cathode flow channel

In a single cell DMFC the graphite plate has flow channels machined on only one surface, the surface contacting with the diffusion layer (Fig. 3.1). The establishment of the heat transport equations involved the consideration of sections 1 and 2 in the graphite plate. Section 2 is treated as a finned surface exchanging heat with the cannel fluid [172] and can be found in Appendix B (10.5). If we consider that the heat removed by the anode or cathode stream is equal to the symmetric heat transfer from the fin (Eq. 3.49), we can relate the heat flux in section 1 and section 2.

$$Q^{AF/CF} = -Q_{fin} = n_{channels} \eta_{fin} h A_{fin} \left(T_{A/C} - T_{5/10} \right) \tag{3.49}$$

where *h* represents the heat transfer coefficient, see Appendix B (10.6).

In section 1 the heat is transferred by conduction and the resulting equations are:

$$Q_1 = -K^{G} \frac{dT}{dx} \tag{3.50}$$

$$Q_2 = -K^G \frac{dT}{dx} \tag{3.51}$$

Anode and Cathode catalyst layer

The differential equations describing the temperature profiles in these layers are:

$$\frac{d^2T}{dx^2} = \frac{Q^{AC}}{K^{AC}\delta^{AC}} \tag{3.52}$$

$$\frac{d^2T}{dx^2} = \frac{Q^{CC}}{K^{CC}\delta^{CC}} \tag{3.53}$$

where Q^{AC} and Q^{CC} are, respectively, the heat generated in the anode catalyst layer and cathode catalyst layer.

The boundary conditions for Eq. (3.52) and (3.53) are the temperatures at the walls (T_6, T_7, T_8 and T_9).

For these layers. Fourier's law gives

$$At\ x = x_5: \quad Q_3 = -K^{AC} \frac{dT}{dx} \tag{3.54}$$

$$At\ x = x_7: \quad Q_5 = -K^{CC} \frac{dT}{dx} \tag{3.55}$$

where $\frac{dT}{dx}$ is calculated using the temperature profile obtained from the integration of equations (3.52) and (3.53).

3.4. Cell performance

The determination of methanol and oxygen concentrations at the catalyst layers, the temperature profiles and the anodic and cathodic overpotentials from the model equations enables prediction of the cell voltage, which can be expressed as:

$$V_{Cell} = E_{Cell} - \eta_A - \eta_C - I_{Cell} R_{Cell} \tag{3.56}$$

where

$$E_{Cell} = U_{O_2} - U_{CH_3OH} + \Delta T\left(\frac{\partial E}{\partial T}\right), \tag{3.57}$$

η_A and η_C are the anode and cathode overpotencials and the membrane resistance R_{Cell} is given by

$$R_{Cell} = \frac{\delta^M}{\kappa} \tag{3.58}$$

where δ^M is membrane thickness and κ is the ionic conductivity of the membrane.

3.5. Analytical solutions

3.5.1. Mass transport

The methanol and water concentration profile in AF can be obtained combining Eqs. (3.4) and (3.11) or (3.4) and (3.12):

$$C_{CH_3OH}^{AF} = C_{CH_3OH}^{0} - \frac{A^S}{q^{AF}}\left(\frac{I_{Cell}}{6F} + N_{CH_3OH}^{M}\right) \tag{3.59}$$

$$C_{H_2O}^{AF} = C_{H_2O}^{0,AF} - \frac{A^S I_{Cell}}{q^{AF} 6F}(\alpha + 1) \tag{3.60}$$

Combining equations (3.6), (3.8) and (3.11) or (3.12) yields the concentration profile in AD. To obtain the concentration profile in AC we combine Eqs. (3.7), (3.9) and (3.11) or (3.12). The solutions are respectively:

$$C_{CH_3OH}^{AD} = K_4 C_{CH_3OH}^{AF} + \frac{I_{Cell}}{6FD_{CH_3OH}^{eff,AD}}(x_4 - x) + \frac{N_{CH_3OH}^{M}}{D_{CH_3OH}^{eff,AD}}(x_4 - x) \tag{3.61}$$

$$C_{H_2O}^{AD} = K_4 C_{H_2O}^{AF} + \frac{I_{Cell}(\alpha+1)}{6FD_{H_2O}^{eff,AD}}(x_4 - x) \tag{3.62}$$

$$C_{CH_3OH}^{AC} = C_{5,CH_3OH}^{AC} + \frac{I_{Cell}}{6FD_{CH_3OH}^{eff,AC}}(x_5 - x) + \frac{N_{CH_3OH}^{M}}{D_{CH_3OH}^{eff,AC}}(x_5 - x) \tag{3.63}$$

$$C_{H_2O}^{AC} = C_{5,H_2O}^{AC} + \frac{I_{Cell}(\alpha+1)}{6FD_{H_2O}^{eff,AC}}(x_5 - x) \tag{3.64}$$

The concentration of methanol and water through the membrane can be obtained by using Eqs. (3.13) and (3.14):

$$C_{CH_3OH}^{M} = K_6 C_{6,CH_3OH}^{AC} + \frac{N_{CH_3OH}^{M} - \frac{\xi_{CH_3OH} I_{Cell}}{F}}{D_{CH_3OH}^{eff,M}}(x_6 - x) \tag{3.65}$$

$$C_{H_2O}^{M} = K_6 C_{6,H_2O}^{AC} + \frac{I_{Cell}}{6FD_{H_2O}^{eff,M}}(x_6 - x) - \frac{2.5 I_{Cell}}{FD_{H_2O}^{eff,M}}(x_6 - x) \tag{3.66}$$

Combining Eqs. (3.13), (3.15) and (3.17) we obtained an expression to calculate the methanol flux through the membrane:

$$N_{CH_3OH}^{M} = \frac{D_{CH_3OH}^{eff,M}}{\delta^{M}}\left(K_6 C_{6,CH_3OH}^{AC} - C_{7,CH_3OH}^{M}\right) + \frac{\xi_{CH_3OH} I_{Cell}}{F} \tag{3.67}$$

The concentration of methanol, water and oxygen through the CC can be obtained combining Eqs. (3.16), (3.17) and (3.18):

$$C_{CH_3OH}^{CC} = C_{7,CH_3OH}^{CC} - \frac{I_{Cell}}{6FD_{CH_3OH}^{eff,CC}}(x_7 - x) + \frac{N_{CH_3OH}^{M}}{D_{CH_3OH}^{eff,CC}}(x_7 - x) \tag{3.68}$$

$$C_{H_2O}^{CC} = C_{7,H_2O}^{CC} + \frac{(x_7 - x)}{D_{H_2O}^{eff,CC}}\left(\frac{\alpha I_{Cell}}{6F} + \frac{0.5 I_{Cell}}{F} + \frac{I_{CH_3OH}}{3F}\right) \tag{3.69}$$

$$C_{O_2}^{CC} = C_{8,O_2}^{CC} + \frac{I_{Cell}}{4FD_{O_2}^{eff,CC}}(x_8 - x) + \frac{3}{2}\frac{N_{CH_3OH}^{M}}{D_{O_2}^{eff,CC}}(x_8 - x) \tag{3.70}$$

Combining equations (3.19), (3.21) and (3.22) or (3.20), (3.21), and (3.22) we obtained the concentration profile in CD:

$$C_{O_2}^{CD} = K_{8,O_2}C_{8,O_2}^{CC} + \frac{I_{Cell}}{4FD_{O_2}^{eff,CD}}(x_8 - x) + \frac{3}{2}\frac{N_{CH_3OH}^{M}}{D_{O_2}^{eff,CD}}(x_8 - x) \tag{3.71}$$

$$C_{H_2O}^{CD} = K_{8,H_2O}C_{8,H_2O}^{CC} + \frac{(x_8 - x)}{D_{H_2O}^{eff,CD}}\left(\frac{\alpha I_{Cell}}{6F} + \frac{0.5I_{Cell}}{F} + \frac{I_{CH_3OH}}{3F}\right) \tag{3.72}$$

The concentration of oxygen and water through the CF can be obtained using Eqs. (3.19) and (3.24) or (3.20) and (3.24):

$$C_{O_2}^{CF} = C_{O_2}^{0} - \frac{A^S}{q^{CF}}\left(\frac{I_{Cell}}{4F} + \frac{3}{2}N_{CH_3OH}^{M}\right) \tag{3.73}$$

$$C_{H_2O}^{CF} = C_{H_2O}^{0,CF} + \frac{A^S}{q^{CF}}\left(\frac{\alpha I_{Cell}}{6F} + \frac{0.5I_{Cell}}{F} + \frac{I_{CH_3OH}}{3F}\right) \tag{3.74}$$

From the solutions above we obtain a expression to calculate the C_{6,CH_3OH}^{AC}, C_{7,CH_3OH}^{M}, C_{8,O_2}^{CC} and α:

$$C_{6,CH_3OH}^{AC} = \frac{K_5K_4C_{CH_3OH}^{0} - \frac{I_{Cell}C_1}{6F} - \frac{\xi_{CH_3OH}I_{Cell}C_1}{F} + \frac{D_{CH_3OH}^{eff,M}C_1C_{7,CH_3OH}^{M}}{\delta^M}}{1 + \frac{D_{CH_3OH}^{eff,M}K_6C_1}{\delta^M}} \tag{3.75}$$

where:

$$C_1 = \frac{\delta^{AD}K_5}{D_{CH_3OH}^{eff,AD}} + \frac{\delta^{AC}}{D_{CH_3OH}^{eff,AC}} - \frac{A^SK_4K_5}{q^{AF}} \tag{3.76}$$

$$C_{7,CH_3OH}^{M} = \frac{-\dfrac{I_{Cell}\delta^{CC}}{6FD_{CH_3OH}^{eff,CC}K_7} + \dfrac{\xi_{CH_3OH}I_{Cell}\delta^{CC}}{FD_{CH_3OH}^{eff,CC}K_7} + \dfrac{D_{CH_3OH}^{eff,M}\delta^{CC}K_6C_{6,CH_3OH}^{AC}}{\delta^{M}D_{CH_3OH}^{eff,CC}K_7}}{1+\dfrac{D_{CH_3OH}^{eff,M}\delta^{CC}}{\delta^{M}D_{CH_3OH}^{eff,CC}K_7}} \tag{3.77}$$

$$C_{7,O_2}^{CC} = \frac{C_{O_2}^{0}}{K_{8,O_2}K_{9,O_2}} + \frac{C_2 I_{Cell}}{4F} + \frac{C_2 3N_{CH_3OH}^{M}}{2} \tag{3.78}$$

where:

$$C_2 = \frac{\delta^{CD}}{D_{O_2}^{eff,CD}K_{8,O_2}} - \frac{A^S}{q^{CF}K_{8,O_2}K_{9,O_2}} \tag{3.79}$$

$$C_{6,H_2O}^{M} = K_6K_5K_4C_{H_2O}^{0} - \frac{C_3 I_{Cell}(\alpha+1)}{6F} \tag{3.80}$$

where:

$$C_3 = \frac{K_6K_5K_4A^S}{q^{AF}} + \frac{K_6K_5\delta^{AD}}{D_{H_2O}^{eff,AD}} + \frac{K_5\delta^{AC}}{D_{H_2O}^{eff,AC}} \tag{3.81}$$

$$C_{7,H_2O}^{M} = \frac{C_{H_2O}^{0}}{K_{8,H_2}oK_{7,H_2O}K_{9,H_2O}} + \left(\frac{\alpha I_{Cell}}{6F} + \frac{I_{Cell}}{2F} + \frac{I_{CH_3OH}}{3F}\right)C_4 \tag{3.82}$$

where:

$$C_4 = \frac{\delta^{CD}}{K_{8,H_2O}K_{7,H_2O}D_{H_2O}^{eff,CD}} + \frac{\delta^{CC}}{K_{7,H_2O}D_{CH_3OH}^{eff,CC}} + \frac{A^S}{q^{CF}K_{8,H_2O}K_{9,H_2O}K_{7,H_2O}} \tag{3.83}$$

$$\alpha = -\frac{6FD_{H_2O}^{eff,M}}{I_{Cell}}\left(\frac{C_{7,H_2O}^{M} - C_{6,H_2O}^{M}}{\delta^{M}}\right) + 6n_d \tag{3.84}$$

3.5.2. Heat transport

Solving equation (3.47) for T_1 and T_4 we obtained:

$$Q_1 = \frac{(T_4 - T_1)}{R_{T,1}} \tag{3.85}$$

where $R_{T,1}$ is the total thermal resistance

$$R_{T,1} = R_1 + R_2 + R_3 \tag{3.86}$$

and R_1, R_2, R_3 are the thermal resistance of AAP, ARP and ACP

$$R_1 = \frac{x_1}{K_{AAP}}, \tag{3.87}$$

$$R_2 = \frac{x_2 - x_1}{K_{ARP}}, \tag{3.88}$$

$$R_3 = \frac{x_3 - x_2}{K_{ACP}} \tag{3.89}$$

The solution to Eqs. (3.31), (3.33), (3.35), (3.38), (3.48), (3.49) and (3.85) is:

$$\frac{\frac{T_5(A_1 + A_2) - A_1 T_{AF}}{A_2} - T_1}{R_{T,2}} = I_{Cell}\eta_A - \beta_1 - \beta_2(T_{AC} - 298) - \frac{(T_7 - T_8)}{R_6} - A_1(T_5 - T_{AF}) \tag{3.90}$$

where

$$A_1 = \frac{q^{AF}\rho_{H_2O}Cp_{H_2O,1}}{A^S}, \tag{3.91}$$

$$A_2 = n_{channels}\eta_{fin}hA_{fin}, \tag{3.92}$$

$$R_{T,2} = R_{T,1} + R_{Section\,I}, \tag{3.93}$$

$$R_6 = \frac{x_7 - x_6}{K_M} \text{ and} \tag{3.94}$$

$$R_{Section\,I} = \frac{x_A - x_3}{K_{AF}} \tag{3.95}$$

$R_{T,2}$ is the total thermal resistance, R_6 is the thermal resistance of the membrane and $R_{Section\,I}$ is the total thermal resistance of section I.

Solving Eqs. (3.33), (3.38) and (3.48) and (3.34), (3.43) and (3.48) the following equations are obtained:

$$\frac{T_6 - T_5}{R_4} = I_{Cell}\eta_A - \beta_1 - \beta_2\left(T_{AC} - 298\right) - \frac{\left(T_7 - T_8\right)}{R_6} \tag{3.96}$$

where R_4 is the thermal resistance of AD

$$R_4 = \frac{x_5 - x_4}{K_{AD}} \tag{3.97}$$

and

$$\frac{T_9 - T_{10}}{R_8} = \left(I_{Cell} + I_{CH_3OH}\right)\eta_C - \beta_3 - \beta_4\left(T_{CC} - 298\right) + \frac{\left(T_7 - T_8\right)}{R_6} \tag{3.98}$$

where R_8 is the thermal resistance of CD

$$R_8 = \frac{x_9 - x_8}{K_{CD}} \tag{3.99}$$

The model simulations presented in this Chapter and in Chapter 5 were obtained based on the parameters listed in Table 3.1. The physical properties and the expressions used to calculate the effective diffusion coefficients, porosities, effective thermal conductivities can be found in Appendix B (B.1, B.2, B.3 and B.4).

Is should be mentioned that all the parameters used were carefully chosen from recent literature, namely reference exchange current density and transfer coefficients. In numerous published works, there are numerous values for the same parameter, and it

seems that some authors use the parameters that better fit their experimental results that could be or not the most adequate to their operating/design conditions.

Table 3.1 – Values for the parameters used in the model equations.

Parameter	Value	Reference
U_{O_2}	1.24 V	[120]
U_{CH_3OH}	0.03 V	[120]
$\partial E/\partial T$	-1.4 $\times 10^{-4}$V/K	[166]
κ	0.036 S/cm	[120]
δ^{M}	0.018 cm	[120]
$\delta^{AF}, \delta^{CF}, \delta^{sectionII}, e$	0.20 cm	real value
δ^{AD}, δ^{CD}	0.015 cm	[120]
δ^{AC}, δ^{CC}	0.0023 cm	[120]
$\varepsilon^{AD}, \varepsilon^{CD}$	0.71	[173]
ε^{AC}	0.81	[173]
ε^{CC}	0.86	[173]
a	1000 cm^{-1}	[120]
$I_{0,ref}^{CH_3OH}$	$9.425\times10^{-3}\exp((35570/R)(1/353-1/T))$ A/cm^2	[166]
$I_{0,ref}^{O_2}$	$4.222\times10^{-6}\exp((73200/R)(1/353-1/T))$ A/cm^2	[166]
k	7.5×10^{-4}	[120]
λ	2.8×10^{-9} mol/cm^3	[120]
α_A	0.52	[120]
α_C	1.55	[120]
K_{4-6}, K_{8-9,H_2O}	0.8	assumed
K_{8-9,O_2}	1.25	assumed
K_7	0.001	assumed
q^{AF}	0.33 cm^3/s	real value
q^{CF}	1.67 cm^3/s	real value
$n_{channels}$	15	real value
w	5 cm	real value
P_{air}	1 atm	[120]

$D_{O_2}^{eff,CD,CC}$	$\varepsilon^{CD,CC^{2.5}}\left[\left(T^{1.75}\times 5.8\times 10^{-4}\right)/\left(27.772\times P\right)\right]$ cm^2/s	[174]
$D_{CH_3OH}^{eff,AD,AC}$	$\varepsilon^{AD,AC^{2.5}}\left[\left(7.608\times 10^{-7}\times T\right)/\left(\mu_{H_2O}\times 9.485\right)\right]$ cm^2/s	[174]
$D_{CH_3OH}^{eff,CC}$	$\varepsilon^{CC^{2.5}}\left[\left(T^{1.75}\times 5.8\times 10^{-4}\right)/\left(33.904\times P\right)\right]$ cm^2/s	[174]
$D_{CH_3OH}^{eff,M}$	$4.9\times 10^{-6}\exp\left(2436\times\left(1/333-1/T\right)\right)$ cm^2/s	[120]
$D_{H_2O}^{eff,AD,AC}$	$\varepsilon^{AD,AC^{2.5}}\left[\left(6.295\times 10^{-7}\times T\right)/\left(\mu_{CH_3OH}\times 5.833\right)\right]$ cm^2/s	[174]
$D_{H_2O}^{eff,CD,CC}$	$\varepsilon^{CD,CC^{2.5}}\left[\left(T^{1.75}\times 6.2\times 10^{-4}\right)/\left(25.523\times P\right)\right]$ cm^2/s	[174]
$D_{H_2O}^{eff,M}$	$2.0\times 10^{-6}\exp\left(2060\times\left(1/303-1/T\right)\right)$ cm^2/s	[87]
ξ_{CH_3OH}	$2.5\times x_{CH_3OH}$	[120]
n_d	$2.9\exp\left(1029\times\left(1/333-1/T\right)\right)$	[166]
$\delta^{AAP}, \delta^{CAP}$	2 cm	real value
$\delta^{ARP}, \delta^{CRP}$	0.1 cm	real value
$\delta^{ACP}, \delta^{CCP}$	0.05 cm	real value
$\delta^{section\ I}$	0.15 cm	real value
K^{M}	0.0043 W/cmK	[173]
K^{AD}	$1.95+6.57\times 10^{-4}T$ W/mK	[173]
K^{CD}	$1.71+2.96\times 10^{-5}T$ W/mK	[173]
K^{AC}	$\left(1-\varepsilon^{AC}\right)\times 86.7+\varepsilon^{AC}\left(0.341+9.26\times 10^{-4}\right)$ W/mK	[173]
K^{CC}	$\left(1-\varepsilon^{CC}\right)\times 71+\varepsilon^{CC}\left(0.0034+7.60\times 10^{-5}\right)$ W/mK	[173]
T_{AF}, T_1, T_{14}	343 K	real value
T_{CF}	293 K	real value

3.6. Results and discussion

The developed model coupling the heat and mass transfer processes occurring in the DMFC is rapidly implemented with simple numerical tools: Matlab and Excel. In this section, examples of model predictions obtained after implementation of the model are presented. The conditions chosen to generate the simulations are similar to those used by Brenda *et al.* [120] in their experiments. This work was selected since the authors give a complete characterization of the MEA structure, reporting data essential to use in the present model. The cell used by them had an active area of 25 cm^2 with a Nafion 117 membrane. They used E-TEK 40% Platinum/C as both anode and cathode gas

diffusion layers. The anode catalyst loading was 3 mg/cm^2 of Pt/Ru and the cathode catalyst loading was 1 mg/cm^2 of Pt.

Predicted methanol concentration profiles across de anode and membrane, are depicted in Figure 3.2, when the cell is feed with a 0.5M methanol solution at current densities of 50, 100 and 150 mA/cm^2. The concentration profile at the anode flow channel is constant because it is treated as a CSTR. In the other layers, the methanol concentration decreases due to mass transfer diffusion, methanol consumption in the catalyst layer and the methanol crossover. The slope of the concentration profile in the membrane is higher for the lower current density showing a higher methanol crossover for this condition.

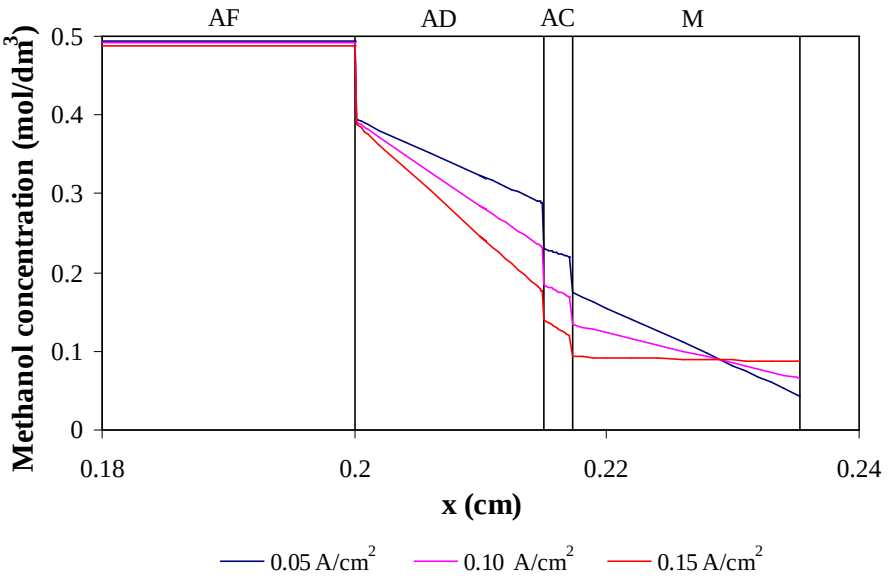

Figure 3.2 – Predicted methanol concentration profiles in the cell for different current densities. Operating conditions: temperature 70 ºC, pressure 1 atm, q^{AF} = 0.33 cm^3/s and q^{CF} = 1.67 cm^3/s.

Figure 3.3 shows the predictions of the methanol crossover as a function of current density for different methanol feed concentrations. At the cathode, the methanol that crosses the membrane reacts with oxygen in a corrosion reaction. Therefore the leakage current formed due to methanol oxidation represents fuel losses. Expressing the methanol crossover in terms of a leakage current gives a more understanding idea of the effect of the loss in efficiency due to methanol crossover. As can be seen in Fig. 3.3, the leakage current can be reduced by running the cell at low methanol concentrations and high current densities. The leakage current goes to zero at the limiting current density value for all concentrations. This provides a check that the transport equations, used in

the development of this simple model, give a physically meaningful methanol concentration profile, and influence of methanol concentration in the anode feed on the methanol losses.

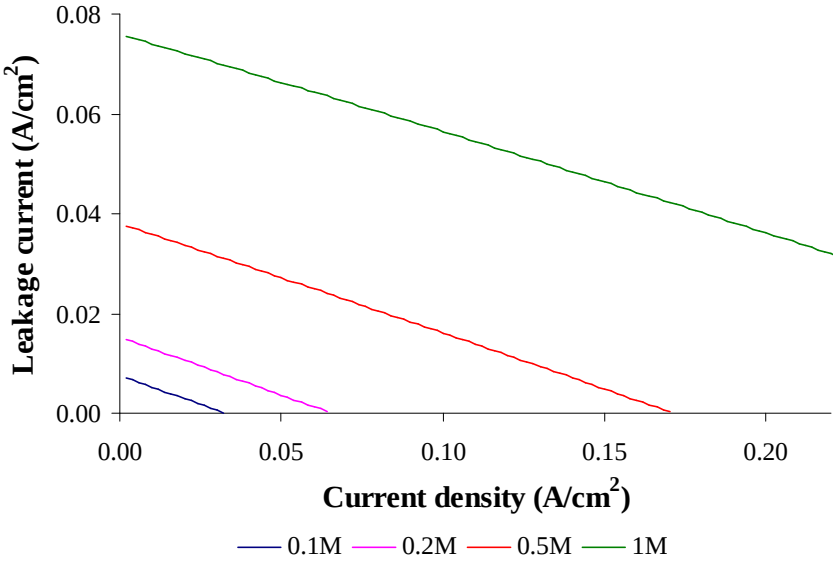

Figure 3.3 – Model prediction for methanol crossover for different methanol feed concentrations. Operating conditions: temperature 70 ºC, pressure 1 atm, q^{AF} = 0.33 cm^3/s and q^{CF} = 1.67 cm^3/s.

Figures 3.4 (a) and (b) show the water concentration across the anode, membrane and cathode. As is evident from these figures, the water concentration in the anode and membrane is higher than in the cathode. This is because it is assumed that liquid water exists at the anode, and water vapour, at the cathode. Although water diffusion occurs in AD and AC and water consumption in AC, the water concentration profile across these layers appears to be nearly constant. This can be explained by the fact that these layers are full of water so, the water loss by consumption and diffusion is irrelevant when compared with the total amount of water present. For the simulated conditions presented, the net water flow through the membrane occurs from the anode to the cathode. In CC and CD, the water concentration decreases according to the direction of water diffusion in air, toward the cell exit. In AF and CF the water concentration profile is constant, because, as was already referred, these layers were treated as CSTR.

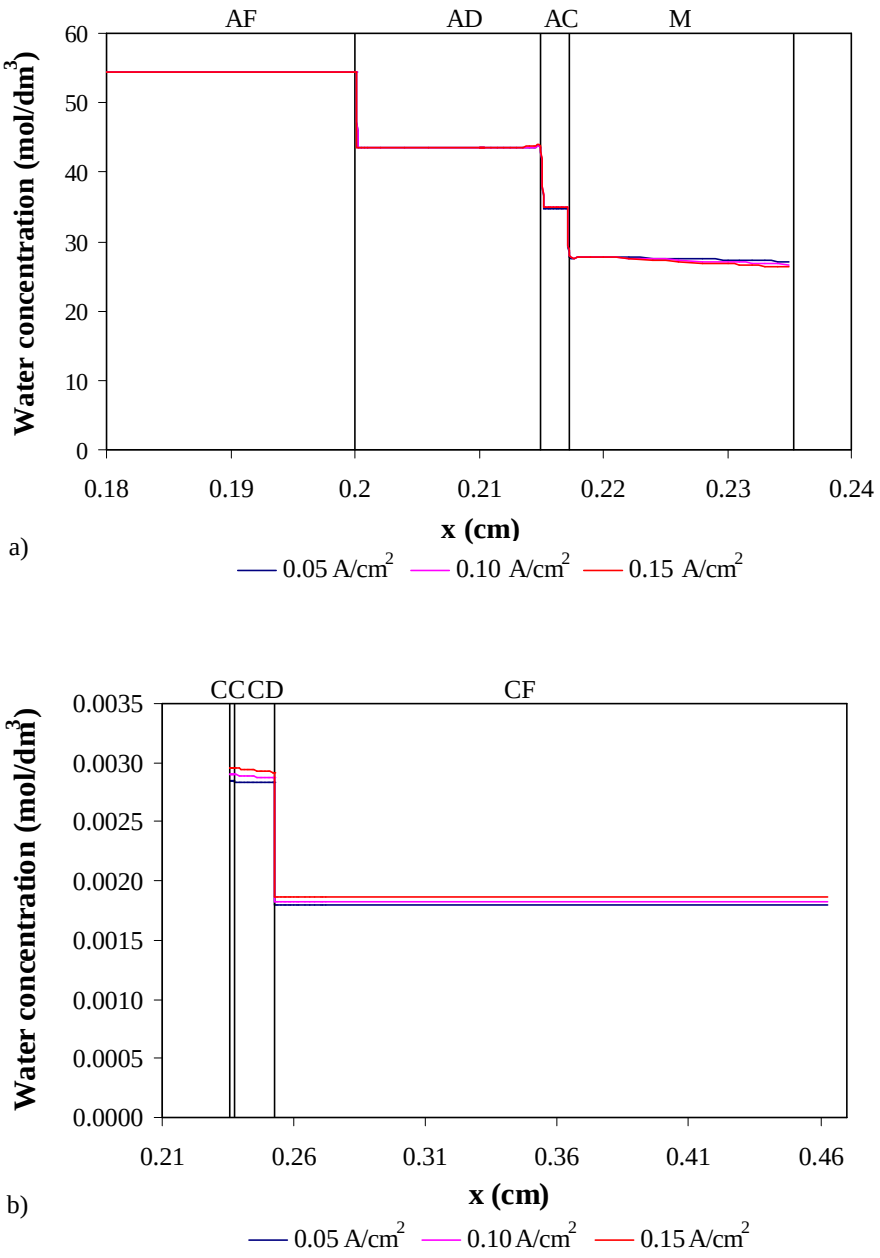

Figure 3.4 – Predicted water concentration distribution in the cell at different current densities: (a) anode and membrane and (b) cathode. Operating conditions: methanol concentration 0.5M, temperature 70 ºC, pressure 1 atm, q^{AF} = 0.33 cm^3/s and q^{CF} = 1.67 cm^3/s.

Model predictions of the net water transport coefficient, α, are presented in Figure 3.5 as a function of current density for different methanol feed concentrations. It should be remembered that positive α corresponds to a net water flow from anode to cathode while negative α indicates that the net flow occurs in the opposite side. Figure 3.5 shows that for all the methanol concentrations used the values of α are positive, although they are higher for low feed methanol concentrations. This occurs because for low methanol feed concentrations there is almost always a higher water concentration at

the anode side, especially for the lower values of current density. The transport of water due to electroosmotic drag and diffusion towards the cathode is dominant. For high methanol concentrations in the gas feed and low current densities the water production in the cathode gives higher water concentrations in the cathode side. Therefore the water transport from the anode to the cathode is lower corresponding to small values of α. As already explained in Chapter 2, working under low or even negative values of α, (corresponding to a low water crossover) may be essential to enable operation of a DMFC under high concentration of methanol in the feed solution, increasing therefore the power density of the cell.

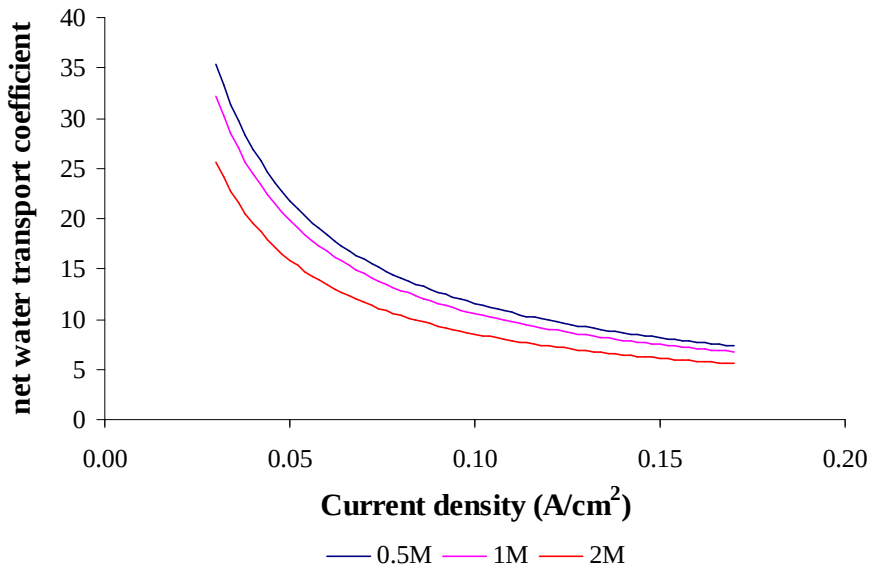

Figure 3.5 – Model predictions of the net water transport coefficient for different methanol concentrations. Operating conditions: temperature 70 °C, pressure 1 atm, q^{AF} = 0.33 cm^3/s and q^{CF} = 1.67 cm^3/s.

In Figure 3.6, model predictions of α as a function of methanol feed concentration for different current densities are presented. It is evident that the methanol concentration has a large impact on the α values. High methanol concentrations result in low values of α. It is also evident that for higher values of the current density the impact of methanol concentration decreases. The model predicts the correct trends of the influence of the current density on water crossover. The trends predicted by the model are in accordance to the ones proposed by the authors Liu *et al.* [90]. The developed model can be used to perform further studies with different MEA structures to set-up operating conditions

enabling low values of the water crossover and methanol crossover and relatively high values for the methanol concentration.

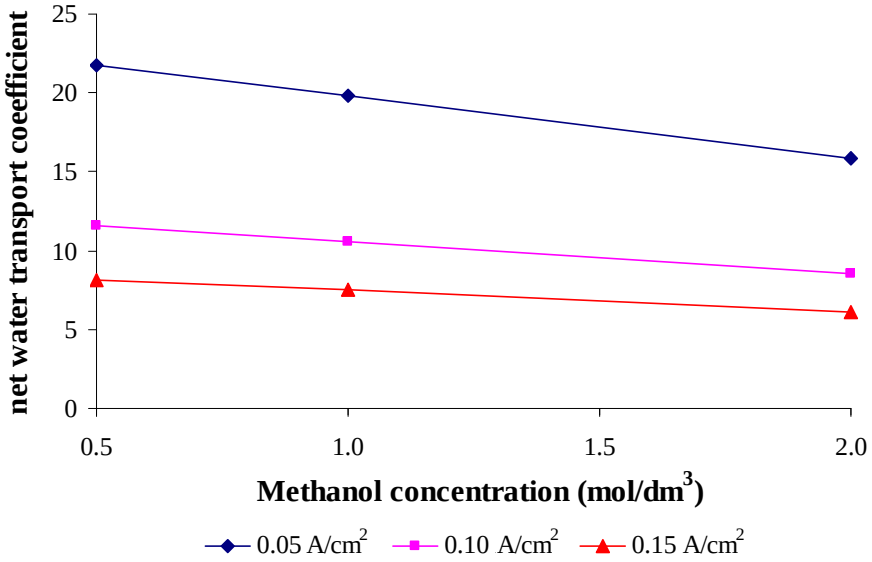

Figure 3.6 – Influence of methanol concentration on the net water transport coefficient at different current densities. Operating conditions: temperature 70 ºC, pressure 1 atm, q^{AF} = 0.33 cm^3/s and q^{CF} = 1.67 cm^3/s.

As, we are aware up to now there is only one work that provides alfa values measured experimentally. To validate our model in terms of the net water transport coefficient, the model predictions for alfa values are compared with the recent experimental data from Liu *et al.* [175], for different cathode relative humidities. The conditions used to generate the simulations are the same as those reported by the authors. The fuel cell temperature used was 60ºC, ambient pressure, 2M methanol concentration solution and air were fed to the anode and cathode side, respectively, at 0.33 ml/s and 1.67 ml/s. The fuel cell area used for simulation is the same used by Liu *et al.* [175] and is 12 cm^2. The values of the net water transport coefficient for different values of the cathode relative humidity together with the absolute deviation between model and experimental results are presented in Table 3.2. The values presented in this table correspond to a constant current density of 0.15 A/cm^2. As can be seen from the values displayed, the model predictions show good agreement with the experimental data, with very low values of absolute deviations.

Table 3.2 – Comparison between model predictions, for the net water transport coefficient, and experimental data from Liu *et al.* [175] and absolute deviation for 60 ºC, Nafion212 at 0.15 A/cm^2.

RH, % (Relative Humidity)	Data from Liu *et al.* [175]	Model	Absolute deviation
0	0.70	0.72	0.02
30	0.48	0.48	0.00
50	0.25	0.26	0.01
70	-0.15	-0.16	0.01
100	-0.70	-0.70	0.00

Figure 3.7 shows the temperature distribution in the active section of the cell for a feed methanol concentration of 0.5M methanol solution and operating at different current densities. The data points represent the temperatures at the several layer interfaces. It is seen from Fig. 3.7 that, under the presented operating conditions, the temperature in the anode side is lower than that in the cathode. This is because the heat generation rate by the anodic overpotential is less than the endothermic heat demanded by the electrochemical reaction of methanol oxidation. As a result some heat has to be taken from the cathode.

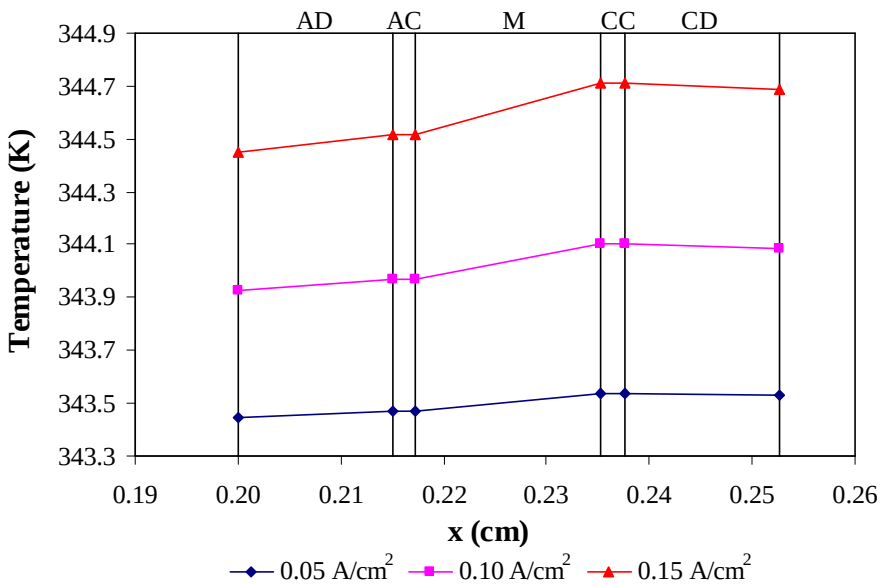

Figure 3.7 – Prediction for the temperature distribution in the cell at different current densities. Operating conditions: methanol concentration 0.5M, pressure 1 atm, q^{AF} = 0.33 cm^3/s and q^{CF} = 1.67 cm^3/s.

In Figure 3.8, the predictions from the developed model and from the model described by Brenda *et al.* [120] are presented. Comparing the two approaches it can be seen that both predictions are generally in good accordance with the experimental determined cell performance. The present model however, predicts better the performance of the DMFC cell studied by [120] mainly at low to moderate current intensities, probably due to the introduction of the mass transfer effects on the cathode side and of the heat transfer effects.

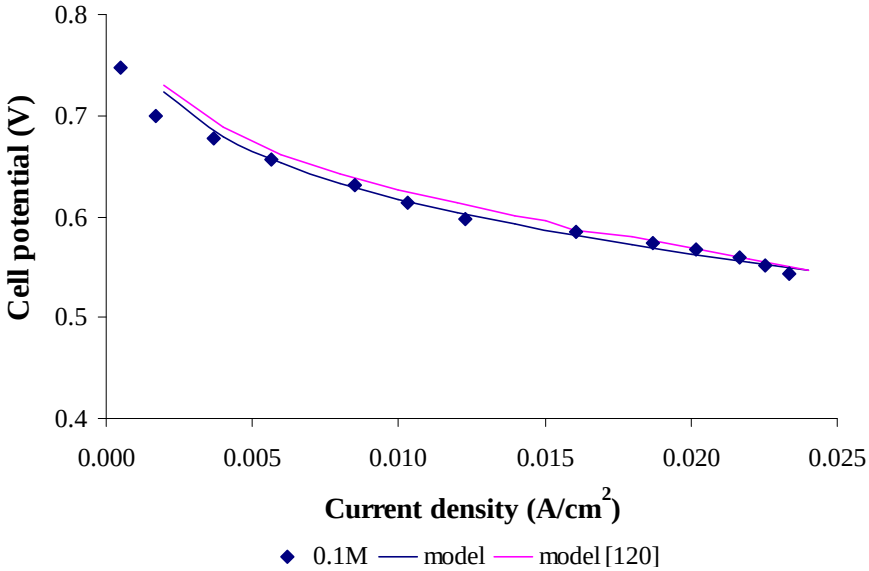

Figure 3.8 – Comparison of the presented model predictions and the model developed by Brenda *et al.*; dots: experimental data from [120], lines: model predictions. Operating conditions: methanol concentration 0.1M, temperature 70 ºC, pressure 1 atm, q^{AF} = 0.33 cm^3/s and q^{CF} = 1.67 cm^3/s.

In Figure 3.9 the predicted polarization curves for 0.1M, 0.2M and 0.5M methanol solutions, are presented. The open-circuit voltage, predicted by the model, is much lower than the thermodynamic equilibrium cell voltage as a result of methanol crossover. This prediction is in accordance with experimental observations [120]. It can be seen that, for low current densities and higher feed methanol concentrations the cell performance is lower. This is due to the fact that higher methanol concentrations result in a higher methanol crossover. At the cathode side, methanol reacts with the oxygen to form a mixed potential. Hence, a higher methanol concentration leads to a higher mixed potential, thereby causing a lower cell performance. According to Fig. 3.9, the model predictions are close to experimental performance curves presented by [120].

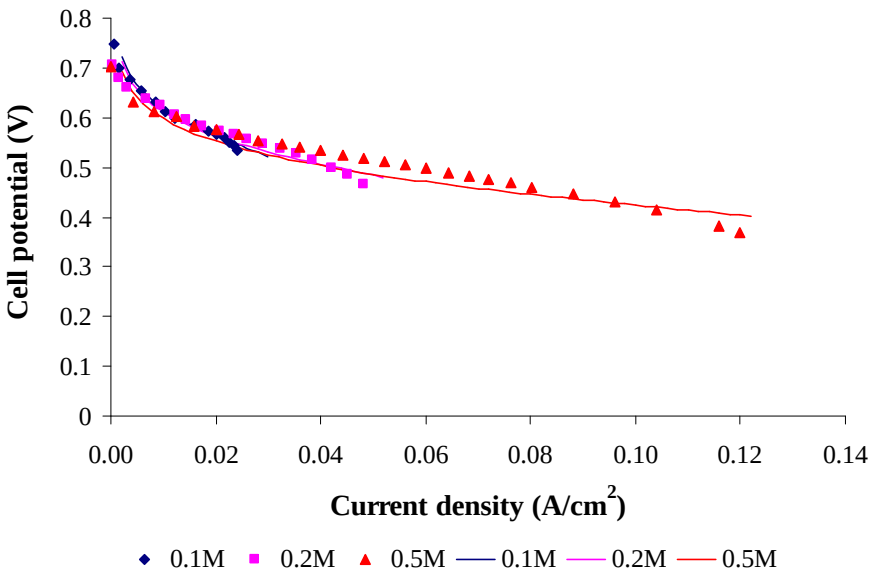

Figure 3.9 – Comparison of the model predictions of polarization curves for different methanol concentrations; dots: experimental data from [120], lines: model predictions. Operating conditions: temperature 70 ºC, pressure 1 atm, q^{AF} = 0.33 cm^3/s and q^{CF} = 1.67 cm^3/s.

Generally, DMFC models predict less accurately the experimental data at low voltages, where complex phenomena, like water flooding, may occur. As can be seen in Fig. 3.9 the present model describes well the experimental results for low current densities due to the integration, on the model, of the mass transfer effects at the cathode side. The most significant discrepancies between the model and experimental data are for conditions near the limiting current densities due to the fact that the model neglects two phase flow effects. When compared with models which account the two-phase flow effects [146], the present one is less accurate at high current densities where the influence of two-phase flow effects is more important. Under these conditions, the bubbles considerably reduce the limiting current density of the cell. However the model uses simple numerical tools, like Matlab, which allows the rapid prediction of the DMFC performance.

3.7. Concluding remarks

In this Chapter a steady state, 1D model accounting for coupled heat and mass transfer, along with the electrochemical reactions occurring in the DMFC was presented.

The model allows the assessment of the effect of operating parameters (such as methanol and oxygen feed concentration, flow-rate and current density) and the design

parameters (channel geometry, active area and material properties) on the temperature and concentration profiles along the cell and consequently on the cell performance. Special attention is devoted to the effects of different parameters such as the methanol feed concentrations and the current density on the water balance between the anode and cathode in the DMFC. The model predicts the correct trends of the influence of these parameters and is in accordance with the trends proposed by Liu *et al.* [90, 175].

With this easily to implement model, suitable operating conditions can be set-up for tailored MEAs in order to work at a high methanol concentration level without the sacrifice of performance. The presented model can be a useful tool to improve DMFC understanding and to optimize fuel cell design as will be presented in Chapter 5. Since the developed model is rapidly implemented with simple numerical tools like, Matlab and Excel it can be used in real-time system level DMFC calculations.

CHAPTER 4

4. EXPERIMENTAL SETUP FOR AN ACTIVE FEED DMFC

For the experimental investigations of the liquid feed direct methanol fuel cells (DMFCs), an active feed DMFC was used. The different cell geometries which have been designed constructed and tested as well as the necessary equipment and facilities for running the tests are presented in this chapter.

4.1. Fuel cell design

The in house fuel cell was designed bearing in mind the following basic demands:

- use of standard state of the art materials which are available on the market;
- high flexibility, i. e. easy change of flow fields, exchange media connections;
- easy handling in terms of assembly and connections;

The cell consists of the following elements (Fig. 4.1):

- three-layer membrane electrode assembly (MEA)
- diffusion layers consisting of carbon-fibber-based porous materials
- monopolar plates with flow fields
- connector plates for electrical contacting
- insulating plates
- end plates

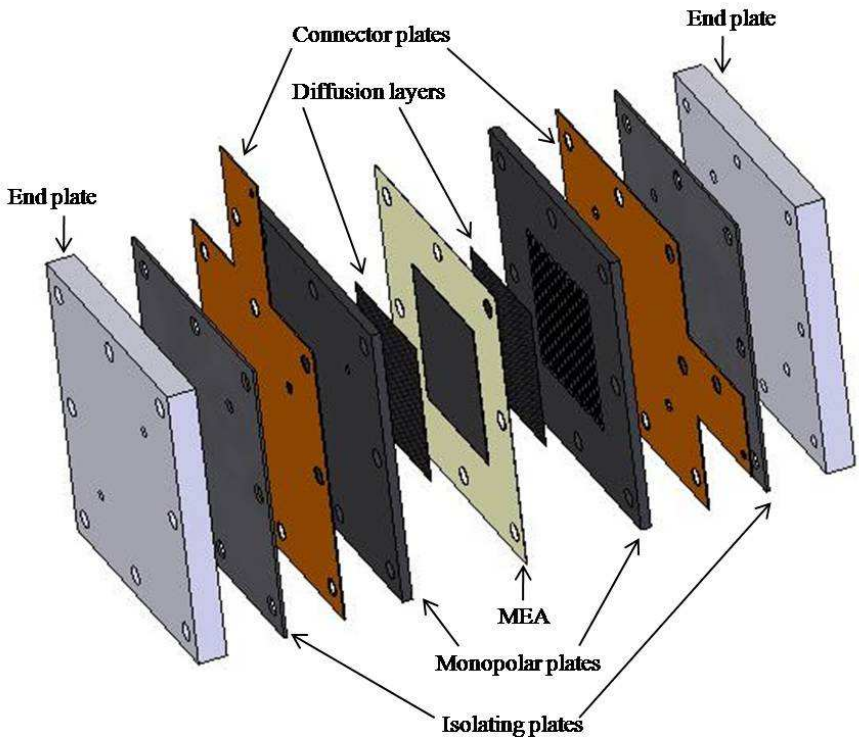

Figure 4.1 – 3D CAD drawing of the active feed DMFC.

The fuel cell specifications, namely the cell components, their quantities and dimensions and the materials used, are presented in Table 4.1.

Table 4.1 – Different elements of a fuel cell

Fuel cell – Specifications			
Cell active area	25 cm^2		
Total cell area	100 cm^2		
Cell components	**Material**	**Quantity**	**Dimensions (cm)**
Monopolar plates	graphite	2	10x10x0.35
Connector plates	gold plated copper	2	10x10x0.05
End plates	aluminium	2	10x10x1
Isolating plates	rubber	2	10x10x0.1
Anode catalyst layer	Platinum/Ruthenium 4 mg/cm^2 or 8 mg/cm^2	1	5x5x(#)
Cathode catalyst layer	Platinum black 4 mg/cm^2 or 8 mg/cm^2	1	5x5x(#)
Membrane	Nafion 117, 115, 212	1	5x5x(*)
Diffusion layers	Carbon paper, carbon cloth or ELAT	2	5x5x(*)

(#) this dimension depends of the catalyst loading; (*) this dimension depends on the used material.

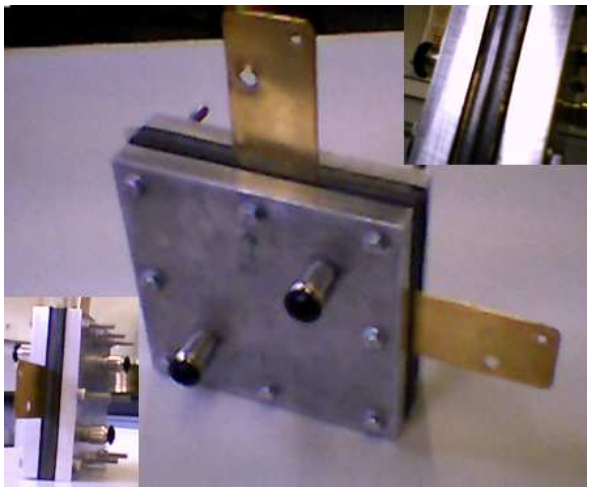

Figure 4.2 – Photograph of an «in-house» designed DMFC.

4.1.1. End Plates

For bracing the cell and applying the desired tension on the cell elements, 10 mm thick aluminium plates are used (Fig. 4.3). Both end plates are connected by a total of 8 bolts (diameter 6.2 mm), running through plastic bushes to prevent electrical contact between the end plates. As a standard, the cell is assembled applying a torque of 5 Nm on the bolts.

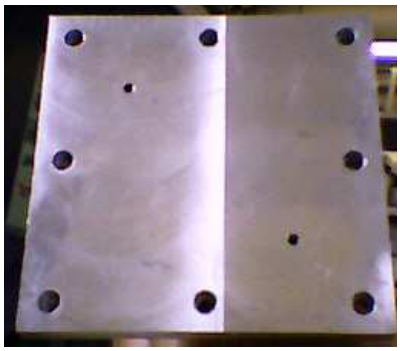

Figure 4.3 – Photograph of an end plate (aluminium)

4.1.2. Insulating Plates

To avoid electrical contact between connector plates and the respective end plates, and to ensure an even pressure distribution over the monopolar plates, rubber plates (thickness 1 mm) are put between the connectors and end plates, respectively (Fig. 4.4).

Figure 4.4 – Photograph of an isolating plate (rubber).

4.1.3. Connector plates

For the electrical connection of the graphite monopolar plates, gold plated copper plates of 0.5 mm thickness are used (Fig. 4.5). Also all further electrical connectors are gold plated to ensure minimal ohmic resistances at various connection points.

Figure 4.5 – Photograph of a connector plate.

4.1.4. Monopolar plates

The monopolar plates are made from graphite supplied by Schunk Portugal, Lda. The necessary flowbed structures for the reactant distribution over the MEA surface are millcut into the plates. The flowbed area is 25 cm^2. The table 4.2 shows the different flow field configurations used in the present work.

Table 4.2 – Different flow field designs used.

Design 1		
Number of channels	15	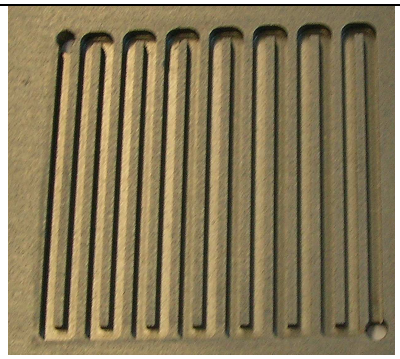
Type of channels	Serpentine (SFF)	
Channel length	50 mm	
Channel depth	2 mm	
Channel width	2 mm	
Channel ribs	1.5 mm	

Design 2		
Number of channels	15	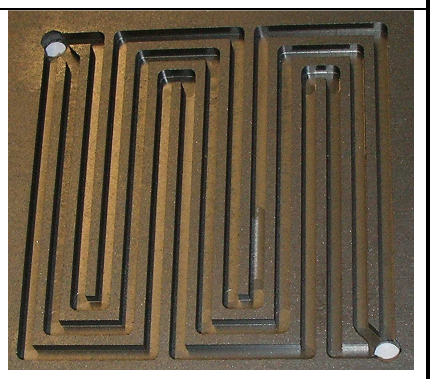
Type of channels	Multiserpentine (MSFF) (3 serpentine channels)	
Channel length	50 mm	
Channel depth	2 mm	
Channel width	2 mm	
Channel ribs	1.5 mm	

Design 3		
Number of channels	14	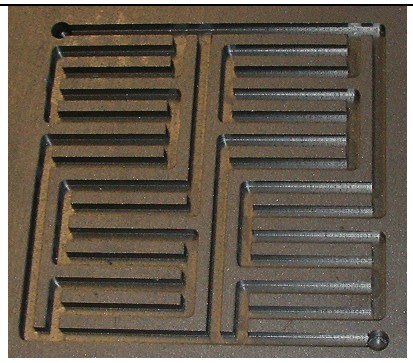
Type of channels	Mixed (MFF) (serpentine and parallel)	
Channel length	-----	
Channel depth	2 mm	
Channel width	2 mm	
Channel ribs	1.7 mm	

The influence of the flow field is treated in the present work. A serpentine flow field was selected, as based configuration for all the tests, following the generally accepted idea that this design results in a better cell performance facilitating the removal of reaction products, such as carbon dioxide on the anode and water on the cathode side, and enhancing two-phase mass transport [39, 106, 107]. The flow fields, consisting of machined one-pass serpentine grooves blocks, were identical for both anode and cathode.

4.1.5. Membrane Electrode Assembly (MEA)

In the remaining text, the abbreviation MEA always refers to a membrane coated with catalyst layers but without diffusion layers. The MEA's used were supplied by Lynntech and had an active area of 25cm^2 (5x5cm) and a total area of 110.67cm^2 (10.52x10.52cm). The membranes tested were made by Nafion 117, 115 e 212. Unsupported platinum black and platinum-ruthenium were used as catalyst (Fig. 4.6). The catalyst was Pt/Ru on the anode side with a loading of 4 mg/cm^2 and Pt on the cathode side with a loading of 4 mg/cm^2.

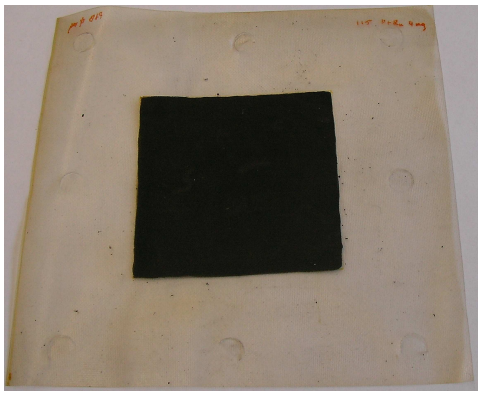

Figure 4.6 – Photograph of a Membrane Electrode Assembly (MEA)

An important physical parameter of the catalyst layer is the porosity and it can be calculated from the catalyst loading, the ink composition and some physical properties of the used materials. The calculation is presented in the Appendix B. The porosity values obtained are high, which is of course desired to a certain degree to achieve as many accessible catalyst sites as possible for the fluid phases.

4.1.6. Diffusion layers

Different types of diffusion layers are usually used in DMFCs: carbon paper and carbon cloth. As already referred, some authors [89, 90] report the use of these two materials coated with a highly hydrophobic microporous layer (MPL) enhancing fuel cell performance through a minimised water crossover. The most common GDLs commercially available do not have MPL layers. Bearing in mind that the one purpose of this work was the optimization of a DMFC using the materials available

commercially, we therefore selected carbon paper and carbon cloth without MPL as GDL materials and also used a single side ELAT electrode from E-TEK which uses treated carbon cloth.

For convenience, carbon paper, carbon cloth and ELAT carbon cloth are denoted as CP, CC and ELAT, respectively, in the present work.

Both, carbon paper and carbon cloth are carbon-fiber-based porous materials, but carbon paper is non-woven while carbon cloth is woven fabric. Usually, carbon paper has a uniform pore size with a peak around 50 μm while the carbon cloth has a broad pore size distribution from 5 to 100 μm [176].

Both materials are commercially available and may have different denominations due to their thickness. The anode gas diffusion layers used were carbon cloth type A (CC) from E-TEK or carbon paper TGPH060 (CP) from Toray both with a PTFE content of 30 wt.%.

The cathode gas diffusion layers used were ELAT carbon cloth (ELAT) from E-TEK, carbon paper TGPH060 (CP) from Toray or carbon cloth type A (CC) from E-TEK all with a PTFE content of 30 wt.% (Fig. 4.7). The structural properties of the diffusion layers materials used can be found in Appendix B. Carbon cloth is more porous, less tortuous and thicker than carbon paper [176-178]. The ELAT material formed of carbon cloth type A treated on one side is less porous, thicker and more tortuous that carbon cloth.

The diffusion layers can be put on either side of the MEA, and the whole sandwich structure can be mounted between the monopolar plates of the fuel cell.

Figure 4.7 – Photograph of diffusion layers.

4.2. Methanol Test Kit Testing Unit

The test unit used for experiments with DMFCs was developed and bought to Fideris Incorporated. In one compact unit, the Methanol Test Kit (MTK) testing unit contains six subsystems: methanol handling system, oxidant gas handling system, fuel cell heater control system (optional), linear electronic load, I/O capabilities and the hardwired emergency stop system. To obtain the highest performance of the fuel cell test equipment, Fideris Incorporated recommends operation of all equipment using the FCPower software. This software package has been written especially for the fuel cell researcher to provide complete control of all aspects of fuel cell testing. Figure 4.8 and 4.9 show a schematic of laboratory-scale test facility.

Figure 4.8 – Photograph of the experimental setup.

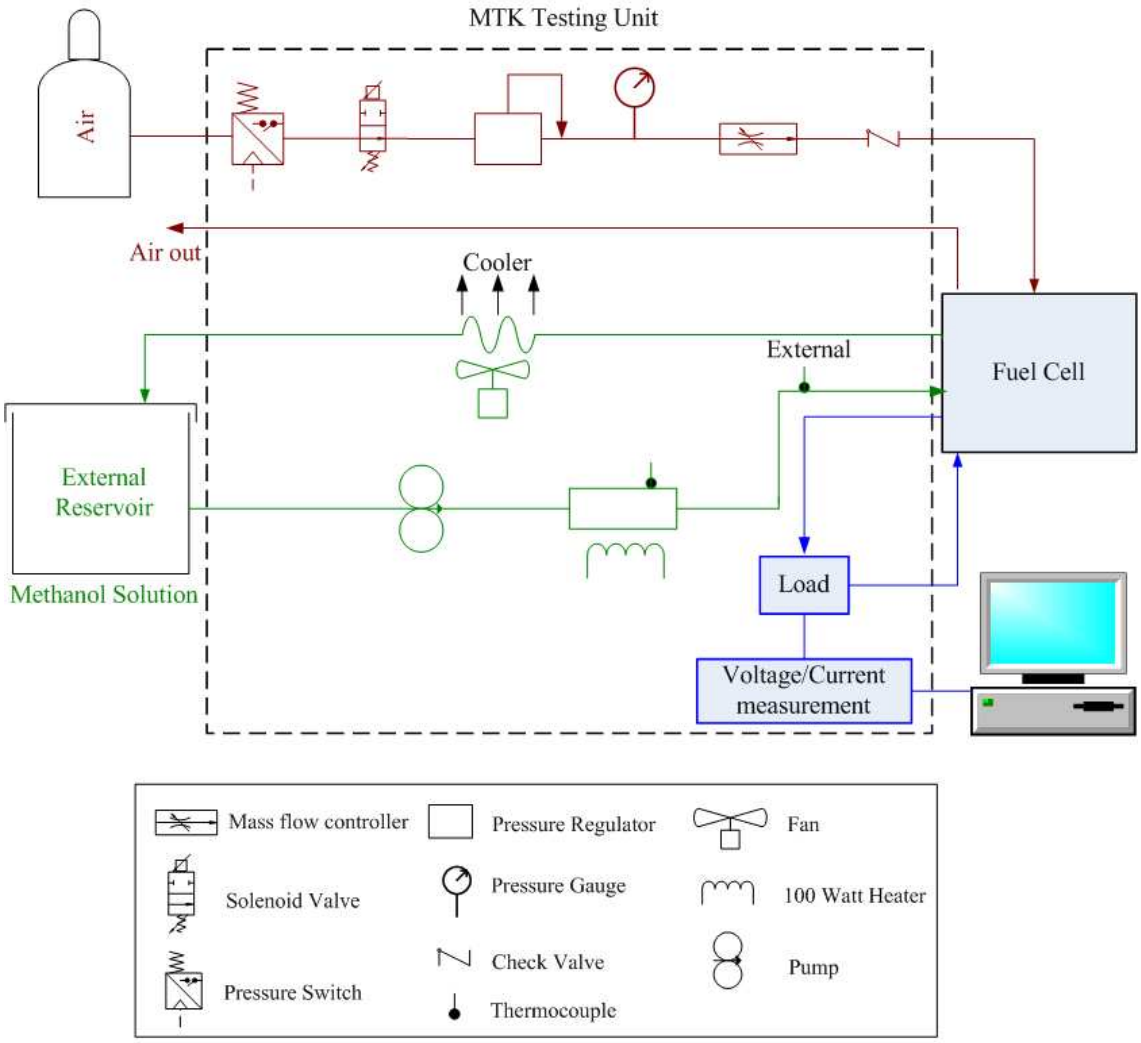

Figure 4.9 – Schematic diagram of the experimental set-up.

The major specifications of the Methanol Test Kit unit are displayed in Table 4.3.

Table 4.3 – Specifications of MTK [179].

Methanol handling system	
Liquid reactant control	Micropump: Magnetic drive gear pump Series 180
Maximum pump rate	85 ml/min
Maximum temperature	95ºC
Heating system capacity	400 W
Cooling system capacity	350 W
External reservoir capacity	1 Liter
Gas handling system	
Reactant gas control	Computer controlled mass flow control of oxidant
Maximum gas flow	10 l/min
Inlet gas pressure range	80-200 psi
Loadbank system	
Type	MOSFET variable resistance loadbank
Measurement	Power, Voltage e Current
Control modes	Constant, Pulse e Ramp
Maximum current rating	50 A
Maximum voltage rating	20 V
Maximum power rating	100 W
Nominal short circuit resistance	< 2.2 mΩ
Corrosion protection	All critical components are gold plated
Electrical Requirments	
Voltage	120/230-240 VAC (field changeable)
Frequency	50-60 Hz
Power rating	800 W
Software	
Software recommended by Fideris: FCPower	

4.2.1. Methanol handling system

As shown in Fig. 4.10 the methanol handling system includes an external reservoir equipped with a low level float which will set a software alarm after a low level timeout

period. A computer controlled variable speed recirculating pump is used to pump the methanol solution from the reservoir through the handling system and fuel cell and return it to the reservoir. The pump used is a magnetic drive gear pump which allows a maximum methanol solution rate of 85 ml/min. Included in the recirculating loop are a heater equipped with over temperature protection and a cooling system which can cool the methanol solution to ambient temperature. An external thermocouple allows the measurement of the methanol solution as it enters the fuel cell. The user can enable the methanol flow and methanol heater. These systems are enabled when their respective box is checked (Fig. 4.11). The recirculation pump speed can be set up to the maximum speed as well as the temperature set point for the methanol solution can be set from ambient to 95ºC.

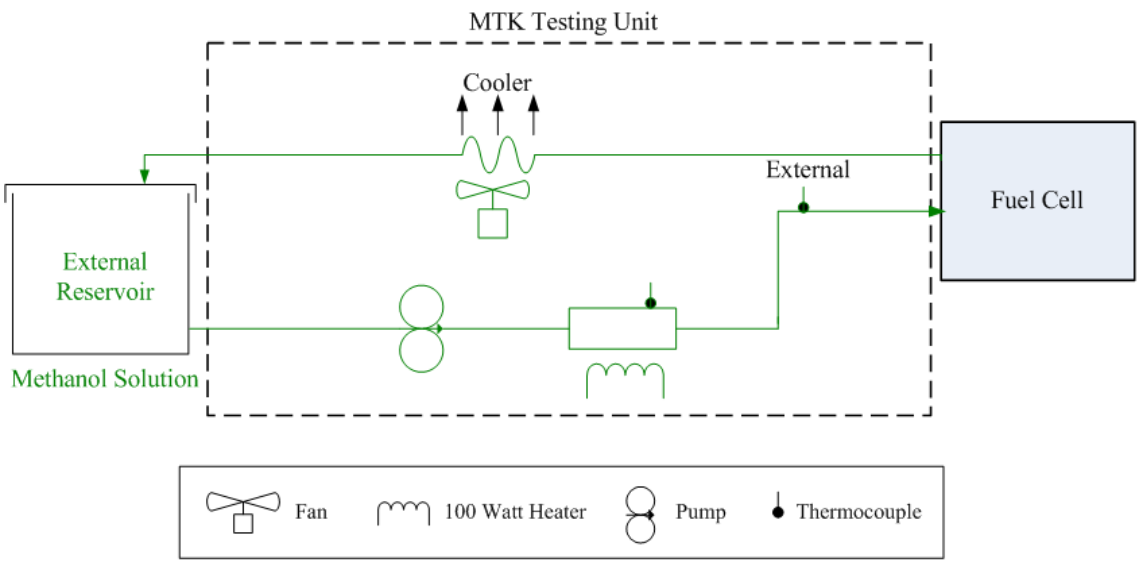

Figure 4.10 – Schematic diagram of the methanol handling system.

METHANOL CONTROL				
Enable Methanol Flow	☑	Enabled		
Enable Methanol Heater	☑	Disabled: Recirc...		
Enable Water Makeup Pump	☐	Disabled: Low L...		
Enable Methanol Makeup Pump	☐	Disabled: Low L...		
Recirculation Pump Speed (ccpm)	3.000		Full Scale Flow (ccpm)	85.000
Raw Recirculation Pump Speed	144.529		Recirculation Pump Speed Minimum (% of range)	5.000
Water Makeup Pump Speed (ccpm)	0.000		Full Scale Flow (ccpm)	85.000
Raw Water Makeup Pump Speed	0.000			
Methanol Makeup Pump Speed (ccpm)	0.000		Full Scale Flow (ccpm)	85.000
Raw Methanol Makeup Pump Speed	0.000			
	Setpoint	Actual		
Temperature (°C)	20.000	22.250		
Recirculation Tank Level	OK		Recirculation Tank Level Timeout (sec)	5
Recirculation Tank Level Alarm				
Water Makeup Tank Level	Low		Water Makeup Tank Level Timeout (sec)	5
Water Makeup Tank Level Alarm			Disable Master On Alarm	☐
Methanol Makeup Tank Level	Low		Methanol Makeup Tank Level Timeout (sec)	5
Methanol Makeup Tank Level Alarm			Disable Master On Alarm	☐
Methanol Temperature Deviation Alarm			Methanol Temperature Deviation Max (% of setpoint)	5.000
Heater Block Temperature (°C)	23.313			
Heater Block Temperature Max Alarm			Heater Block Temperature Max (°C)	100.000
Temperature Units	°C		Heater Duty Cycle	0.000
Flow Units	ccpm		Cooling Fan Duty Cycle	0.000
	K1	K2	K3	Period (sec)
Heater PID	0.200	0.000	0.000	5.000

Figure 4.11 – MTK software panel with methanol control option.

4.2.2. Gas handling system

To supply the fuel cell with an oxidant gas, the MTK is equipped with a gas handling system. A pressure switch is included to ensure sufficient pressure is available, and a computer controlled solenoid valve allows for the oxidant gas to enter the system. An internal pressure regulator controls the pressure of the gas, which is necessary for accurate metering of the gas through the mass flow controller (MFC) (Fig. 4.12). The regulated inlet pressure is displayed on the front of the unit. The computer controlled MFC allows a metered amount of gas, as set on the computer, to be supplied to the fuel cell. The user can enable de gas flow and set the gas flow rate by imputing the desired MFC flow rate in the space provided. The gas flow rate can be set to a maximum of 10 l/min. The user can set the gas control mode to either constant mode or stoichiometric mode. All the experiments were conducted at constant mode (Fig. 4.13).

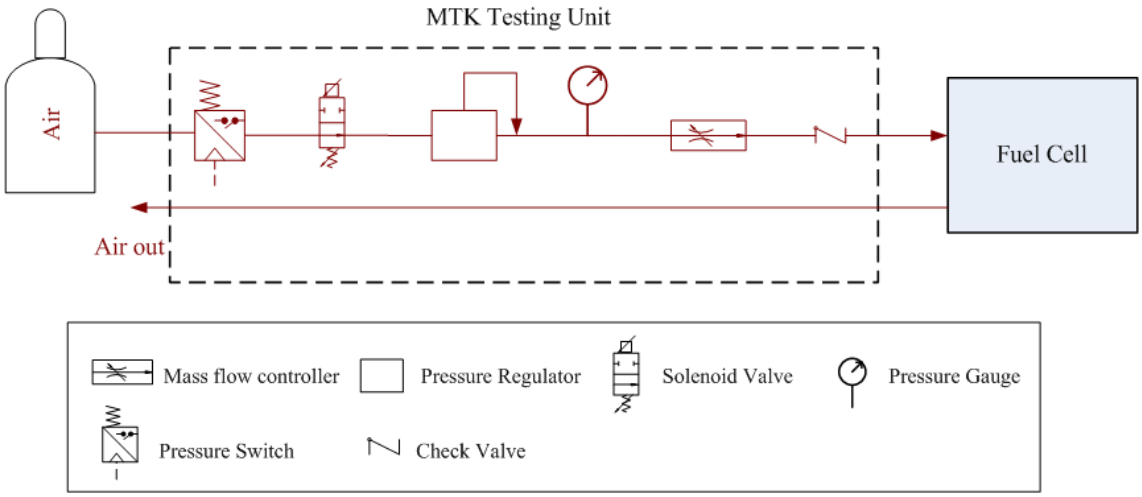

Figure 4.12 – Schematic diagram of the gas handling system.

AIR CONTROL				
Enable Gas Flow	☑	Enabled		
Gas Inlet Pressure	OK			
Gas Inlet Valve State	Open		Gas Minimum Threshold (% of range)	2.000
	Setpoint	Actual		
MFC Flow (lpm)	1.000	0.979	MFC Full Scale Flow (lpm)	10.000
MFC Flow (raw)	819.000	802.000		
Flow Deviation Alarm			Flow Deviation Max (% of setpoint)	5.000
Gas Units	lpm		Stoichiometric Ratio	2.000
Gas Name	Air		Equivalence Factor (e-/mole)	4.000
Gas Control Mode	Constant		Stoichiometric Gas Constant	22.000
Calibration Gas Factor	2.000		Cell Area (cm²)	25.000
Actual Gas Factor	1.000		Number of Cells	1

Figure 4.13 – MTK software panel with air control option.

4.2.3. Loadbank system

The loadbank subsystem acts as a large variable power resistor. With the control software, the user controls the amount of impedance by selecting either how much current is passed through the loadbank, the voltage across the loadbank or power dissipated by the loadbank. To meet the requirements of any given experiment, the user can also set upper and lower limits on the current, voltage and power. The computer constantly monitors both current and voltage and these parameters are used to calculate and track the amount of power that the loadbank is dissipating at any one time. The computer program will not permit the power to exceed 100 W. The set points for the control parameters can be previously chosen. The set points are used when running in constant mode (Fig. 4.14).

ELECTRONIC LOAD				
Enable Load	☑	Enabled		
	Lower Limit	Setpoint	Upper Limit	Actual
Current (A)	0.000	0.200	50.000	0.195
Voltage (V)	0.000	0.000	20.000	0.449
Power (W)	0.000	0.000	100.000	0.088
Control Mode	Constant		Control Parameter	Current
	Low	High		
Pulse Time (sec)	0.000	0.000		
Pulse Value	0.000	0.000		
	Initial Value	Final Value	Period (sec)	
Ramp	0.000	0.000	0.000	
Current Deviation Alarm			Current Deviation Max (% of setpoint)	5.000
Voltage Deviation Alarm			Voltage Deviation Max (% of setpoint)	5.000
Power Deviation Alarm			Power Deviation Max (% of setpoint)	5.000
Shunt Full Load Current (A)	50		Shunt Percentage	0.004
Raw Output	19			

Figure 4.14 – MTK software panel with electronic load option.

The current, voltage and power are known as control parameters. The loadbank has three different control modes to choose from constant, pulse and ramp mode.

- Constant mode – to run in constant mode, set the control mode to constant, select the desired control parameter and enter the appropriate set point. Only the set point for the control parameter is used.

- Pulse mode – to run in pulse mode, set the control mode to pulse, select the desired control parameter and enter the pulse high and pulse low values for the selected control parameter. It is also necessary to set the pulse high time and pulse low time (in seconds). The pulse width can be up to 1000s.

- Ramp mode – to run in ramp mode, set the control mode to ramp, select the desired control parameter and enter the ramp initial and ramp final values for the selected control parameter. The parameter can be increasing or decreasing. The ramp period must be set (in seconds) with a lower limit of 0.5 and an upper limit of 1000.

All the experiments were conducted at constant mode

4.3. Fuel cell heater control system

Instead of using the fuel cell heater control from Fideris, an optional system was designed and used in the present work. A heater resistance with 50W/m and 2 m of length was placed across the fuel cell. To allow a uniform heating of the fuel cell and to minimize the heat loss to ambient a spongy material was placed on the outside of the heater resistance (Fig. 4.15). The resistance was connected to a digital temperature controller allowing the control of the fuel cell temperature (Fig. 4.16). To measure and control the fuel cell temperature two thermocouples were placed on the aluminium plate on each side of the fuel cell (anode and cathode side).

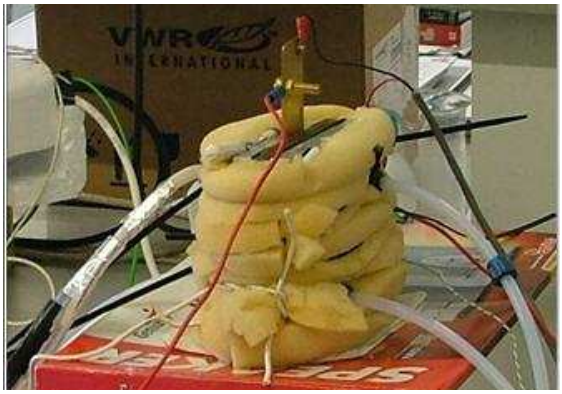

Figure 4.15 – Photograph of a fuel cell with heater resistance.

Figure 4.16 – Photograph of the front panel of the digital controller.

4.4. Experimental procedure

The start-up procedure was as follows:

1. Fill the reservoir with the methanol solution needed for the experiment;

2. Turn on the oxidant gas supply for the system and verify that it is held in the operating range required for the test unit;
3. Turn on computer, the MTK unit and the FCPower software;
4. Set the methanol temperature, methanol flow rate and air flow rate value;
5. Set the fuel cell temperature value.
6. The cell was operated galvanostatically, so the current applied range values was 0 to maximum current allowed by the fuel cell, with a step of 0.1A. At open circuit conditions the cell was operated fifteen minutes and at the other values of current applied, the cell was operated three minutes to reach the steady state.
7. For each value of current applied the cell voltage was measured and power was calculated;
8. Turn off the MTK system;
9. Close the FCPower software;
10. Turn off the gas supply.

CHAPTER 5

5. EXPERIMENTAL AND MODELLING STUDIES OF AN ACTIVE FEED DMFC

A detailed experimental study on the performance of an «in-house» developed DMFC with 25 cm^2 of active membrane area, working near ambient pressure is described. As was mentioned before there are several operating and design parameters that affect the fuel cell performance. The operating parameters studied were the methanol feed concentration, methanol and air flow rate and cell temperature. The effect of design parameters such as membrane thickness, catalyst loading, flow field design and diffusion layers material and thickness was, also, studied. The experimental polarization curves are successfully compared with the predictions of the steady state, one-dimensional model accounting for coupled heat and mass transfer, along with the electrochemical reactions occurring in the DMFC presented in Chapter 3. The operating conditions studied were selected bearing in mind the present state of the art of DMFCs. As referred previously, there are few studies on this type of fuel cells operating with high methanol concentrations, with different membranes and gas diffusion layers and most of them were performed under high temperature and pressure. However, less severe conditions (ambient temperature and pressure) are favourable especially for portable applications. The main goal is to systematically vary commercial MEA materials and check their influence on fuel cell performance. The influence of the different parameters on the cell performance is explained under the light of the predictions from the developed model. Tailored MEAs (membrane electrode assemblies), with different structures and combinations of gas diffusion layers (GDL), were designed and tested in order to select optimal working conditions at high methanol concentration levels without significant performance losses. Model predictions of the effect of different parameters on the water management in an active feed DMFC are also, presented.

The contents of this Chapter conducted to the preparation and submission of papers: Oliveira, V.B, Rangel, C.M. and Pinto, A.M.F.R., "Performance of a Direct Methanol Fuel Cell operating near ambient conditions" submitted to Journal of

Fuel Cell Science and Technology and Oliveira, V.B, Rangel, C.M. and Pinto, A.M.F.R., "Effect of anode and cathode flow field design on the performance of a direct methanol fuel cell" submitted to Chemical Engineering Journal.

The contents of this Chapter were partially published in Oliveira, V.B, Rangel, C.M. and Pinto, A.M.F.R., "Modelling and experimental studies on a Direct Methanol Fuel Cell working under low methanol crossover and high methanol concentrations", International Journal of Hydrogen Energy 34 (2009) 6443-6451 and Oliveira, V.B, Rangel, C.M. and Pinto, A.M.F.R., "Water management in direct Methanol Fuel Cells" International Journal of Hydrogen Energy (2009) doi:10.1016/j.ijhydene.2009.07.111.

5.1. Results and Discussion

The performance of the design fuel cell was determined by a set of tests in order to obtain the cell polarization and power density curves. The test consisted of applying a load to the cell, measuring the corresponding voltage value (recall Chapter 4) and then calculating the cell power.

For each set of operating conditions, tests were performed until obtaining at least two similar results. Tests were accepted if differences between corresponding readings were below 5%.

Active direct methanol fuel cells characteristically require high stoichiometric flow rates in order to optimize their performance. A relatively high anode stoichiometry is needed to prevent the CO_2 gas clogging. At the cathode side excessive high humidity effects are believed to induce GDL flooding at low air flow rates near stoichiometry. Following suggestions of previous works [38, 180] an anode stoichiometry (for 150 mA/ cm^2) between 15 and 40 and a cathode stoichiometry of around 6 were used.

In each section presented in the following parts of this chapter, due to the large amount of tests performed and results obtained, a sub-set of conditions was selected and is presented. The remaining results can be found in Appendix C.

Whenever is possible, and as already mentioned, the experimental results were explained under the light of the developed model (Chapter 3).

5.1.1. Effect of diffusion layers

Figures 5.1 and 5.2 show the comparison of the polarization and power curves for experiments performed without and with gas diffusion layers. It should be clarified that the experiments without gas diffusion layer correspond to the use of a three layer MEA (membrane, anode and cathode catalyst layer) and with gas diffusion layer correspond to a five layer MEA (membrane, anode and cathode catalyst layer and anode and cathode diffusion layer). In the tests reposted in Figures 5.1 and 5.2 the methanol flow rate was, respectively, 8 ml/min and 3 ml/min and the air flow rate 3.6 l/min. In the experiments with gas diffusion layers, carbon cloth type A and ELAT (E-TEK) were employed at the anode and at the cathode side, respectively. As is evident from the plots the presence of the gas diffusion layers both at the anode and at the cathode side strongly affects the cell voltage and power. It is clear that the cell voltage and power increase significantly with the introduction of these two additional layers on the fuel cell. It should be noted that although the gas diffusion layers do not directly participate in the electrochemical reactions they have several important functions. These layers provide a pathway for reactants from the flow field channels to the catalyst layers, allowing their access to the entire active area, a pathway for products from the catalyst layers to the flow field channels. The GDLs also electrically connect the catalyst layers to the graphite plates, allowing the electrons to complete the electrical circuit, serve to conduct heat generated in the electrochemical reactions in the catalyst layers to the graphite plates and provide mechanical support to the MEA preventing it from sagging into the flow field channels. For these reasons the fuel cell performance is significantly enhanced by introducing the diffusion layers on the anode and cathode side. As described in Chapter 2, this finding is commonly accepted but there are no significant published works treating it quantitatively.

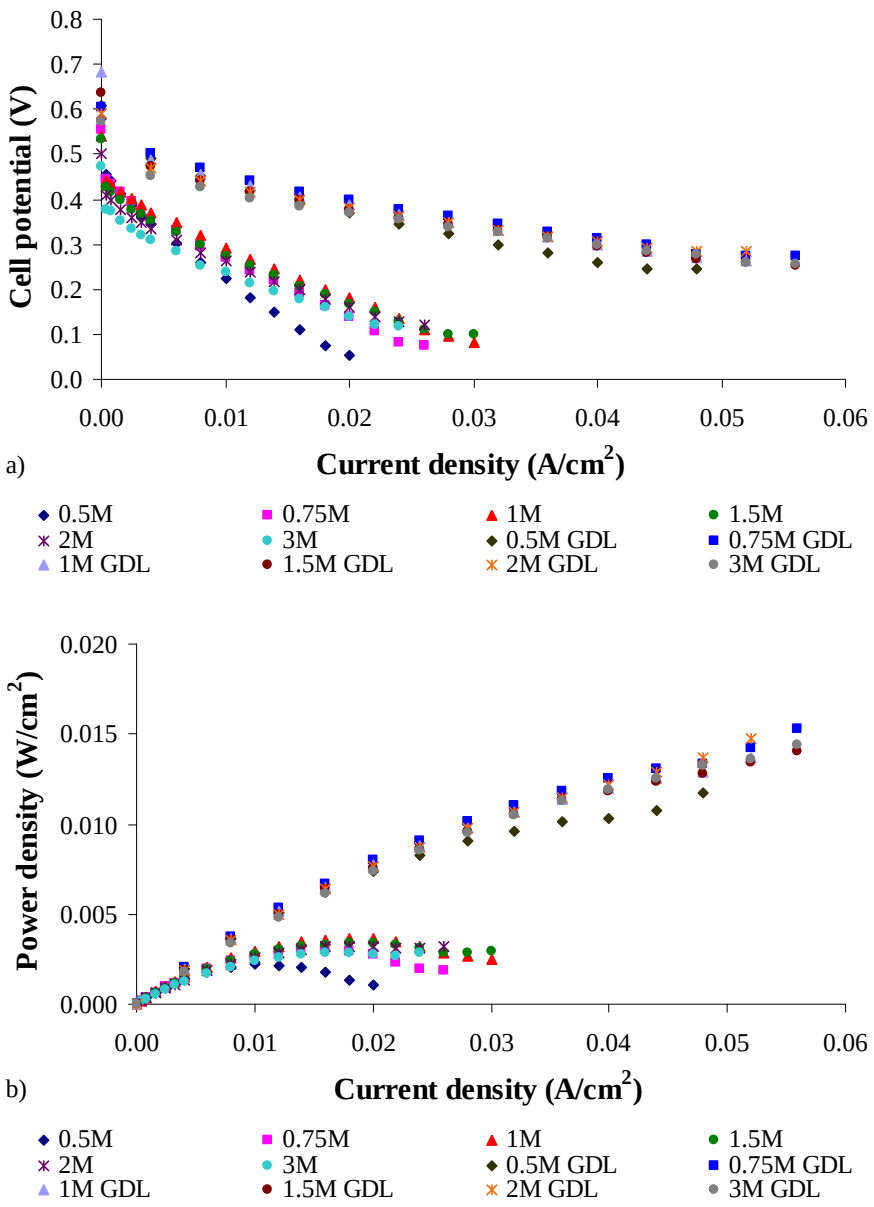

Figure 5.1 – Influence of gas diffusion layers on a) cell performance and b) power density for different methanol concentrations. Operating conditions: methanol flow rate 8 ml/min, air flow rate 3.6 l/min and fuel cell temperature 20ºC. Gas diffusion layers materials: carbon cloth at the anode and ELAT (E-TEK) at the cathode.

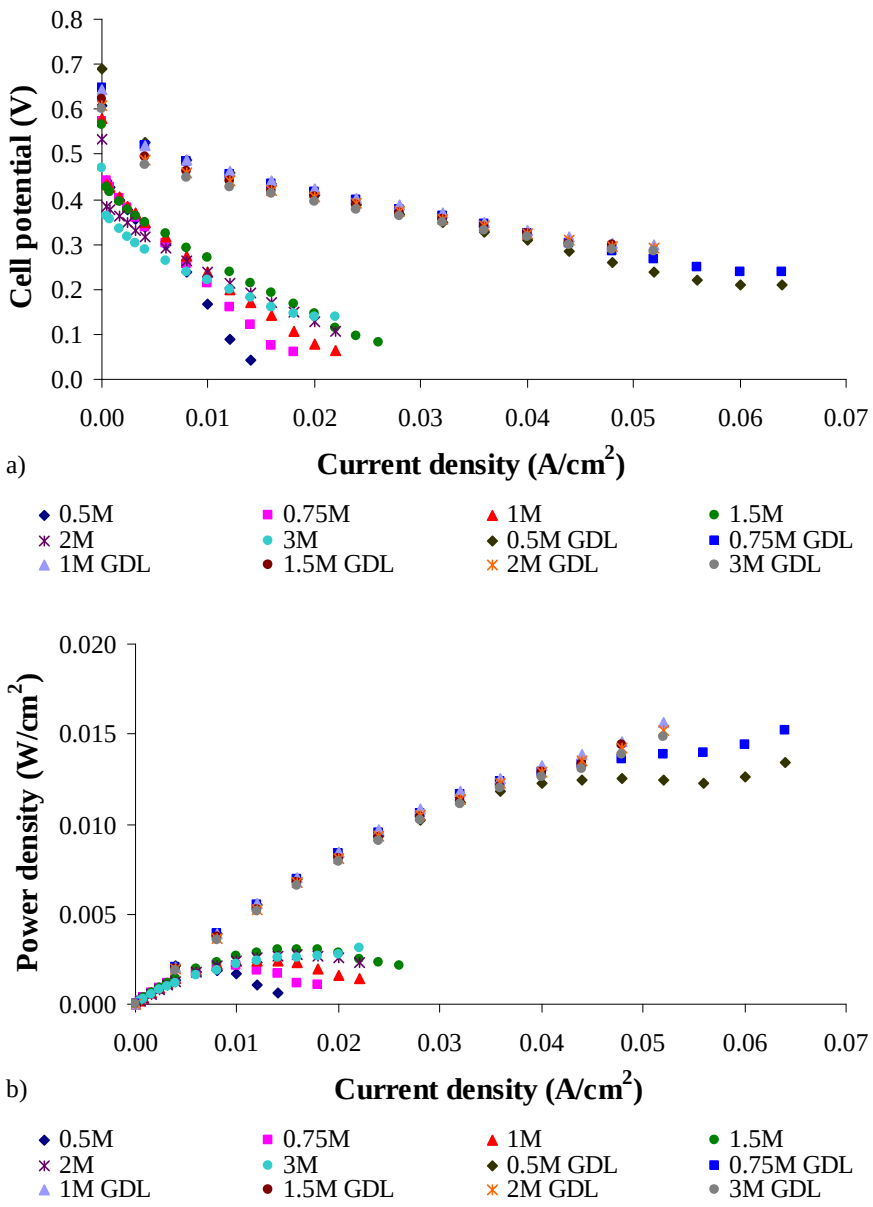

Figure 5.2 – Influence of gas diffusion layers on a) cell performance and b) power density for different methanol concentrations. Operating conditions: methanol flow rate 3 ml/min, air flow rate 3.6 l/min and fuel cell temperature 20ºC. Gas diffusion layers materials: carbon cloth at the anode and ELAT (E-TEK) at the cathode.

5.1.2. Effect of operating conditions

All the results presented in this section were obtained in experiments with a DMFC with the characteristics presented in the Table 5.1.

Table 5.1 – Set of DMFC characteristics used to analyse the effect of the operating conditions on the cell performance.

Diffusion layer	Anode	Carbon cloth type A
	Cathode	ELAT (E-TEK)
Catalyst loading	Anode	4 mg/cm^2 Pt/Ru
	Cathode	4 mg/cm^2 Pt
Flow field design	Anode	Serpentine
	Cathode	Serpentine
Membrane		Nafion 117

5.1.2.1. Effect of methanol concentration

The set of operating conditions selected to study the effect of the methanol concentration on the fuel cell performance is displayed in Table 5.2

Table 5.2 – Set of operating conditions used to analyse the effect of methanol concentration on the cell performance.

C_{CH_3OH} (M)	q_{CH_3OH} (ml/min)	q_{air} (l/min)	Cell temperature (ºC)
0.25	8	3.6	20
0.5			
0.75			
1			
1.5			
2			
3			
0.25	3	3.6	20
0.5			
0.75			
1			
1.5			
2			
3			
5			
0.25	3	1	20
0.5			
0.75			
1			
1.5			
2			
3			

The influence of the methanol concentration on the cell voltage and power is shown in Fig. 5.3. For the set of experiments selected the methanol flow rate was 8 ml/min and the air flow rate 3.6 l/min. the cell temperature was controlled at a temperature close to room conditions (20ºC). The plots presented show that the best performance curve and the higher cell power density correspond to the feed concentration of 0.75 M, especially for medium to high current densities. For all the experiments the open-circuit voltage is much lower than the thermodynamic equilibrium cell voltage as a result of methanol crossover. It can be seen that, at low current densities and high feed methanol concentrations the cell performance is lower. This is due to the fact that higher methanol concentrations result in a higher methanol crossover, as shown in Fig. 5.4 were the represented curves correspond to the model predictions for the methanol crossover for different methanol feed concentrations. At the cathode side, methanol reacts with the oxygen to form a mixed potential. Hence, a higher methanol concentration leads to a higher mixed potential, causing a lower cell performance.

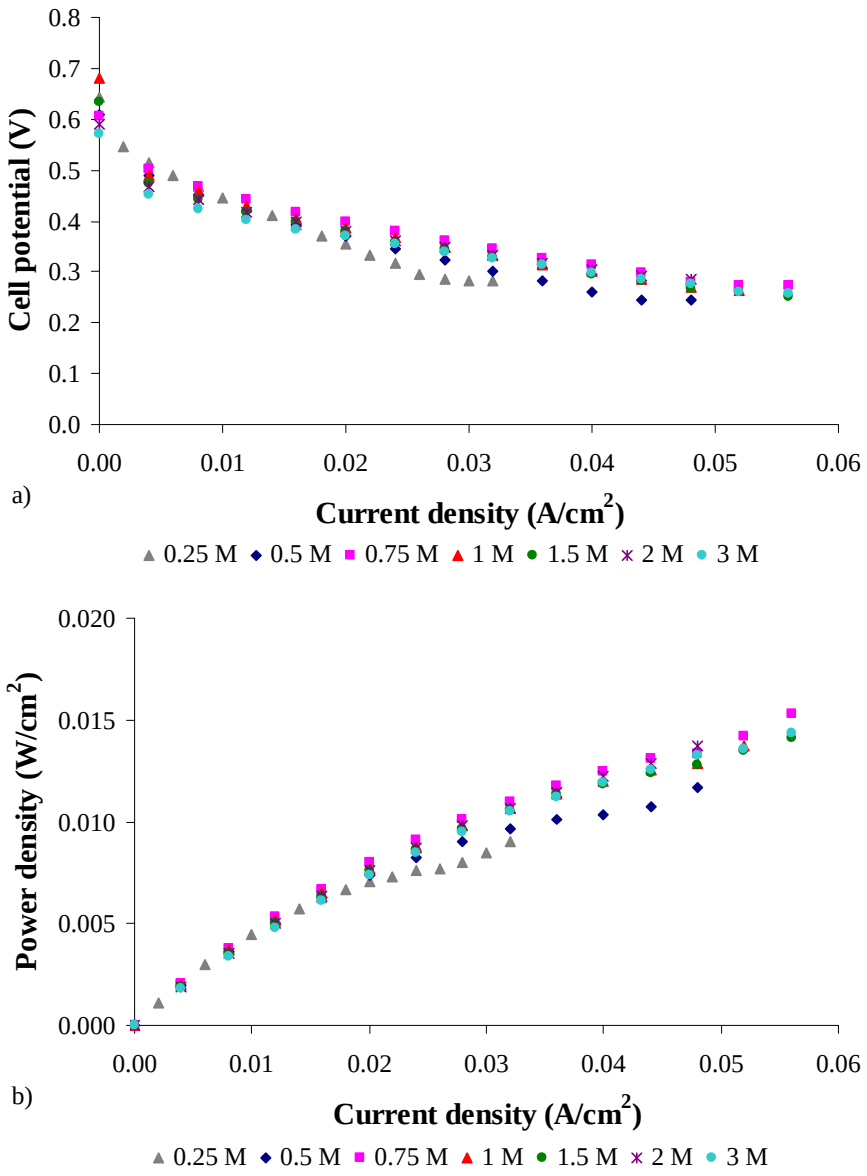

Figure 5.3 – Effect of methanol concentration on a) cell performance and b) power density. Operating conditions: methanol flow rate 8 ml/min, air flow rate 3.6 l/min and fuel cell temperature 20ºC.

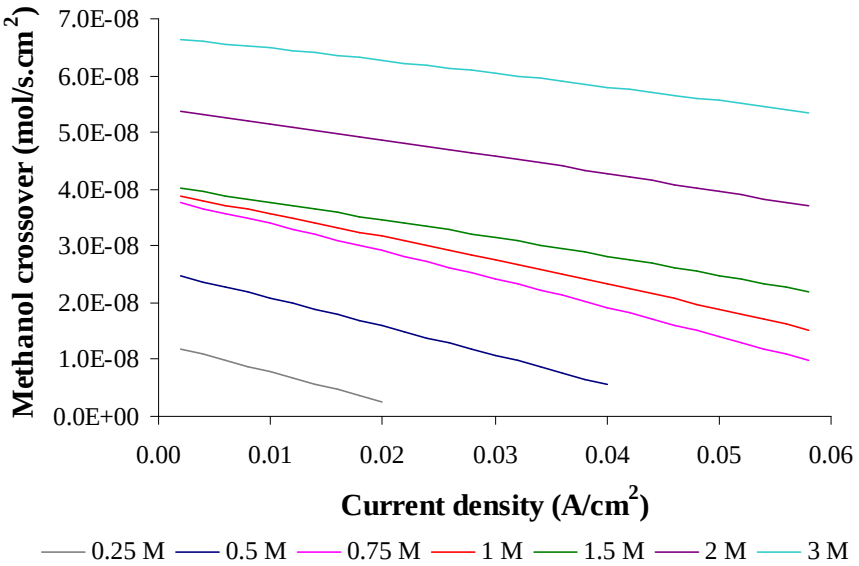

Figure 5.4 – Model predictions for the methanol crossover for different methanol feed concentrations. Operating conditions: methanol flow rate 8 ml/min, air flow rate 3.6 l/min and fuel cell temperature 20ºC.

The developed model is also used to predict the polarization and power curves for two different methanol feed concentration (0.75M and 2M), as presented in Fig. 5.5 together with the experimental data. As is evident from the plots, the model describes very well the experimental results for low current densities due to the integration, on the model, of the mass transfer effects at the cathode side. The most significant discrepancies between the two curves are for conditions near the limiting current densities due to the fact that the model neglects two-phase flow effects. These effects are more important in these conditions.

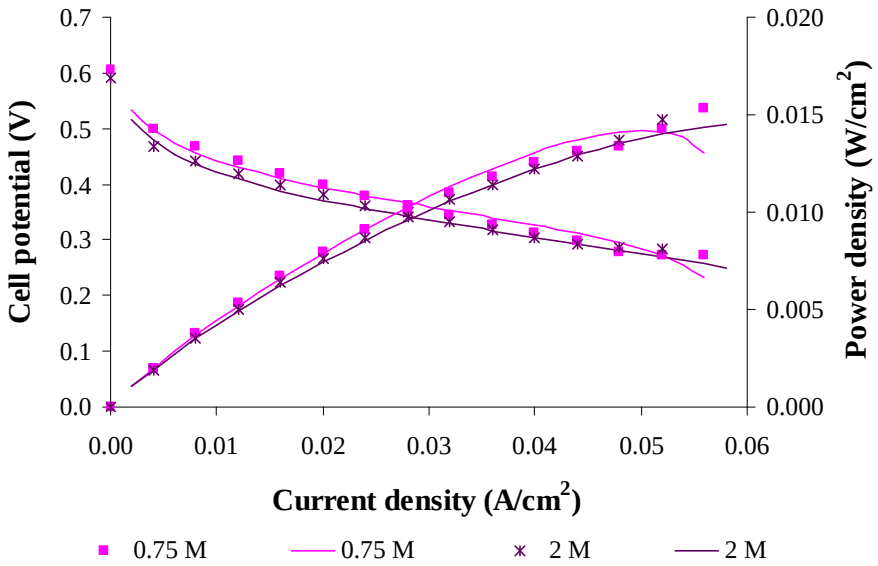

Figure 5.5 – Comparison of model predictions on cell performance and power density; dots: experimental data, lines: model predictions. Operating conditions: methanol flow rate 8 ml/min, air flow rate 3.6 l/min and fuel cell temperature 20°C.

Model predictions of the effect of methanol concentration on the net water transport coefficient, α, (from Eq. 3.84) are presented in Fig. 5.6 as a function of current density. It is evident that the methanol concentration has a large impact on the net water transport coefficient. High methanol concentrations result in low values of α. This occurs because for low values of methanol feed concentration, there is almost always a higher water concentration on the anode side, especially for the lower values of current density. The transport of water toward the cathode is dominant. For high methanol concentrations, the water concentration on the anode side is smaller and the water production in the cathode gives higher water concentration, in this side. The water transport from the cathode to the anode side is therefore dominant corresponding to smaller or even negative values of α. The trends of the influence of methanol concentration on water crossover predicted by the present model are in accordance to those proposed by Liu *et al.* [90] as shown in section 3.6, Chapter 3.

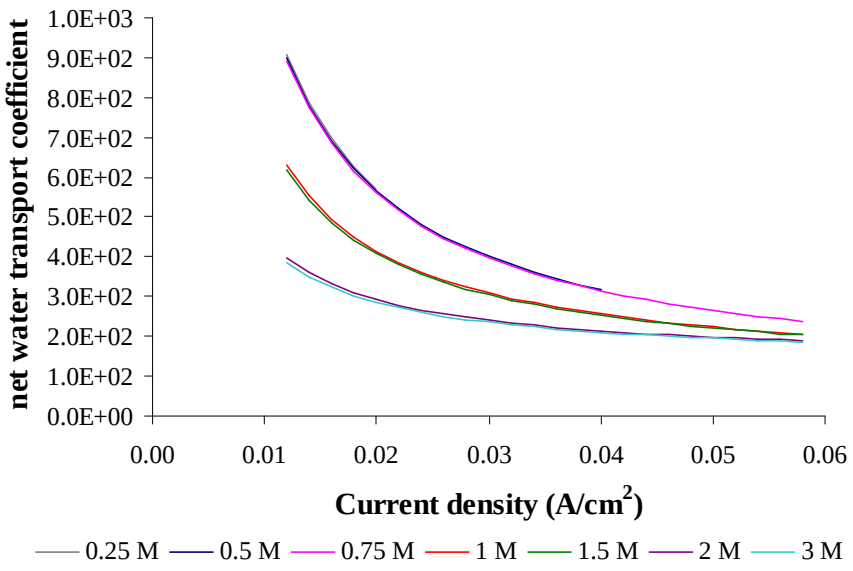

Figure 5.6 – Model prediction for net water transport coefficient for different methanol feed concentrations. Operating conditions: methanol flow rate 8 ml/min, air flow rate 3.6 l/min and fuel cell temperature 20ºC.

5.1.2.2. Effect of fuel cell temperature

The set of operating conditions used for the study of the effect of temperature on cell performance is presented in Table 5.3

Table 5.3 – Set of operating conditions used to analyse the effect of cell temperature on the cell performance.

C_{CH_3OH} (M)	q_{CH_3OH} (ml/min)	q_{air} (l/min)	Cell temperature (ºC)
0.75	8	3.6	20
			40
			60
			70
			80
0.75	3	3.6	20
			40
			60
			70
			80
0.75	3	1	20
			40
			60
			70
			80

The polarization and power density curves are plotted in Figures 5.7 a) and b) for a methanol feed concentration of 0.75M a methanol flow rate of 8 ml/min, an air flow rate of 3.6 l/min for different temperatures.

The maximum temperature used was 80ºC, since the operation of a DMFC with temperatures close to the boiling temperature of the methanol solution decreases the methanol concentration and consequently the fuel cell performance due to the formation of methanol vapour bubbles obstructing the fuel pathway.

As can be seen from the plots the fuel cell performance and power density increases with increasing temperature, due to an enhancement of the electrochemical kinetics on the anode and cathode side. The open circuit voltage also increases with temperature according to the Arrhenius relation due to a reduction in the activation overvoltage. According to equations (2.21) and (2.22) presented in section 2.3.3, an enhanced electrochemical kinetics of the methanol oxidation and oxygen reduction leads to a decrease of the anode and cathode overpotential, as can be confirmed by the model predictions in, respectively, Fig. 5.8 and Fig. 5.9. A decrease on the anode and cathode overpotential leads to an increase of the fuel cell performance and power.

However, increasing the fuel cell temperature can have negative impacts on the cell performance, due to an increase on the methanol crossover as put in evidence in Fig. 5.10. Higher temperatures generate, also, an increase on the water crossover as shown by the model predictions in Fig. 5.11. The additional water on the cathode side increases the liquid water fraction in both the cathode catalyst and diffusion layer, causing an increase in the concentration polarization. The membrane stability also decreases with an increase of fuel cell temperature and the oxygen partial pressure decreases with an increase of fuel cell temperature, due to an increase of water vapour partial pressure, which causes both decreases in open cell potential and increases the concentration overpotential.

The effect of temperature on fuel cell performance is the result of both positive effects on kinetics and the combined negative effects. According to Fig. 5.7 for the set of operating conditions studied, the positive effect on the kinetics is more significant that the referred negative effects of temperature. It should be mentioned that for other set of cooperating conditions the results may be different, since the negative effects of temperature could be dominant leading to a decrease of fuel cell performance with an increase on fuel cell temperature.

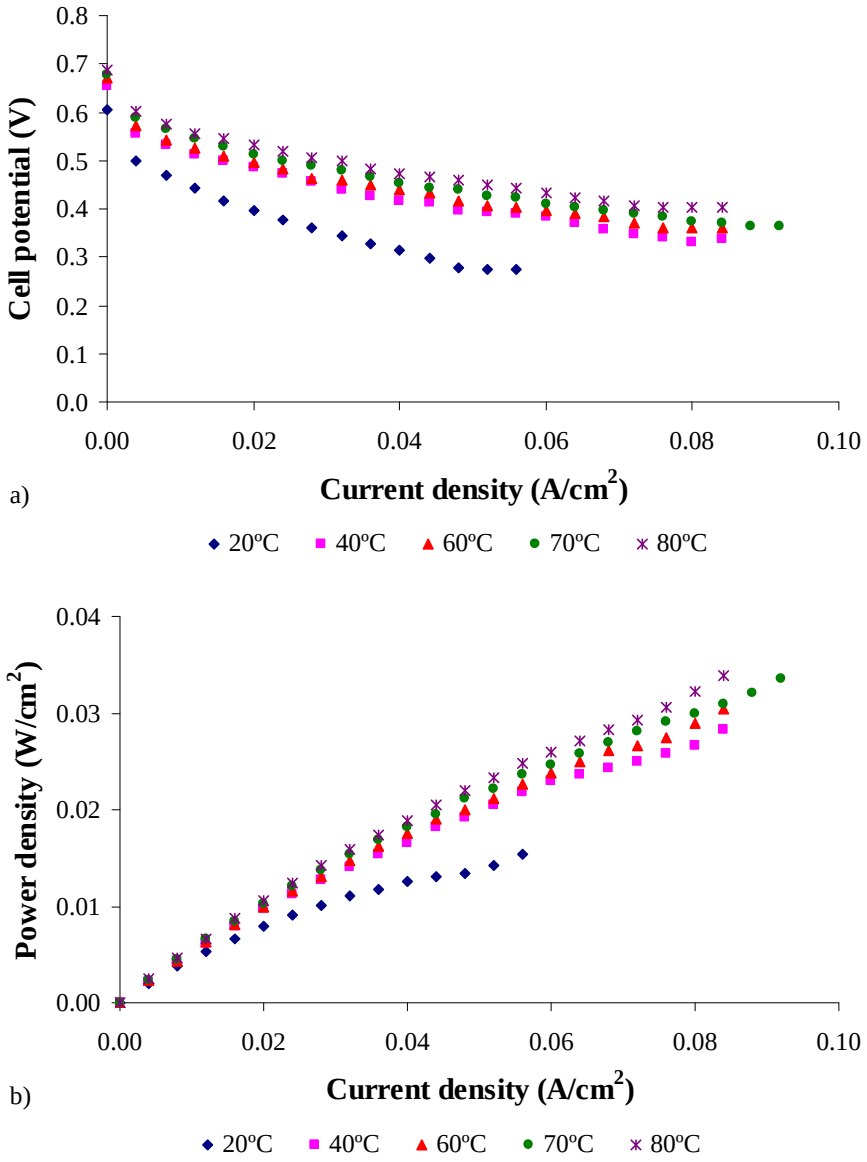

Figure 5.7 – Effect of fuel cell temperature on a) cell performance and b) power density. Operating conditions: methanol flow rate 8 ml/min, air flow rate 3.6 l/min and methanol concentration 0.75M.

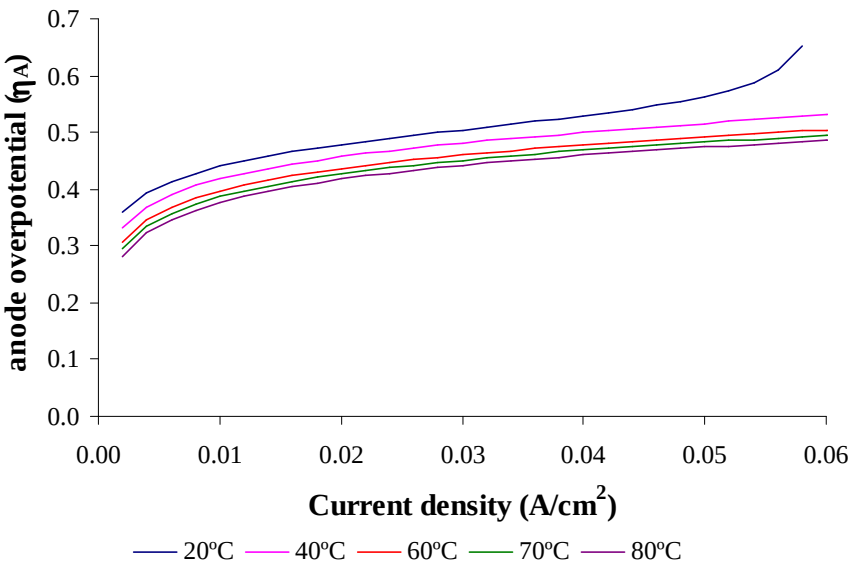

Figure 5.8 – Model predictions for the anode overpotential for different fuel cell temperatures. Operating conditions: methanol flow rate 8 ml/min, air flow rate 3.6 l/min and methanol concentration 0.75M.

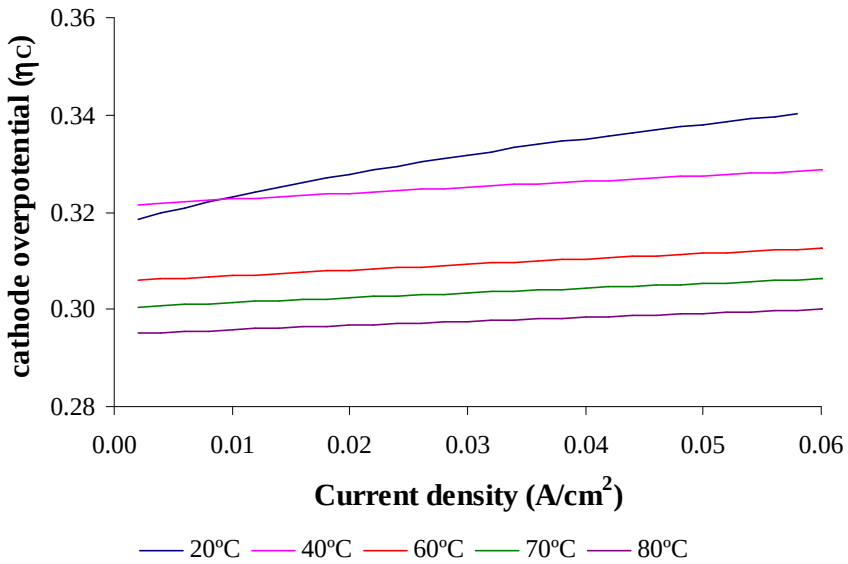

Figure 5.9 – Model predictions for the cathode overpotential for different fuel cell temperatures. Operating conditions: methanol flow rate 8 ml/min, air flow rate 3.6 l/min and methanol concentration 0.75M.

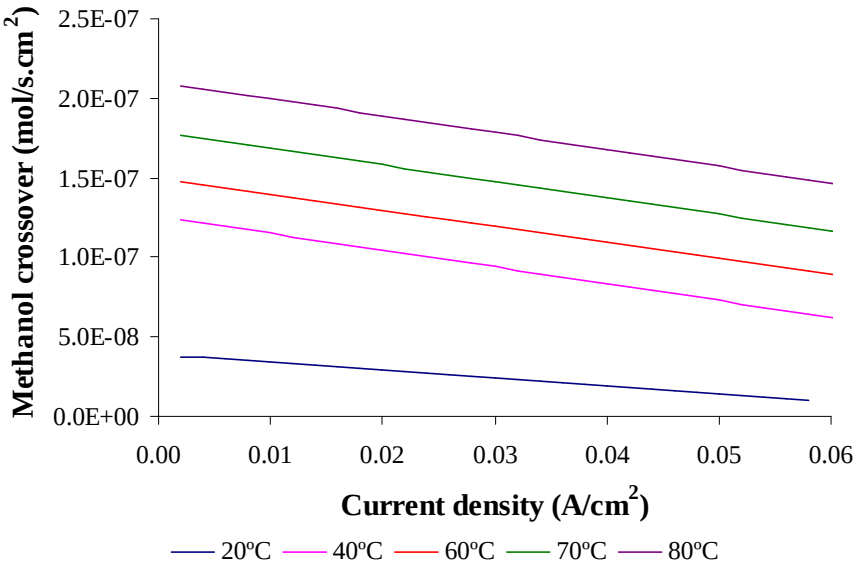

Figure 5.10 – Model predictions for the methanol crossover for different methanol feed concentrations. Operating conditions: methanol flow rate 8 ml/min, air flow rate 3.6 l/min and methanol concentration 0.75M.

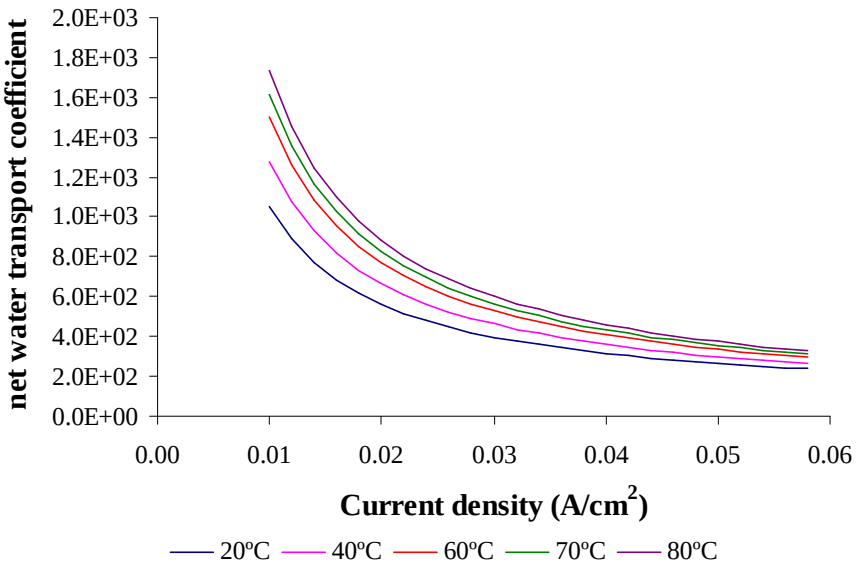

Figure 5.11 – Model predictions for net water transport coefficient for different fuel cell temperatures. Operating conditions: methanol flow rate 8 ml/min and air flow rate 3.6 l/min, methanol concentration 0.75M.

A comparison between the model predictions and the experimental results for two different fuel cell temperatures (20ºC and 60ºC) is presented in Fig. 5.12. As can be seen, the model predicts with great accuracy the effect of fuel cell temperature on the cell performance and power density.

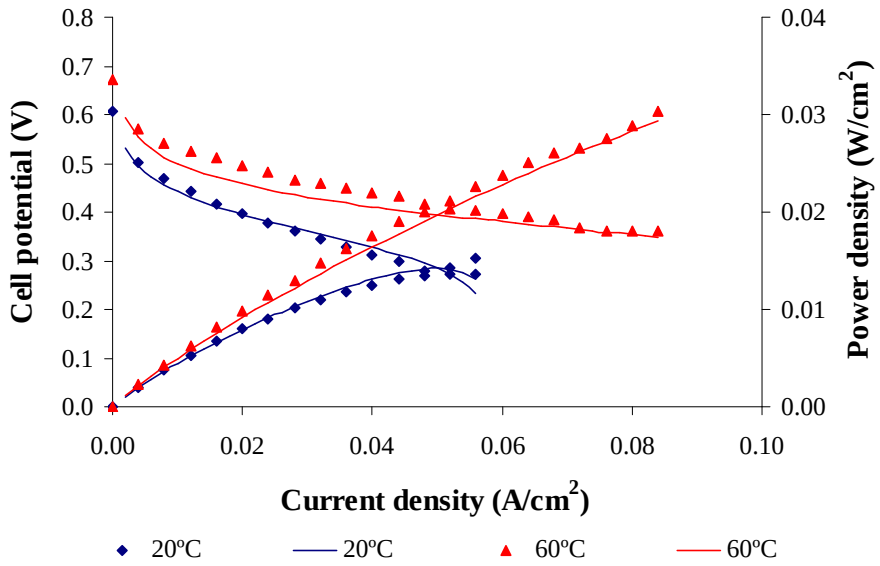

Figure 5.12 – Comparison of model predictions on cell performance and power density; dots: experimental data, lines: model predictions. Operating conditions: methanol concentration 0.75M, methanol flow rate 8 ml/min and air flow rate 3.6 l/min.

5.1.2.3. Effect of methanol flow rate

The operating conditions used in the experimental study of the effect of the methanol flow rate are presented in Table 5.4.

Table 5.4 – Set of operating conditions used to analyse the effect of methanol flow rate on the cell performance.

C_{CH_3OH} (M)	q_{CH_3OH} (ml/min)	q_{air} (l/min)	Cell temperature (ºC)
0.25	20	3.6	20
	16		
	14		
	12		
	10		
	8		
	3		
0.75	20	3.6	20
	16		
	14		
	12		
	10		
	8		
	3		
0.75	10	1	20
	8		
	3		

Figure 5.13 shows the results of a sub-set of experiments for different anode flow rates, using a methanol concentration of 0.75 M and an air flow rate of 3.6 l/min. As can be seen from the plots, the cell voltage and power slightly increase with the anode feed flow rate. For this set of operation conditions, higher methanol flow rates lead to a high methanol concentration along the flow channels and consequently high methanol concentration in the catalyst layer, facilitating the anode reactivity. Also, higher flow rates are more efficient in carbon dioxide bubbles removal at the anode side [180], leading the pathway free for the fuel and consequently more fuel reaches the anode catalyst layer.

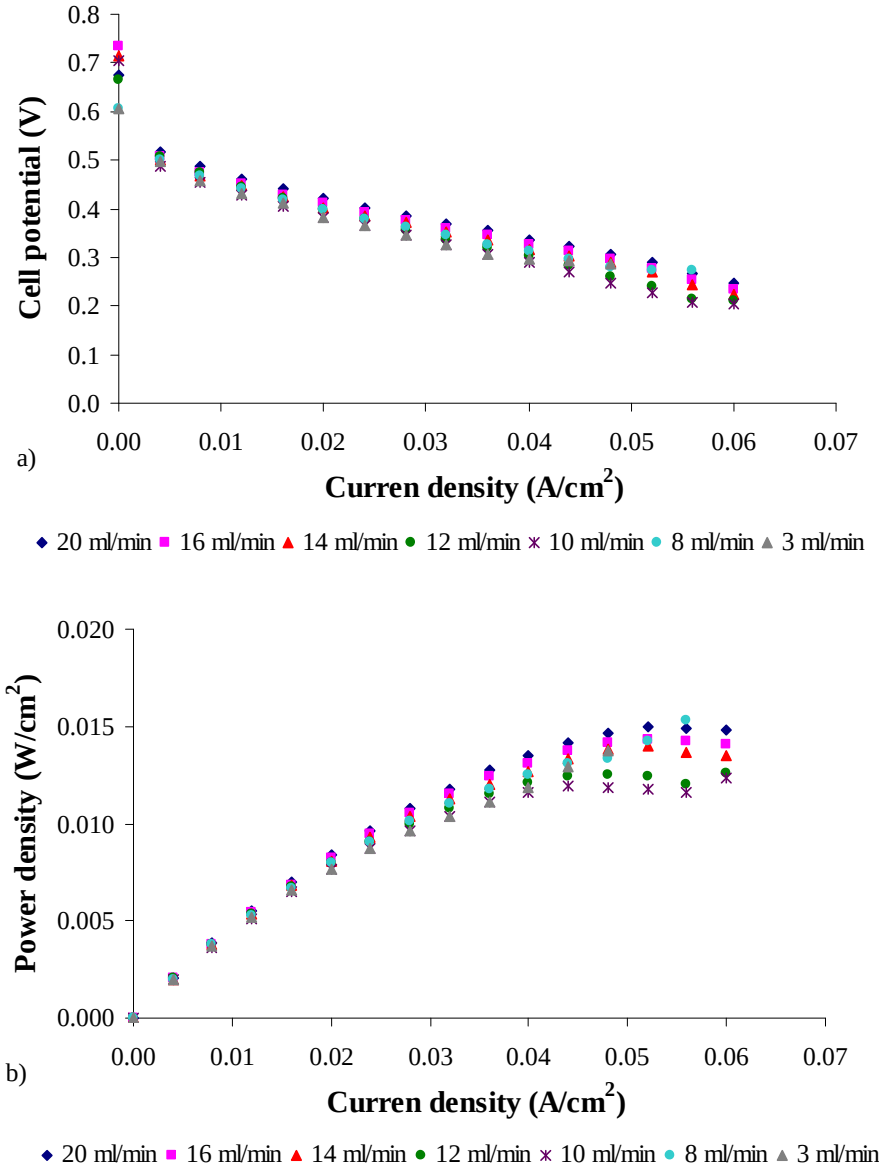

Figure 5.13 – Effect of methanol flow rate on a) cell performance and b) power density. Operating conditions: methanol concentration 0.75M, fuel cell temperature 20ºC and air flow rate 3.6 l/min.

The model predictions of the methanol concentration profiles in the anode catalyst layer are presented in Fig. 5.14 for the same set of experiments (corresponding to a current density of 0.03 A/cm^2). The curves represented in the figure show that higher methanol flow rates lead to a high methanol concentration in the catalyst layer. These predicted methanol concentration profiles explain the relative position of the curves represented in Fig. 5.13.

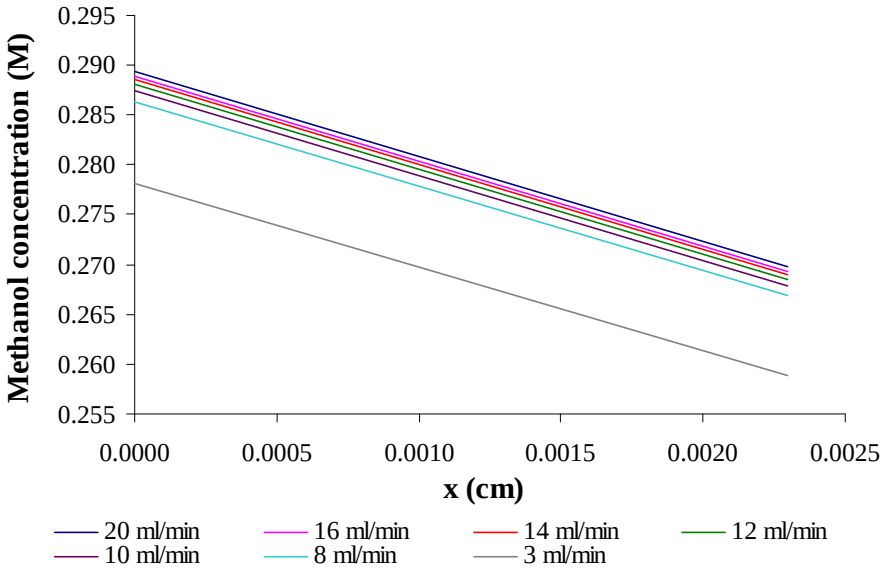

Figure 5.14 – Predicted methanol concentration profiles in the anode catalyst layer (thickness 0.0023 cm) for different methanol flow rates. Operating conditions: methanol concentration 0.75M, air flow rate 3.6 l/min and a current density of 0.03 A/cm^2.

Model predictions of the methanol crossover for the different values of methanol flow rate are presented in Fig. 5.15 as a function of current density. As can be seen, higher methanol flow rates result in higher values of methanol concentration on the cathode catalyst layer and slightly higher methanol crossover rates. However, for the range of flow rates studies, the impact on the methanol crossover is not significant.

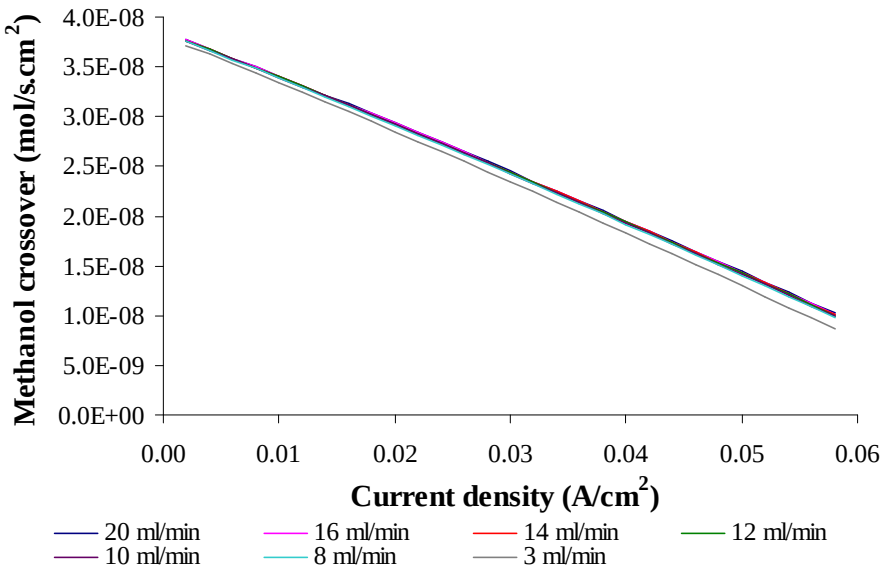

Figure 5.15 – Model predictions for the methanol crossover for different methanol flow rates. Operating conditions: air flow rate 3.6 l/min, methanol concentration 0.75M and fuel cell temperature 20°C.

Model predictions of the effect of methanol flow rate on the net water transport coefficient (α value) are presented in Fig. 5.16 as a function of current density. It is evident from the plots that the methanol flow rate seems to have almost no effect on the net water transport coefficient. As the methanol feed concentration (0.75M) is always the same for all the tests, the amount of water at the anode, largely in excess, does not change significantly, leading to similar values of α.

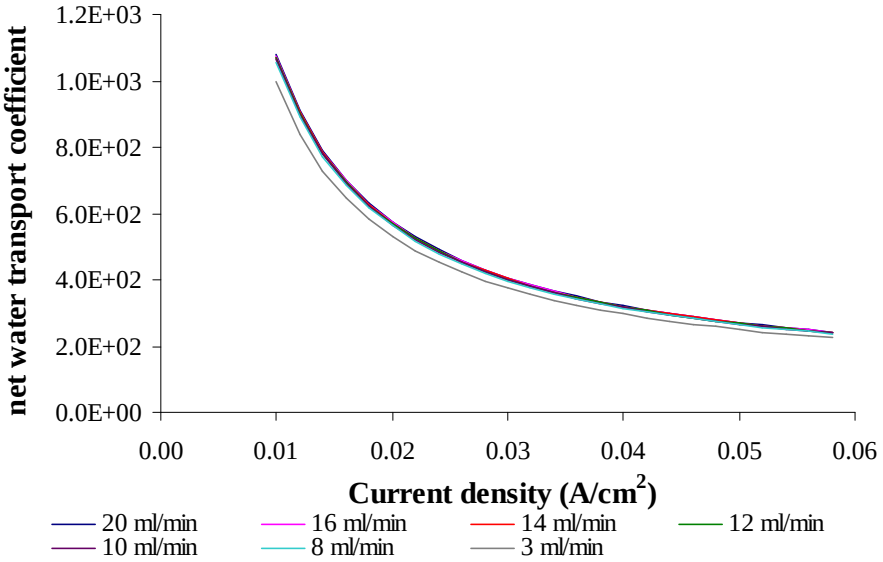

Figure 5.16 – Model predictions for net water transport coefficient for different methanol flow rates. Operating conditions: air flow rate 3.6 l/min, methanol concentration 0.75M and fuel cell temperature 20ºC.

Model predictions and experimental results, for two values of methanol flow rate (20 ml/min and 8 ml/min) are presented in Fig. 5.17. The model predicts the correct trends of the effect of the methanol flow rate on fuel cell performance and power.

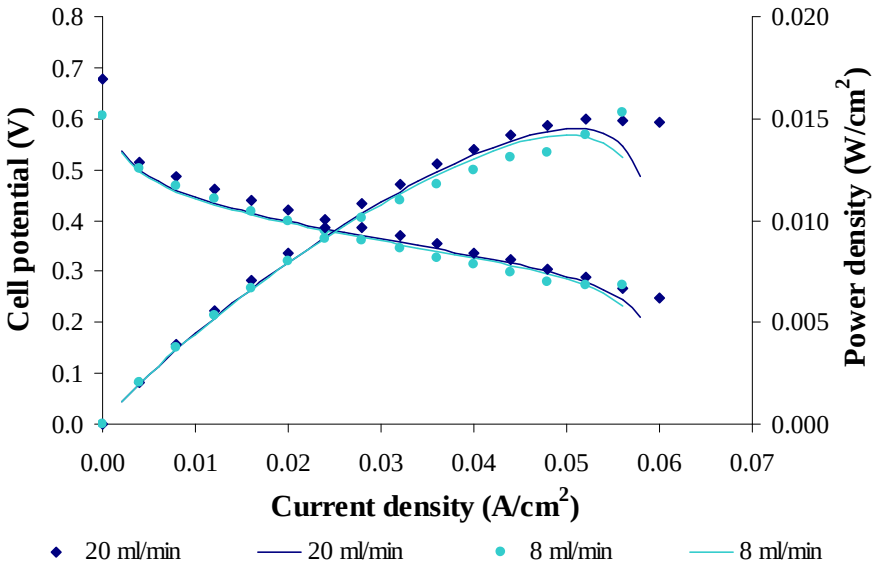

Figure 5.17 – Comparison of model predictions on cell performance and power density; dots: experimental data, lines: model predictions. Operating conditions: methanol concentration 0.75M, fuel cell temperature 20ºC and air flow rate 3.6 l/min.

5.1.2.4. Effect of air flow rate

The operating conditions used in the experimental study to evaluate the effect of the air flow rate on fuel cell performance presented are in Table 5.5.

Table 5.5 – Set of operating conditions used to analyse the effect of air flow rate on the cell performance.

C_{CH_3OH} (M)	q_{CH_3OH} (ml/min)	q_{air} (l/min)	Cell temperature (ºC)
0.25	8	3.6	20
		2	
		1	
		0.75	
		0.5	
0.75	8	3.6	20
		2	
		1.5	
		1	
0.75	3	3.6	20
		2	
		1	
		0.75	
		0.5	

The plots in Fig. 5.18 show the effect of the air flow rate on the cell performance and power density. The experiments correspond to a methanol concentration of 0.75 M and a methanol flow rate of 8 ml/min. For the set of air flow rates studied, it seems that the cell performance and cell power slightly increase with an increase of the air flow rate. When the cell is operating under lower air flow rate the oxygen concentration decreases along the cathode flow channels resulting in lower cell voltage and power. Higher air flow rates also lead to a more efficient water droplets removal on the cathode side and consequently a higher oxygen concentration on the cathode catalyst layer. When large amounts of droplets are presented on the cathode side, they may obstruct the oxygen molecules to reach the catalyst layer, reducing the oxygen concentration and the fuel cell performance and power. When the air flow rate is high enough, any further increase will only slightly change the oxygen concentration profile, with a negligible effect on the cell performance.

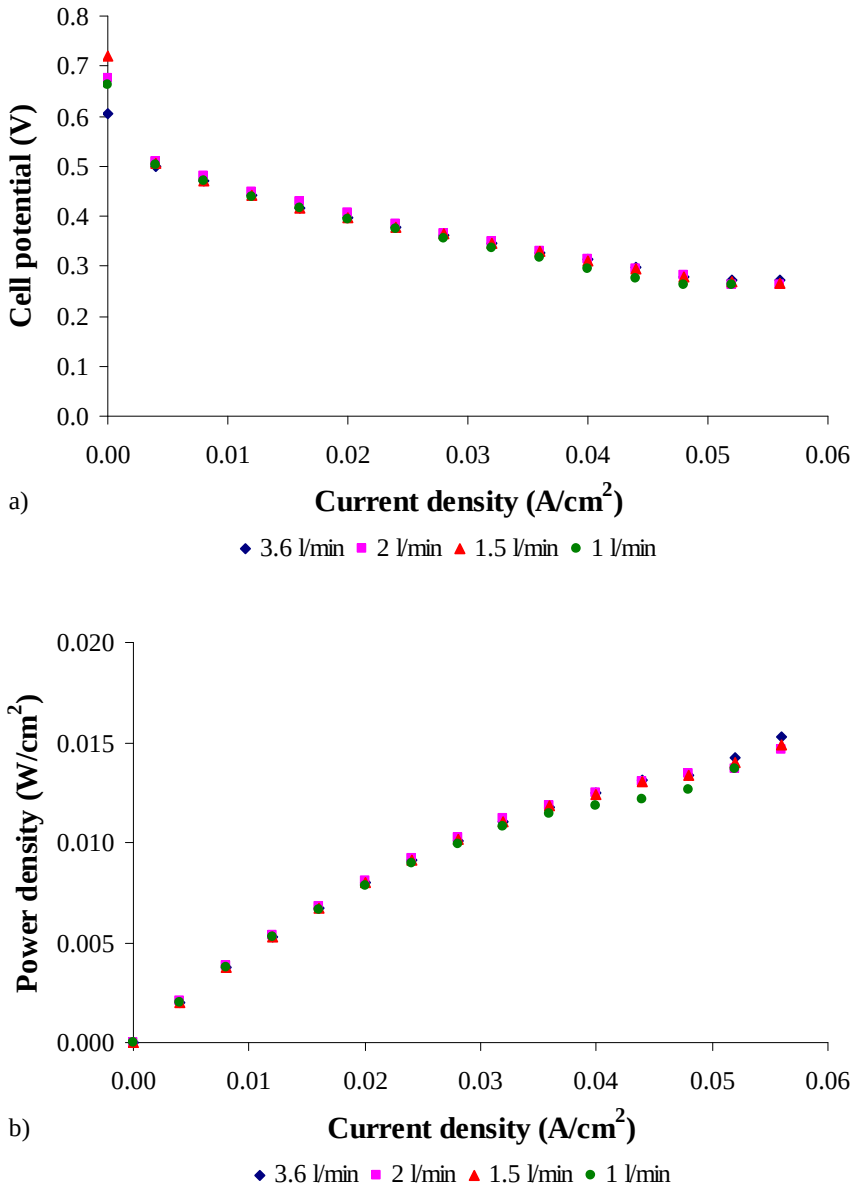

Figure 5.18 – Effect of air flow rate on a) cell performance and b) power density. Operating conditions: methanol concentration 0.75M, fuel cell temperature 20°C, methanol flow rate 8 ml/min.

The model predictions of the oxygen concentration profile in the cathode diffusion layer are presented in Fig. 5.19 for the same set experiments (corresponding to a current density of 0.03 A/cm^2). As can be seen, from the plotted curves, the higher air flow rates lead to a slightly higher oxygen concentration in the catalyst layer, leading to slightly better performance.

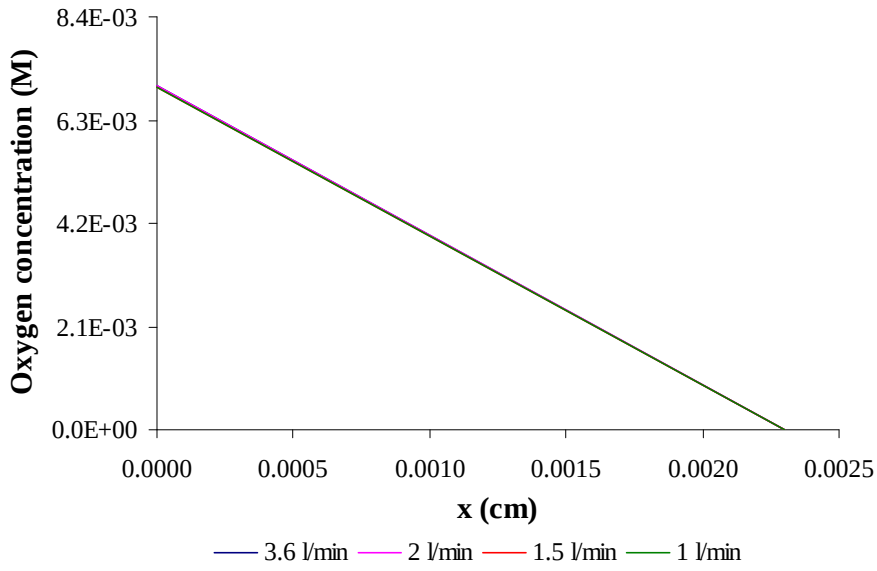

Figure 5.19 – Predicted oxygen concentration profile in the cathode catalyst layer (thickness 0.0023 cm) for different air flow rates. Operating conditions: methanol concentration 0.75M, methanol flow rate 8 ml/min a current density of 0.03 A/cm^2.

Model predictions of the effect of air flow rate on the net water transport coefficient (α value) are presented in Fig. 5.20 as a function of current density. An increase of the air flow rate leads to an increase of the values of the net water transport coefficient. Higher air flow rates remove higher quantities of water produced at the cathode decreasing the water concentration and contributing to an increase of the water gradient across the membrane. In this way, due to the water diffusion mechanism, more water is transported form the anode to the cathode side.

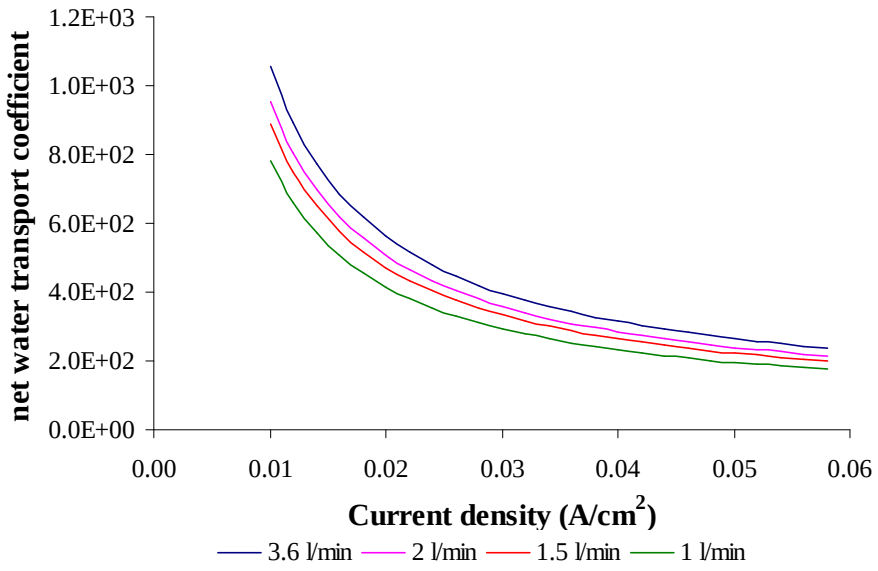

Figure 5.20 – Model prediction for net water transport coefficient for different air flow rates. Operating conditions: methanol flow rate 8 ml/min, methanol concentration 0.75M and fuel cell temperature 20ºC.

Model predictions and experimental results, for two values of air flow rate (3.6 l/min and 1 l/min) are presented in Fig. 5.21, showing that the model predicts the correct trends of the effect of the air flow rate on fuel cell performance and power.

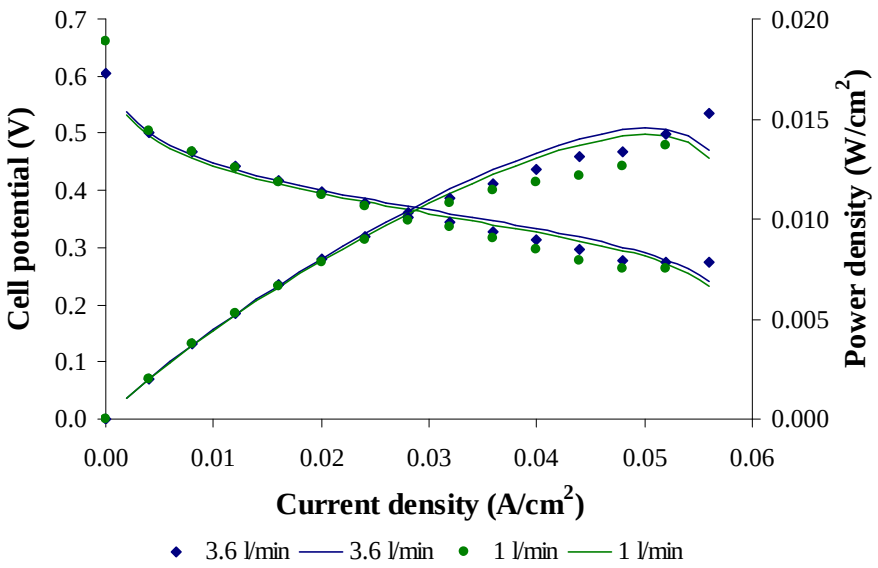

Figure 5.21 – Comparison of model predictions on cell performance and power density; dots: experimental data, lines: model predictions. Operating conditions: methanol concentration 0.75M, fuel cell temperature 20ºC and methanol flow rate 8 ml/min.

5.1.3. Effect of design parameters

A systematic study to elucidate the effect of design parameters such as diffusion layer material and thickness, catalyst loading, membrane thickness and anode and cathode flow field design on the performance of a DMFC, is presented. The set of operating conditions used is summarized in Table 5.6.

Table 5.6 – Set of operating conditions used to analyse the effect of design parameters on the cell performance.

C_{CH_3OH} (M)	q_{CH_3OH} (ml/min)	q_{air} (l/min)	Cell temperature (ºC)
0.75	20	3.6	20
	8	3.6	
	8	1	
	3	3.6	
	8	3.6	60
	3	3.6	
	3	1	
2	8	3.6	20
	3	3.6	
	3	1	
5	3	3.6	20

5.1.3.1. Effect of anode diffusion layer material

The set of conditions displayed on Table 5.6 was used in the experiments performed to study the impact of the anode diffusion layer on the cell performance. As in the previous sections a sub-set of tests was selected.

Several material and design parameters of the anode diffusion layer affect the fuel cell performance: i) layer thickness; ii) the tortuosity, which influences the species transport and iii) the surface properties, the wettability and roughness, controlling the droplet/bubble attachment or coverage on the diffusion layer surface. Differences in porosity, permeability, pore size distribution, surface wettability and liquid retention of the two diffusion media result in different two-phase flow and transport characteristics.

As already referred, the two types of gas diffusion layers commonly used as anode diffusion layer in DMFCs are carbon cloth and carbon paper. Carbon paper has a microscopically complex fibrous structure with pore size distribution ranging from a few microns to tens of microns with a large fraction of blocked passages. Carbon cloth, in other hand, is a woven structure and is generally coarser than carbon paper. Carbon cloth is more porous and less tortuous than carbon paper [177, 178].

Some structural properties of the diffusion layers materials used are presented in Table 5.7. As can be seen carbon cloth is more porous, less tortuous and thicker than carbon paper [177, 178]. The ELAT material formed of carbon cloth type A treated on one side is less porous, thicker and more tortuous that carbon cloth.

Table 5.7 – Structural characteristics of the common materials used as gas diffusion layers [177, 178].

Material	Porosity	Tortuosity	Thickness (cm)
Carbon cloth (type A)	0.83	1.11	0.035
Carbon paper (TGPH060)	0.78	2.75	0.019
Single-side ELAT	0.80	1.5	0.040

The flow fields used was the serpentine design in both sides of the fuel cell. The membrane used was Nafion 117 and Nafion 212 (DuPont) the catalyst was Pt/Ru on the anode side with a loading of 4 mg/cm^2 and Pt on the cathode side with a loading of 4 mg/cm^2. The anode gas diffusion layers used were carbon cloth type A (CC) from E-TEK or carbon paper TGPH060 (CP) from Toray both with a PTFE content of 30 wt.%.

The influence of the anode gas diffusion layer material on the cell performance for three different methanol flow rates (20 ml/min, 8 ml/min and 3 ml/min) is shown in Fig. 5.22. The methanol feed concentration used was 0.75M, the air flow rate 3.6 l/min and the fuel cell temperature 20ºC.

On the anode side, gaseous carbon dioxide is produced by the anode reaction and must be removed from the diffusion layer by the anode flow. If the carbon dioxide bubbles cannot be removed from the catalyst surface they cover the surface decreasing therefore the effective mass transfer area.

As can be seen from Fig. 5.22, for the set of conditions studied the cell performance and power curves are enhanced using the carbon cloth as the anode diffusion layer. Since

carbon cloth has a pore structure with a low tortuosity and a rough textural surface, bubbles tend to detach from the surface maintaining the area for reactant diffusion relatively free from bubbles [33, 34]. The texture of the carbon paper surface with a highly tortuous structure enhances the interactions between the bubbles and the solid. Hence the gas remains attached to the surface leading to a blockage of the flow channels and lowering the methanol concentration at the catalyst layer (see Fig. 5.23).

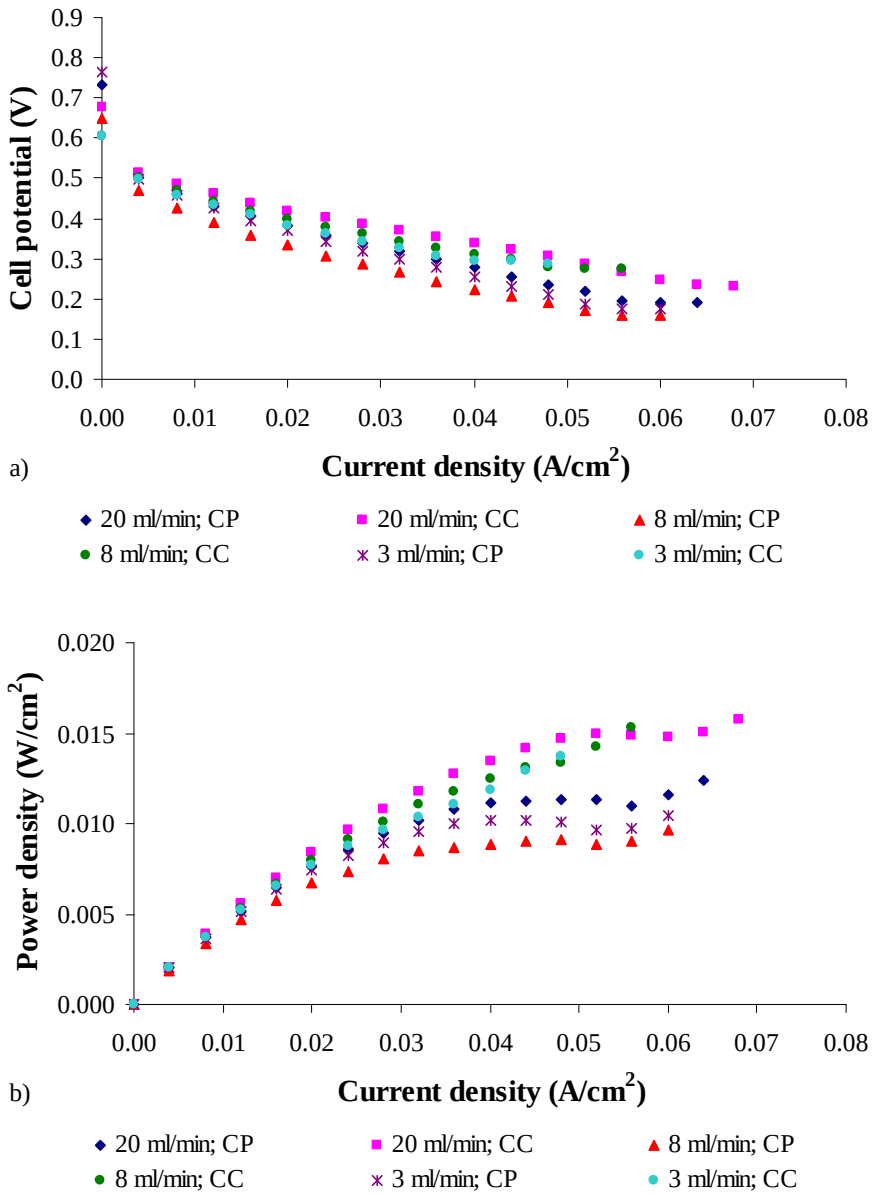

Figure 5.22 – Effect of anode diffusion layer material on a) cell performance and b) power density. Operating conditions: methanol concentration 0.75M, air flow rate 3.6 l/min and fuel cell temperature 20ºC. Design parameters: Nafion 117 and ELAT (E-TEK) at the cathode gas diffusion layer.

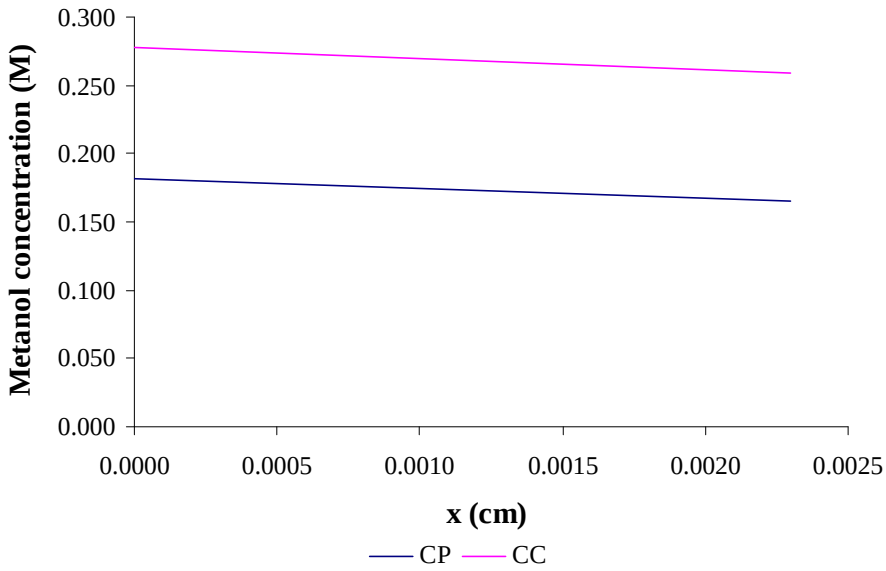

Figure 5.23 – Predicted methanol concentration profile in the anode catalyst layer (thickness 0.0023 cm) for different anode gas diffusion layer materials. Operating conditions: methanol concentration 0.75M, methanol flow rate 3 ml/min, air flow rate 3.6 l/min and fuel cell temperature 20ºC. Design parameters: Nafion 117 and ELAT (E-TEK) at the cathode gas diffusion layer.

The influence of the anode gas diffusion layer material on the cell performance for two different methanol concentrations (0.75M and 5M) is shown in Fig. 5.24. Model predictions and experimental results are, also, presented. The methanol flow rate used was 3 ml/min, the air flow rate 3.6 l/min and the fuel cell temperature 20ºC. As can be seen by the plots the model predicts the correct trends of the effect of the anode gas diffusion layer material on fuel cell performance and power density for the different methanol concentration levels.

As can be seen from Fig. 5.24, for high methanol concentrations (5M), the cell performance is enhanced using the carbon paper as the anode diffusion layer. When a DMFC is operated with high methanol concentrations large amounts of methanol crossover are generated. Since the carbon paper is less porous than carbon cloth, it limits the amount of methanol that reaching the catalyst layer and consequently the methanol that crosses the membrane. The use of carbon paper will probably induce less significant levels of methanol crossover. This effect is shown in Fig. 5.25 confirming that the methanol crossover rate through the membrane is lower when carbon paper is used as anode diffusion layer material. Lower methanol crossover rates lead to higher fuel cell performances. The carbon paper GDL also exhibits a lower thickness (table 5.7) which, as already mentioned, corresponds to a lower mass transfer resistance. As

both materials have the same PTFE content the wettability is probably similar and therefore does not explain the differences in cell performance.

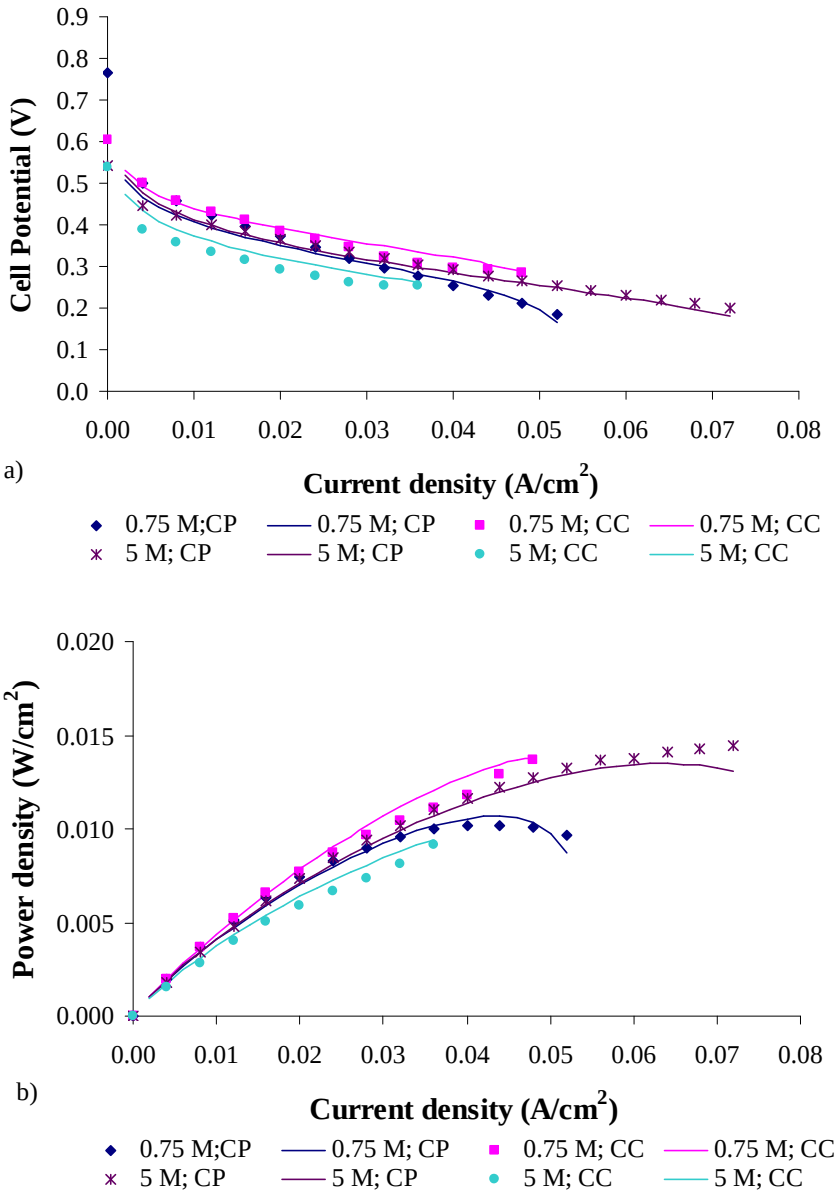

Figure 5.24 – Comparison of model predictions on a) cell performance and b) power density; dots: experimental data, lines: model predictions. Operating conditions: methanol concentration 0.75M and 5M, methanol flow rate 3 ml/min and air flow rate 3.6 l/min. Design parameters: Nafion 117 and ELAT (E-TEK) at the cathode gas diffusion layer.

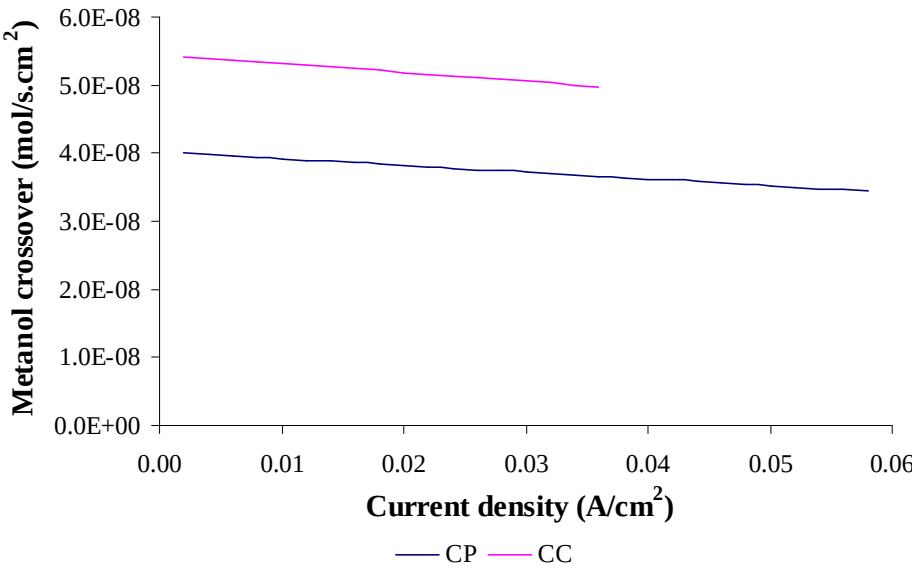

Figure 5.25 – Model predictions for the methanol crossover for different anode gas diffusion layer materials. Operating conditions: methanol concentration 5M, methanol flow rate 3 ml/min, air flow rate 3.6 l/min and fuel cell temperature 20ºC. Design parameters: Nafion 117 and ELAT (E-TEK) at the cathode gas diffusion layer.

Model predictions of the effect of the anode gas diffusion layer material on the net water transport coefficient are shown in Fig. 5.26. The plots of the figure show that for a given value of the current density, lower values of α are obtained for the thinner GDL material (carbon paper). These results show that there is a tendency to an enhancement of the transport toward the anode for low thicknesses of the GDL.

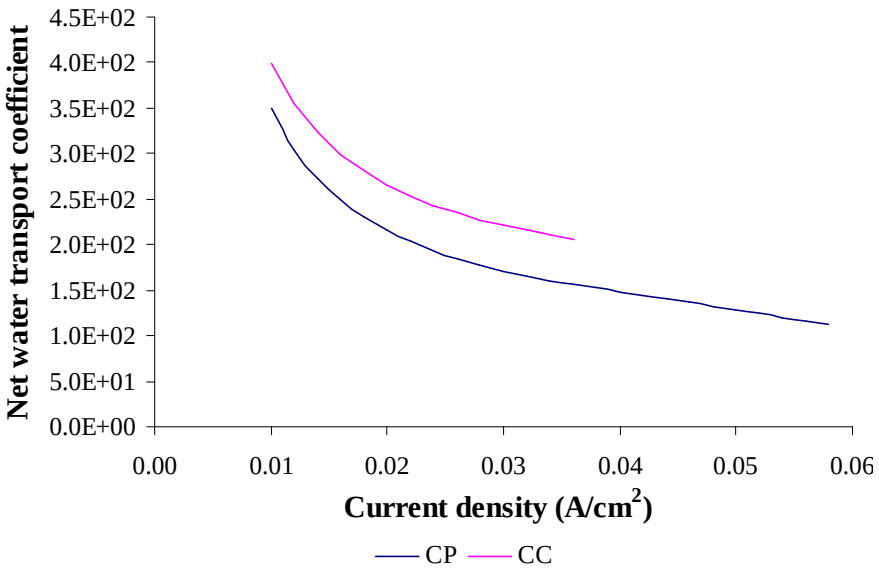

Figure 5.26 – Model predictions for net water transport coefficient for different anode gas diffusion layer materials. Operating conditions: methanol concentration 5M, methanol flow rate 3 ml/min, air flow rate 3.6 l/min and fuel cell temperature 20ºC. Design parameters: Nafion 117 and ELAT (E-TEK) at the cathode gas diffusion layer.

The effect of anode gas diffusion layer material on cell performance and power density for two different fuel cell temperatures (20ºC and 60ºC) are provided in Fig. 5.27. The methanol concentration used was 0.75M, the methanol flow rate 8 ml/min and the air flow rate 3.6 l/min. As can be seen by the plots, for this methanol concentration, a better performance is achieved using carbon cloth as anode gas diffusion layer both for low and high fuel cell temperatures.

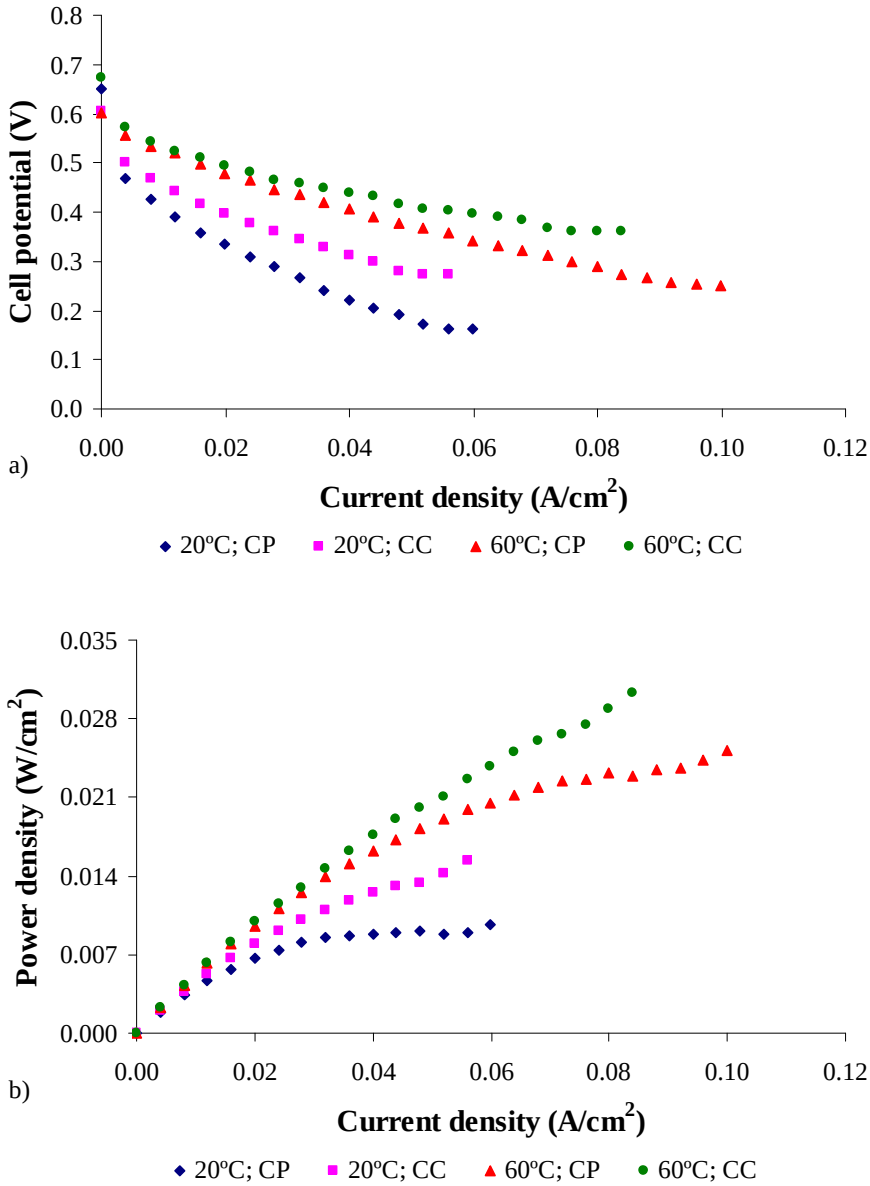

Figure 5.27 – Effect of anode diffusion layer material on a) cell performance and b) power density. Operating conditions: methanol concentration 0.75M, methanol flow rate 8 ml/min and air flow rate 3.6 l/min. Design parameters: Nafion 117 and ELAT (E-TEK) at the cathode gas diffusion layer.

5.1.3.2. Effect of cathode diffusion layer material

The set of conditions displayed on Table 5.6 was used in the experiments performed to study the impact of the cathode diffusion layer on the cell performance. As in the previous sections a sub-set of tests was selected.

The materials selected to study the effect of the cathode diffusion layer on the cell performance were ELAT carbon cloth (ELAT) from E-TEK, carbon paper TGPH060 (CP) from Toray or carbon cloth type A (CC) from E-TEK all with a PTFE content of 30 wt.%. In all tests, carbon cloth type A was used as anode diffusion layer. The structural properties of the diffusion layers materials used are presented in Table 5.7.

The flow field used was the serpentine design in both sides of the fuel cell. The membrane used was Nafion 117 and Nafion 212 (DuPont) the catalyst was Pt/Ru on the anode side with a loading of 4 mg/cm^2 and Pt on the cathode side with a loading of 4 mg/cm^2.

Figures 5.28 a) and b) show, respectively, the cell polarization and power density curves for two different air flow rates (3.6 l/min and 1 l/min), a methanol feed concentration of 0.75M, a methanol flow rate of 8 ml/min a the fuel cell temperature of 20ºC. It seems clear that the carbon cloth material shows the best performance. It should be noted that the variation in performance with different gas diffusion media at the cathode results from the cell internal resistance and the ability of facilitate the oxygen transport. The carbon cloth electrode has an increased capacity to remove the liquid water, as reported by Liu *et al.* [90] probably due to a boarder distribution of pore sizes contributing therefore to avoid severe flooding at the cathode catalyst layer. Decreasing the water coverage on the cathode diffusion layer surface will benefit the oxygen access to the catalyst site. Also when compared to carbon paper, the carbon cloth with its low tortuosity imposes a lower transport resistance with higher oxygen concentration. When compared to carbon cloth, the ELAT diffusion layer has a slightly lower performance probably due to a higher tortuosity. Due to the importance of oxygen polarization under high current densities, the differences in performance and power for the curves are higher at these conditions.

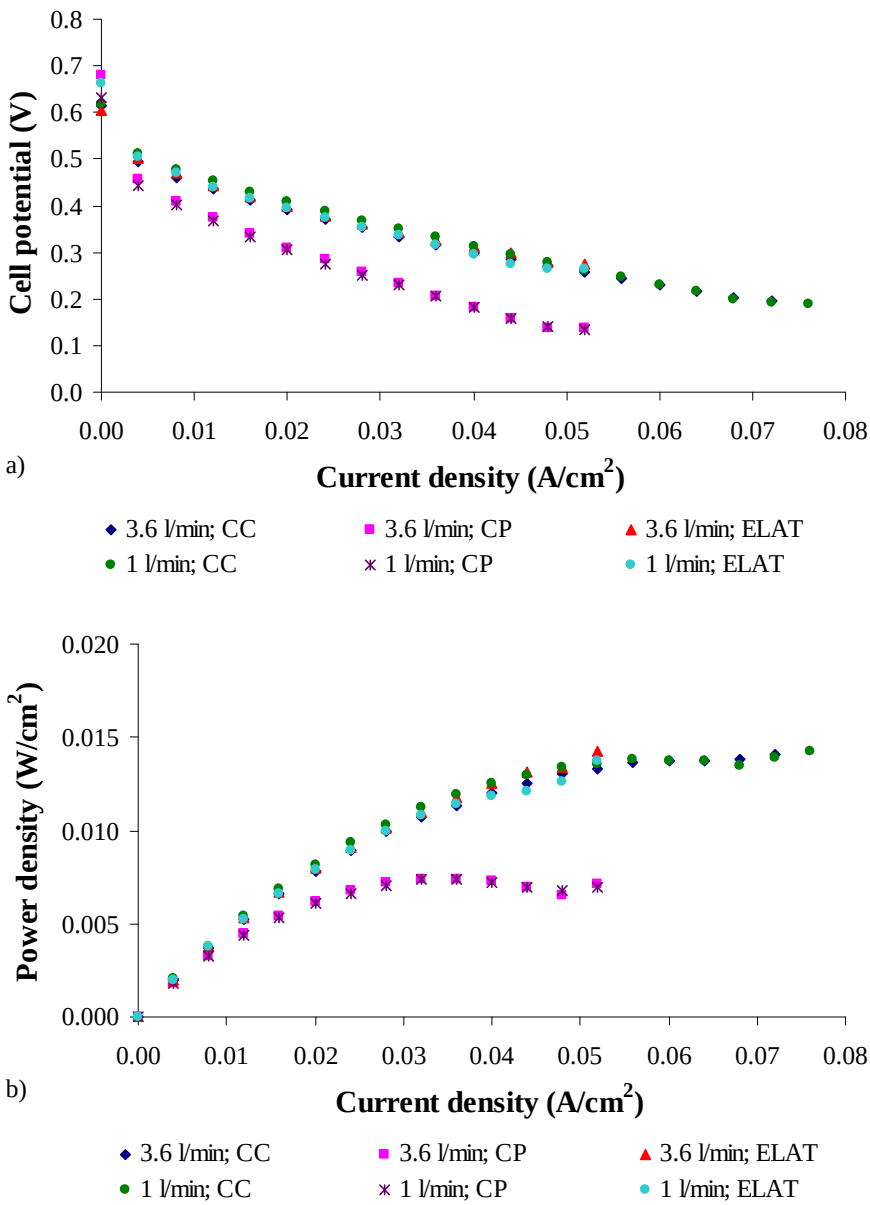

Figure 5.28 – Effect of cathode diffusion layer material on a) cell performance and b) power density. Operating conditions: methanol concentration 0.75M, methanol flow rate 8 ml/min and cell temperature 20ºC. Design parameters: Nafion117 and carbon cloth as anode gas diffusion layer.

The influence of the cathode gas diffusion layer material on the cell performance for two different methanol concentrations (0.75M and 5M) is shown in Fig. 5.29. Model predictions and experimental results are, also, presented. The methanol flow rate used was 3 ml/min, the air flow rate 3.6 l/min and the fuel cell temperature 20ºC. As can be seen by the plots the model predicts the correct trends of the effect of the cathode gas diffusion layer material on fuel cell performance and power density. The more significant discrepancies occur for high current densities and when carbon paper is used, corresponding to conditions where two-phase flow effects are more important.

The plots confirm that the cell performance is enhanced using the carbon cloth as cathode diffusion layer, at higher methanol concentrations. Under these conditions the increased capacity of carbon cloth for water removal is even more important to facilitate the oxygen access to the active catalyst sites. This leads to a higher oxygen concentration on the cathode catalyst layer and consequently higher fuel cell performances, as can be seen in Fig. 5.30, where model predictions for the oxygen concentration profile at the cathode catalyst layer are plotted, for a methanol feed concentration of 5M and a current density of 0.03 A/cm^2.

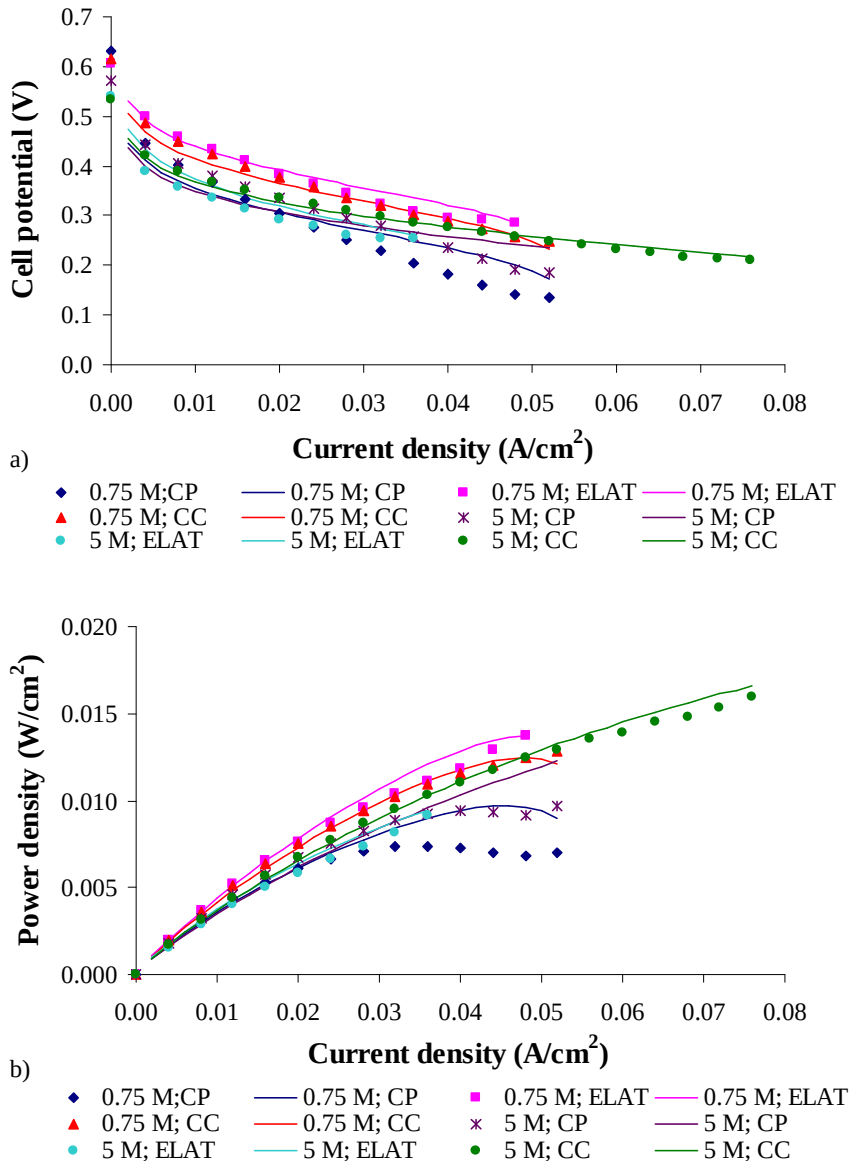

Figure 5.29 – Comparison of model predictions on a) cell performance and b) power density; dots: experimental data, lines: model predictions. Operating conditions: methanol concentration 0.75M and 5M, methanol flow rate 3 ml/min and air flow rate 3.6 l/min. Design parameters: Nafion 117 and carbon cloth as anode gas diffusion layer.

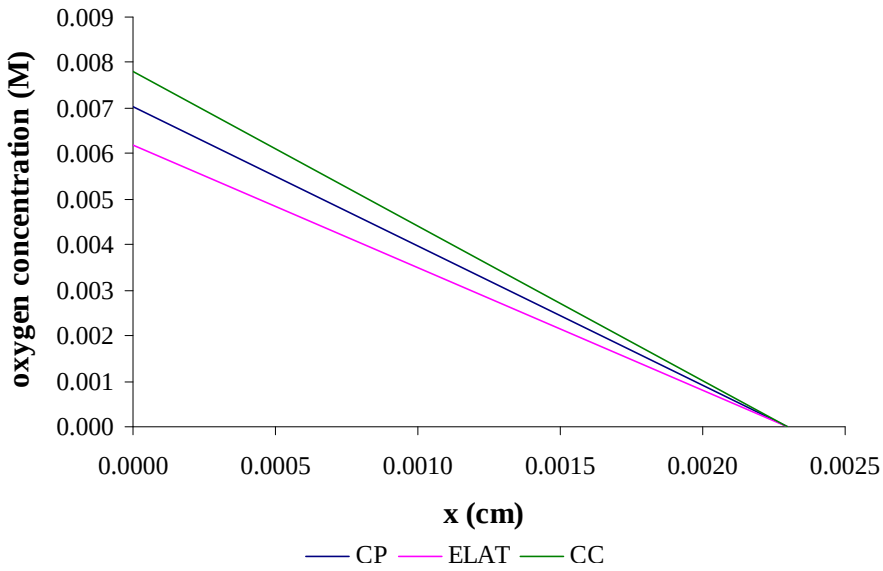

Figure 5.30 – Predicted oxygen concentration profile in the cathode catalyst layer (thickness 0.0023 cm) for different cathode gas diffusion layer materials. Operating conditions: methanol concentration 5M, methanol flow rate 3 ml/min, air flow rate 3.6 l/min and fuel cell temperature 20ºC. Design parameters: Nafion 117 and carbon cloth as anode gas diffusion layer.

The model predictions of the net water transport coefficient (α) are presented in Fig. 5.31 for the three cathode gas diffusion layer materials tested (carbon cloth, ELAT and carbon paper) and contribute to better explain the results shown in the previous Figures. For the conditions studied, the net water transport coefficient is toward the cathode (since all α values are positive) which means that a large amount of water is present at the anode side. The net water transport coefficient is higher when the cell is operating using carbon cloth as cathode gas diffusion layer which means that the water concentration on this side is smaller and the gradient between the anode and cathode side higher. In this situation more water is transported from the anode to the cathode side. These results are in accordance with experiments, since, as already mentioned, the carbon cloth remove efficiently the water from the cathode side, decreasing the water concentration at this side.

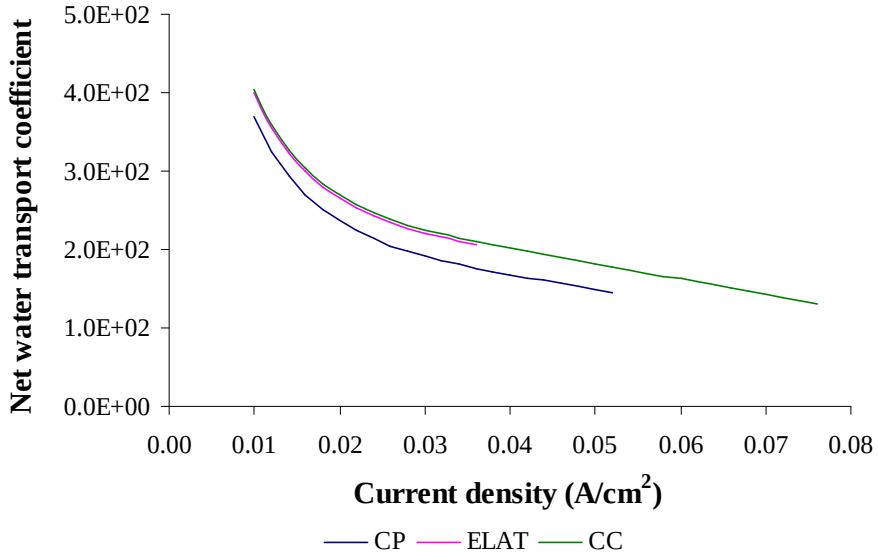

Figure 5.31 – Model predictions for net water transport coefficient for different cathode gas diffusion layer materials. Operating conditions: methanol concentration 5M, methanol flow rate 3 ml/min, air flow rate 3.6 l/min and fuel cell temperature 20ºC. Design parameters: Nafion 117 and carbon cloth as anode gas diffusion layer.

The effect of cathode gas diffusion layer material on cell performance and power density for two different fuel cell temperatures (20ºC and 60ºC) are provided in Fig. 5.32, for a methanol concentration of 0.75M. As can be seen by the plots, for low fuel cell temperatures the worst performance is achieved using carbon paper as cathode gas diffusion layer due to its poorest ability to remove the water and the carbon dioxide from the cathode side. Regarding the higher fuel cell temperatures, the three materials used have similar performances as power densities curves. In these conditions, some water passes to the vapour phase, reducing the amount of liquid water, and it seems that the flooding may me avoid in some extend so the water removal problems are less important.

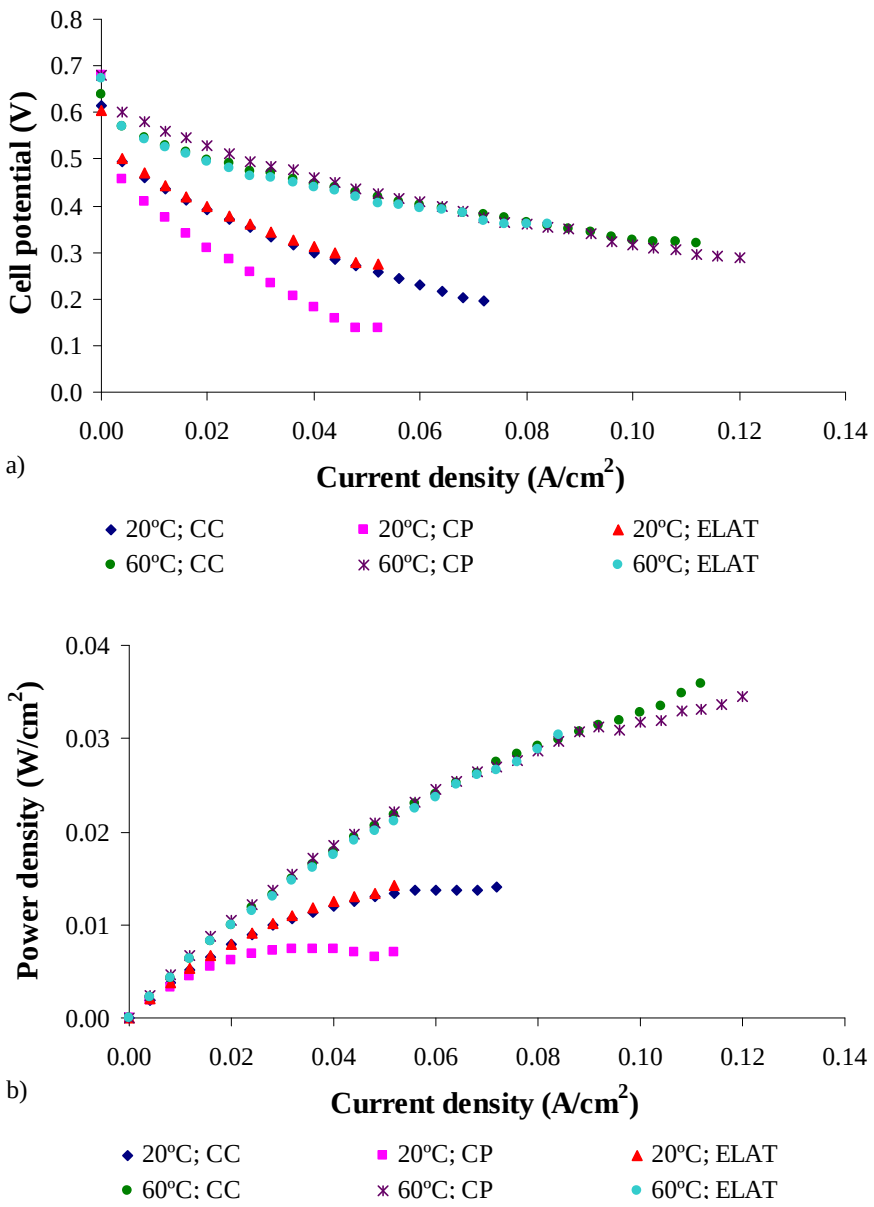

Figure 5.32 – Effect of cathode diffusion layer material on a) cell performance and b) power density. Operating conditions: methanol concentration 0.75M, methanol flow rate 8 ml/min and air flow rate 3.6 l/min. Design parameters: Nafion 117 and carbon cloth as anode gas diffusion layer.

5.1.3.3. Effect of membrane thickness

The set of operating conditions displayed on Table 5.6 was used in the experiments performed to study the impact of the membrane thickness on the cell performance.

In this section, results from experiments using three different Nafion membranes with different thicknesses (Nafion 117 0.0187 cm, Nafion 115 0.0153 cm and Nafion 212 0.0051 cm) are presented. In all cases, carbon cloth type A was used as both anode and

cathode diffusion layers. The flow field design and the catalyst load used were the same employed in the previous reported tests.

Figure 5.33 a) and b) shows, respectively, the cell polarization and power density curves for the three Nafion membranes and two different methanol flow rates (20 ml/min and 3 ml/min). The methanol feed concentration used was 0.75M, the air flow rate 3.6 l/min and the fuel cell temperature 20ºC. For the set of conditions studied the cell performance and power curves are enhanced using thicker Nafion membranes for very low and relative high current densities. It should be noted that methanol transport through the cell is enhanced or diminished by using different membrane thicknesses. Figure 5.34 shows the methanol crossover rate through the different membranes used. As expected, thicker membranes generate lower methanol crossover rates, which lead to an increase in the fuel cell performance. As can be seen in Fig. 5.33 the fuel cell performance is similar when Nafion 117 and Nafion 115 membranes are used. This is probably due to the fact that although the Nafion 115 generates a slightly higher methanol crossover it has a lower internal mass transfer resistance, due to its lower thickness. For intermediate current densities, the differences in cell performances are lower because within this operation range the higher methanol crossover through Nafion 212 membrane is compensated by a lower internal cell mass transfer resistance (lower thickness). The plots from Fig. 5.33 also show higher performances for higher methanol flow rates (recall section 5.1.2.3).

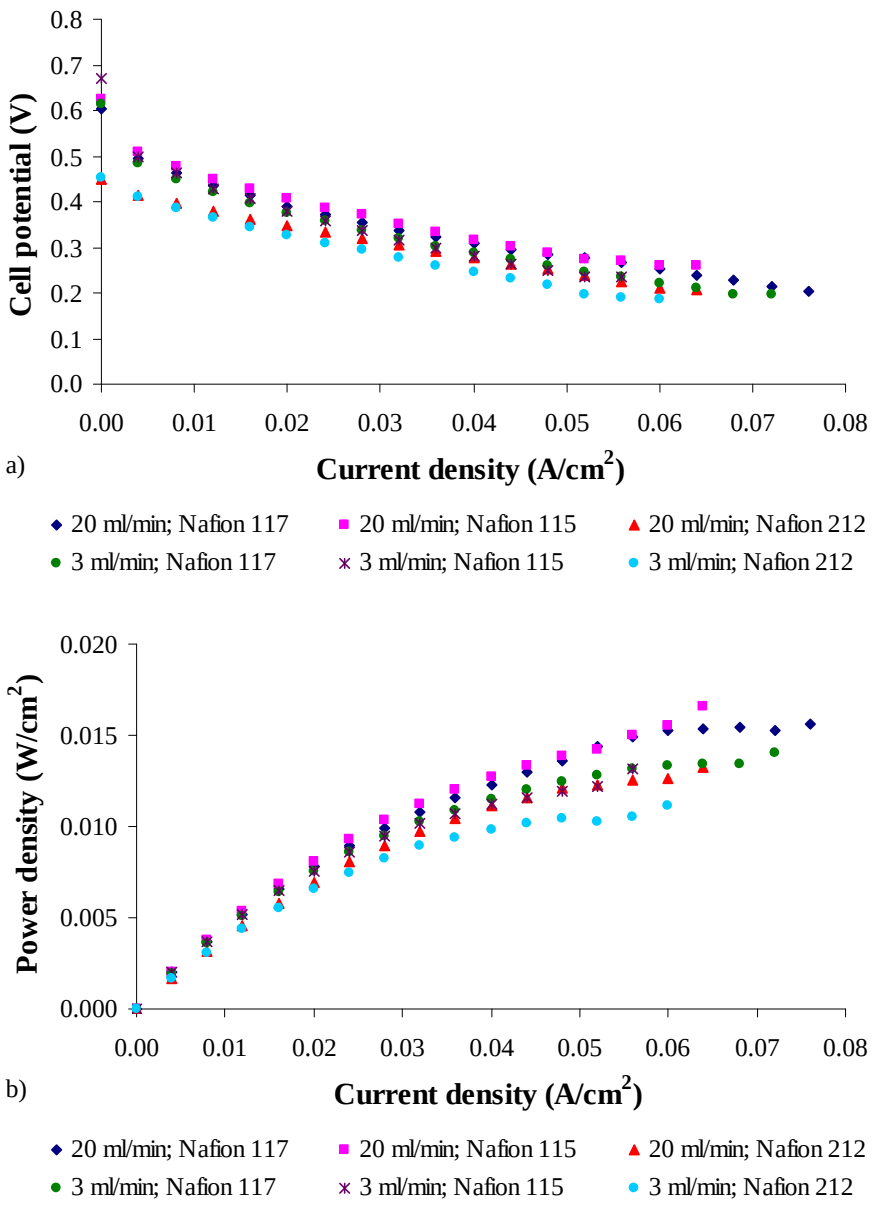

Figure 5.33 – Effect of membrane thickness on a) cell performance and b) power density. Operating conditions: methanol concentration 0.75M, air flow rate 3.6 l/min and cell temperature 20ºC.

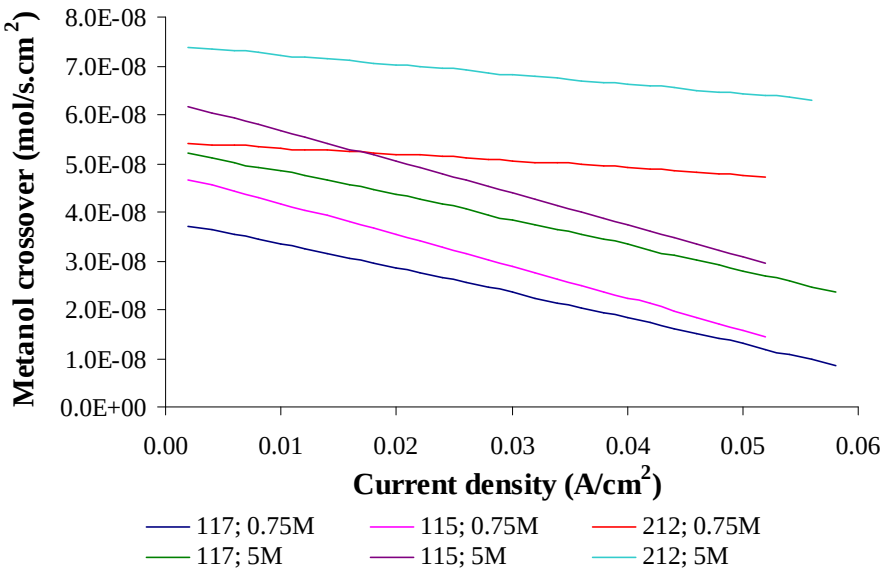

Figure 5.34 – Model predictions for the methanol crossover for different membrane thicknesses. Operating conditions: methanol concentration 0.75M and 5M, methanol flow rate 3 ml/min, air flow rate 3.6 l/min and fuel cell temperature 20ºC.

The influence of the membrane thickness on the cell performance for two different methanol concentrations (0.75M and 5M) is shown in Fig. 5.35. The methanol flow rate used was 3 ml/min, the air flow rate 3.6 l/min and the fuel cell temperature 20ºC. As expected the thinner membrane shows the worst performance due to the generation of large amounts of methanol crossover (Fig. 5.34). As referred before, the most considerable differences in the polarization curves for the three membranes used were found at low current densities and at high current density regime. The thicker membrane, Nafion 117, revealed no appreciable mass transfer limit even in high current regimes.

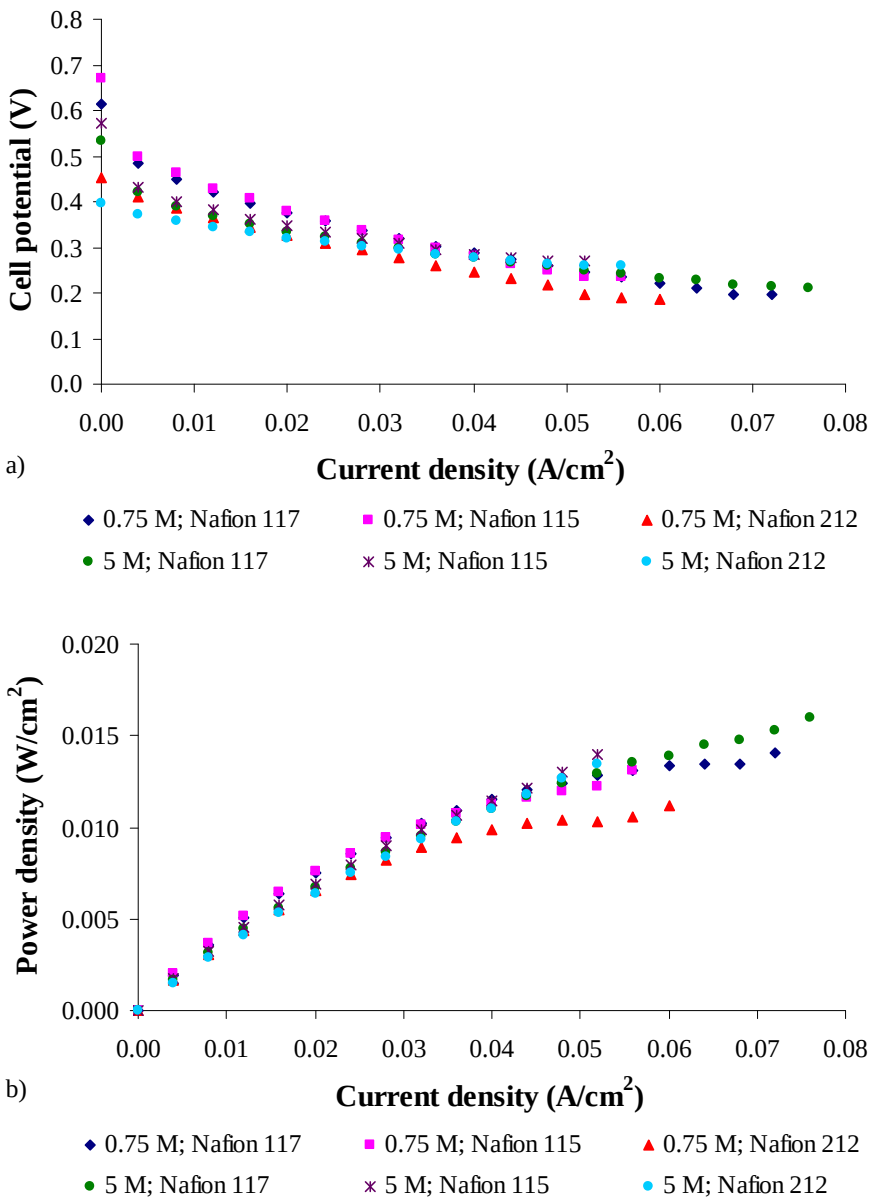

Figure 5.35 – Effect of membrane thickness on a) cell performance and b) power density. Operating conditions: air flow rate 3.6 l/min, methanol flow rate 3 ml/min and cell temperature 20ºC.

The model predictions of the net water transport coefficient (α) are presented in Fig. 5.36 for the three Nafion membranes (Nafion 117, Nafion 115 and Nafion 212). For the conditions studied, the net water transport coefficient has positive values indicating that the water transport is toward the cathode. When comparing the values of α for identical values of current density and different membrane thicknesses, lower values of α are obtained with the thinner membrane, because the resistance of water back-flow from the cathode to the anode via hydraulic permeation is much reduced in this case. This is a

very important result bearing in mind the operation of a DMFC under high methanol concentration.

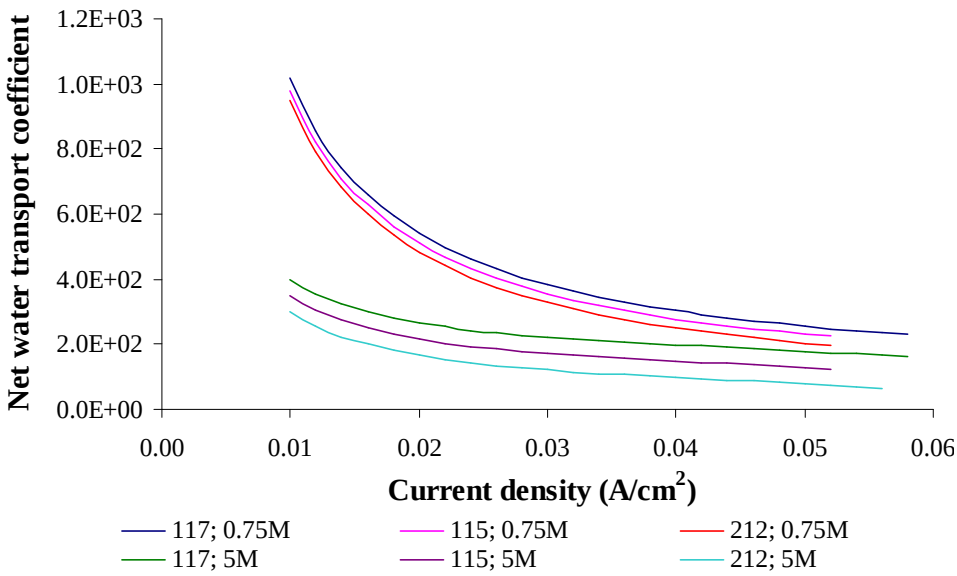

Figure 5.36 – Model predictions for the net water transport coefficient for different membrane thicknesses. Operating conditions: methanol concentration 0.75M and 5M, methanol flow rate 3 ml/min, air flow rate 3.6 l/min and fuel cell temperature 20ºC.

The effect of membrane thickness on cell performance and power density for two different fuel cell temperatures (20ºC and 60ºC) are provided in Fig. 5.37. As expected, the worst performances are achieved using Nafion 212 membranes for low and high fuel cell temperatures.

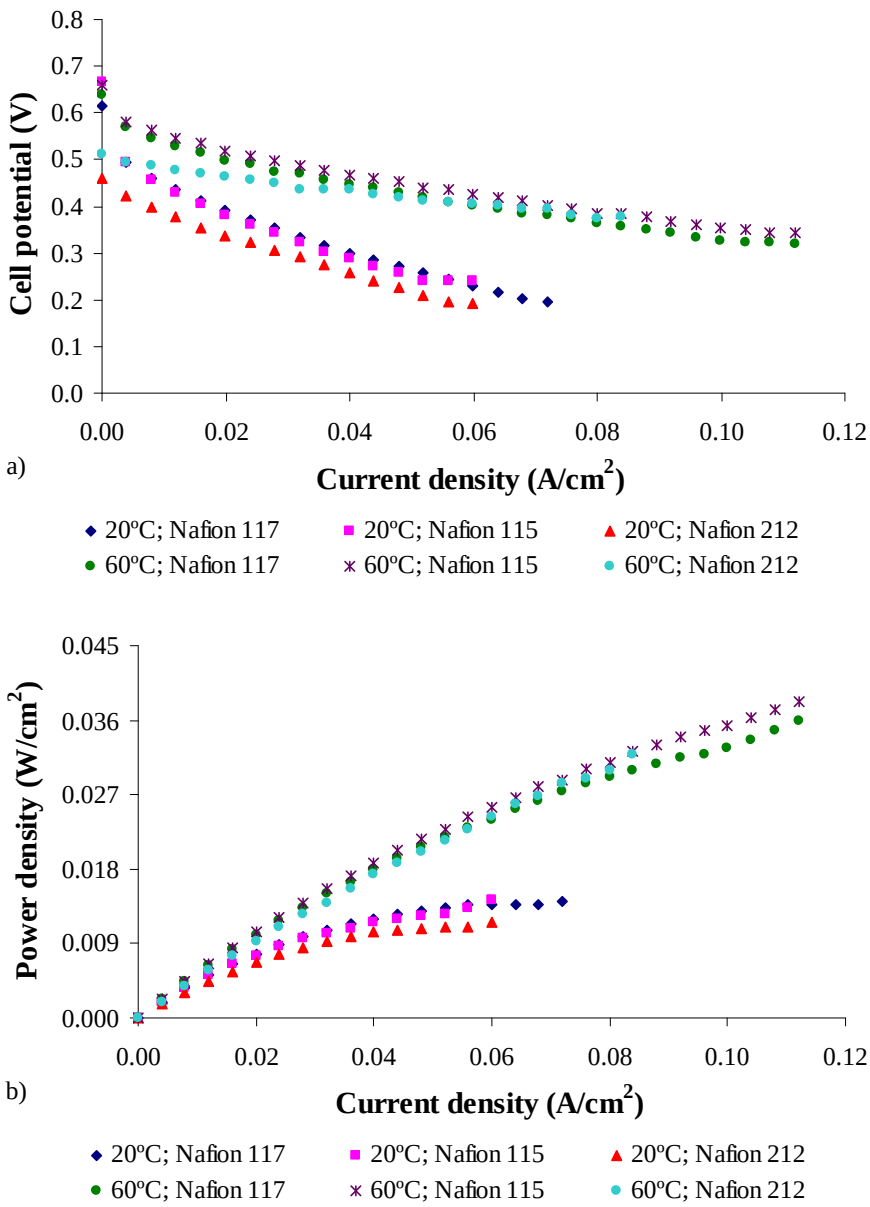

Figure 5.37 – Effect of membrane thickness on a) cell performance and b) power density. Operating conditions: methanol concentration 0.75M, methanol flow rate 8 ml/min and air flow rate 3.6 l/min.

Model predictions and experimental results, for two values of methanol concentration (0.75M and 2M) are presented in Fig. 5.38. The methanol flow rate used was 3 ml/min, the air flow rate 3.6 l/min and the fuel cell temperature 20ºC. The model predicts the correct trends of the effect of the membrane thickness on fuel cell performance and power density.

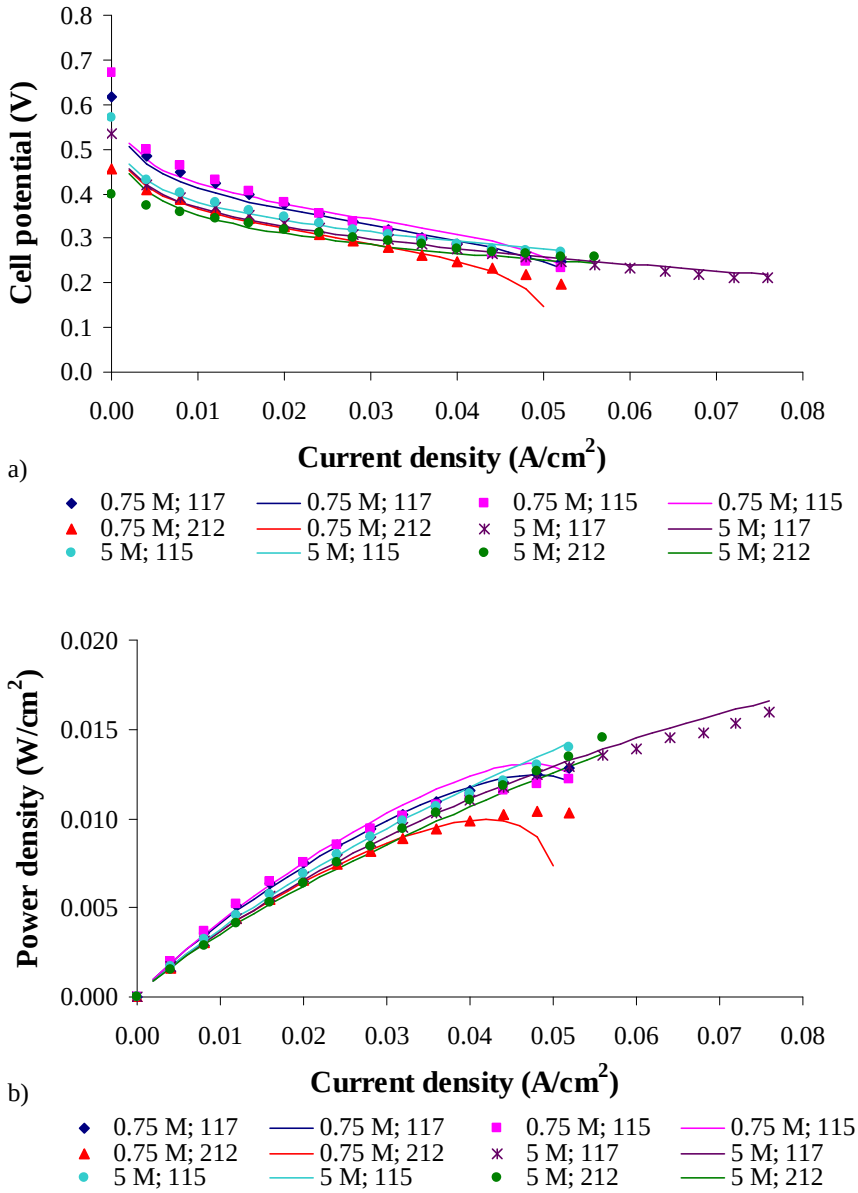

Figure 5.38 – Comparison of model predictions on a) cell performance and b) power density; dots: experimental data, lines: model predictions. Operating conditions: methanol concentration 0.75M and 5M, methanol flow rate 3 ml/min and air flow rate 3.6 l/min.

5.1.3.4. Effect of Catalyst loading

Based on the set of operating conditions tested and presented in Table 5.6, a sub-set of results was chosen to be presented in this section. For the set of tests presented in the following, a single serpentine flow field design and carbon cloth type A for both anode and cathode were used.

The catalyst loading used on the anode and cathode electrode was, respectively 4 mg/cm^2 (SL - standard loading) Pt/Ru and Pt and 8 mg/cm^2 (HL - high loading) Pt/Ru and Pt-B.

The influence of the catalyst loading on the cell performance for two different methanol flow rates (20 ml/min and 3 ml/min) is put in evidence by the plots in Fig. 5.39, for a methanol feed concentration of 0.75M. The reduction of noble metal loading leads to a decrease in the cell performance. There are three essential properties of the electrode that may be affected when reducing the catalyst loading: the catalytically active surface area, the electronic conductivity and the thickness of the electrode. The reduction of the catalyst loading conducts to a reduction of the catalyst layer that leads to a reduction on the active surface area, an increase on resistivity and consequently a decrease in electronic conductivity. An increase on the catalyst loading leads to an increase on the catalyst active surface, more active sites for the methanol oxidation, a decrease of the anode overpotential and consequently an increase in the fuel cell performance. The effect of the catalyst loading on both anode and cathode overpotential is shown in Figures 5.40 and 5.41, respectively, for a methanol concentration of 0.75M. As expected, higher catalyst loadings result in lower values of anode and cathode overpotentials. An increase on the catalyst loading causes an increase in the electrode thickness. A thicker electrode leads to a higher mass transport resistance but, on the other hand, it may also be advantageous, specially, at the cathode, since mixed potential formation may be avoided to some extent. In a thicker electrode, less catalyst particles are reached by the permeated methanol flux, so more active sites are free for the oxygen reduction reaction. The cathode overpotential decreases leading to an increase of the fuel cell performance.

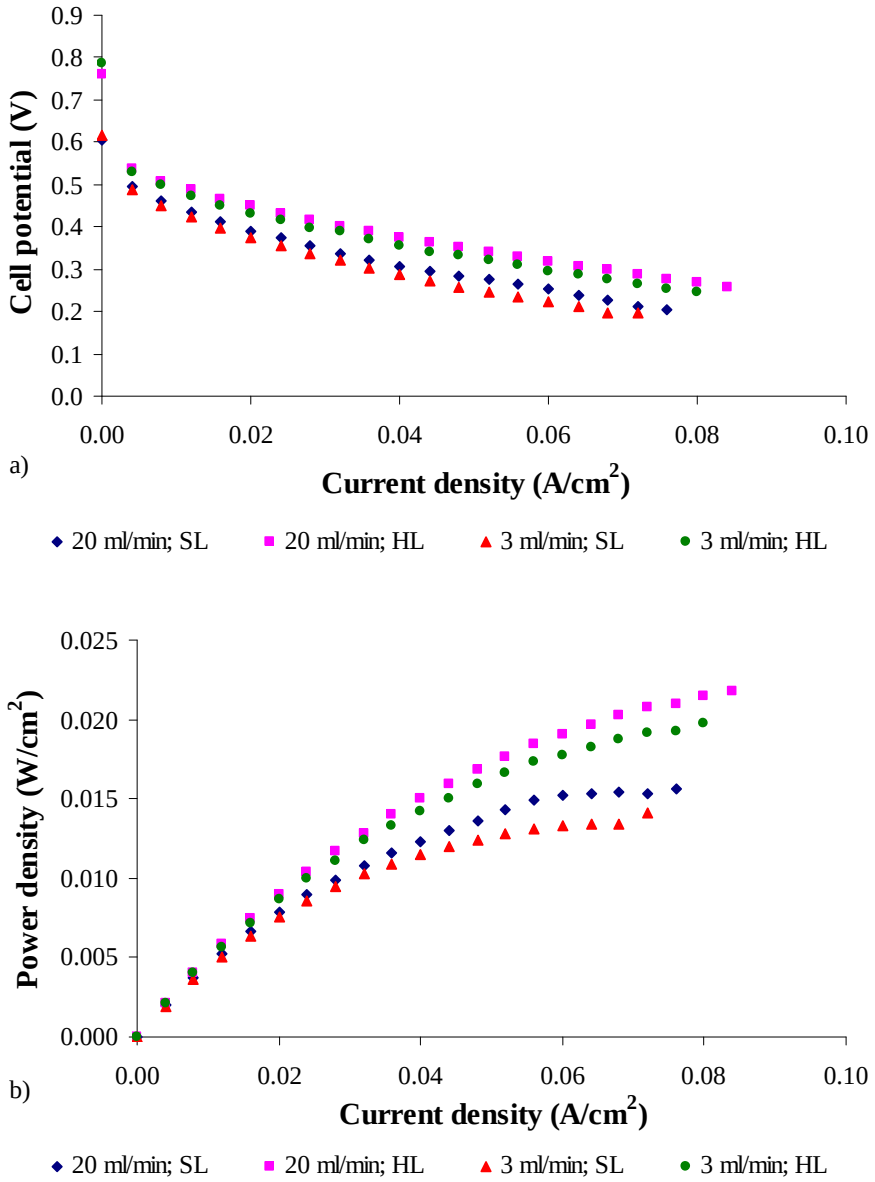

Figure 5.39 – Effect of catalyst loading on a) cell performance and b) power density. Operating conditions: methanol concentration 0.75M, air flow rate 3.6 l/min and cell temperature 20ºC. Design parameters: catalyst loading SL (4 mg/cm^2) and HL (8 mg/cm^2).

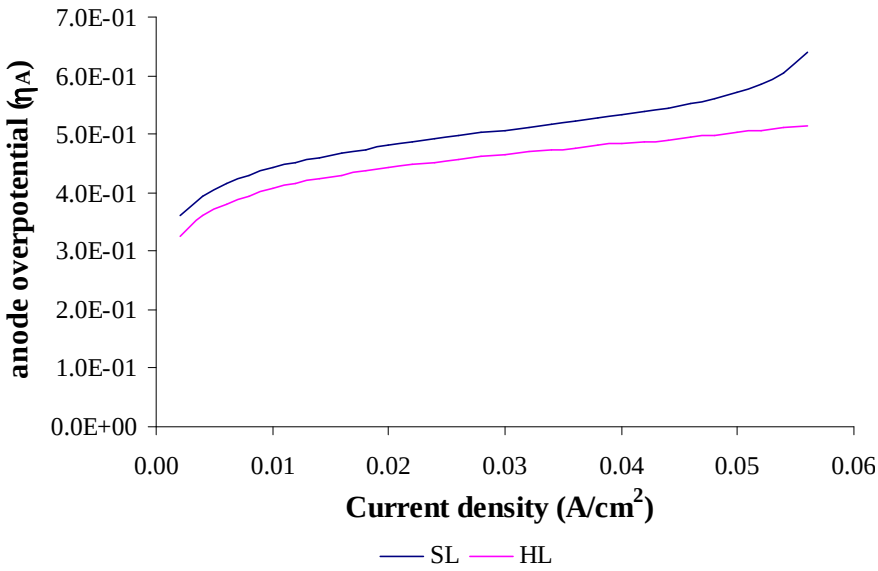

Figure 5.40 – Model predictions for the anode overpotential for different catalyst loadings. Operating conditions: methanol flow rate 3 ml/min, air flow rate 3.6 l/min and methanol concentration 0.75M. Design parameters: catalyst loading SL (4 mg/cm^2) and HL (8 mg/cm^2).

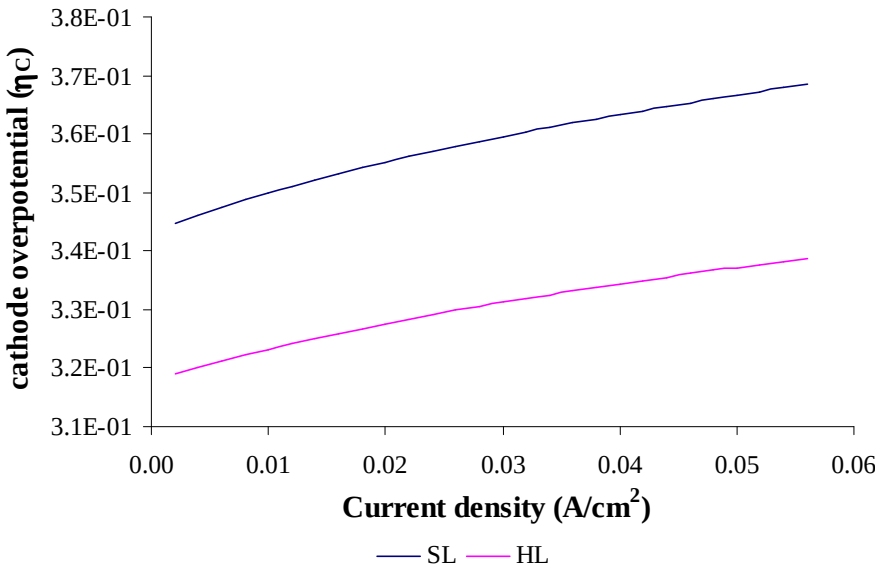

Figure 5.41 – Model predictions for the cathode overpotential for different catalyst loadings. Operating conditions: methanol flow rate 3 ml/min, air flow rate 3.6 l/min and methanol concentration 0.75M. Design parameters: catalyst loading SL (4 mg/cm^2) and HL (8 mg/cm^2).

The influence of the catalyst loading for three different methanol concentrations (0.75M, 2M and 5M) is shown in Fig. 5.42. A better performance is obtained, as expected, for the highest value of catalyst loading, for the three values of methanol concentration tested.

The model predictions for the methanol crossover are presented in Fig. 5.43 for the methanol concentration of 0.75 M and 5M for the two levels of catalyst loading. With the increasing catalyst loading, the thickness of the catalyst layer increase and therefore the mass transfer resistance through this layer becomes greater. In spite of this, the cell performance increases with the metal loading because the thicker anode catalyst layer creates a higher resistance to methanol transport thereby controlling the rate of methanol reaching the membrane and reducing the methanol crossover as is well brought out by the curves shown in the figure. This reduction leads to a reduction of the parasite current formed due to the oxidation of methanol at the cathode side and consequently the cell performance increases.

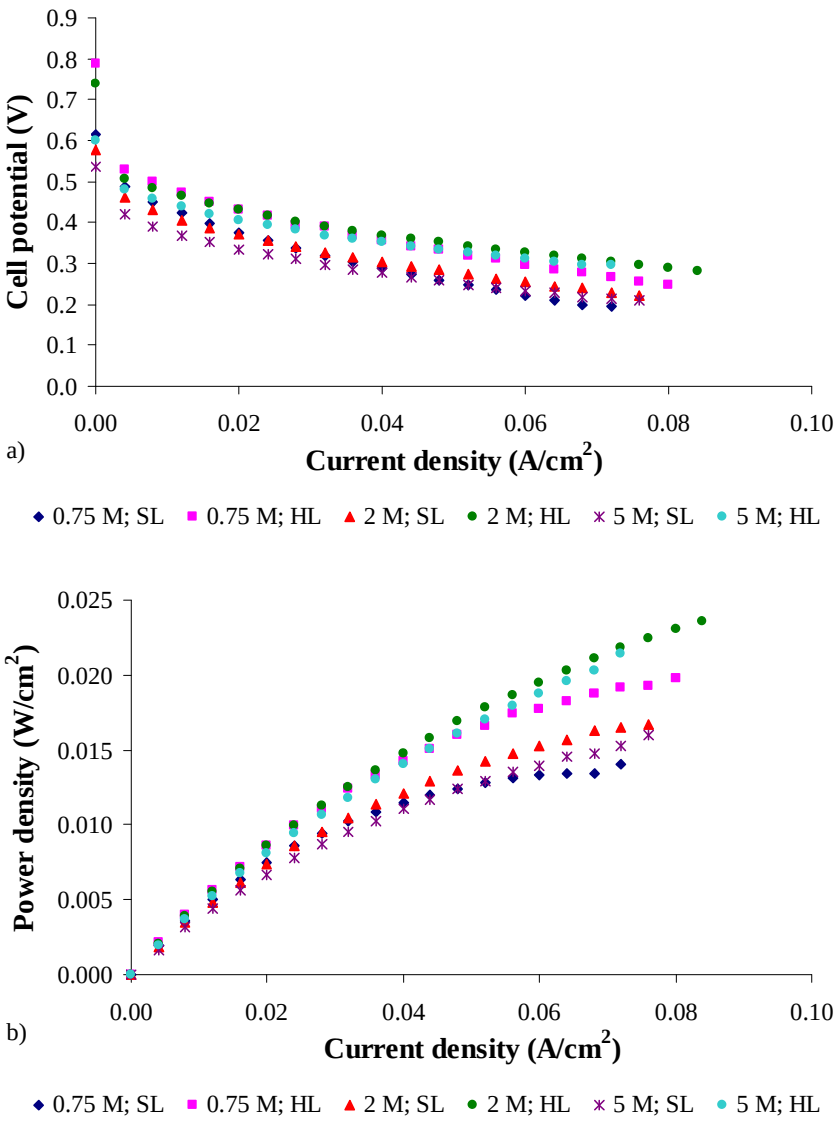

Figure 5.42 – Effect of catalyst loading on a) cell performance and b) power density. Operating conditions: air flow rate 3.6 l/min, methanol flow rate 3 ml/min and cell temperature 20ºC. Design parameters: catalyst loading SL (4 mg/cm^2) and HL (8 mg/cm^2).

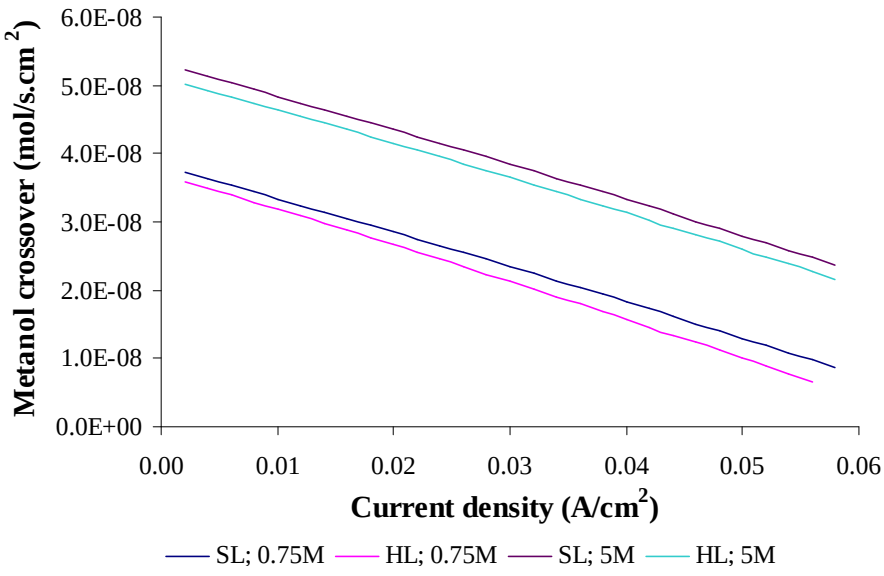

Figure 5.43 – Model predictions for the methanol crossover for different catalyst loadings. Operating conditions: methanol concentration 0.75M and 5M, methanol flow rate 3 ml/min, air flow rate 3.6 l/min and fuel cell temperature 20ºC. Design parameters: catalyst loading SL (4 mg/cm^2) and HL (8 mg/cm^2).

The model predictions of the net water transport coefficient (α) are presented in Fig. 5.44 for the two catalyst loadings tested (SL (4 mg/cm^2) and HL (8 mg/cm^2)), and for the methanol concentrations of 0.75M and 5M. For the conditions studied, the net water transport coefficient has positive values meaning that the water transport is toward the cathode. When comparing the values of α for identical values of current density and different catalyst loadings, the values of α are slightly lower for the HL catalyst loading, probably because higher loadings on the cathode side lead to more active sites free for the oxygen reduction reaction and more intense water formation decreasing the water concentration gradient between the anode and cathode side.

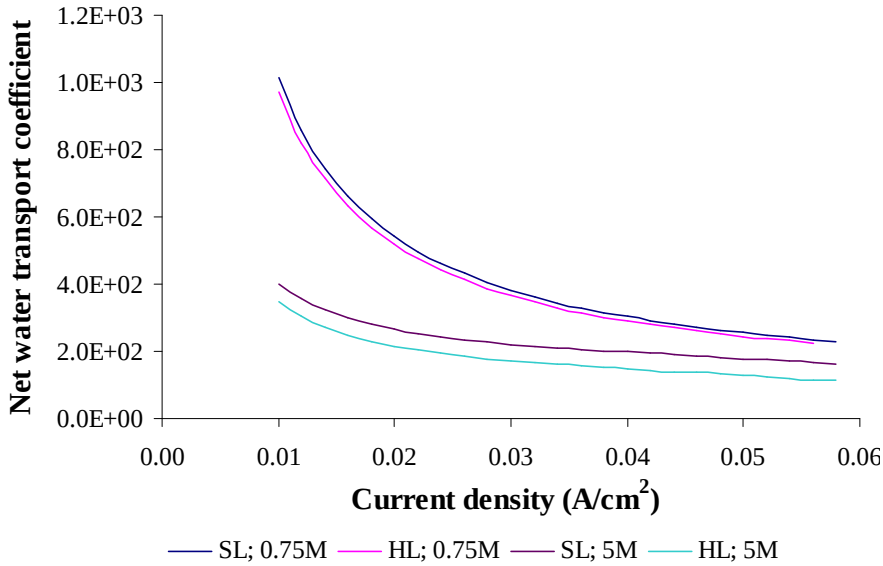

Figure 5.44 – Model predictions for the net water transport coefficient for different catalyst loadings. Operating conditions: methanol concentration 0.75M and 5M, methanol flow rate 3 ml/min, air flow rate 3.6 l/min and fuel cell temperature 20ºC. Design parameters: catalyst loading SL (4 mg/cm^2) and HL (8 mg/cm^2).

The effect of catalyst loading, for two different fuel cell temperatures (20ºC and 60ºC) and two catalyst loadings, on cell performance are provided in Fig. 5.45. As expected, the lower performances are achieved using the lower catalyst loadings for the lower and higher fuel cell temperatures.

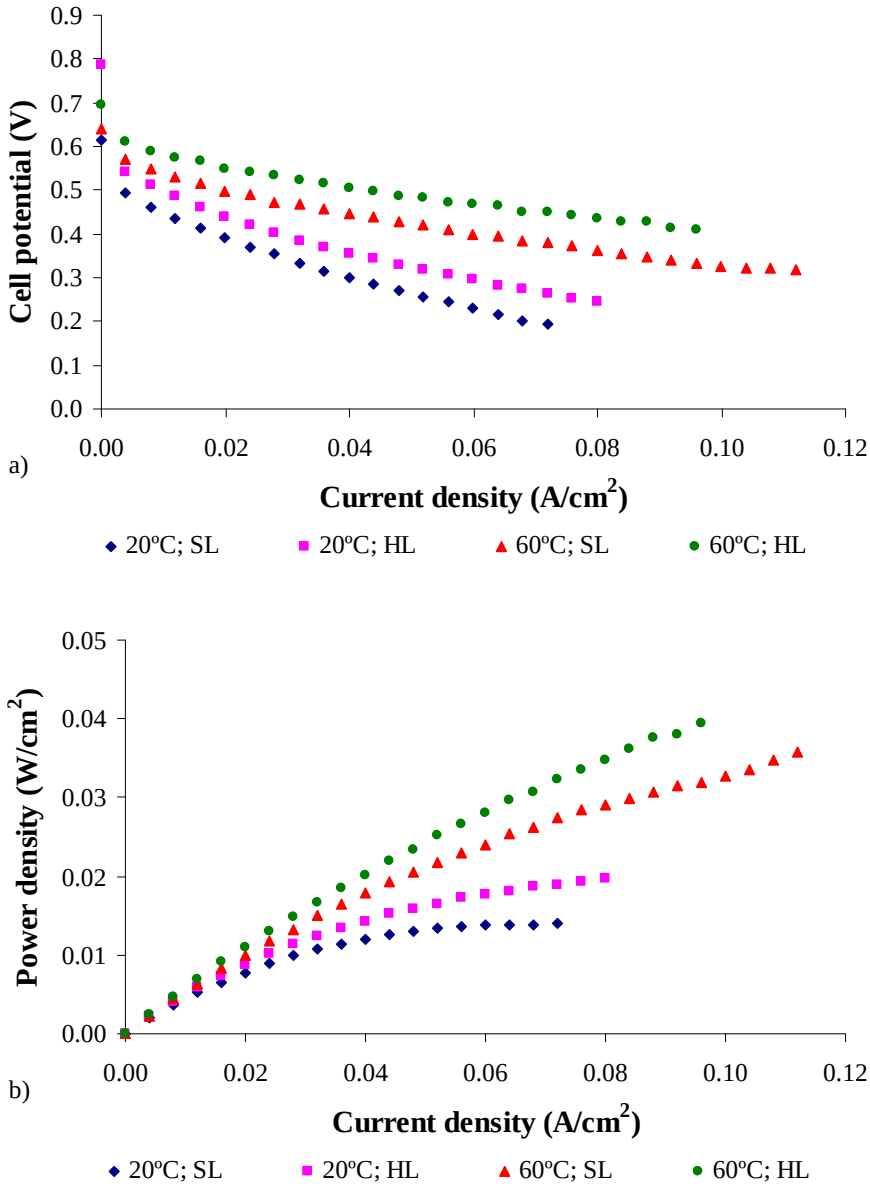

Figure 5.45 – Effect of catalyst loading on a) cell performance and b) power density. Operating conditions: methanol concentration 0.75M, methanol flow rate 8 ml/min and air flow rate 3.6 l/min. Design parameters: catalyst loading SL (4 mg/cm^2) and HL (8 mg/cm^2).

Finally, the comparison between model predictions and experimental results, for two values of methanol concentration (0.75M and 5M) and for the two catalyst loadings tested are presented in Fig. 5.46, showing once again that the model predicts the correct trends of the effect of the catalyst loading on fuel cell performance and power density.

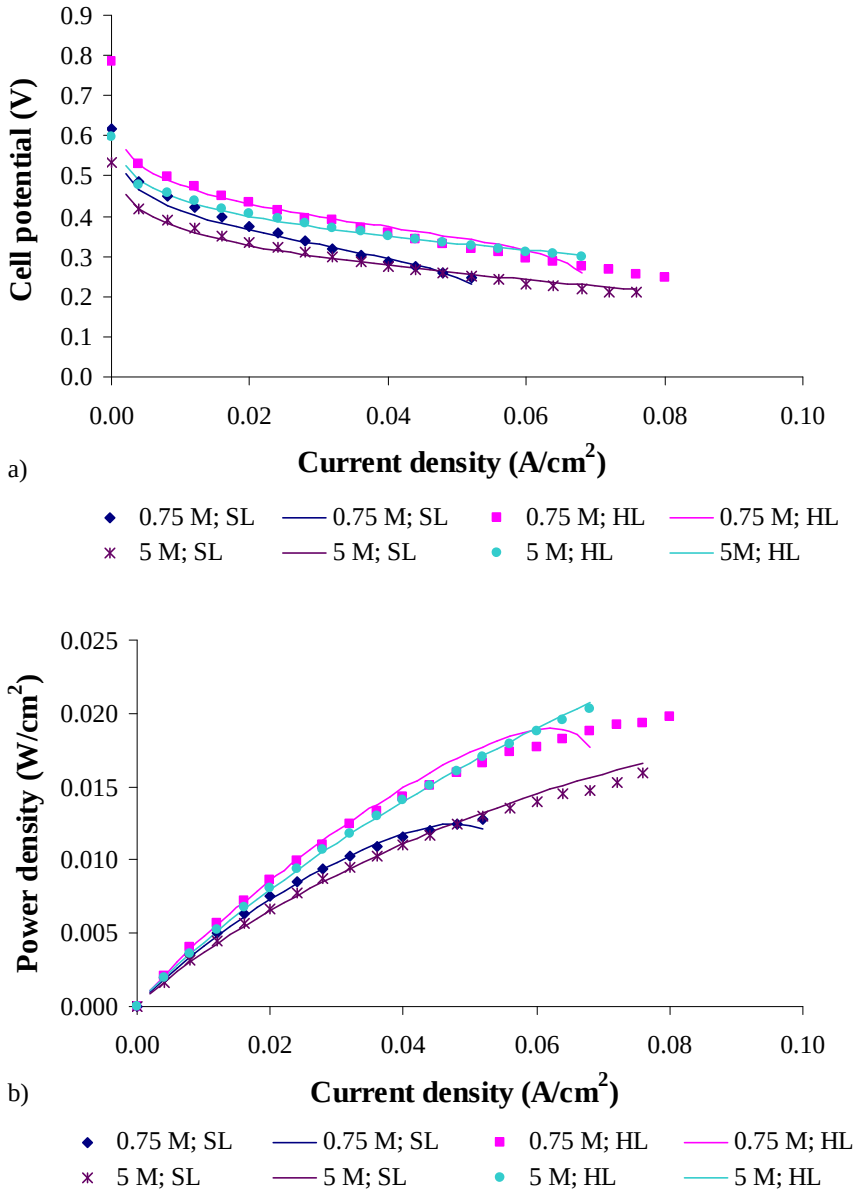

Figure 5.46 – Comparison of model predictions on a) cell performance and b) power density; dots: experimental data, lines: model predictions. Operating conditions: methanol concentration 0.75M and 5M, methanol flow rate 3 ml/min and air flow rate 3.6 l/min. Design parameters: catalyst loading SL (4 mg/cm^2) and HL (8 mg/cm^2).

5.1.3.5. Effect of anode flow field

In this section, the results from the experimental study of the effect of the anode flow field design on the fuel cell performance are presented, based on the set of operating conditions tested and presented in Table 5.6.

Three anode flow fields (single serpentine (SFF), multi-serpentine (MSFF) and an original design mixed serpentine and parallel (MFF)) were tested by keeping the same cathode flow field the single serpentine design. The membrane used in all the tests was Nafion 117, the anode and cathode catalyst loading was 4 mg/cm^2 and the anode and cathode diffusion layers were carbon cloth type A.

The data plotted in Fig. 5.47 were obtained in experiments with a 0.75M methanol solution fed at three flow rates (3, 8 and 20 ml/min) and at a fixed fuel cell temperature of 20ºC and an air flow rate of 3.6 l/min. As is evident from this figure, for the same methanol flow rate the performance of the fuel cell equipped with MFF is slightly better than that with SFF and much better than that with MSFF. The SFF has as the advantage of forcing the reactant flow to traverse the entire active area of the corresponding electrode thereby eliminating areas of stagnant flow. However, this channel layout results in a relatively long reactant flow path, hence a substantial pressure drop and significant concentration gradients from the flow inlet and outlet. Although the MSFF design reduce the reactant pressure drop relative to a single serpentine design, the reactant pressure drop through each of the serpentine channels remains relatively high due to the relatively long flow path of each channel, thus the reactant concentration changes significantly from the flow inlet region to the exit region. The MFF design is divided in several sections with separate inlet and outlet, and each of flow sectors has parallel flow channels, which are further sub-divided into few sets of channels connected in series. This design gives combined advantages from grid, parallel and serpentine design since it generates lower pressure drops preventing the formation of stagnant flow areas, distributing reactants more uniformly with higher average reactant concentrations. The advantages of the MFF, mentioned before, are slightly more important when the fuel cell is operating at high current densities, were the anode produces a large amount of carbon dioxide bubbles. The bubbles formation raises the pressure drop, so it is advantageous to use a design minimizing additional pressure drops.

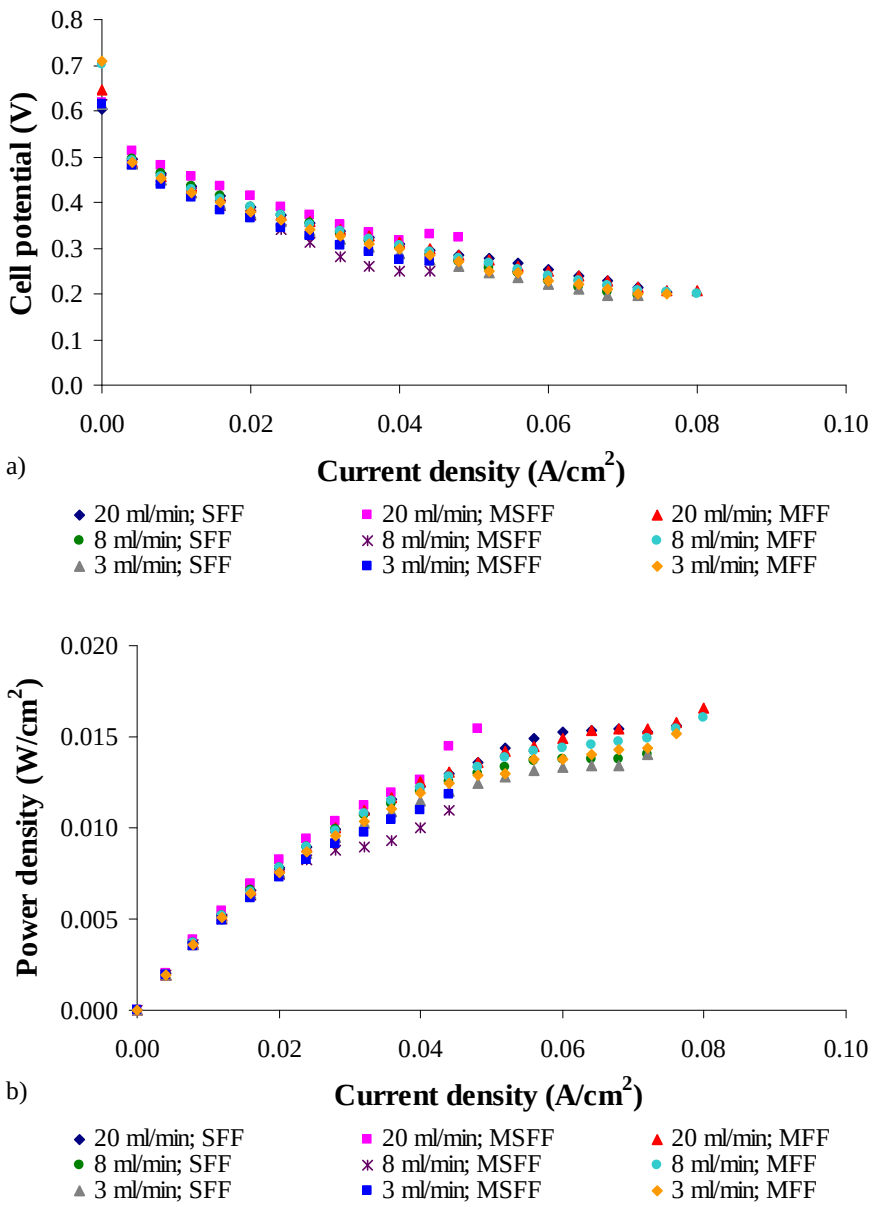

Figure 5.47 – Effect of anode flow field design on a) cell performance and b) power density. Operating conditions: methanol concentration 0.75M, air flow rate 3.6 l/min and cell temperature 20ºC.

Results from experiments conducted with three different methanol concentrations (0.75M, 2M and 5M) fed at a methanol flow rate of 3 ml/min, at a fuel cell temperature of 20ºC and air flow rate 3.6 l/min are plotted in Fig. 5.48. For a methanol feed concentration of 0.75M the best performance is achieved with MFF while for the methanol concentration of 2M and 5M the best performance is achieved with MSFF. A DMFC operating with high methanol concentrations generates large amounts of methanol crossover which causes a mixed potential on the cathode side and decreases

the fuel cell performance. So, it seems that the use of a MSFF with reduced pressure drop when compared to the SFF and reduced dead zones when compared to the MFF, is favorable for high methanol feed concentrations.

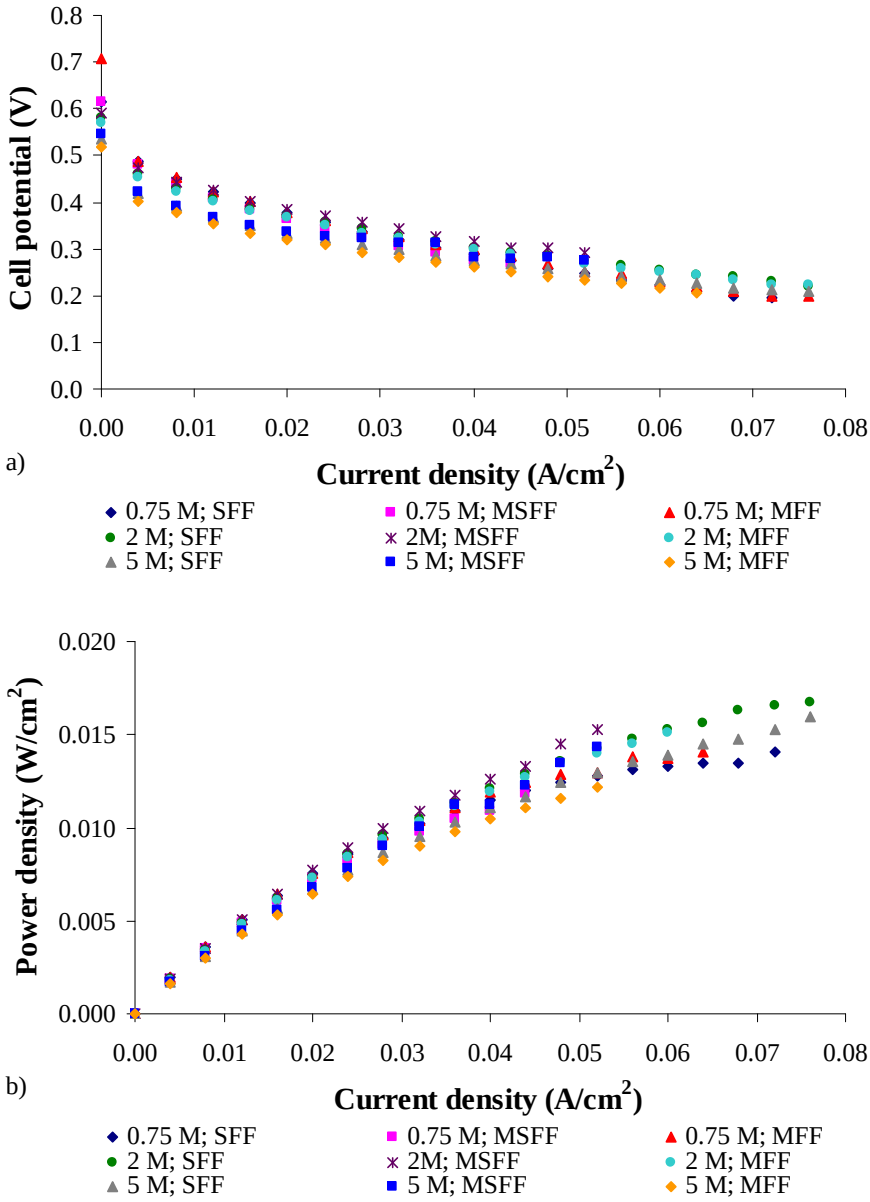

Figure 5.48 – Effect of anode flow field design on a) cell performance and b) power density. Operating conditions: air flow rate 3.6 l/min, methanol flow rate 3 ml/min and cell temperature 20ºC.

The polarization and power curves represented in Fig. 5.49 concern experiments with a methanol feed concentration of 0.75M, a methanol flow rate of 8 ml/min a air flow rate 3.6 l/min and two different fuel cell temperatures (20ºC and 60ºC). For a DMFC operating at 20ºC, similar performances are achieved with the SFF and the MFF designs

with a slight better performance for the latter. These results are explained by the same reason mentioned previously, related to the fact that this design combines the advantages from the grid, the parallel and the serpentine designs, generates low pressure drops and enhances two-phase mass transport, allowing a efficient removal of the reaction products. For 60ºC the three designs used as anode flow channels (SFF, MSFF and MFF) give similar performances for low current densities. For high current densities the MFF and the SFF have slightly better performance than the MSFF. An increase on fuel cell temperature leads to an increase of the electrochemical reaction rate, more methanol is oxidized at the anode side and more carbon dioxide is formed. The MSFF design with a relatively long flow path of each channel and a corresponding reactant pressure drop generates a less uniform distribution of reactant which may cause the appearance of a less uniform distribution of bubbles. It seems that this non homogeneity induces a slower gas removal for higher temperatures.

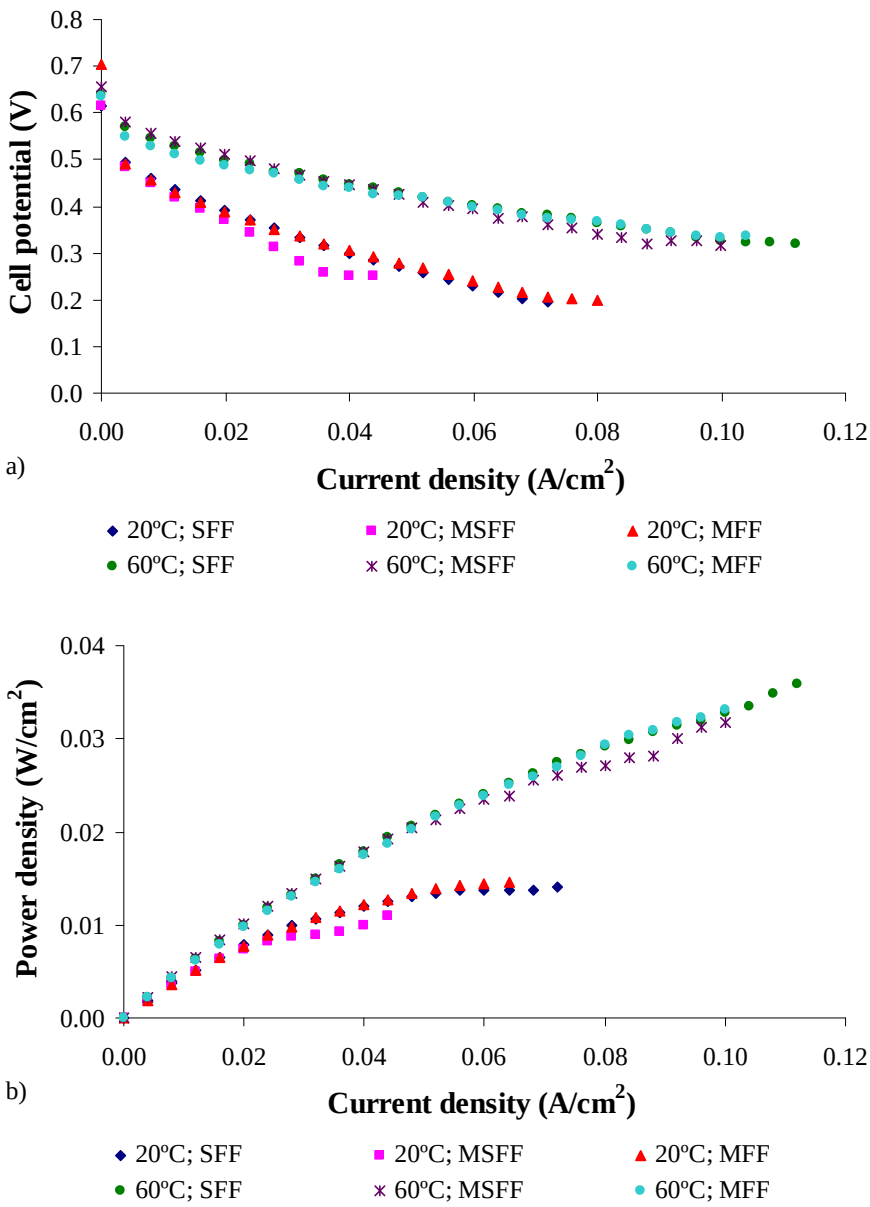

Figure 5.49 – Effect of anode flow field design on a) cell performance and b) power density. Operating conditions: methanol concentration 0.75M, methanol flow rate 8 ml/min and air flow rate 3.6 l/min.

5.1.3.6. Cathode flow field

Based on the set of operating conditions tested and presented in table 5.6, the three cathode flow field designs were tested by keeping the same anode flow field having a single serpentine flow field (SFF).

The design of the cathode flow field affects the air mass transfer rate and the drainage. If the water is not efficiently removed from the cathode at a sufficient rate, flooding may occur and transport of reactants is hindered [181].

Although in the anode side the advantages of the MFF seems to be superior that the disadvantages, in the cathode side the opposite is found since the performance for all the conditions tested using the MFF is lower. Figures 5.50, 5.51 and 5.52 show the polarization and power curves for the three different cathode flow fields.

Polarization and power curves obtained from experiments with 0.75M methanol solution fed at 8 ml/min, at a fixed fuel cell temperature of 20ºC and two air flow rates (1 l/min and 3.6 l/min), are presented in Fig. 5.50. For the same air flow rate, the best performance is obtained when the multi-serpentine flow field (MSFF) is used, probably because this design has the advantages of the serpentine designs at the cathode side, ensuring adequate water removal by the gas flow through the several channels and no formation of stagnant areas at the cathode surface due to water accumulation. These results are in accordance with the simulation results obtained by Jung *et al.* [179]. The effect of the methanol flow rate is as expected: higher performances for higher methanol flow rates.

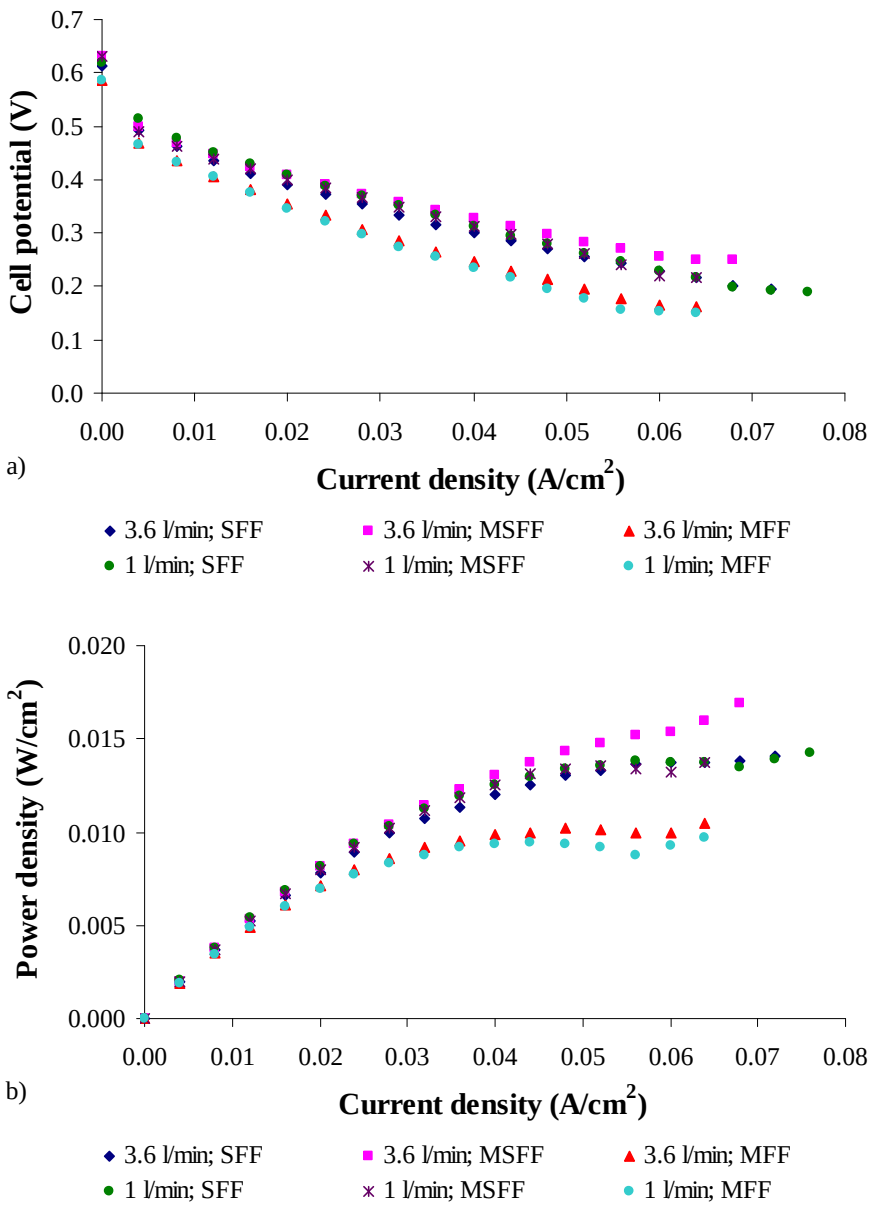

Figure 5.50 – Effect of cathode flow field design on a) cell performance and b) power density. Operating conditions: methanol concentration 0.75M, methanol flow rate 8 ml/min and cell temperature 20ºC.

The data plotted in Fig. 5.51 were obtained in experiments with 0.75M, 2M and 5M methanol solution fed at 3 ml/min, at a fixed fuel cell temperature of 20ºC and an air flow rates 3.6 l/min. For a methanol feed concentration of 0.75M the best performance is achieved with MSFF while for the methanol concentrations of 2M and 5M the higher performances are achieved with MSFF and SFF. When a DMFC operates with a 0.75M methanol solution, a large amount of water is present at the anode side and the net water flux tends to be toward the cathode side generating more accumulation of water at the cathode side. Since the MSFF is a design which allows an efficient water removal this

flow field gives the best performance. For the 2M and 5M methanol solution, the water concentration at the anode side is smaller and the water production at the cathode give higher concentrations generating lower water crossover. The use of MSFF or SFF configurations seem to generate similar performances, since both designs have good mass transfer ability and can exclude water due to the high pressure drop. Contrarily, the MFF design seems to be inefficient in water drops removal at the cathode side, since this design induces lower pressure drops. Pressure drop effects at the cathode side are essential to correct water removal.

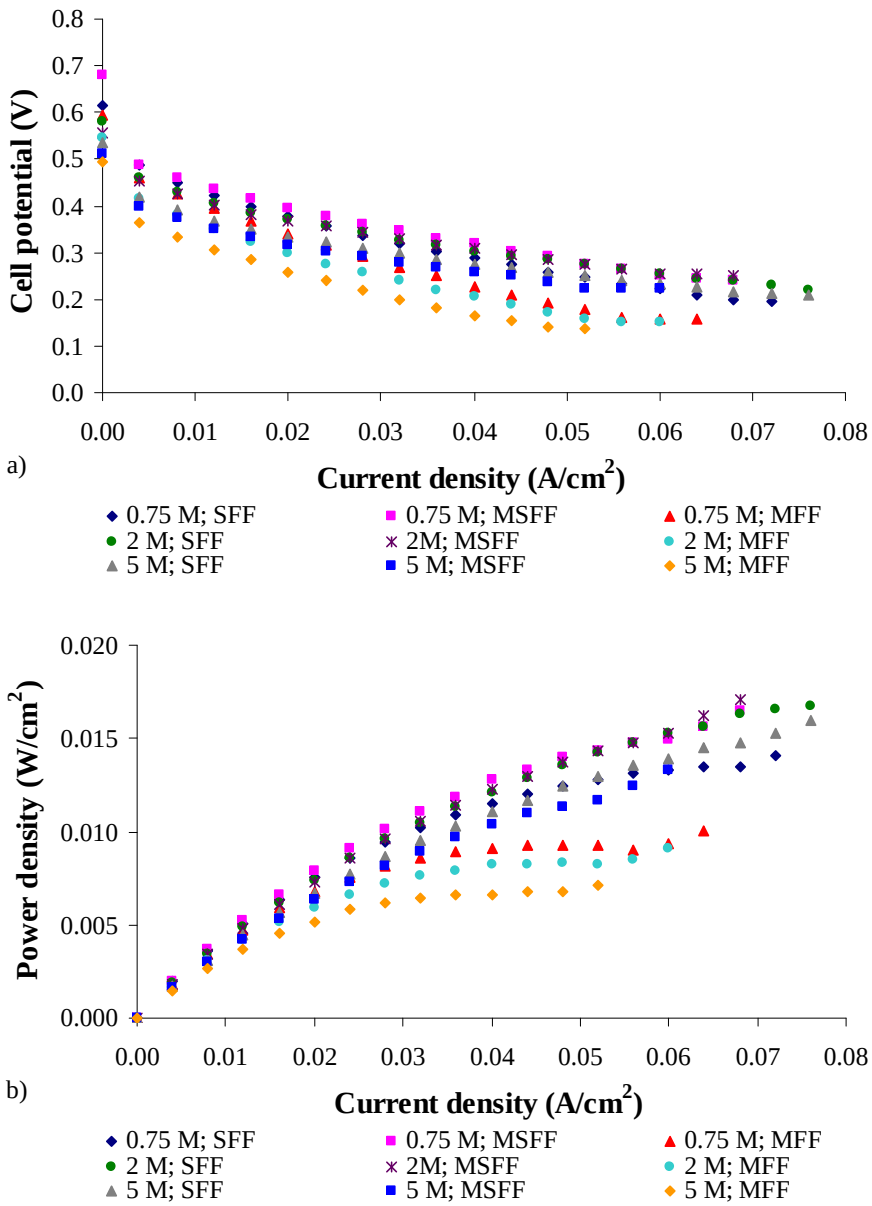

Figure 5.51 – Effect of cathode flow field design on a) cell performance and b) power density. Operating conditions: air flow rate 3.6 l/min, methanol flow rate 3 ml/min and cell temperature 20ºC.

Results from experiments conducted with a methanol feed concentration of 0.75M, a methanol flow rate of 8 ml/min a air flow rate 3.6 l/min and two different fuel cell temperatures (20ºC and 60ºC), are plotted in Fig. 5.52. As can be seen from the plots both MSFF and SFF give enhanced performances. For 20ºC a better performance is achieved using MSFF as cathode flow field design, while for 60ºC a slight better performance is achieved using SFF. These results can be explained under the light of the pressure effects on water removal, as explained above. The serpentine design due to the pressure-driven mass flow in the channels allows a correct water removal and forces the reactant flow to traverse the entire active area thereby eliminating areas of stagnant flow. The use of MFF shows the worst performance due to the fact that oxygen and water may flow in one or more of the many channels resulting in a bad distribution of reactant It should, also, be mentioned that the amount of water in the cathode side is smaller for 60ºC than for 20ºC, since at this temperature more water vaporizes and is removed by the gas stream. In this way a fuel cell operating at 60ºC should have less problems of flooding, so the single serpentine flow fields seems to be more adequate in this conditions, leading to the best performance.

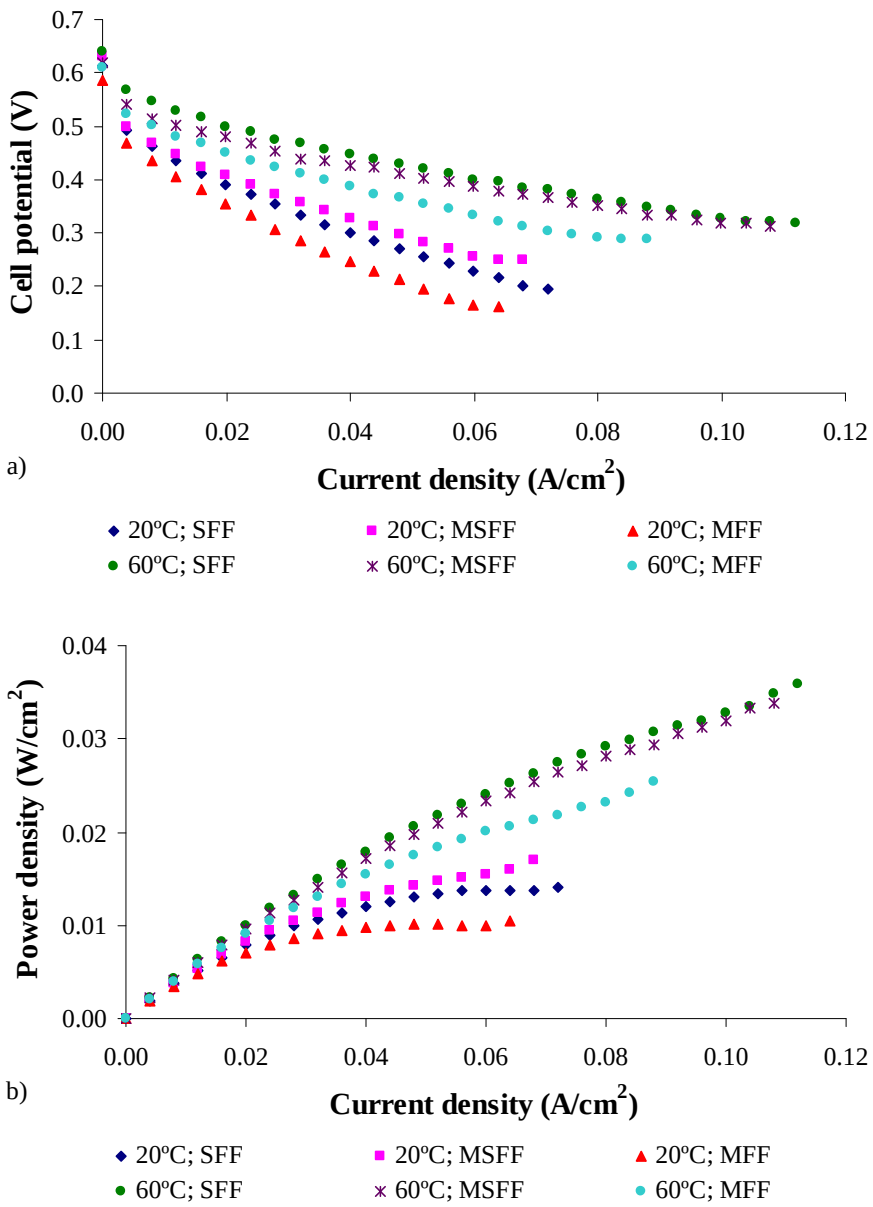

Figure 5.52 – Effect of cathode flow field design on a) cell performance and b) power density. Operating conditions: methanol concentration 0.75M, methanol flow rate 8 ml/min and air flow rate 3.6 l/min.

5.1.4. Tailored MEAs (Membrane Electrode Assemblies)

As already referred, reducing the membrane water and methanol transport from the anode to the cathode of a DMFC is of significant importance to achieve higher cell performances and consequently increased power densities. Following the results presented in the previous sections, the next goal was tailoring a MEA to achieve a better performance with higher methanol feed concentrations.

One membrane named commercial Nafion 117 was considered with 30 wt% carbon cloth type A (E-TEK) as gas diffusion layer on the anode and ELAT (E-TEK) on the cathode side with 4mg/cm^2 Pt/Ru and Pt as catalyst load for anode and cathode respectively. One tailored MEA with a thinner membrane Nafion 212, a 30% wet-proofed carbon paper TGPH060 as anode gas diffusion layer and a 30% wet-proofed carbon cloth type A as cathode gas diffusion layer and 4 mg/cm^2 Pt/Ru and Pt as catalyst load for anode and cathode respectively was also proposed.

A methanol feed concentration of 5M was used to check if it is possible to work with high methanol concentration without significant sacrifice of fuel cell performance. As verified in the previous results with high methanol concentrations and thinner membranes, the net water transport coefficient toward the cathode is reduced. A single serpentine flow field design was used both for anode and cathode sides.

The next three figures emerge as a result of the analyses made previously to predict the influence of different operating conditions and configuration parameters on the cell performance, on the net water transport coefficient and on the methanol crossover.

Figure 5.53 shows the experimental and predicted polarization and power density curves for the two types of MEAs, using the selected methanol concentration of 5M. The tailored MEA has a slightly better performance and power density especially for medium to high current densities. This is due to the fact that in this region, concentration overpotential is a major portion in the total overvoltage so a decrease in membrane thickness leads to a reduction on mass transfer resistance. Working with thinner membranes has advantages such as the lower cost and the possibility of working with a favorable water transport direction. Decreasing the membrane thickness enhances back transport of water, from the cathode to the anode, an essential operating condition when working with high methanol concentrations [89, 90]. According to the suggestions of Liu *et al.* [90], it is possible to reduce the methanol crossover using thinner membranes and thicker gas diffusion layers.

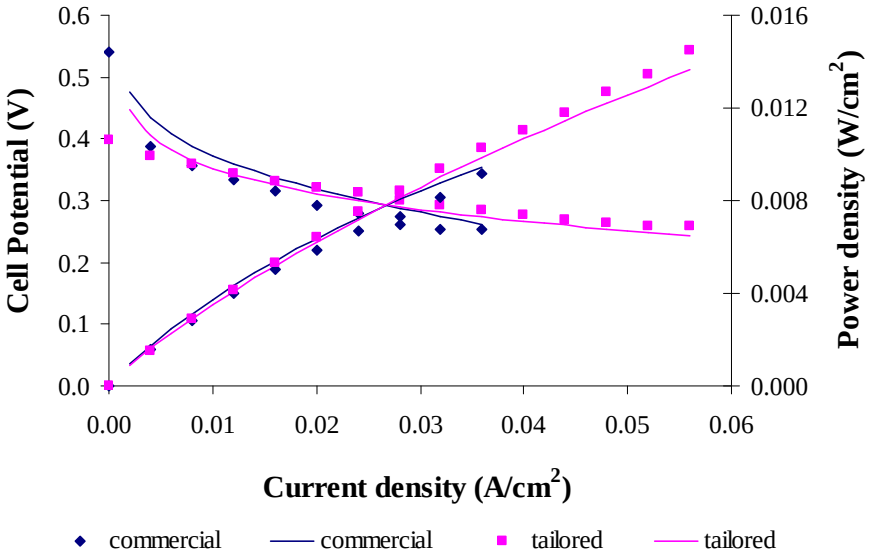

Figure 5.53 – Comparison of model predictions on cell performance and power density; dots: experimental data, lines: model predictions. Operating conditions: methanol concentration 5M, methanol flow rate 3 ml/min, air flow rate 3.6 l/min and fuel cell temperature 20ºC.

Model predictions of the methanol crossover for the two MEAs tested (commercial and tailored) are presented in Fig. 5.54 as a function of current density. As can be seen, and as already mentioned, higher methanol crossover rates are achieved using commercial membranes. The tailored membranes are thinner which conducts to a higher methanol crossover, but the anode diffusion layer material used is carbon paper and this material was found to limit the amount of methanol that reaches the cathode side. In overall, the tailored MEA can reduce the methanol crossover rate and enhance the fuel cell performance. With this MEA modification it is possible to work a DMFC with high methanol concentrations and low methanol crossover rates. This is one of the major goals on the DMFC development.

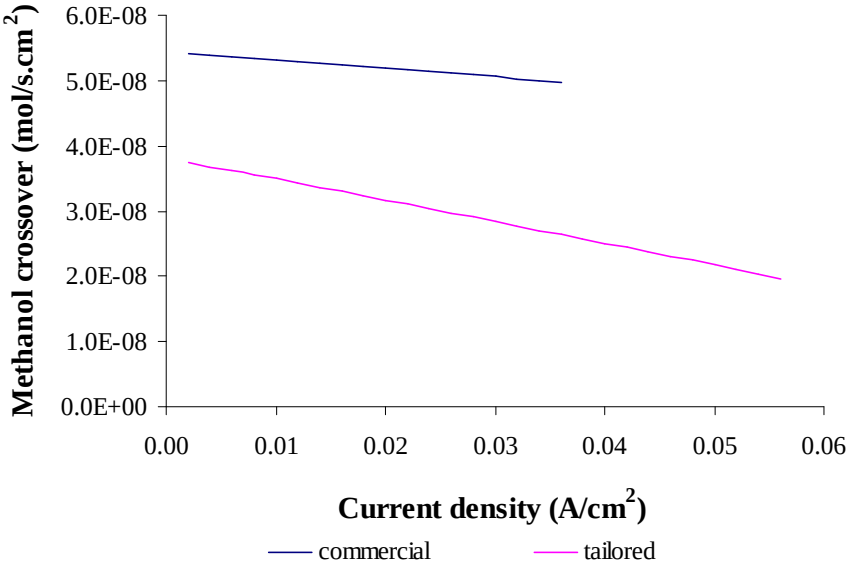

Figure 5.54 – Model prediction for the methanol crossover for different MEAs. Operating conditions: Operating conditions: methanol concentration 5M, methanol flow rate 3 ml/min, air flow rate 3.6 l/min and fuel cell temperature 20ºC.

The model predictions of the net water transport coefficient (α) are presented in Fig. 5.55 for the two MEAs tested (commercial and tailored). For the operating and design conditions studied, the net water transport coefficient has positive values for the entire range of current densities. When comparing the values of α for identical values of current density and the two MEAs, lower values of α are obtained with the thinner membrane (tailored MEA), as expected. As already verified, the use of carbon paper as anode gas diffusion layer, also, limits the amount of water that reaches the cathode side reducing the net water transport coefficient. With this MEA modification it is possible to work a DMFC with low net water transport coefficients and consequently low water crossover rates. This is another major goal to the DMFC development.

The results obtained seem to point out optimized conditions for operation of DMFCs with tailored MEAs and high methanol concentrations with an increased performance.

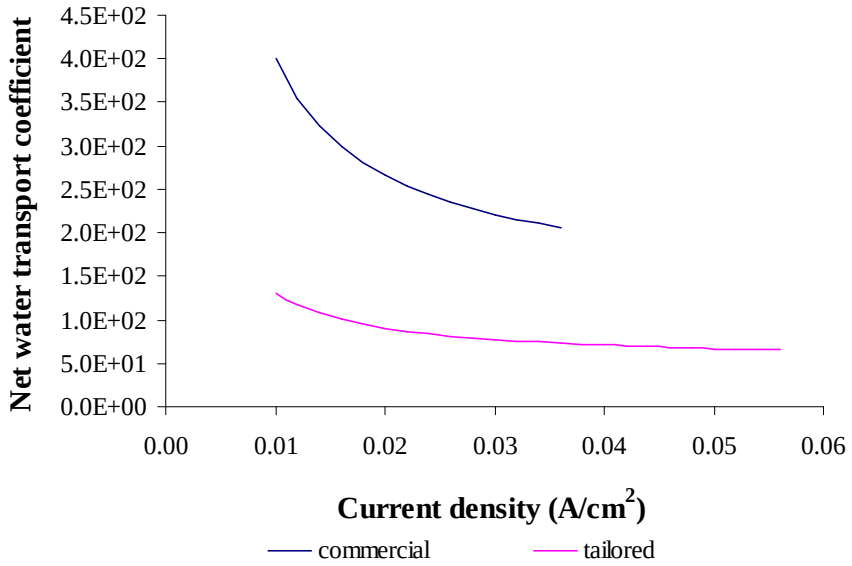

Figure 5.55 – Model prediction for the net water transport coefficient for different MEAs. Operating conditions: methanol concentration 5M, methanol flow rate 3 ml/min, air flow rate 3.6 l/min and fuel cell temperature 20ºC.

5.2. Concluding remarks

The performance of a direct methanol fuel cell operating near atmospheric pressure has been studied to systematically evaluate the effects of operating parameters such as methanol concentration, fuel cell temperature, methanol and air flow rates and design parameters on the DMFC performance.

The effect of the design parameters such as the anode gas diffusion layer media, the cathode gas diffusion layer media, the membrane thickness, the catalyst loading and the anode and cathode flow field design on the direct methanol fuel cell performance and power, has been, also, experimentally investigated. Most of the obtained results were explained under the light of the predictions of the methanol crossover rate, the methanol and oxygen concentration profiles, the net water transport coefficient and the anode and cathode overpotential from the developed and validated model presented in Chapter 3.

Based on the results presented in this chapter it can be concluded that the fuel cell performance significantly increases with the introduction of the gas diffusion layers. For this specific cell design and operating conditions the optimum methanol concentration is 0.75 M with air as oxidant. Higher values of methanol and air flow rates have a positive effect on cell voltage and power. The effect of the air flow rate is less pronounced than

the impact of methanol flow rate. Regarding the design parameters it was found that the choice of material to be used as anode gas diffusion layer depends on the methanol concentration. Using carbon paper instead of carbon cloth for anode diffusion layer increases the cell performance for higher methanol concentration levels. In opposite for low methanol concentration, the use of carbon cloth instead of carbon paper increases the fuel performance. When a fuel cell is operated with high methanol concentration, large amounts of methanol crossover are generated. Since carbon paper is less porous than carbon cloth limits the amount of methanol that crosses the membrane reducing in some extend the major loss on performance when working a fuel cell with high methanol concentrations. For the cathode side, using carbon cloth instead of carbon paper and ELAT as gas diffusion layer increases the cell performance. Increasing the membrane thickness leads to a lower methanol crossover rate through the membrane increasing the fuel cell performance. Thicker anode catalyst layers create a higher resistance to methanol diffusion reducing the methanol crossover. Thicker cathode catalyst layers enable an increase of the number of catalyst particles available for the oxygen reduction.

The effect of anode and cathode flow field design on the direct methanol fuel cell performance, operating near ambient pressure, has been, also, experimentally investigated. It has been shown that various flow field designs have a large impact on the fuel cell performance and power due to their different ability to provide fuel and remove produced water and carbon dioxide. Based on the results of these experiments, for this specific cell design and operating conditions, it can be concluded that the fuel cell performance significantly increases with the use of MFF as the anode flow field design and MSFF as the cathode flow field design. For the three values of methanol flow rate tested, for low values of fuel cell temperature and low values of methanol concentration the use of MFF as anode flow field design has a positive effect on cell voltage and power. For high values of fuel cell temperature the three anode flow field designs used show similar performances. For high values of methanol feed concentrations, an important operating condition for portable applications, the use of MSFF as the anode flow field design conducts to a better performance. Similarly, for the two values of air flow rate tested, for low values of fuel cell temperature and low values of methanol concentration the use of MSFF as cathode flow field design has a positive effect on cell voltage and power. For high values of fuel cell temperature the

use of SFF as cathode flow field design conducts to a better performance. For higher values of methanol concentration the use of SFF and MSFF as cathode flow field design shows similar performances. The results presented can be used for the validation of CDF models.

Reducing the membrane water and methanol transport from the anode to the cathode of a DMFC is of significant importance to achieve higher cell performances and consequently increased power densities, especially for portable applications. Based on the experimental results, a tailored MEA was proposed to achieve low methanol and water crossover and high power density, operating at high methanol concentrations. The resulting MEA provides a basic element for future DMFC systems using high concentration or pure methanol.

CHAPTER 6

6. PASSIVE FEED DIRECT METHANOL FUEL CELL

The imminent introduction of the passive DMFCs in the market strongly motivated the development of the work presented in this chapter.

As was mentioned before, models are a fundamental tool for the design process of fuel cells and fuel cell systems. Based on the model developed for the active feed direct methanol fuel cell, a steady state, one-dimensional, multi-component and thermal model is described and applied to simulate the operation of a passive direct methanol fuel cell. The model takes into account the thermal and mass transfer effects, along with the electrochemical reactions occurring in the passive DMFC. The model can be used to predict the methanol, oxygen, carbon dioxide and water concentration profiles in the anode, cathode and membrane as well as to estimate the methanol and water crossover and the temperature profile across the cell. The model was validated with data from experiments conducted in an «in-house» designed passive DMFC and with recent published data [160]. For the experimental studies of the passive feed direct methanol fuel cells (DMFCs), the necessary equipment and facilities for running the tests were installed. The last part of the experimental setup section describes the passive feed DMFC designed and constructed for this work. Steady state experiments at ambient pressure, close to room temperature at different methanol concentrations were carried out. The effect of design parameters (such as the membrane thickness, catalyst loading, diffusion layers materials and thicknesses) on the fuel cell performance and net water transport coefficient was studied under the light of the developed model for the passive DMFC.

The contents of this Chapter conducted to the preparation and submission of two papers: Oliveira, V.B, Rangel, C.M. and Pinto, A.M.F.R., "One-dimensional and non-isothermal model for a passive DMFC" submitted to International Journal of Heat and Mass Transfer and Oliveira, V.B, Rangel, C.M. and Pinto, A.M.F.R., "Water management in a passive DMFC" submitted to Journal of Power Sources.

6.1. Model Formulation for a passive feed DMFC

6.1.1. General model structure

A schematic representation of a passive feed direct methanol fuel cell is shown in Fig. 6.1, consisting of

- an acrylic plate (AAP) containing the fuel tank, a copper plate (ACP), a diffusion layer (AD) and a catalyst layer (AC) at the anode side;
- a polymer electrolyte membrane (M);
- a catalyst layer (CC), a diffusion layer (CD), a copper plate (CCP), and an acrylic plate (CAP) at the cathode side.

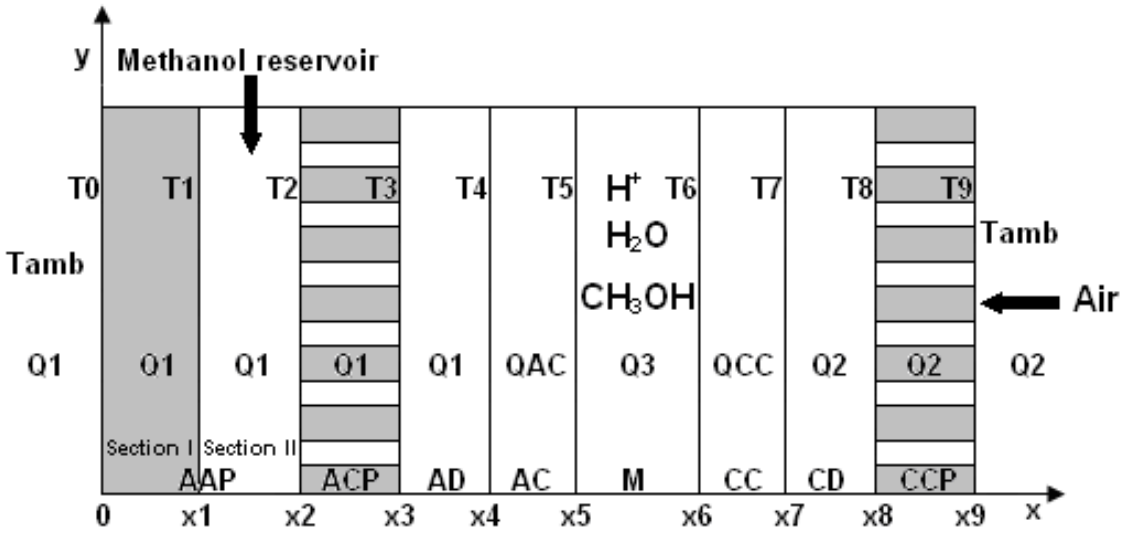

Figure 6.1 – Schematic representation of a passive DMFC.

In a passive-feed DMFC the fuel, methanol or an aqueous methanol solution, and the oxidant are supplied to the reaction zone by natural convection. From the ACP through the AD and from the AC through the M, methanol solution is transported primarily by diffusion. In a similar way the transport of oxygen on the CCP, CD and CC is enhanced by diffusion. After being produced by methanol oxidation, which takes place in the AC, the carbon dioxide produced moves counter-currently toward the fuel tank. At sufficiently high current densities carbon dioxide emerges in the form of gas bubbles from the surface of the AC. In the CC, oxygen reacts with protons and electrons

generating water. The water produced in CC moves counter-currently toward the open channels of the CCP and also under some operating conditions, by back diffusion toward the anode.

6.1.2. Model assumptions

As already referred, the direct methanol fuel cell is a multiphase system involving simultaneous mass, charge and energy transfer. Following the modelling studies presented in Chapter 3 for the active feed DMFC a one-dimensional model is presented now, for the passive feed DMFC, with the following simplifications and assumptions:

- the fuel cell is assumed to operate under steady-state conditions;
- the transport of heat and mass through the gas diffusion and catalyst layers is assumed to be a diffusion-predominated process and the convection effect is negligible;
- mass transport in the diffusion layers and membrane is described using effective Fick models;
- the thermal energy model is based on the differential thermal energy conservation equation (Fourier's law);
- pressure gradient across the layers is negligible;
- only the liquid phase is considered in the anode side, so carbon dioxide remains dissolved in solution;
- gaseous methanol and water are considered in the cathode;
- solutions are considered ideal and dilute;
- local equilibrium at interfaces is represented by partition functions;
- the catalyst layers are assumed to be macro-homogeneous porous electrodes so reactions in these layers are modelled as a homogeneous reaction;
- anode kinetics is described by step mechanism, with a rate expression similar to the used by Meyers *et al.* [26];
- the anodic and cathodic overpotential is constant through the catalyst layers;

- cathode kinetics is described by Tafel equation;
- methanol and water transport through the membrane is assumed to be due to the combined effect of the concentration gradient between the anode and the cathode and the electro-osmosis force;
- on the anode side, the heat and mass transfer of methanol from the bulk solution to the ACP is assumed to be driven by natural convection;
- on the cathode side, the heat and mass are transfer between the CCP and the ambient by natural convection;
- the heat generation by electrochemical reactions occurring in the catalyst layers is considered;
- when compared with the heat generated by electrochemical reactions and overpotential, the heat released by joule effects is ignored;
- the temperatures of the external walls of the cell (T_0 and T_9 in Fig. 6.1) are known;
- the heat flux generated in the catalyst layers is assumed to be constant.

The major differences between the two models (active and passive feed DMFC) regard the end plate, current collector plate and the flow field channels. The passive feed does not have the flow field layer. The end plates are made by different materials and the current collector plates have holes. In the passive feed systems, and as already referred, the fuel and the oxidant supply is made by natural convection instead of forced convection (active feed) having the two models, for this reason, different correlations and equations.

6.1.3. Governing equations and Boundary conditions – Anode and Cathode

6.1.3.1. Mass transport

<u>Anode reaction:</u>

Methanol oxidation: $CH_3OH + H_2O \rightarrow CO_2 + 6H^+ + 6e^-$ (6.1)

Cathode reaction:

Oxygen reduction: $O_2 + 4H^+ + 4e^- \rightarrow 2H_2O$ (6.2)

Methanol oxidation: $CH_3OH + \frac{3}{2}O_2 \rightarrow CO_2 + 2H_2O$ (6.3)

The transport processes of methanol and water from the fuel tank to the ACP are described by

$$N_j = h_{mass,j}^{AAP}\left(C_j^0 - C_j^{AAP}\right) \quad (6.4)$$

where j represents methanol or water and the $h_{mass,j}^{AAP}$ represents the mass transfer coefficient of the species j

In the anode copper plate, diffusion and catalyst layer, the methanol and water flux are related to the corresponding concentration gradients by assuming Fickian diffusion [171] with an effective diffusivity $D_j^{eff,ACP}$ in the ACP, $D_j^{eff,AD}$ in the AD and $D_j^{eff,AC}$ in the AC. The methanol and water fluxes can be determined from:

$$N_j = -D_j^{eff,ACP}\frac{dC_j^{ACP}}{dx}, \ j \text{ represents methanol or water,} \quad (6.5)$$

$$N_j = -D_j^{eff,AD}\frac{dC_j^{AD}}{dx}, \ j \text{ represents methanol or water} \quad (6.6)$$

and

$$N_j = -D_j^{eff,AC}\frac{dC_j^{AC}}{dx}, \ j \text{ represents methanol or water} \quad (6.7)$$

The concentration at the AAP/ACP, ACP/AD and AD/AC interfaces is given by assuming local equilibrium with partition coefficients K_2, K_3 and K_4, respectively. The boundary conditions for Eq. (6.5), (6.6) and (6.7) are (see Fig. 6.1)

$$At\ x = x_2: \quad C_{2,j}^{ACP} = K_2 C_j^{AAP},\ j \text{ represents methanol or water} \tag{6.8}$$

$$At\ x = x_3: \quad C_{3,j}^{AD} = K_3 C_{3,j}^{ACP},\ j \text{ represents methanol or water} \tag{6.9}$$

$$At\ x = x_4: \quad C_{4,j}^{AC} = K_4 C_{4,j}^{AD},\ j \text{ represents methanol or water} \tag{6.10}$$

$$At\ x = x_5: \quad C_j^{AC} = C_{5,j}^{AC},\ j \text{ represents methanol or water} \tag{6.11}$$

In fuel cells, all the fluxes can be related to a single characteristic flux, the current density or charge flux of the fuel cell. In the DMFC, the methanol flux is related to the current density and the permeation flux of methanol through the membrane, ($N_{CH_3OH}^{M}$), by:

$$N_{CH_3OH} = \frac{I_{Cell}}{6F} + N_{CH_3OH}^{M} \tag{6.12}$$

At the anode side, the water flux is related to the current density and to the net water transport coefficient, α (defined, as before, as the ratio of the net water flux though the membrane from the anode to the cathode normalized by the protonic flux), by:

$$N_{H_2O} = \frac{I_{Cell}}{6F}(\alpha + 1) \tag{6.13}$$

As well as for the model presented in Chapter 3, the transport of methanol and water through the membrane is assumed to be due to the combined effect of the concentration gradient and the electro-osmosis force. The fluxes can be determined from:

$$N_{CH_3OH}^{M} = -D_{CH_3OH}^{eff,M} \frac{dC_{CH_3OH}^{M}}{dx} + \xi_{CH_3OH} \frac{I_{Cell}}{F} \tag{6.14}$$

$$N_{H_2O}^{M} = \alpha \frac{I_{Cell}}{6F} = -D_{H_2O}^{eff,M} \frac{dC_{H_2O}^{M}}{dx} + n_d \frac{I_{Cell}}{F} \tag{6.15}$$

The electro-osmotic drag (ξ_{CH_3OH}, n_d), in equations (6.14) and (6.15), is defined as the number of methanol or water molecules dragged by the hydrogen ions moving through the membrane.

The net water transport coefficient, α, can be calculated using the equation (6.15).
The concentration at the AC/membrane interface is given by assuming local equilibrium with a partition coefficient K_5. The boundary conditions for the integration of equations (6.14) and (6.15) is given by

$$At\ x = x_5: \quad C_{5,j}^{M} = K_5 C_{5,j}^{AC},\ j \text{ represents methanol or water} \tag{6.16}$$

In the cathode catalyst layer, the methanol, water and oxygen flux are related to the concentration gradient by assuming Fickian diffusion [171] with an effective diffusivity $D_j^{eff,CC}$. The flux can be determined from:

$$N_j = -D_j^{eff,CC} \frac{dC_j^{CC}}{dx},\ j \text{ represents methanol, water or oxygen} \tag{6.17}$$

As for the active feed DMFC it is here considered that the entire methanol crossing the membrane reacts at the cathode catalyst layer so the concentration at the CC/CD interface is zero. It is assumed that there is no oxygen crossover, so the oxygen concentration in CC/M interface is zero. The concentration of water and methanol at the membrane/CC interface and the concentration of water and oxygen at the CC/CD interface are given by assuming local equilibrium with a partition coefficient K_6 and K_7, respectively. The boundary conditions for Eq. (6.17) are:

$$At\ x = x_6: \quad C_{6,j}^{CC} = K_6 C_{6,j}^{M},\ j \text{ represents methanol or water and } C_{6,O_2}^{CC} = 0 \tag{6.18}$$

$$At\ x = x_7: \quad C_{CH_3OH}^{CC} \cong 0,\ C_{H_2O}^{CC} = C_{7,H_2O}^{CC} \text{ and } C_{O_2}^{CC} = C_{7,O_2}^{CC} \tag{6.19}$$

At the cathode catalyst layer, the oxygen reacts with the electrons and protons to produce water. However, part of oxygen fed is consumed due to methanol crossover to form an internal current and a mixed potential. Therefore the oxygen flux is related to the current density and the permeation flux of methanol through the membrane by

$$N_{O_2} = \upsilon_{O_2} \frac{I_{Cell}}{4F} + \upsilon_{cross,O_2} N_{CH_3OH}^{M} \tag{6.20}$$

where

$\upsilon_{O_2} = 1$ and $\upsilon_{cross,O_2} = 3/2$

At the cathode side, the water flux is related to the water production from the oxygen reduction reaction and methanol crossover oxidation and to the net water flux transported from the anode to the cathode by:

$$N_{H_2O} = \upsilon_{H_2O} \frac{I_{Cell}}{4F} + \upsilon_{cross,H_2O} N^{M}_{CH_3OH} + N^{M}_{H_2O} \tag{6.21}$$

where

$\upsilon_{H_2O} = 2$, $\upsilon_{cross,H_2O} = 2$

In the cathode diffusion layer and cathode copper plate the oxygen and water fluxes are related to the corresponding concentration gradients by

$$N_i = -D_i^{eff,CD} \frac{dC_i^{CD}}{dx}, \; i \text{ represents oxygen or water vapour} \tag{6.22}$$

$$N_i = -D_i^{eff,CCP} \frac{dC_i^{CCP}}{dx}, \; i \text{ represents oxygen or water vapour} \tag{6.23}$$

where $D_i^{eff,CD}$ and $D_i^{eff,CCP}$ are the effective diffusion coefficients of oxygen and water in the CD and CCP.

The concentration at the CC/CD and CD/CCP interfaces is given by assuming local equilibrium with a partition coefficient K_7 and K_8. The boundary conditions for Eq. (6.22) and (6.23) are

$$At\ x = x_7: \quad C_{7,i}^{CD} = K_{7,i} C_{7,i}^{CC}, \; i \text{ represents oxygen or water vapour} \tag{6.24}$$

$$At\ x = x_8: \quad C_{8,i}^{CCP} = K_{8,i} C_{8,i}^{CD}, \; i \text{ represents oxygen or water vapour} \tag{6.25}$$

Like at the anode side, the transport process of oxygen from the air to the CCP is described by

$$N_i = h^C_{mass,i}\left(C^0_i - C^{CCP}_{9,i}\right) \tag{6.26}$$

where i represents oxygen and $h^C_{mass,i}$ represents the mass transfer coefficient of the species i

It is assumed that the air at the CCP is in a saturated state, then the water vapour feed concentration (C^0_{8,H_2O}) is equal to water vapour concentration ($C^{0,sat}_{8,H_2O}$) and can be determined from the saturated pressure of moist air.

To account for the effect of methanol crossover on the cathode overpotential it is assumed that the methanol crossing the membrane completely reacts electrochemically at the cathode. In this way the internal current (I_{CH_3OH}) due to methanol oxidation can be written as

$$I_{CH_3OH} = 6FN^M_{CH_3OH} \tag{6.27}$$

where the methanol flux in the membrane ($N^M_{CH_3OH}$) is obtained from Eq. (6.14).

The volumetric current density expression for methanol oxidation is taken from Meyers *et al.* [26] as

$$j_A = aI^{CH_3OH}_{0,ref}\frac{kC^{AC}_{CH_3OH}}{C^{AC}_{CH_3OH} + \lambda\exp\left(\dfrac{\alpha_A\eta_A F}{RT_{AC}}\right)}\exp\left(\frac{\alpha_A\eta_A F}{RT_{AC}}\right) \tag{6.28}$$

The current density is related to the volumetric current density using the following equation

$$I_{Cell} = \int_{x_{51}}^{x_6} j_A\,dx = \int_{x_5}^{x_6} aI^{CH_3OH}_{0,ref}\frac{kC^{AC}_{CH_3OH}}{C^{AC}_{CH_3OH} + \lambda\exp\left(\dfrac{\alpha_A\eta_A F}{RT_{AC}}\right)}\exp\left(\frac{\alpha_A\eta_A F}{RT_{AC}}\right)dx \tag{6.29}$$

Equation (6.29) is used to calculate the anode overpotential for a given I_{Cell}, assuming η_A as constant in the anode catalyst layer AC.

At the cathode, the electrochemical reaction is modelled using Tafel equation for the oxygen reduction taking in account the mixed potential. The cathode overpotential can then be determined from:

$$I_{Cell} + I_{CH_3OH} = I_{0,ref}^{O_2} \frac{C_{O_2}^{CC}}{C_{O_2,ref}^{CC}} \exp\left(\frac{\alpha_C \eta_C F}{RT_{CC}}\right) \tag{6.30}$$

The mass transfer coefficient in Eq. (6.4) can be determined from [172]:

$$Sh = \frac{h_{mass} L}{D} = \left[0.825 + \frac{0.387 \times Ra^{1/6}}{\left(1 + (0.492/Sc)^{9/16}\right)^{8/27}}\right]^2 \tag{6.31}$$

where Ra is the Rayleigh number ($Ra = Gr \times Sc$), Sc the Schmidt number ($Sc = \nu / D$) and Gr is the Grashof number $\left(Gr = \frac{g \Delta C L^3}{C \nu^2}\right)$.

6.1.3.2. Heat transport

Based on the simplifications and assumptions described previously, the following overall heat transfer equation can be proposed (see Fig. 6.1):

$$Q^{AC} + Q^{CC} = Q_1 + Q_2 \tag{6.32}$$

The total heat generated in the DMFC is equal to the heat losses to the surrounding environment at the anode and cathode.
Complementarly, the following heat transfer balances can be written:

$$Q_3 = Q^{AC} - Q_1 \tag{6.33}$$

$$Q_2 = Q^{CC} + Q_3 \tag{6.34}$$

At the anode, heat generated by the electrochemical reaction in the AC is given by

$$Q^{AC} = I_{Cell}\eta_A - I_{Cell}\left(\frac{\Delta H_A - \Delta G_A}{6F}\right) \tag{6.35}$$

In this equation the first term represents the heat due to the activation and mass transfer overpotentials at the anode and the second term represents the entropy change of the anodic electrochemical reaction, with ΔH_A denoting the anodic reaction enthalpy and ΔG_A the Gibbs free energy.

In a similar way, the heat generated at the CC, can be determined from

$$Q^{CC} = (I_{Cell} + I_{CH_3OH})\eta_C - I_{Cell}\left(\frac{\Delta H_C - \Delta G_C}{4F}\right) \tag{6.36}$$

where the first term represents the heat due to the activation and mass transfer overpotentials and mixed potential caused by methanol crossover through the cathode and the second term represents the entropy change of the cathodic electrochemical reaction, with ΔH_C denoting the cathodic reaction enthalpy and ΔG_C, the Gibbs free energy.

In the anode acrylic plate section I and diffusion layer the heat flux Q_1 can be related to the temperature gradient across each layer, using the Fourier's law, as

$$Q = -K^l A_a \frac{dT}{dx} \tag{6.37}$$

where l represents $AAP_{sectionI}$ or AD and A_a represents the active area

In the anode acrylic plate section II the heat flux Q_1 can, also, be related to the temperature gradient across this layer, using Newton's law, as

$$Q = -h_{heat} A_t \Delta T \tag{6.38}$$

At the cathode side and membrane, the heat fluxes Q_2 and Q_3 can be related to the temperature gradient across the CD and M layers as

$$Q = -K^{t} A_a \frac{dT}{dx} \tag{6.39}$$

where t represents CD or M.

In a passive DMFC the copper plate has holes machined on the surface, to allow the reactant to reach the catalyst layers (Fig. 6.1). The establishment of the heat transport equations, in this layer, involved the consideration of two zones. In one zone the heat is transferred by conduction and in the other (holes) the heat is transferred by convection. Using the thermal resistance concept [172] we get:

$$Q = \frac{\Delta T}{R_{total}} \text{ were} \tag{6.40}$$

$$\frac{1}{R_{total}} = \frac{1}{R_{cond}} + \frac{1}{R_{conv}} \text{ since the resistances are in parallel} \tag{6.41}$$

$$R_{cond} = \frac{\delta}{A_1 \times K} \tag{6.42}$$

$$R_{conv} = \frac{1}{A_{holes} \times h_{heat}} \text{ and} \tag{6.43}$$

$$A_a = A_1 + A_{holes} \tag{6.44}$$

The differential equations describing the temperature profiles at the anode and cathode catalyst layers are:

$$\frac{d^2T}{dx^2} = \frac{Q^{AC}}{K^{AC}\delta^{AC}} \tag{6.45}$$

$$\frac{d^2T}{dx^2} = \frac{Q^{CC}}{K^{CC}\delta^{CC}} \tag{6.46}$$

where Q^{AC} and Q^{CC} are, respectively, the heat generated in the anode catalyst layer and cathode catalyst layer.

The boundary conditions for Eq. (6.45) and (6.46) are the temperatures at the walls (T_4, T_5, T_6 and T_7).

For these layers. Fourier's law gives

$$At\ x = x_4: \quad Q_1 = -K^{AC} A_a \frac{dT}{dx} \tag{6.47}$$

$$At\ x = x_6: \quad Q_3 = -K^{CC} A_a \frac{dT}{dx} \tag{6.48}$$

where $\frac{dT}{dx}$ is calculated using the temperature profile obtained from the integration of equations (6.45) and (6.46).

Finally, the heat transfer from the AAP section I and CCP to the ambient air can be described using the Newton's law as

$$Q = -h_{heat} A_t \Delta T \tag{6.49}$$

The heat transfer coefficient, due to natural convection (Eq. 6.38), can be determined from [172]:

$$Nu = \frac{h_{heat} L}{K} = \left[0.825 + \frac{0.387 \times Ra^{1/6}}{\left(1 + \left(0.492 / \Pr\right)^{9/16}\right)^{8/27}} \right]^2 \tag{6.50}$$

where Ra is the Rayleigh number ($Ra = Gr \times \Pr$), Pr the Prandtl number ($\Pr = \nu / K$), Gr is the Grashof number $\left(Gr = \frac{g\beta \Delta T L^3}{\nu^2} \right)$ and L is the length of the active area, cm.

6.1.4. Cell performance

The determination of methanol and oxygen concentrations at the catalyst layers, the temperature profiles and the anodic and cathodic overpotentials from the model equations enables prediction of the cell voltage, which can be expressed as:

$$V_{Cell} = E_{Cell} - \eta_A - \eta_C - I_{Cell} R_{Cell} \tag{6.51}$$

where

$$E_{Cell} = U_{O_2} - U_{CH_3OH} + \Delta T\left(\frac{\partial E}{\partial T}\right), \tag{6.52}$$

η_A and η_C are the anode and cathode overpotencials and the membrane resistance R_{Cell} is given by

$$R_{Cell} = \frac{\delta^M}{\kappa} \tag{6.53}$$

where δ^M is membrane thickness and κ is the ionic conductivity of the membrane.

6.1.5. Analytical solutions - Mass transport

The methanol and water concentration profiles in AAP (section II) can be obtained combining Eqs. (6.4) and (6.12) or (6.4) and (6.13):

$$C_{CH_3OH}^{AAP} = C_{CH_3OH}^{0} - \frac{1}{h_{mass,CH_3OH}^{AAP}}\left(\frac{I_{Cell}}{6F} + N_{CH_3OH}^{M}\right) \tag{6.54}$$

$$C_{H_2O}^{AAP} = C_{H_2O}^{0} - \frac{I_{Cell}}{h_{mass,H_2O}^{AAP}\,6F}(\alpha+1) \tag{6.55}$$

Combining equations (6.5), (6.8) and (6.12) or (6.13) yields the concentration profile in holes section of the ACP. The concentration profiles in the AD are obtained by combining Eqs. (6.6), (6.9) and (6.12) or (6.13). The solutions are:

$$C_{CH_3OH}^{ACP} = K_2 C_{CH_3OH}^{AAP} + \frac{I_{Cell}}{6FD_{CH_3OH}^{eff,AD}}(x_2 - x) + \frac{N_{CH_3OH}^{M}}{D_{CH_3OH}^{eff,AD}}(x_2 - x) \tag{6.56}$$

$$C_{H_2O}^{ACP} = K_2 C_{H_2O}^{AAP} + \frac{I_{Cell}(\alpha+1)}{6FD_{H_2O}^{eff,AD}}(x_2 - x) \tag{6.57}$$

$$C_{CH_3OH}^{AD} = K_3 C_{3,CH_3OH}^{ACP} + \frac{I_{Cell}}{6FD_{CH_3OH}^{eff,AD}}(x_3 - x) + \frac{N_{CH_3OH}^{M}}{D_{CH_3OH}^{eff,AD}}(x_3 - x) \tag{6.58}$$

$$C_{H_2O}^{AD} = K_3 C_{3,H_2O}^{ACP} + \frac{I_{Cell}(\alpha + 1)}{6FD_{H_2O}^{eff,AD}}(x_3 - x) \tag{6.59}$$

The methanol and water concentration profile in the AC can be obtained combining Eqs. (6.7), (6.10) and (6.12) or (6.7), (6.10) and (6.13):

$$C_{CH_3OH}^{AC} = K_4 C_{4,CH_3OH}^{AD} + \frac{I_{Cell}}{6FD_{CH_3OH}^{eff,AC}}(x_4 - x) + \frac{N_{CH_3OH}^{M}}{D_{CH_3OH}^{eff,AC}}(x_4 - x) \tag{6.60}$$

$$C_{H_2O}^{AC} = K_4 C_{4,H_2O}^{AD} + \frac{I_{Cell}(\alpha + 1)}{6FD_{H_2O}^{eff,AC}}(x_4 - x) \tag{6.61}$$

The concentration of methanol and water through the membrane can be obtained by using Eqs. (6.12) and (6.16) or (6.13) and (6.16):

$$C_{CH_3OH}^{M} = K_5 C_{5,CH_3OH}^{AC} + \frac{N_{CH_3OH}^{M} - \frac{\xi_{CH_3OH} I_{Cell}}{F}}{D_{CH_3OH}^{eff,M}}(x_5 - x) \tag{6.62}$$

$$C_{H_2O}^{M} = K_5 C_{5,H_2O}^{AC} + \frac{I_{Cell}}{6FD_{H_2O}^{eff,M}}(x_5 - x) - \frac{ndI_{Cell}}{FD_{H_2O}^{eff,M}}(x_5 - x) \tag{6.63}$$

Combining Eqs. (6.12), (6.16) and (6.18) leads to an expression to calculate the methanol flux through the membrane:

$$N_{CH_3OH}^{M} = \frac{D_{CH_3OH}^{eff,M}}{\delta^{M}}\left(K_5 C_{5,CH_3OH}^{AC} - C_{6,CH_3OH}^{M}\right) + \frac{\xi_{CH_3OH} I_{Cell}}{F} \tag{6.64}$$

The concentration of methanol, water and oxygen through the CC can be obtained by combining Eqs. (6.17), (6.18), (6.19), (6.20) and (6.21):

$$C_{CH_3OH}^{CC} = C_{6,CH_3OH}^{CC} - \frac{I_{Cell}}{6FD_{CH_3OH}^{eff,CC}}(x_6 - x) + \frac{N_{CH_3OH}^{M}}{D_{CH_3OH}^{eff,CC}}(x_6 - x) \tag{6.65}$$

$$C_{H_2O}^{CC} = C_{6,H_2O}^{CC} + \frac{(x_6 - x)}{D_{H_2O}^{eff,CC}}\left(\frac{\alpha I_{Cell}}{6F} + \frac{0.5 I_{Cell}}{F} + \frac{I_{CH_3OH}}{3F}\right) \tag{6.66}$$

$$C_{O_2}^{CC} = C_{7,O_2}^{CC} + \frac{I_{Cell}}{4FD_{O_2}^{eff,CC}}(x_7 - x) + \frac{3}{2}\frac{N_{CH_3OH}^{M}}{D_{O_2}^{eff,CC}}(x_7 - x) \tag{6.67}$$

Combining equations (6.21), (6.22) and (6.24) or (6.20), (6.22), and (6.24) gives the concentration profile in CD.

$$C_{O_2}^{CD} = K_{7,O_2} C_{7,O_2}^{CC} + \frac{I_{Cell}}{4FD_{O_2}^{eff,CD}}(x_7 - x) + \frac{3}{2}\frac{N_{CH_3OH}^{M}}{D_{O_2}^{eff,CD}}(x_7 - x) \tag{6.68}$$

$$C_{H_2O}^{CD} = K_{7,H_2O} C_{7,H_2O}^{CC} + \frac{(x_7 - x)}{D_{H_2O}^{eff,CD}}\left(\frac{\alpha I_{Cell}}{6F} + \frac{0.5 I_{Cell}}{F} + \frac{I_{CH_3OH}}{3F}\right) \tag{6.69}$$

The concentration of oxygen and water through the CCP can be obtained using Eqs. (6.21), (6.23) and (6.25), (6.20) or (6.23) and (6.25):

$$C_{O_2}^{CCP} = K_{8,O_2} C_{8,O_2}^{CD} + \frac{I_{Cell}}{4FD_{O_2}^{eff,CCP}}(x_8 - x) + \frac{3}{2}\frac{N_{CH_3OH}^{M}}{D_{O_2}^{eff,CD}}(x_8 - x) \tag{6.70}$$

$$C_{H_2O}^{CCP} = K_{8,H_2O} C_{8,H_2O}^{CD} + \frac{(x_8 - x)}{D_{H_2O}^{eff,CCP}}\left(\frac{\alpha I_{Cell}}{6F} + \frac{0.5 I_{Cell}}{F} + \frac{I_{CH_3OH}}{3F}\right) \tag{6.71}$$

From the solutions above a expression to calculate the C_{5,CH_3OH}^{AC}, C_{6,CH_3OH}^{M}, C_{7,O_2}^{CC}, C_{5,H_2O}^{M}, C_{6,H_2O}^{M} and α is obtained:

$$C_{5,CH_3OH}^{AC} = \frac{K_4 K_3 K_2 C_{CH_3OH}^0 - \frac{I_{Cell} C_1}{6F} - \frac{\xi_{CH_3OH} I_{Cell} C_1}{F} + \frac{D_{CH_3OH}^{eff,M} C_1 C_{6,CH_3OH}^M}{\delta^M}}{1 + \frac{D_{CH_3OH}^{eff,M} K_5 C_1}{\delta^M}} \tag{6.72}$$

where:

$$C_1 = \frac{\delta^{AC}}{D_{CH_3OH}^{eff,AC}} + \frac{K_4 \delta^{AD}}{D_{CH_3OH}^{eff,AD}} + \frac{K_4 K_3 \delta^{ACP}}{D_{CH_3OH}^{eff,ACP}} + \frac{K_4 K_3 K_2}{h_{mass,CH_3OH}^{ACP}} \tag{6.73}$$

$$C_{6,CH_3OH}^M = \frac{-\frac{I_{Cell} \delta^{CC}}{6F D_{CH_3OH}^{eff,CC} K_6} + \frac{\xi_{CH_3OH} I_{Cell} \delta^{CC}}{F D_{CH_3OH}^{eff,CC} K_6} + \frac{D_{CH_3OH}^{eff,M} \delta^{CC} K_5 C_{5,CH_3OH}^{AC}}{\delta^M D_{CH_3OH}^{eff,CC} K_6}}{1 + \frac{D_{CH_3OH}^{eff,M} \delta^{CC}}{\delta^M D_{CH_3OH}^{eff,CC} K_6}} \tag{6.74}$$

$$C_{7,O_2}^{CC} = \frac{C_{O_2}^0}{K_{8,O_2} K_{7,O_2}} + \frac{C_2 I_{Cell}}{4F} + \frac{C_2 3 N_{CH_3OH}^M}{2} \tag{6.75}$$

where:

$$C_2 = \frac{\delta^{CD}}{D_{O_2}^{eff,CD} K_{7,O_2}} + \frac{\delta^{CCP}}{D_{O_2}^{eff,CCP} K_{8,O_2} K_{7,O_2}} - \frac{1}{h_{mass,O_2}^{CCP} K_{8,O_2} K_{7,O_2}} \tag{6.76}$$

$$C_{5,H_2O}^M = K_2 K_3 K_4 C_{H_2O}^0 - \frac{C_3 I_{Cell} (\alpha + 1)}{6F} \tag{6.77}$$

where:

$$C_3 = \frac{K_5 K_4 K_3 K_2}{h_{mass,H_2O}^{ACP}} + \frac{K_5 K_4 K_3 \delta^{ACP}}{D_{H_2O}^{eff,ACP}} + \frac{K_4 K_5 \delta^{AD}}{D_{H_2O}^{eff,AD}} + \frac{K_5 \delta^{AC}}{D_{H_2O}^{eff,AC}} \tag{6.78}$$

$$C_{6,H_2O}^M = \frac{C_{H_2O}^{sat}}{K_{8,H_2O} K_{7,H_2O} K_6} + \left(\frac{\alpha I_{Cell}}{6F} + \frac{I_{Cell}}{2F} + \frac{I_{CH_3OH}}{3F} \right) C_4 \tag{6.79}$$

where:

$$C_4 = \frac{\delta^{CD}}{K_{7,H_2O} K_6 D_{H_2O}^{eff,CD}} + \frac{\delta^{CC}}{K_6 D_{CH_3OH}^{eff,CC}} \tag{6.80}$$

and

$$\alpha = -\frac{6FD_{H_2O}^{eff,M}}{I_{Cell}} \left(\frac{C_{6,H_2O}^{M} - C_{5,H_2O}^{M}}{\delta^{M}} \right) + 6n_d \tag{6.81}$$

The model simulations presented in Chapter 6 section 6.3 were obtained based on the parameters listed in Table 6.1 and presented in Appendix B.

Table 6.1 – Values for the parameters used in the model equations.

Parameter	Value	Reference
U_{O_2}	1.24 V	[120]
U_{CH_3OH}	0.03 V	[120]
$\partial E / \partial T$	-1.4 $\times 10^{-4}$V/K	[166]
κ	0.036 S/cm	[120]
δ^{M}	0.018 cm	[120]
$\delta^{AAP\,section I,II}$	0.50 cm	real value
δ^{AD}, δ^{CD}	0.015 cm	real value
δ^{AC}, δ^{CC}	0.0023 cm	real value
$\varepsilon^{AD}, \varepsilon^{CD}$	0.71	[173]
ε^{AC}	0.81	[173]
ε^{CC}	0.86	[173]
a	1000 cm^{-1}	[120]
$I_{0,ref}^{CH_3OH}$	$9.425\times10^{-3} \exp((35570/R)(1/353 - 1/T))$ A/cm^2	[166]
$I_{0,ref}^{O_2}$	$4.222\times10^{-6} \exp((73200/R)(1/353 - 1/T))$ A/cm^2	[166]
k	7.5×10^{-4}	[120]
λ	2.8×10^{-9} mol/cm^3	[120]
α_A	0.52	[120]
α_C	1.55	[120]

K_{2-5} , K_{7-8,H_2O}	0.8	assumed
K_{7-8,O_2}	1.25	assumed
K_6	0.001	assumed
L	5 cm	real value
$D_{O_2}^{eff,CD,CC}$	$\varepsilon^{CD,CC^{2.5}}\left[\left(T^{1.75}\times 5.8\times 10^{-4}\right)/\left(27.772\times P\right)\right]$ cm^2/s	[174]
$D_{O_2}^{eff,CCP}$	$\left[\left(T^{1.75}\times 5.8\times 10^{-4}\right)/\left(27.772\times P\right)\right]$ cm^2/s	[174]
$D_{CH_3OH}^{eff,ACP}$	$\left[\left(7.608\times 10^{-7}\times T\right)/\left(\mu_{H_2O}\times 9.485\right)\right]$ cm^2/s	[174]
$D_{CH_3OH}^{eff,AD,AC}$	$\varepsilon^{AD,AC^{2.5}}\left[\left(7.608\times 10^{-7}\times T\right)/\left(\mu_{H_2O}\times 9.485\right)\right]$ cm^2/s	[174]
$D_{CH_3OH}^{eff,CC}$	$\varepsilon^{CC^{2.5}}\left[\left(T^{1.75}\times 5.8\times 10^{-4}\right)/\left(33.904\times P\right)\right]$ cm^2/s	[174]
$D_{CH_3OH}^{eff,M}$	$4.9\times 10^{-6}\exp\left(2436\times\left(1/333-1/T\right)\right)$ cm^2/s	[120]
$D_{H_2O}^{eff,ACP}$	$\left[\left(6.295\times 10^{-7}\times T\right)/\left(\mu_{CH_3OH}\times 5.833\right)\right]$ cm^2/s	[174]
$D_{H_2O}^{eff,AD,AC}$	$\varepsilon^{AD,AC^{2.5}}\left[\left(6.295\times 10^{-7}\times T\right)/\left(\mu_{CH_3OH}\times 5.833\right)\right]$ cm^2/s	[174]
$D_{H_2O}^{eff,CD,CC}$	$\varepsilon^{CD,CC^{2.5}}\left[\left(T^{1.75}\times 6.2\times 10^{-4}\right)/\left(25.523\times P\right)\right]$ cm^2/s	[174]
$D_{H_2O}^{eff,M}$	$2.0\times 10^{-6}\exp\left(2060\times\left(1/303-1/T\right)\right)$ cm^2/s	[87]
ξ_{CH_3OH}	$2.5\times x_{CH_3OH}$	[120]
n_d	$2.9\exp\left(1029\times\left(1/333-1/T\right)\right)$	[166]
δ^{ACP} , δ^{CCP}	0.05 cm	real value
K^M	0.0043 W/cmK	[173]
K^{AD}	$1.95+6.57\times 10^{-4}T$ W/mK	[173]
K^{CD}	$1.71+2.96\times 10^{-5}T$ W/mK	[173]
K^{AC}	$\left(1-\varepsilon^{AC}\right)\times 86.7+\varepsilon^{AC}\left(0.341+9.26\times 10^{-4}\right)$ W/mK	[173]
K^{CC}	$\left(1-\varepsilon^{CC}\right)\times 71+\varepsilon^{CC}\left(0.0034+7.60\times 10^{-5}\right)$ W/mK	[173]

6.2. Experimental Setup for a passive feed DMFC

6.2.1. Fuel cell design

A passive feed DMFC was «in-house» developed following the basic demands:

- use of standard state of the art materials available on the market;
- high flexibility, i. e. easy change exchange media connections;

- easy handling in terms of assembly and connections.

The cell consists of the following elements:

- membrane electrode assembly (MEA);
- diffusion layers;
- connector plates for electrical contacting and with holes to allow the reactants supply;
- isolating plates;
- end plates.

presented in Figures 6.2. and 6.3.

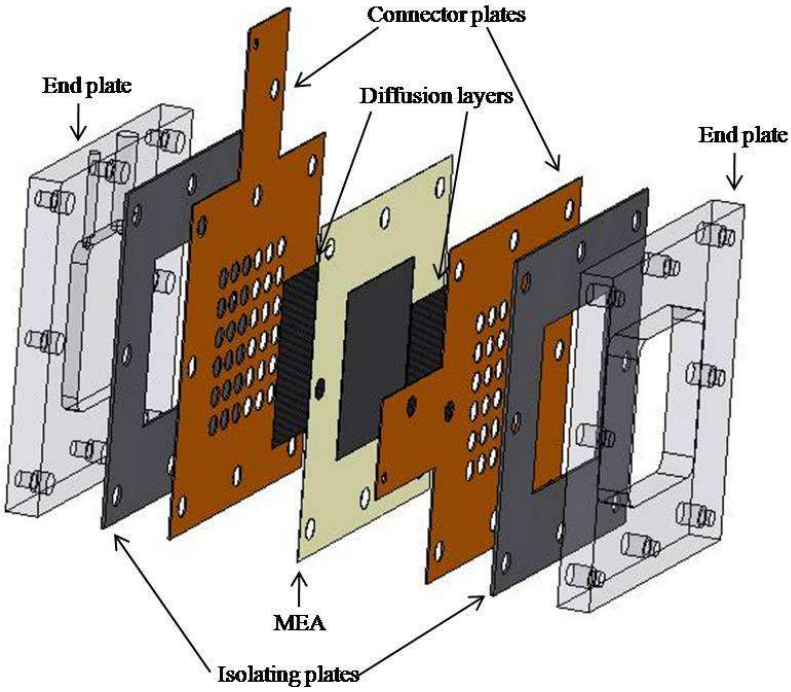

Figure 6.2 – 3D CAD drawing of the passive feed DMFC..

The fuel cell specifications, namely the cell components, their quantities and dimensions and the materials used, are displayed in Table 6.2.

Table 6.2 – Different elements of the passive feed DMFC.

Fuel cell – Specifications			
Cell active area	25 cm^2		
Total cell area	100 cm^2		
Cell components	**Material**	**Quantity**	**Dimensions (cm)**
Connector plates	gold plated copper	2	10x10x0.05
End plates	acrylic	2	10x10x1
Isolating plates	rubber	2	10x10x0.1
Anode catalyst layer	Platinum/Ruthenium 4 mg/cm^2	1	5x5x0.0023
Cathode catalyst layer	Platinum black 4 mg/cm^2	1	5x5x0.0023
Membrane	Nafion 117 and 115	1	5x5x(*)
Diffusion layers	carbon cloth	2	5x5x0.035

(*) this dimension depends on the material used.

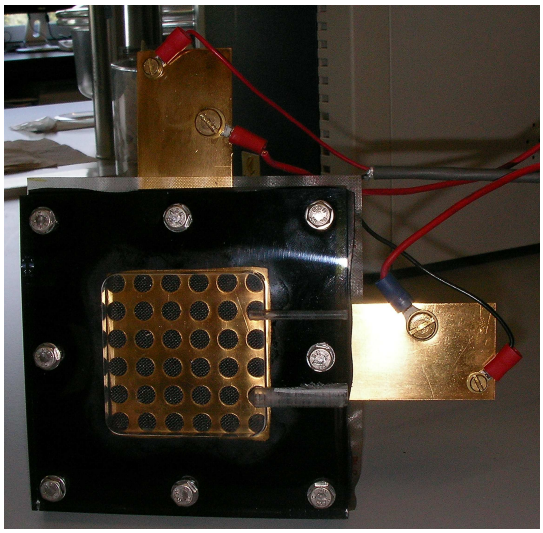

Figure 6.3 – Photograph of an «in-house» designed passive feed DMFC.

6.2.1.1. End Plates

Two 10 mm thick acrylic plates are used for bracing the cell and apply the desired tension on the cell elements, (Fig. 6.4 and Fig. 6.5). Both end plates are connected by a total of 8 bolts (diameter 6.2 mm), running through plastic bushes to prevent electrical contact between the end plates. As a standard, the cell is assembled applying a torque of 5 Nm on the bolts. The anode end plate, contacting with the copper plate, contains a chamber with 5 mm were the methanol solution is introduced (Fig. 6.4).

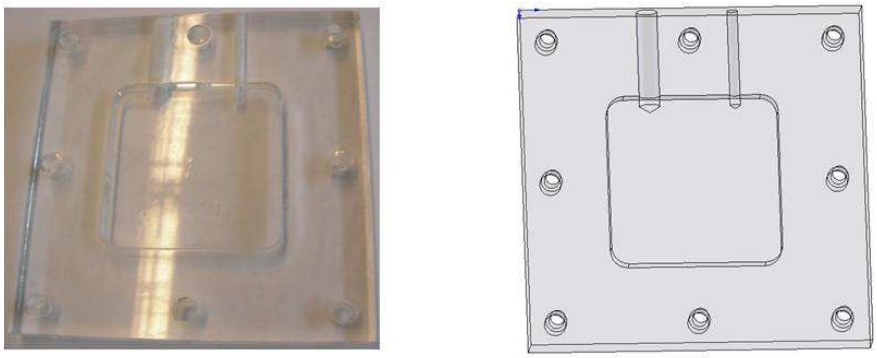

a) b)

Figure 6.4 – Anode end plate (acrylic) (a) photograph, (b) 3D CAD drawing.

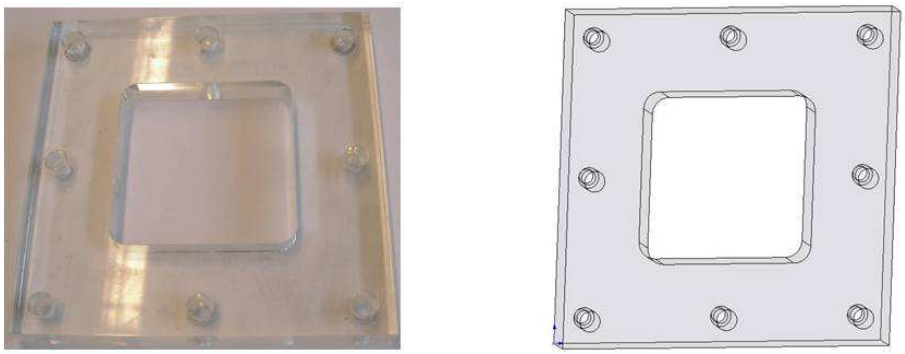

a) b)

Figure 6.5 – Cathode end plate (acrylic) (a) photograph, (b) 3D CAD drawing.

6.2.1.2. Insulating Plates

To avoid electrical contact between connector plates and the end plates, a rubber plate (thickness 1 mm) is placed between both plates. This rubber plate has a hole in the centre, 5 cm x 5 cm, to allow the flow of the reactants (Fig. 6.6).

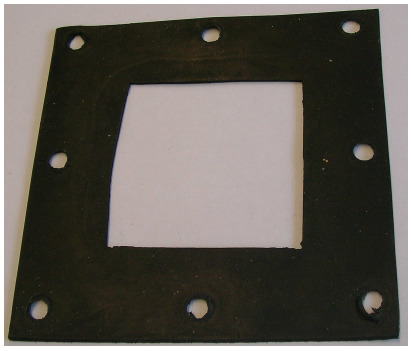

Figure 6.6 – Photograph of the isolating plates.

6.2.1.3. Connector plates

For the electrical connection two gold plated copper plates of 0.5 mm thickness are used. Also all the electrical connectors are gold plated to ensure minimal ohmic resistances at various connection points. The connector plate has 36 holes in the centre, 5 cm x 5 cm, with a diameter of 6 mm to allow the reactants supply (Fig. 6.7).

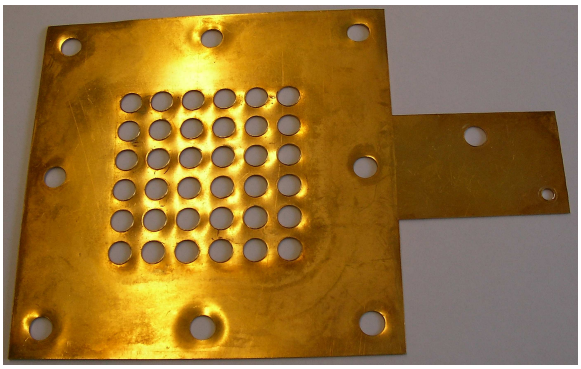

Figure 6.7 – Photograph of the connector plates.

6.2.1.4. Membrane Electrode Assembly (MEA) and diffusion layers

As before, the abbreviation MEA always refers to the membrane coated with catalyst layers but without diffusion layers. The MEAs used were similar to those used in the active feed DMFC with an active area of 25 cm^2 (5 cm x 5 cm) and a total area of 100 cm^2. The membranes tested were made by Nafion 117 and 115. Unsupported platinum black and platinum-ruthenium were used as catalyst (recall Fig. 4.6).

Carbon cloth and carbon paper (recall Fig. 4.7) were used both as anode and cathode diffusion layers. To achieve a higher hydrophobicity these layers are coated with PTFE with a content of 30 wt%.

The diffusion layers are put on both sides of the MEA, and the whole sandwich structure mounted between the connector plates of the fuel cell. The physical properties of all the materials used can be found in the Appendix B.

6.2.2. Methanol Test Kit Testing Unit

The test unit used for the active feed DMFC (described in section 4.2) was also employed for the passive DMFC, although in this case only with the loadbank subsystem acting as a large variable power resistor as described in detailed in section 4.2.3.

6.2.3. Experimental procedure

The start-up procedure performance was:

1. The fuel cell tank in the AAP (regarding the Figures 6.3 and 6.4) was filled with the methanol solution needed for the experiment;
2. The computer, the MTK unit and the FCPower software were turned on;
3. The cell was operated galvanostatically, so the current applied range values was 0 to maximum current allowed by the fuel cell, with a step of 0.1A. At the open circuit conditions the cell was operated fifteen minutes and at the other values of current applied, the cell was operated three minutes until reaching the steady state conditions.
4. For each value of current applied, the cell voltage was measured and the power calculated;
5. The MTK system was turned off;
6. The FCPower software was closed.

6.3. Experimental and Modelling studies for a passive feed DMFC

6.3.1. Results and Discussion

As in the experimental studies reported in Chapter 5, for each set of operating conditions, different tests were performed until obtaining agreement.

6.3.1.1. Model validation

In this section, examples of model predictions obtained after implementation of the model are presented. The conditions chosen to generate the simulations are similar to those used by the authors in the experiments.

To validate the model developed for a passive feed DMFC a set of experiments was performed with five different methanol concentrations, 1M, 2M, 3M, 4M and 5M, using a Nafion 115 membrane. A 30 wt% carbon cloth type A (E-TEK) gas diffusion layer was used on the anode and on the cathode side. An anode catalyst loading of 4 mg/cm^2 Pt/Ru and a cathode catalyst loading of 4 mg/cm^2 Pt was used. Since in passive DMFC systems the temperature rises with time due to the electrochemical reactions, in order to minimize this effect on the results presented in this section all the experiments were conducted at a controlled temperature, ensuring a constant temperature value during each experiment.

In Fig. 6.8, the predicted polarization curves for 1M to 5M methanol solutions are presented. The open-circuit voltage is much lower than the thermodynamic equilibrium cell voltage as a result of methanol crossover. The fuel cell performance increases with an increase of the methanol feed concentration. As can be seen in Fig. 6.8, the present model describes well the experimental results for all the range of current densities due to the integration, on the model, of the mass transfer effects at the cathode side.

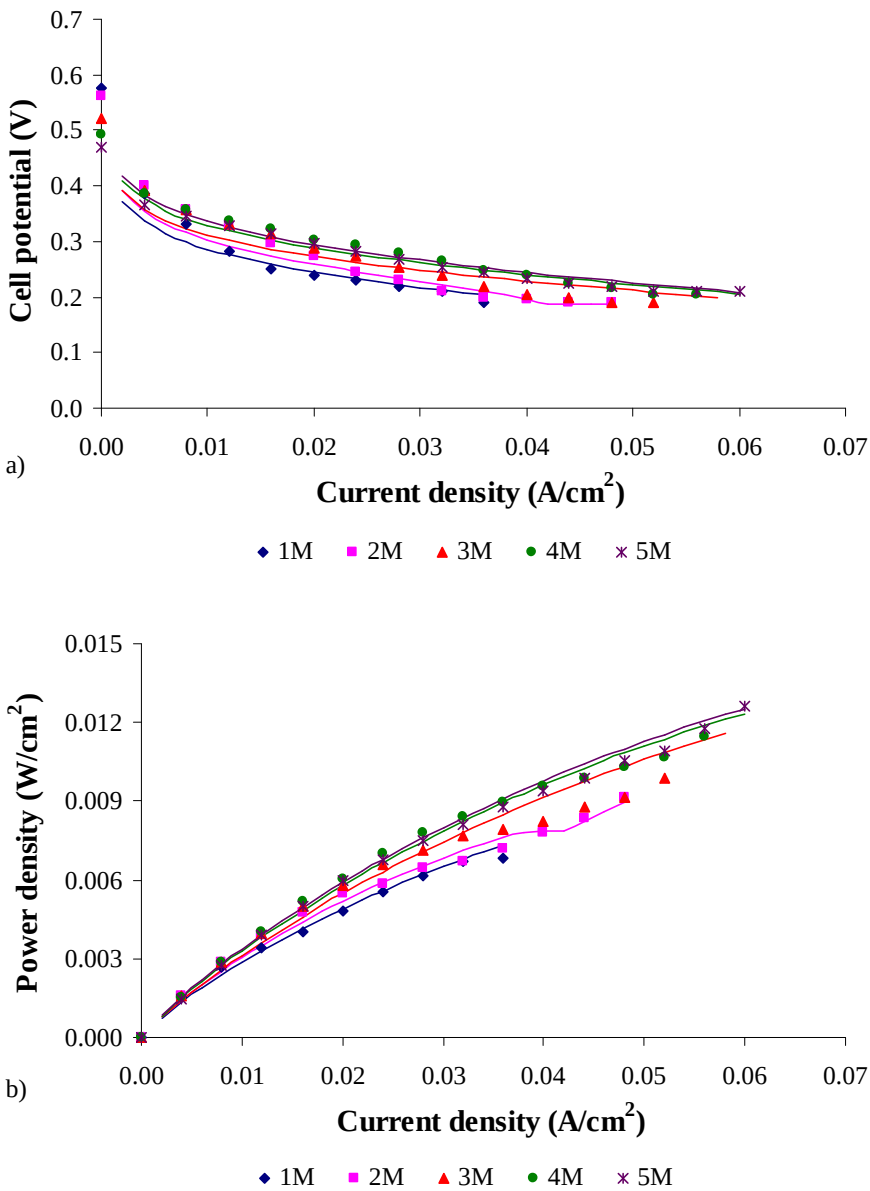

Figure 6.8 – Comparison of the model predictions of a) polarization curves and b) power for different methanol concentrations; dots: experimental data, lines: model predictions.

Another set of experiments were performed with two different methanol concentrations, 1M and 5M. A Nafion 117 membrane, a 30 wt% carbon cloth type A (E-TEK) as gas diffusion layer on the anode and cathode side an anode catalyst loading of 4 mg/cm^2 Pt/Ru and a cathode catalyst loading of 4 mg/cm^2 Pt was used.

The experimental and the predicted polarization curves for 1M and 5M methanol solutions are presented in Fig. 6.9. The model predictions are in agreement with experimental data, for the two values of methanol feed concentrations used. As expected, for low current densities, higher methanol concentrations lead to lower

performances due to higher methanol crossover. The methanol that crosses the membrane reacts with the oxygen, at the cathode side, to form a mixed potential. Higher methanol concentration leads to a higher mixed potential, thereby causing a lower cell performance. For high current densities the more concentrated methanol solution shows a better performance, due to an enhance on the methanol oxidation reaction and consequently a decrease on the anode overpotential.

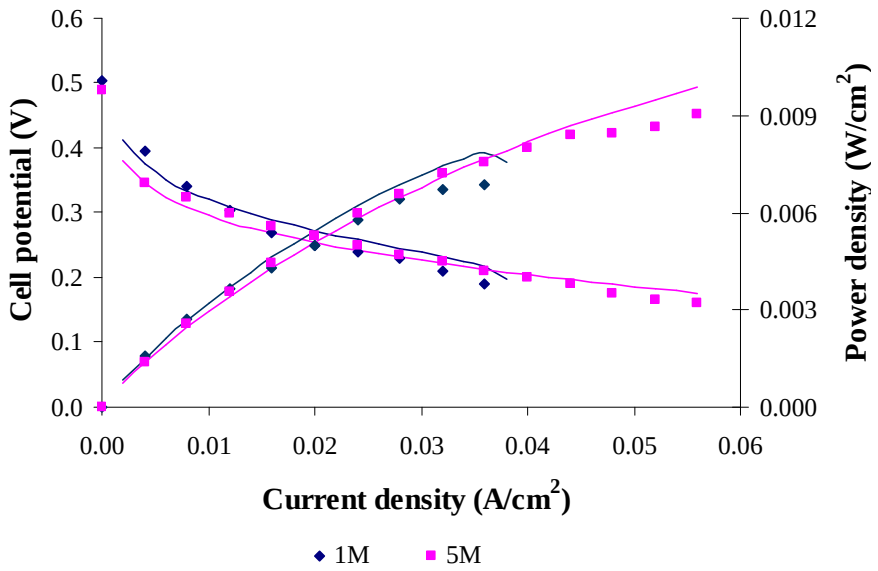

Figure 6.9 – Comparison of the model predictions of a) polarization curves and b) power for different methanol concentrations; dots: experimental data, lines: model predictions.

In Fig. 6.10, data from Pan [160] were used to validate the model. This work was chosen since the operating and design parameters used were similar to those reported in the present work. In Fig. 6.10, the predicted polarization curves for 1M and 3M methanol solutions, for a fuel cell temperature of 25ºC, are presented. Model predictions are close to experimental data presented by Pan [160].

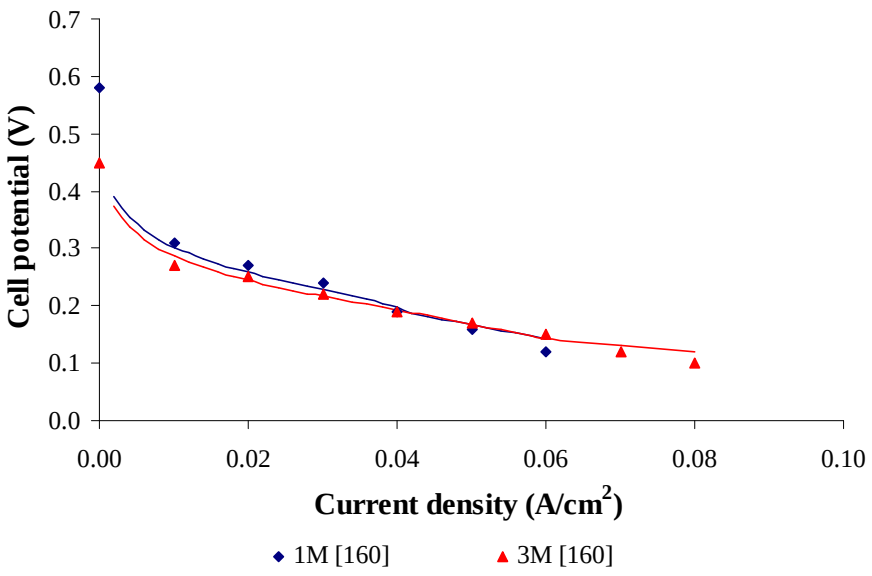

Figure 6.10 – Comparison of the model predictions for different 1M and 3M methanol concentrations; dots: experimental published data [160], lines: model predictions.

Figure 6.11 shows the predictions of the methanol crossover as a function of current density for different methanol concentrations. As already referred the methanol that crosses the membrane reacts with oxygen on the cathode side forming a mixed potential and consequently a parasite current. This parasite current named leakage current represents fuel losses. According to Eq. (6.27), the methanol crossover can be expressed in terms of a leakage current witch gives a more understanding idea of the effect of the loss in efficiency due to methanol crossover. As can be seen in Fig. 6.11, and as expected, the leakage current increases with methanol concentration and decreases with current density. In this way, the leakage current and consequently the methanol crossover can be reduced by running the cell at low methanol concentrations and high current densities.

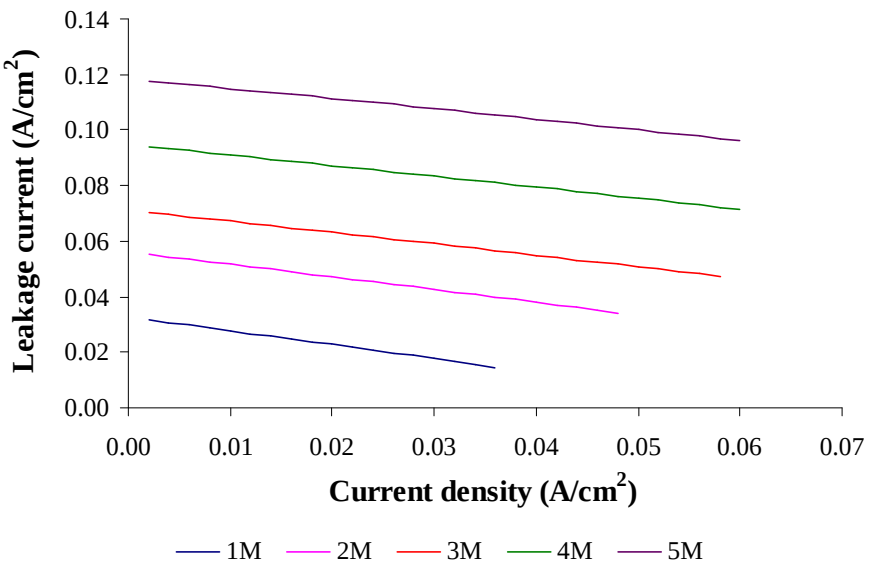

Figure 6.11 – Model prediction for methanol crossover for different methanol feed concentrations.

Predicted methanol concentration profiles across de anode and membrane, are depicted in Fig. 6.12, when the cell is feed with a 3M methanol solution at current densities of 10, 30 and 50 mA/cm^2. During the time considered for the analysis, the concentration profile at the methanol reservoir in the anode acrylic plate slightly decreases near the interface with the copper plate due to the fact that the diffusion of methanol occurs by natural convection (see Eq. (6.4)). In the other layers, the methanol concentration decreases due to mass transfer diffusion, methanol consumption in the catalyst layer and the methanol crossover through the membrane toward the cathode side. As can be seen by the plots of the concentration profile in the membrane presented in this figure, the methanol crossover rate in the membrane decreases with the increase of current density.

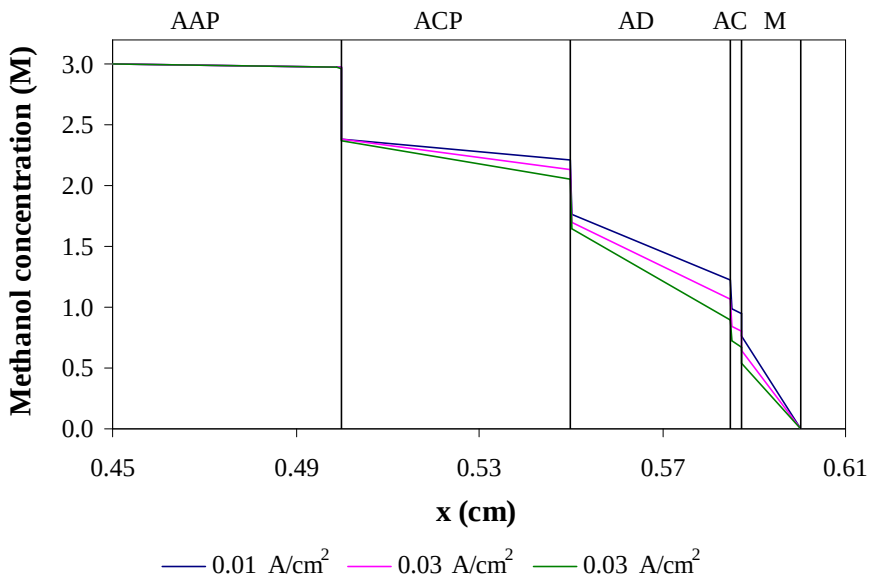

Figure 6.12 – Predicted methanol concentration profiles in the cell for different current densities. Operating conditions: methanol concentration 3M.

Figure 6.13 shows the water concentration across de anode and membrane. As is evident from this figure, water diffusion occurs in ACP, AD, AC and M and water consumption in AC, so the water concentration profile decreases across these layers. The slope of the concentration profile in the membrane is higher than in the other layers showing a significant water crossover toward the cathode side.

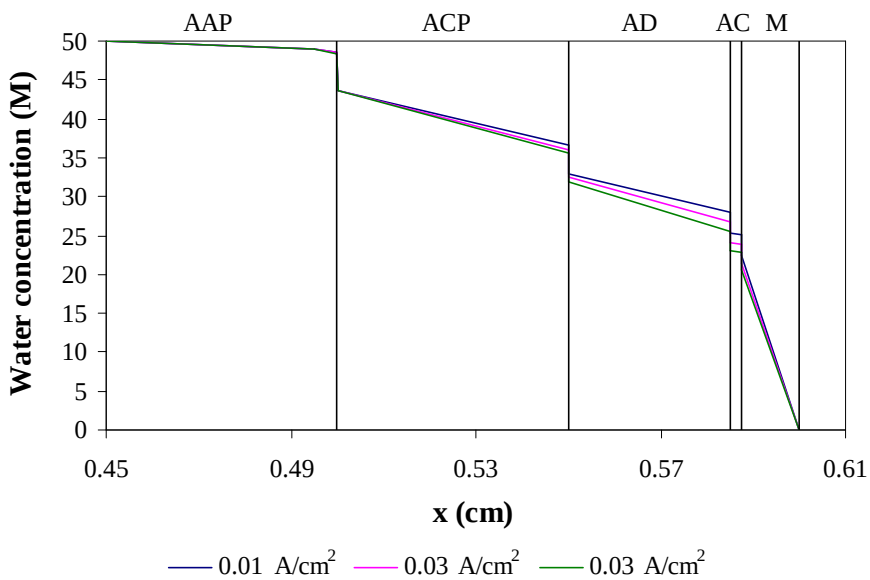

Figure 6.13 – Predicted water concentration distribution in the cell at different current densities. Operating conditions: methanol concentration 3M.

Model predictions of the net water transport coefficient, α, are presented in Fig. 6.14 as a function of current density for different methanol feed concentrations. Figure 6.14 shows that for all the methanol concentration used the values of α are positive, although they are higher with low methanol concentrations. This occurs because for low methanol concentrations there is almost always a higher water concentration at the anode side, especially for the lower values of current density. The transport of water due to electro-osmotic drag and diffusion towards the cathode is dominant. For high methanol concentrations and low current densities the water production in the cathode gives higher water concentrations at the cathode side. Therefore the water transport from the anode to the cathode is less significant corresponding to smaller values of α.

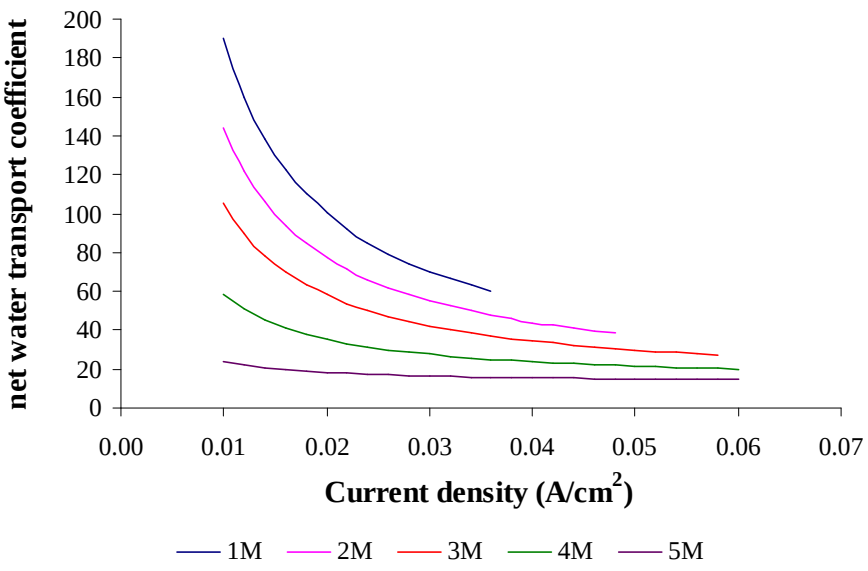

Figure 6.14 – Model predictions of the net water transport coefficient, α, for different methanol concentrations.

In Fig. 6.15, model predictions of α (from Eq. 6.81) as a function of methanol feed concentration for different current densities are presented. It is evident that the methanol concentration has a large impact on the α values. High methanol concentrations result in low values of α. It is also evident that for higher values of the current density the impact of methanol concentration decreases.

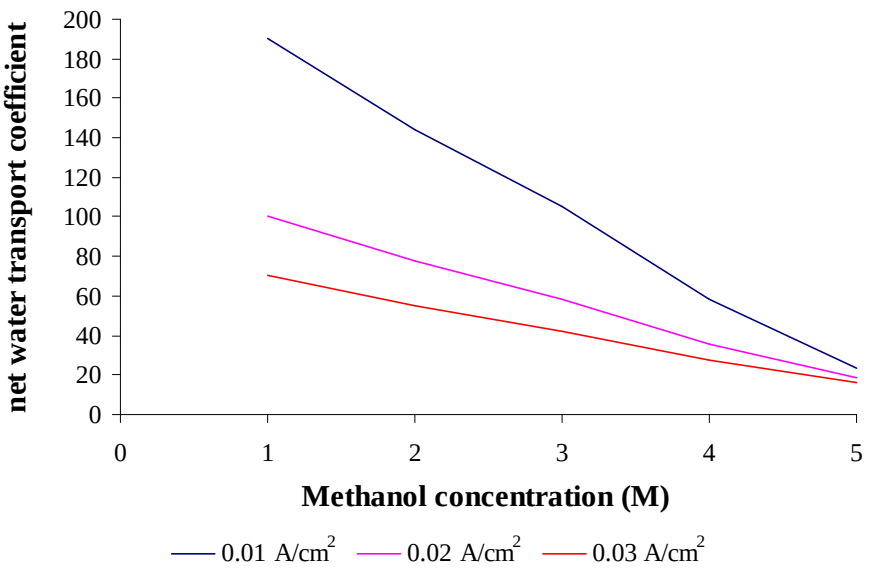

Figure 6.15 – Influence of methanol concentration on the net water transport coefficient at different current densities.

Figure 6.16 shows the temperature distribution in the active section of the cell (anode diffusion and catalyst layer, membrane and cathode catalyst and diffusion layer) for a methanol concentration of 3M and operating at different current densities. For the three values of current density chosen, the temperature in the anode side is higher. This is because the heat generation rate by the anodic overpotential is higher than the endothermic heat demanded by the electrochemical reaction of methanol oxidation. With an increase in current density the difference between the anode and the cathode side increases as is evident in Fig. 6.16.

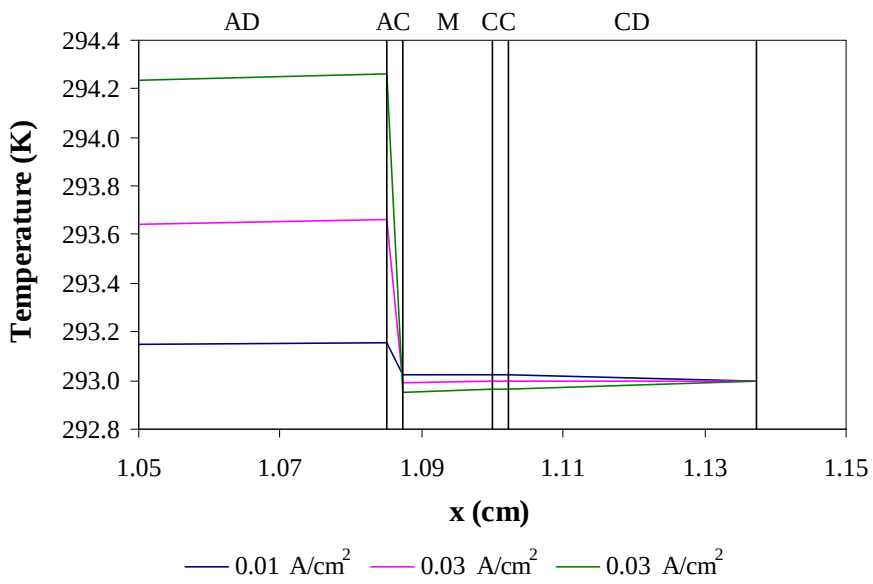

Figure 6.16 – Prediction for the temperature distribution in the cell at different current densities. Operating conditions: methanol concentration 3M.

6.3.1.2. Water Management in a Passive DMFC – model simulations

As already referred the water management is a key issue on the passive DMFCs. In the following, the results of a simulation study using a developed model for passive DMFCs are presented. Particular attention is paid to the water distribution across the cell. The influence of methanol concentration, membrane thicknesses, gas diffusion layers properties and catalyst loading on the net water transport coefficient and on the cell performance is put in evidence. As a result of these modelling results, a tailored MEA was proposed to achieve low methanol and water crossover and high power density, operating at high methanol concentrations. The model was validated with an «in-house» designed passive DMFC.

Model predictions of the net water transport coefficient, α, (from Eq. 6.81) are presented in Fig. 6.17 as a function of current density, for the two methanol feed concentrations studied (1M and 5M). As can be seen from the plots, the methanol concentration has a large influence on the water crossover (α values). Low values of α are achieved using high methanol concentrations. This may be explained by the fact that lower methanol feed concentrations result in higher water concentrations on the anode side. The concentration gradient of water between the anode and cathode side is higher, so the transport of water toward the cathode tends to be dominant. For higher methanol

concentrations the amount of water present on the anode side is smaller and the water production in the cathode gives higher water concentrations in this side. In this situation, the water transport from the anode to the cathode is still dominant but, since the water concentration gradient is smaller the values of α are smaller.

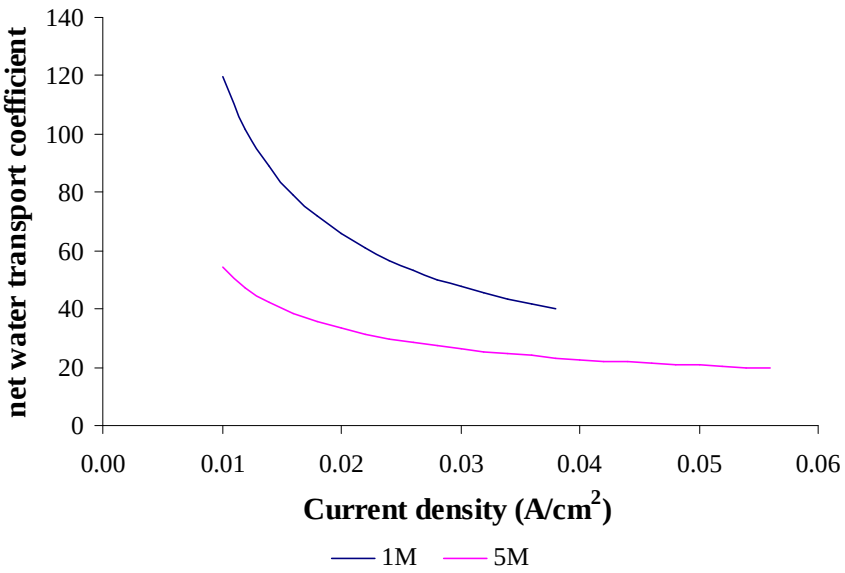

Figure 6.17 – Influence of methanol concentration on net water transport coefficient.

To analyse the effect of the anode gas diffusion layer material and thickness on fuel cell performance and on the net water transport coefficient two different materials were used: carbon cloth and carbon paper, both materials with a PTFE content of 30%. Regarding the carbon cloth, Type A (E-TEK), thickness of 0.35 mm and carbon cloth Type C (E-TEK), thickness of 0.65 mm were used in the simulations. For carbon paper, Toray TGPH-030, thickness of 0.09 mm and Toray TGPH-090, thickness of 0.026 mm were considered in the model predictions.

Carbon paper and carbon cloth with relatively high pore sizes enhance the mass transfer across the anode and contribute for a uniformly distribution of reactants over the entire electrode. Both, materials are carbon-fiber-based porous materials, but carbon paper is non-woven while carbon cloth is woven. Carbon cloth is more porous, less tortuous than carbon paper. The differences in porosity, permeability, pore size distributions, surface wettability and liquid retention between these two materials result in different two-phase flow and transport characteristics.

Figure 6.18 a) and b) shows, respectively, the effect of the anode gas diffusion layer material on the fuel cell performance and on the net water transport coefficient. The plots from the figure show that a slightly better performance is obtained with carbon cloth as the anode gas diffusion layer (GDL), probably due to a thicker thickness of this layer relatively to the carbon paper. Thicker gas diffusion layers lead to lower values of methanol and water crossover due to the fact that thicker electrodes had higher mass transport resistances reducing the amount of water and methanol reaching the membrane. As the cell performance is dependent on the methanol crossover, lower performances are obtained for thinner anodes. The plots of the figure 6.18 b) show that lower values of α are obtained for the thicker GDL material. These results show that the use of thicker gas diffusion layers leads to an enhancement of the water transport toward the anode decreasing the values of α.

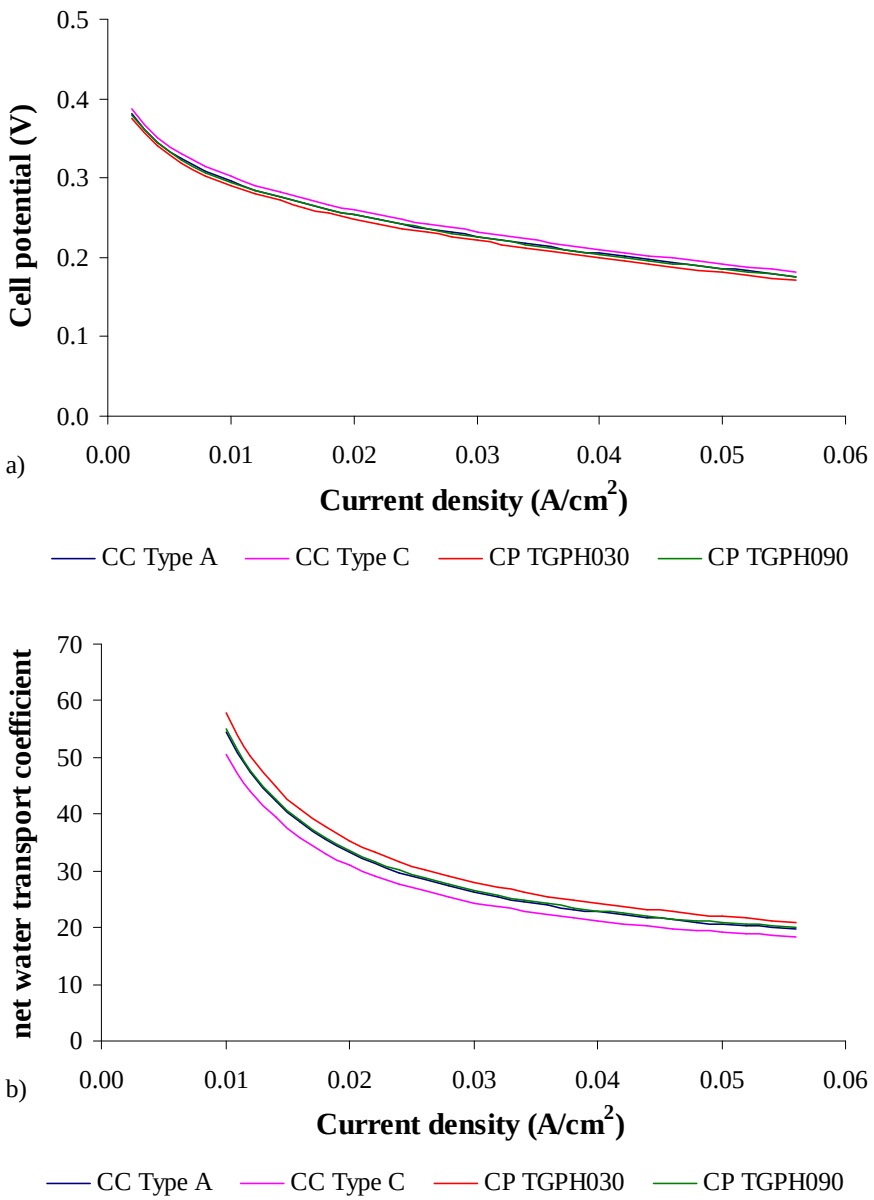

Figure 6.18 – Influence of anode gas diffusion layer structure on a) fuel cell performance and b) net water transport coefficient. Operating conditions: methanol concentration 5M.

The same materials were used as cathode gas diffusion layer to evaluate their effect on fuel cell performance and on the net water transport coefficient as can be seen in figures 6.19 a) and b), respectively. The cathode GDL thickness seems to have a negligible effect on cell performance. It should be noted that the variation in performance with different gas diffusion media results mainly from the ability of facilitating the water removal. All the GDL materials have the same PTFE content and therefore the wettability is probably similar. Accordingly, the plots of the Fig. 6.19 b) show that for

the studied conditions the effect of the cathode GDL on the net water transport coefficient is negligible.

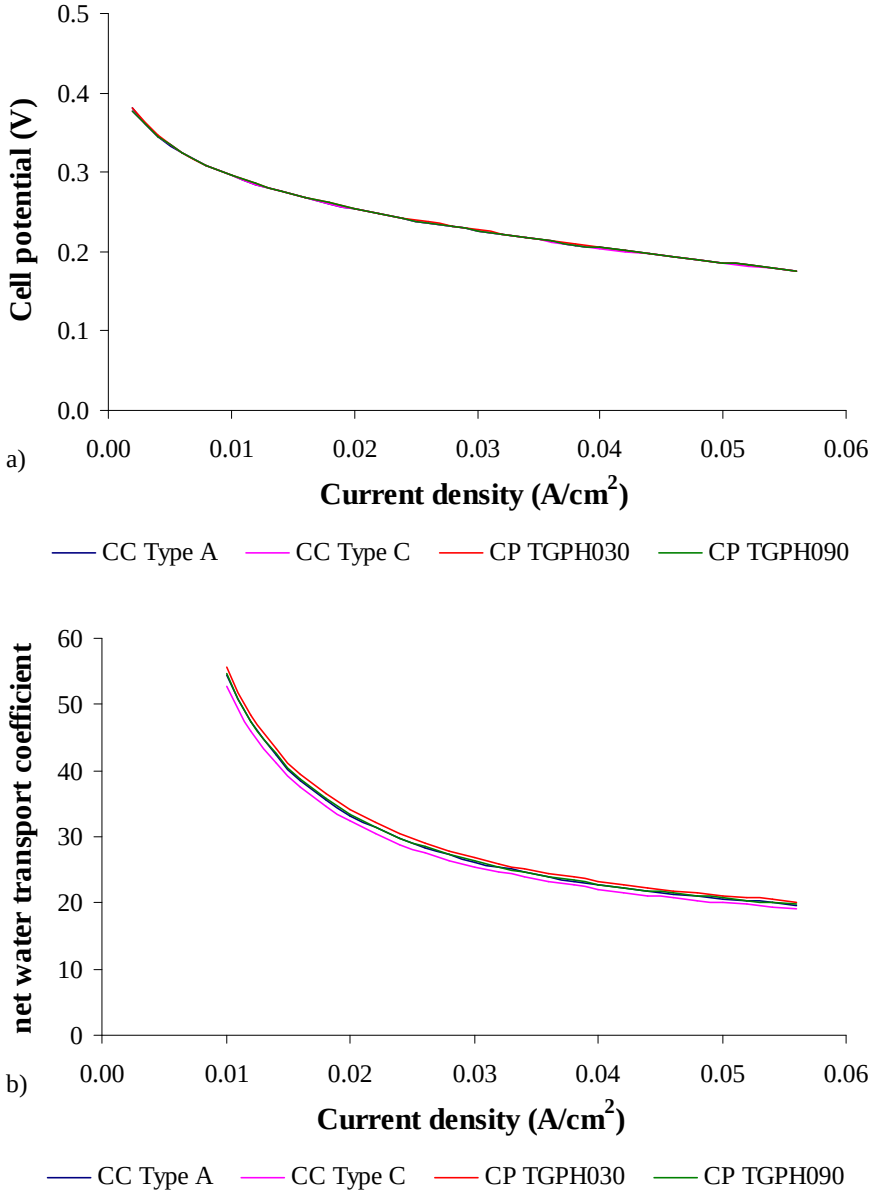

Figure 6.19 – Influence of cathode gas diffusion layer structure on a) fuel cell performance and b) net water transport coefficient. Operating conditions: methanol concentration 5M.

To predict the effect of the anode catalyst layer on fuel cell performance and on the net water transport coefficient the anode catalyst loading (Pt/Ru) was varied from 4 to 8 mg/cm^2 and on the cathode catalyst loading was fixed at 4 mg/cm^2 Pt. As already referred, three essential properties of the electrode may be affected when changing the catalyst loading: the active surface area, the electronic conductivity and the thickness of

the electrode. The reduction of the anode catalyst layer leads to a reduction on the active surface area, an increase on resistivity and consequently a decrease in electronic conductivity.

The predicted polarization curves are presented in Fig. 6.20 a). A slightly better performance is obtained for the highest value of Pt/Ru loading. The cell performance increases with the metal loading because the thicker anode catalyst layer creates a higher resistance to methanol transport thereby controlling the rate of methanol reaching the membrane and reducing the methanol crossover. This reduction leads to a reduction of the parasite current formed due to the oxidation of methanol at the cathode side and consequently the cell performance increases. Also, a higher catalyst loading leads to a thicker electrode and to an increase in the catalyst surface area. More active sites are presented for the methanol oxidation reaction the anode overpotential decreases and the fuel cell performance increases.

The model predictions for the effect of the anode catalyst loading on the net water transport coefficient are presented in Fig. 6.20 b). As can be seen, smaller values of the net water transport coefficient are obtained for the highest value of Pt/Ru loading. This may be due to the fact that higher values of catalyst loading lead to a large methanol and water consumption due to the anodic reaction. In this way the water concentration decreases at the anode side and also decreases the amount of water that crosses the membrane toward the cathode side. Also, thicker electrodes lead to a higher mass transport resistance limiting the amount of water that crosses the membrane.

The influence of the catalyst loading on the cell performance is less significant for the passive DMFC relatively to the active fuel cell (recall figures 5.39, 5.42, 5.45, 5.46).

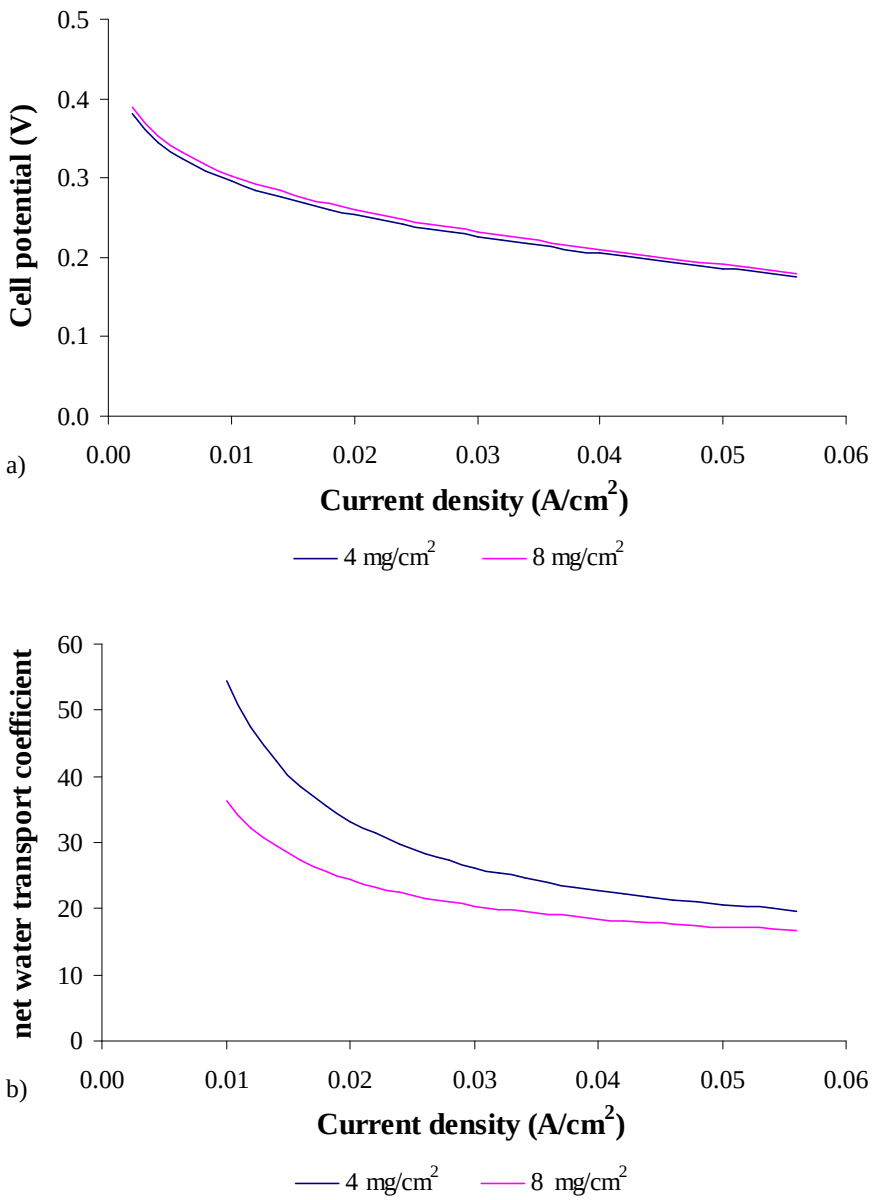

Figure 6.20 – Influence of anode catalyst layer loadings on a) fuel cell performance and b) net water transport coefficient. Operating conditions: methanol concentration 5M.

The model predictions of cell performance for different cathode catalyst loadings are presented in Fig. 6.21 a). Two values were used for the cathode catalyst loading (Pt) 4 and 8 mg/cm^2. The other electrode, anode side, was fixed at 4 mg/cm^2 Pt/Ru. From the plots, it is evident that lower cathode catalyst loadings lead to a slight decrease in the fuel cell performance. This is due to the fact that the reduction of the cathode catalyst layer leads to a reduction on the active surface area. An increase on the catalyst loading causes an increase on the active surface area and an enhanced of the oxygen reduction reaction. This may be very advantageous at the cathode, since mixed potential

formation may be avoided to some extent. In a thicker electrode, less catalyst particles are reached by the permeated methanol flux, so more active sites are free for the oxygen reduction reaction.

Model predictions of the effect of cathode catalyst loading on the net water transport coefficient are shown in Figure 6.21 b). The cathode catalyst loading seems to have an irrelevant effect on the net water transport coefficient.

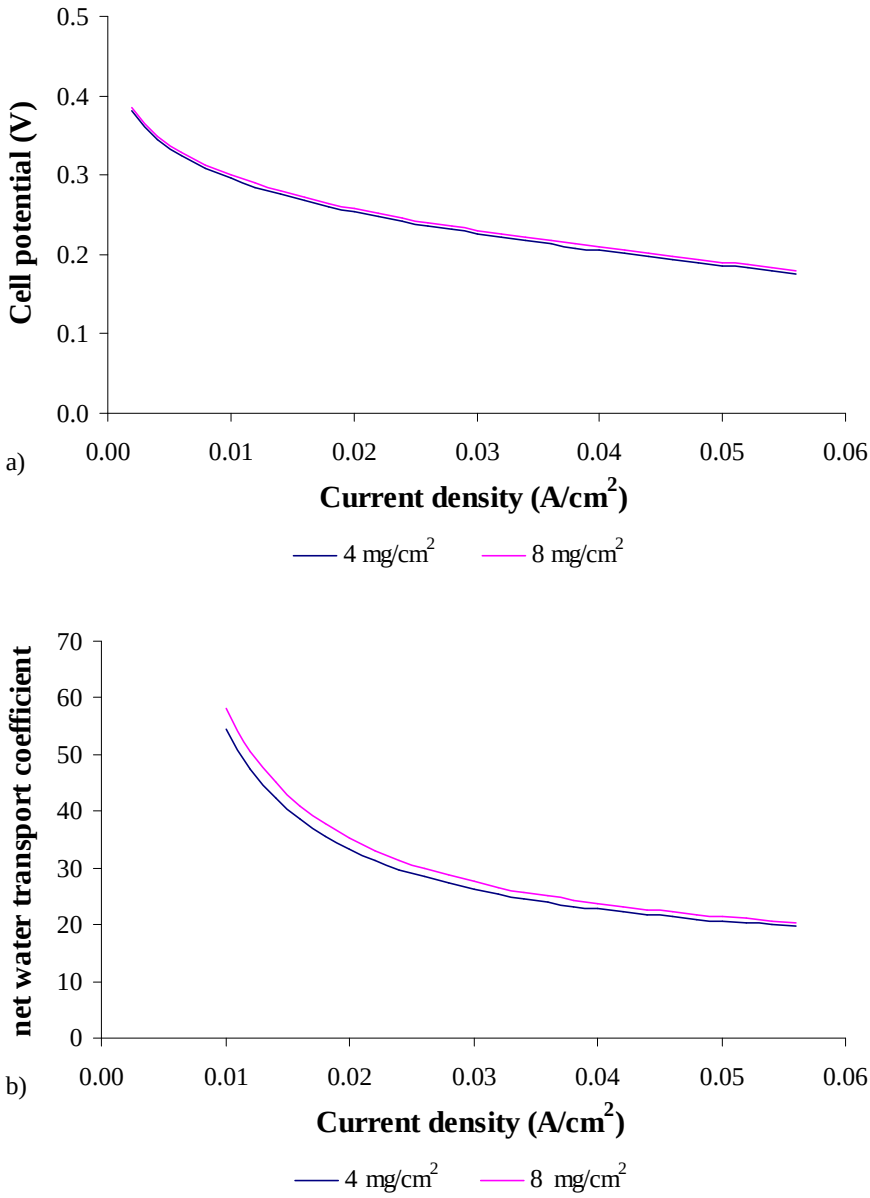

Figure 6.21 – Influence of cathode catalyst layer loadings on a) fuel cell performance and b) net water transport coefficient. Operating conditions: methanol concentration 5M.

To evaluate the effect of the membrane thickness, a Nafion 117 membrane (thickness of 0.18 mm) a Nafion 115 membrane (thickness of 0.127 mm) and a Nafion 212 membrane (thickness of 0.051 mm) were used in the model predictions.

Figure 6.22 a) and b) shows the effect of the membrane thickness on the fuel cell performance and on the net water transport coefficient, respectively. The Nafion 115 membrane had a slight better performance than Nafion 117 and a much better performance than Nafion 212. It should be noted that thinner membranes have lower performances because they have higher methanol loss through crossover, in spite of lower ohmic resistances. In this way, the effect of the membrane thickness on the fuel cell performance must be a combined effect of the positive and the negative effects. For this condition and for the Nafion 115 membrane, it seems that the positive effect on the ohmic loss is more relevant that the negative effect of methanol crossover.

When comparing the values of the net water transport coefficient for identical values of current density and different membrane thicknesses, lower values of the net water transport coefficient are obtained with the thinner membrane, because the resistance of water back-flow from the cathode to the anode via hydraulic permeation is much reduced in this case. The trends of the influence of membrane thickness on water crossover predicted in this paper are in accordance to the ones proposed by Song *et al.* [163] and Jewett *et al.* [164].

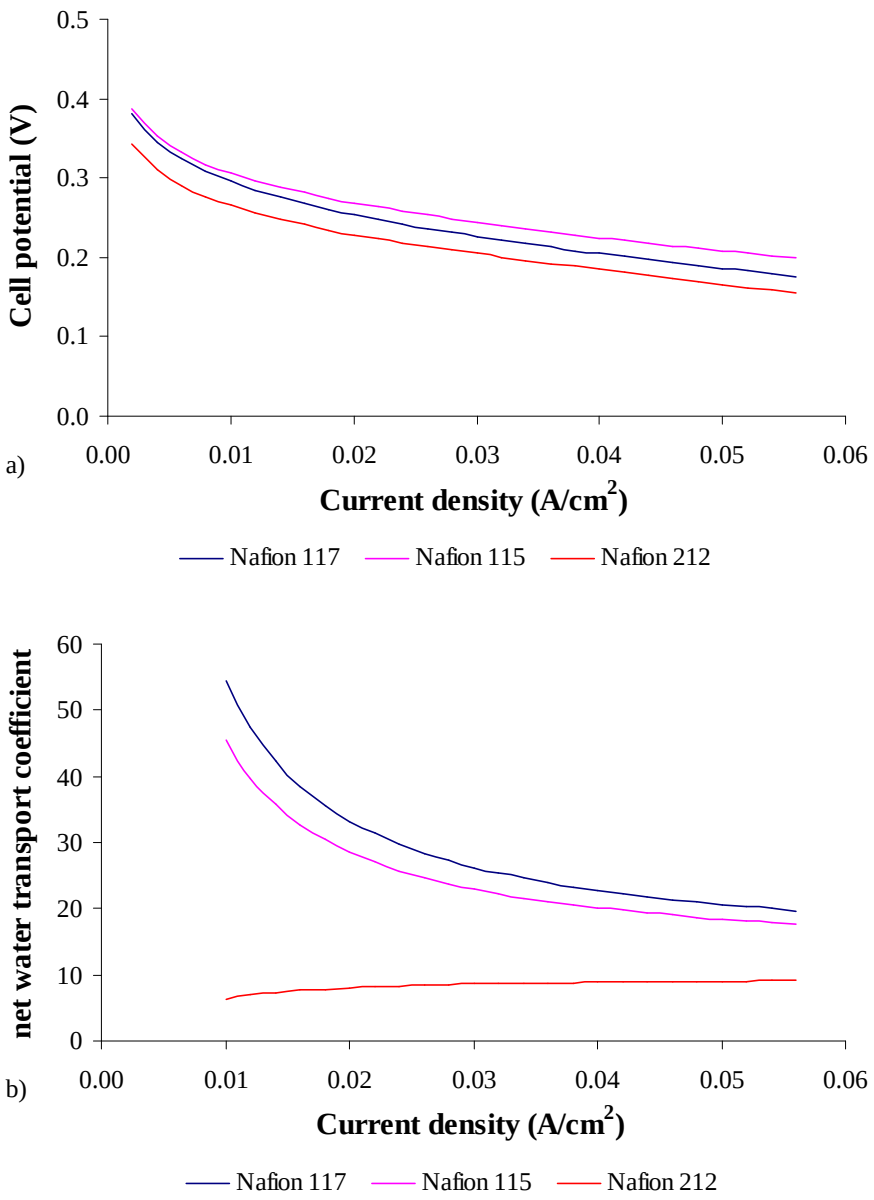

Figure 6.22 – Influence of MEA thickness on a) fuel cell performance and b) net water transport coefficient. Operating conditions: methanol concentration 5M.

6.3.1.3. Tailored MEAs

Based on the results and major conclusions of the previous section, the next goal is to propose a tailored MEA in order to achieve higher fuel cell performances with higher methanol concentrations, and lower methanol and water crossover rates.

One membrane named commercial Nafion 117 is considered with a 30 wt% carbon cloth type A (E-TEK) as gas diffusion layer on the anode and cathode side, with 4mg/cm^2 Pt/Ru and 4 mg/cm^2 Pt as catalyst load for anode and cathode, respectively.

One tailored MEA with a thinner membrane, Nafion 212 had a 30 wt% carbon cloth type C (E-TEK) as gas diffusion layer on the anode and cathode side, an anode catalyst loading of 8 mg/cm^2 Pt/Ru and a cathode catalyst loading of 8 mg/cm^2 Pt.

Figures 6.23 a) and b) show the cell performance and the net water transport coefficient for the two MEAs, using a methanol concentration of 5M. As can be seen, for all the range of current densities studied, the tailored MEA has a better performance and a lower value of the net water transport coefficient. The general significant increase on performance when using thinner membranes is possible because a higher catalyst loading and a thicker GDL both on the anode and cathode side were used. A thicker GDL and catalyst layer on the anode side act as a methanol and water barrier decreasing the methanol and water crossover and, consequently, increasing the current density. Thicker cathode catalyst layer enable an increase of the number of catalyst particles available for the oxygen reduction. Thinner membranes, also, allow operating a passive DMFC with low values of net water transport coefficients which is the goal to an adequate water management in passive DMFCs. The results obtained seem to point out optimized conditions for operation of passive DMFCs with tailored MEAs and high methanol concentrations with an increased performance and are in accordance to those reported in literature [163, 164].

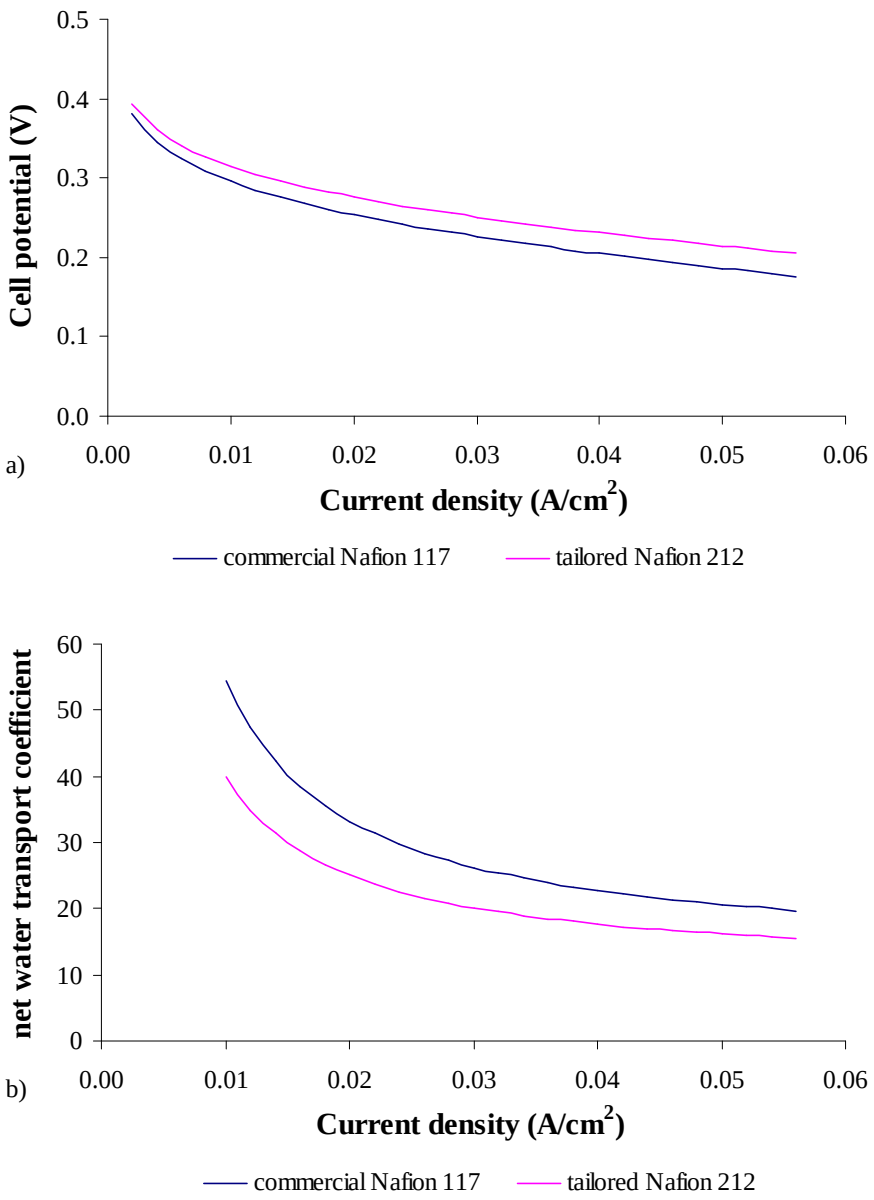

Figure 6.23 – Influence of MEA properties on a) fuel cell performance and b) net water transport coefficient for commercial Nafion 117 and tailored Nafion 212. Operating conditions: methanol concentration 5M.

6.3.1.4. Active feed DMFC vs. Passive feed DMFC

The performance of the DMFC is strongly dependent on the mode of reactants supply, and it is generally accepted that active DMFCs performance is higher than passive ones due to higher mass transport rates in the cells.

The comparison between active and passive DMFC cell performance and power density is displayed in Fig. 6.24. The active DMFC was operated with a methanol flow rate of 3 ml/min and air flow rate 3.6 l/min. For the two values of methanol feed concentration

(2M and 5M) the active mode outperforms the passive one. This is due to the fact that the active systems have higher mass transport rates and to the fact that in the passive DMFC there is an inefficient water removal on the cathode side, since the cathode compartment is fully open to ambient air at room temperature. The water accumulates at the cathode side leading to a lower performance and flooding conditions may occur.

As can be seen by the plots presented in Figures 6.24 a) and b), in passive DMFC systems, higher methanol concentrations (5M) lead to higher fuel cell performances and power densities, contrarily to the active feed DMFC where higher methanol concentrations lead to lower fuel cell performances. This may be due to the fact that in active feed systems large values of methanol crossover are generated due to the higher mass transport rates, more methanol reaches the membrane and consequently more methanol passes toward the cathode side. This situation reveals one advantage of the passive DMFC, their ability to work with higher methanol concentrations leading to higher energy densities, needed for portable applications.

As already referred, both active and passive DMFC systems generate large amounts of water at the cathode side and in some conditions flooding problems may occur. In the active feed the flow of air can remove water more efficiently. In the passive feed, the cathode is opened to the atmosphere and air is supplied only by natural convection leading to a less intense water removal. One possible solution to reduce the water crossover in is to use highly concentrated methanol solutions. It was found that this situation is advantageous in passive DMFC since higher methanol concentrations lead to higher fuel cell performances. As already referred the use of new MEA designs with the aim to reduce the water flooding at the cathode, having lower net water transport coefficients, and consequently to enhance stability is another possible solution in passive DMFC. With a correct water management in passive systems by using new MEAs designs and high methanol concentrations or even pure methanol solutions the power requirements needed for portable applications could be achieved using the passive feed DMFCs.

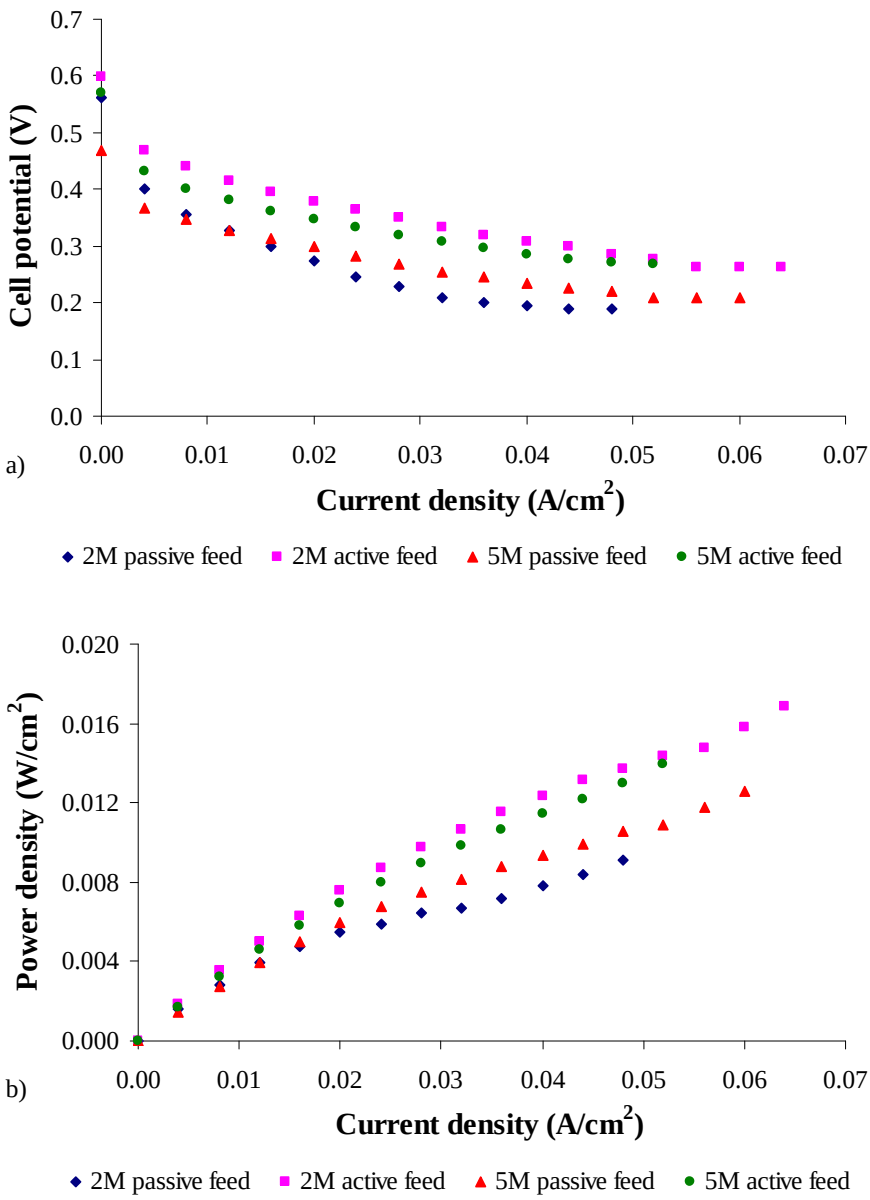

Figure 6.24 – Comparison of the experimental results, for a) polarization curves and b) power, with different reactants feeding. Structural parameters: Nafion 115. Structural parameters: anode and cathode diffusion layer 30% wet-proofed carbon cloth type A, anode catalyst loading 4mg/cm^2 Pt/Ru, cathode catalyst loading 4mg/cm^2 Pt. Operating conditions: temperature 20ºC, methanol flow rate 3 ml/min and air flow rate 3.6 l/min.

6.3.2. Concluding remarks

Reducing the methanol and water crossover from the anode to the cathode side on a passive DMFC is of significant importance to improve cell performances and obtained higher power densities. Thus, it is crucial to better understand the mechanism of water and methanol crossover through the membrane used for this type of fuel cells.

The model developed for the active DMFC was adapted to the passive DMFC and was presented in this chapter.

The model can be used to predict the methanol, oxygen and water concentration profiles in the anode, cathode and membrane, as well as to estimate the methanol and water crossover and the temperature profile across the cell. Polarization curves are numerically simulated and successfully compared with experiments for different methanol feed concentrations. The model predicts with accuracy the influence of the methanol feed concentration on the cell performance and the correct trends of the current density and methanol feed concentration, on methanol and water crossover. The model is rapidly implemented and is therefore suitable for inclusion in real-time system level DMFC calculations. Due to its simplicity the model can be used to help seek for possibilities of optimizing the cell performance of a passive DMFC by studying impacts from variations of the design parameters such as membrane thickness, catalyst loading, diffusion layers type and thicknesses.

Changes in the structure of the diffusion layers, in the catalyst loadings and membrane thicknesses were found to be effective ways to control water crossover. Increasing the thickness of catalyst layer by increasing the catalyst loading could contribute to lower the loss in performance due to methanol crossover. Decreasing the membrane thickness leads to a lower net water transport coefficient as the result of the enhanced transport of water, from the cathode to the anode. Thicker anode gas diffusion layers seem to have a better performance due to low methanol and water crossover. Higher methanol concentrations lead to lower fuel cell performances due to higher methanol crossover, but generate higher performances for high current densities. Also, higher methanol concentrations lead to a decrease on the net water transport coefficient. Finally a tailored MEA is proposed to achieve low methanol and water crossover and high power density. A thick anode diffusion and catalyst layer to reduce methanol and water crossover, a thicker cathode to enhance oxygen reaction and thinner membranes to reduce ohmic losses are suggested. The results presented provide very useful and actual information for future passive DMFC systems using high concentration or pure methanol.

CHAPTER 7

7. CONCLUSIONS AND SUGGESTIONS FOR FUTURE WORK

The main objective of this thesis was to gain a detailed understanding of the transport phenomena occurring in a direct methanol fuel cell together with the electrochemical reactions occurring at the anode and cathode.

One main motivation of the work was to compensate for the lack of experimental characterization of DMFCs (both active and passive feed) operating under conditions close to ambient pressure and temperature, bearing in mind the portable applications of this type of fuel cells.

The fulfilment of the work objectives involved the following steps:

- development of a mathematical model both for active and passive feed DMFCs;
- implementation of an experimental rig (comprising an acquired fuel cell station and a temperature control system) and the design and construction of direct methanol fuel cells (both active and passive feed);
- validation of the developed models both with data from literature and with experimentally obtained results;
- intensive use of the developed models to set-up optimizing conditions leading to enhanced fuel cell performances (both for active and passive feed).

Conclusions from the several parts of this research and recommendations for future work are discussed below.

7.1 Conclusions

A steady state, 1D model accounting for coupled heat and mass transfer was developed, firstly for an active feed DMFC and afterward adapted for a passive feed fuel cell. Emphasis was put on a reduced model, with an easily extendable structure and a detailed modelling of heat and mass transfer phenomena. The model allows the assessment of the effect of operating conditions (such as methanol feed concentration, methanol and air flow rates and current density) and of design parameters (active area

and material properties) on temperature and concentration profiles and consequently on cell performance. Special attention was devoted to the influence of these parameters both on methanol and water crossover, two fundamental issues on DMFC development. The models predict the correct trends of the effects of the different parameters on these two important flows.

Both models (for active and passive DMFCs) describe well the experimental results for low to medium current densities, due to the integration, on the model, of the mass transfer effects at the cathode side. The most significant discrepancies between the model and experimental conditions occur near the limiting current densities, and for active feed DMFC, due to the fact that the model neglects two-phase flow effects. Under these conditions, the carbon dioxide bubbles, on the anode side, and water droplets, on the cathode side, considerably reduce the limiting current density of the cell. However the model uses simple numerical tools, like Matlab, which allows the rapid prediction of the DMFC performance and can be a useful tool to improve DMFC understanding and to optimize fuel cell design.

The obtained results in the detailed experimental study of the active feed DMFC were in accordance with the general trends accepted by the scientific DMFC community:

- The fuel cell performance significantly increased with the introduction of the diffusion layers, meaning that a five layer MEA is much more efficient than a three layer one;
- The optimal methanol concentration was found to be 0.75M, higher methanol concentrations resulted in lower cell performances due to higher values of the generated methanol crossover;
- For the conditions studied the fuel cell performance and power density increased with increasing temperature due to an enhancement of the electrochemical kinetics on the anode and cathode side;
- High values of methanol and air flow rates have a positive impact on fuel cell performance. The impact of the air flow rate is less significant under the operating conditions studied;
- Regarding the choice of the anode diffusion layer material, higher performances are obtained for lower methanol concentration if carbon cloth is used while for

higher methanol concentration the best option is carbon paper. For the cathode diffusion layer the use of carbon cloth is adequate;

- Thicker membranes generate lower values of methanol crossover, increasing the fuel cell performance;
- Thicker anode and cathode catalyst layers lead to an increase in fuel cell performance.

The effect of the anode and cathode flow field design on the active feed DMFC performance was also studied. It was concluded that the fuel cell performance significantly increase with the use of an original design, the MFF (mixed flow field) as the anode flow field and MSFF (multi serpentine flow field) as the cathode flow field design. These results can be very useful for the validation of CDF models.

Reducing the membrane water and methanol crossover is essential to achieve increased power densities, a fundamental requirement for commercialization of portable DMFCs. Based on the experimental results, a tailored MEA was proposed to achieve low methanol and water crossover and high power density, operating at high methanol concentrations. The resulting MEA provides a basic element for future DMFC systems using high concentration or pure methanol.

The results obtained with the passive feed DMFC showed that changes in the structure of the diffusion layers, in the catalyst loadings and membrane thickness, constitute effective ways of control water and methanol crossover. In particular, decreasing the membrane thickness and working with high methanol concentrations lead to a lower net water transport coefficient resulting from the enhanced transfer of water from the cathode to the anode. Thicker anode gas diffusion layers seem to contribute to increase performance due to the ability of generating low methanol crossover values. Increasing the thickness of the catalyst layer by increasing the catalyst loading could, also, result in a decrease in the loss of performance due to methanol crossover. Based on these findings, a tailored MEA was proposed to achieve low methanol and water crossover, providing a basic element for passive DMFCs, and capability of working at high concentration or even pure methanol.

7.2 Suggestions for future work

Regarding the modelling of DMFCs it is necessary to move one step forward in cell optimization and develop a CFD tool (both for active and passive feed cells) in order to explore the two-phase flows effects occurring both at the anode and cathode. The model needs to be validated with carefully designed visualization studies. The CFD tool will enable the optimization of the flow channels configuration to incorporate in new cells together with the tailored MEA proposed by using the simpler numerical tool developed in the present work.

In parallel to the model refinement, more experimental work, especially, for the passive feed fuel cell is needed. Further studies must be performed namely under completely uncontrolled temperature conditions and using higher methanol concentrations. Innovative gas-liquid separators, at the anode side, should also be tested.

One of the main gains of this work was to systematically vary commercial MEA materials and check their influence on the cell performance of a DMFC operating close to room temperature. An interesting suggestion for future work should be the further modification of some structural properties of the gas diffusion layer following some recent published studies, such as for example the introduction of the so called microporous layers (MPL) and to test these novel MEA designs both experimentally and numerically.

CHAPTER 8

8. References

[1] G.Q. Lu and C.Y. Wang, Two-phase microfluidics, mass and heat transport in direct methanol fuel cells, New Developments in Heat Transfer, Chapter 9, pp. 317-358, 2005.

[2] L.J. Burchamand and I.E. Wachs, The origin of the support effect in supported metal oxide catalysts: in situ infrared and kinetic studies during methanol oxidation, Catalysis Today 49 (1999) 467-484.

[3] A.S. Lin, A.D. Kowalak and W.E. O'Grady, Studies of the role of water in the electrocatalysis of methanol oxidation, Journal of Power Sources 58 (1996) 67-72.

[4] L. Liu, C. Pu, R. Viswanathan, Q. Fan, R. Liu and E.S. Smotkin, Carbon supported and unsupported Pt–Ru anodes for liquid feed direct methanol fuel cells, Electrochimica Acta 43 (1998) 3657-3663.

[5] S.F. Baxter, V.S. Battaglia and R.E. White, Methanol Fuel Cell Model: Anode, Journal of the Electrochemical Society 146 (1999) 437-447.

[6] G.T. Burstein, C.J. Barnett, A.R. Kucernak and K.R. Williams, Aspects of the anodic oxidation of methanol, Catalysis Today 38 (1997) 425-437.

[7] A. Hamnett, Mechanism and electrocatalysis in the direct methanol fuel cell, Catalysis Today 38 (1997) 445-457.

[8] J. Sobkowski, K. Franaszczuk and K. Dobrowolska, Effect of anions and pH on the adsorption and oxidation of methanol on a platinum electrode, Journal of Electroanalytical Chemistry 330 (1992) 529-540.

[9] H. Matsui and A. Kunugi, The scheme of methanol oxidation at a platinum electrode in an acid solution, Journal of Electroanalytical Chemistry 292 (1990) 103-113.

[10] X.H. Xia, T. Iwasita, F. Ge and W. Vielstich, Structural effects and reactivity in methanol oxidation on polycrystalline and single crystal platinum, Electrochimica Acta 41 (1996) 711-718.

[11] C. He, H. R. Kunz and J. M. Fenton, Evaluation of Platinum-Based Catalysts for Methanol Electro-oxidation in Phosphoric Acid Electrolyte, Journal of the Electrochemical Society 144 (1997) 970-979.

[12] M. Watanabe, S. Saegusa and P. Stonehart, High platinum electrocatalyst utilizations for direct methanol oxidation, Journal of Electroanalytical Chemistry 271 (1989) 213-220.

[13] R. Parsons and T. Vandernoot, The oxidation of small organic molecules: A survey of recent fuel cell related research, Journal of Electroanalytical Chemistry 257 (1988) 9-45.

[14] M. P. Hogarth and G. A. Hards, Direct Methanol Fuel Cells: Technological advances and further requirements, Platinum Metals Review 40 (1996) 150-159.

[15] K. Chandrasekaran, J. C. Wass, and J. O' M. Bockris, The Potential Dependence of Intermediates in Methanol Oxidation Observed in the Steady State by FTIR Spectroscopy, Journal of the Electrochemical Society 137 (1990) 518-524.

[16] Y. Morimoto and E. B. Yeager, Comparison of methanol oxidations on Pt, Pt/Ru and PtSn electrodes, Journal of Electroanalytical Chemistry 444 (1998) 95-100.

[17] A. B. Anderson, E. Grantscharova and S. Seong, Systematic Theoretical Study of Alloys of Platinum for Enhanced Methanol Fuel Cell Performance, Journal of the Electrochemical Society 143 (1996) 2075-2082.

[18] K.L. Ley, R. Liu, C. Pu, Q. Fan, N. Leyarovska, C. Segre and E.S. Smotkin, Methanol Oxidation on Single-Phase Pt/Ru-Os Ternary Alloys, Journal of the Electrochemical Society 144 (1997) 1543-1548.

[19] L. Liu, R. Viswanathan, R. Liu and E.S. Smotkin, Methanol Oxidation on Nafion Spin-Coated Polycrystalline Platinum and Platinum Alloys, Electrochemical and Solid State Letters 1 (1998) 123-125.

[20] N.A. Hampson, M.J. Willars and B.D. McNicol, The methanol-air fuel cell: A selective review of methanol oxidation mechanisms at platinum electrodes in acid electrolytes, Journal of Power Sources 4 (1979) 191-201.

[21] A. Hamnett and B.J. Kennedy, Bimetallic carbon supported anodes for the direct methanol-air fuel cell, Electrochimica Acta 33 (1988) 1613-1618.

[22] A.S. Arico, Z. Poltarzewski, H. Kim, A. Morana, N. Giordano and V. Antonucci, Investigation of a carbon-supported quaternary Pt/Ru-Sn-W catalyst for direct methanol fuel cells, Journal of Power Sources 55 (1995) 159-166.

[23] M. Götz and H. Wendt, Binary and ternary anode catalyst formulations including the elements W, Sn and Mo for PEMFCs operated on methanol or reformate gas, Electrochimica Acta 43 (1998) 3637-3644.

[24] A.S. Arico, P. Creti, E. Modica, G. Monforte, V. Baglio and V. Antonucci, Investigation of direct methanol fuel cells based on unsupported Pt–Ru anode catalysts with different chemical properties, Electrochimica Acta 45 (2000) 4319-4328.

[25] X. Ren, P. Zelenay, S. Thomas, J. Davey and S. Gottesfeld, Recent advances in direct methanol fuel cells at Los Alamos National Laboratory, Journal of Power Sources 86 (2000) 111-116.

[26] J.P. Meyers and J. Newman, Simulation of the Direct Methanol Fuel Cell-II. Modeling and Data Analysis of Transport and Kinetic Phenomena, Journal of the Electrochemical Society 149 (2002) A718-A728.

[27] S. Mukerjee, S. Srinivasan, Enhanced electrocatalysis of oxygen reduction on platinum alloys in proton exchange membrane fuel cells, Journal of Electroanalytical Chemistry 357 (1993) 201-224.

[28] M.T. Paffet, G.J. Beery, S.Gottesfeld, Oxygen Reduction at $Pt_{0.65}Cr_{0.35}$, $Pt_{0.2}Cr_{0.8}$ and Roughened Platinum, Journal of the Electrochemical Society 153 (1988) 1431-1436.

[29] M. Watanabe, K. Tsurumi, T. Mizukami, T. Nakamura, P. Stonehart, Activity and Stability of Ordered and Disordered Co-Pt Alloys for Phosphoric Acid Fuel Cells, Journal of the Electrochemical Society 141 (1994) 2659-2668.

[30] A. Freund, J. Lang, T. Lehman, K. A. Starz, Improved Pt alloy catalysts for fuel cells, Catalysis Today 27 (1996) 279-283.

[31] M. Eikerling and A.A. Kornyshev, Modelling the performance of the cathode catalyst layer of polymer electrolyte fuel cells, Journal Electroanalytical Chemistry 453 (1998) 89-106.

[32] K. Broka and P. Ekdunge, Oxygen and hydrogen permeation properties and water uptake of Nafion 117 membrane and recast film for PEM fuel cell, Journal of Applied Electrochemistry 27 (1997) 281-289.

[33] P. Argyropoulos, K. Scott and W.M. Taama, Gas evolution and power performance in direct methanol fuel cells, Journal of Applied Electrochemistry 29 (1999) 661-669.

[34] P. Argyropoulos, K. Scott and W.M. Taama, Carbon dioxide evolution patterns in direct methanol fuel cells, Electrochimica Acta 29 (1999) 661-669.

[35] J. Nordlund, C. Picard, E. Birgersson, M. Vynnycky and G. Lindbergh, The design and usage of a visual direct methanol fuel cell, Journal of Applied Electrochemistry 34 (2004) 763-770.

[36] T. Bewer, T. Beckmann, H. Dohle, J. Mergel and D. Stolten, Novel method for investigation of two-phase flow in liquid feed direct methanol fuel cells using an aqueous H_2O_2 solution, Journal of Power Sources 125 (2004) 1-9.

[37] G.Q. Lu and C.Y. Wang, Electrochemical and flow characterization of a direct methanol fuel cell, Journal of Power Sources 134 (2004) 33-40.

[38] H. Yang, T.S. Zhao and Q, Ye, In situ visualization study of CO_2 gas bubble behaviour in DMFC anode flow fields, Journal of Power Sources 139 (2005) 79-90.

[39] H. Yang and T.S. Zhao, Effect of anode flow field design on the performance of liquid feed direct methanol fuel cells, Electrochimica Acta 50 (2005) 3243-3252

[40] Q. Liao, X. Zhu, X. Zheng and Y. Ding, Visualization study on the dynamics of CO_2 bubbles in anode channels and performance of a DMFC, Journal of Power Sources 171 (2007) 644-651.

[41] M.D. Lundin and M.J. McCready, Reduction of carbon dioxide gas formation at the anode of a direct methanol fuel cell using chemically enhanced solubility, Journal of Power Sources 172 (2007) 553-559.

[42] T.E. Springer, T.A. Zawodzinski and S. Gottesfeld, Polymer electrolyte fuel cell model, Journal of the Electrochemical Society 138 (1991) 2334-2341.

[43] Z.H. Wang, C.Y. Wang and K.S. Chen, Two.phase flow and transport in the air cathode of proton exchange membrane fuel cells, Journal of Power Sources 94 (2001) 40-50.

[44] X.G. Yang, F.Y. Zhang, A. Lubawy and C.Y. Wang, Visualization of liquid water transport in a polymer electrolyte fuel cell, Electrochemical and Solid State Letters 7 (11) (2004) A408-A411.

[45] M.M. Mench and C.Y. Wang, An in situ method for determination of current distribution in PEM fuel cells applied to a direct methanol fuel cell, Journal of the Electrochemical Society 150 (2003) 79-85.

[46] K.S. Chen, M.A. Hickner and D.R. Noble, Simplified models for predicting the onset of liquid water droplet instability at the gas diffusion layer/gas flow channel interface, International Journal of Energy Research 29 (2005) 1113-1132.

[47] M.W. Verbrugge, Methanol diffusion in perfluorinated ion-exchange membranes, Journal of the Electrochemical Society 136 (1989) 417-423.

[48] P.S. Kauranen and E. Skou, Methanol permeability in perfluorosulfonate proton exchange membranes at elevated temperatures, Journal of Applied Electrochemistry 26 (1996) 909-917.

[49] V. Tricoli, N. Carretta and M. Bartolozzi, A comparative investigation of proton and methanol transport in fluorinated ionomeric membranes, Journal of the Electrochemical Society 147 (2000) 1286-1290.

[50] S. Hikita, K. Yamane and Y. Nakajima, Measurement of methanol crossover in direct methanol fuel cell, JSAE Review 22 (2001) 151-156.

[51] H. Dohle, J. Divisek, J. Mergel, H.F. Oetjen, C. Zingler and D. Stolten, Recent developments of the measurement of the methanol permeation in a direct methanol fuel cell, Journal of Power Sources 105 (2002) 274-282.

[52] K. Ramya, K.S. Dhathathreyan, Direct methanol fuel cells: determination of fuel crossover in a polymer electrolyte membrane, Journal of Electroanalytical Chemistry 542 (2003) 109-115.

[53] N. Munichandraiah, K. McGrath, G. Prakash, R. Aniszfeld and G. Olah, A potentiometric method of monitoring methanol crossover through polymer

electrolyte membranes of direct methanol fuel cells, Journal of Power Sources 117 (2003) 98-101.

[54] R. Jiang and D. Chu, Comparative studies of methanol crossover and cell performance for a DMFC, Journal of the Electrochemical Society 151 (2004) 69-76.

[55] T.H. Kin, W.Y. Shieh, C.C. Yang and George Yu, Estimating the methanol crossover rate of PEM and the efficiency of DMFC via a current transient analysis, Journal of Power Sources 161 (2006) 1183-1186.

[56] J. Han, H. Liu, Real time measurements of methanol crossover in a DMFC, Journal of Power Sources 164 (2007) 166–173.

[57] J.Y. Park, J.H. Lee, S. Kang, J. Sauk and I. Song, Mass balance research for high electrochemical performance direct methanol fuel cells with reduced methanol crossover at various operating conditions, Journal of Power Sources 178 (2008) 181-187.

[58] M.K. Ravikumar, A.K. Shukla, Effect of methanol crossover in a liquid-feed polymer-electrolyte direct methanol fuel cell, Journal of the Electrochemical Society 143 (1996) 2601-2606.

[59] J. Cruickshank and K. Scott, The degree and effect of methanol crossover in the direct methanol fuel cell, Journal of Power Sources 70 (1998) 40-47.

[60] A. Küver, W. Vielstich, Investigation of methanol crossover and single electrode performance during PEMDMFC operation: A study using a solid polymer electrolyte membrane fuel cell system, Journal of Power Sources 74 (1998) 211-218.

[61] K. Scott, W.M. Taama, P. Argyropoulos and K. Sundmacher, The impact of mass transport and methanol crossover on the direct methanol fuel cell, Journal of Power Sources 83 (1999) 204-216.

[62] B. Gurau and E.S. Smotkin, Methanol crossover in direct methanol fuel cells: a link between power and energy density, Journal of Power Sources 112 (2002) 339-352.

[63] V. Gogel, T. Frey, Z. Yongsheng, K.A. Friedrich, L. Jörissen and J. Garche, Performance and methanol permeation of direct methanol fuel cells: dependence

on operating conditions and on electrode structure, Journal of Power Sources 127 (2004) 172-180.

[64] C.Y. Du, T.S. Zhao and W.W. Yang, Effect of methanol crossover on the cathode behaviour of a DMFC: A half-cell investigation, Electrochimica Acta 52 (2007) 5266–5271.

[65] K. Ramya and K.S. Dhathathreyan, Methanol crossover studies on heat-treated Nafion membranes, Journal of Membrane Science 311 (2008) 121–127.

[66] C. Pu, W. Huang, K.L. Ley and E.S. Smotkin, A methanol impermeable proton conducting composite electrolyte system, Journal of the Electrochemical Society 142 (1995) L119-L120.

[67] J.S. Wainright, J.-T. Wang, D. Weng, R.F. Savinell and M. Litt, Acid-Doped Polybenzimidazoles: A new polymer electrolyte, Journal of the Electrochemical Society 142 (1995) L121-L123.

[68] J.T. Wang, J.S. Wainright, R.F. Savinell and M. Litt, A direct methanol fuel cell using acid-doped polybenzimidazole as polymer electrolyte, Journal of Applied Electrochemistry 26 (1996) 751-756.

[69] A. Küver and K. Potje-Kamloth, Comparative study of methanol crossover across electropolymerized and commercial proton exchange membrane electrolytes for the acid direct methanol fuel cell, Electrochimica Acta 43 (1998) 2527-2535.

[70] V. Tricoli, Proton and methanol transport in poly(perfluorosulfonate) membranes containing Cs^+ and H^+ cations, Journal of the Electrochemical Society 145 (1998) 3798-3801.

[71] W. C. Choi, J. D. Kim and S. I. Woo, Modification of proton conducting membrane for reducing methanol crossover in a direct-methanol fuel cell, Journal of Power Sources 96 (2001) 411-414.

[72] L.J. Hobson, Y. Nakano, H. Ozu and S. Hayase, Targeting improved DMFC performance, Journal of Power Sources 104 (2002) 79-84.

[73] H. Uchida, Y. Mizuno and M. Watanabe, Suppression of methanol crossover and distribution of ohmic resistance in Pt- dispersed PEMs under DMFC operation, Journal of the Electrochemical Society 149 (2002) A682-A687.

[74] B. Yang and A. Manthiram, Multilayered membranes with suppressed fuel crossover for direct methanol fuel cells, Electrochemistry Communications 6 (2004) 231–236.

[75] A. Bettelheim, L. Soifer and E. Korin, Electropolymerized porphyrin films as methanol barriers in direct methanol fuel cells, Journal of Electroanalytical Chemistry 571 (2004) 265-272.

[76] K. Lee, J.H. Nam, J.H. Lee, Y. Lee, S.M. Cho, C.H. Jung, H.G. Choi, Y.Y. Chang, Y.U. Kwon and J.D. Nam, Methanol and proton transport control by using layered double hydroxide nanoplatelets for direct methanol fuel cell, Electrochemistry Communications 7 (2005) 113–118

[77] H. Tang, M. Pan, S. Jiang, Z. Wan and R. Yuan, Self-assembling multi-layer Pd nanoparticles onto Nafion membrane to reduce methanol crossover, Colloids and Surfaces A: Physicochem. Eng. Aspects 262 (2005) 65–70.

[78] S. Mu, H. Tang, Z. Wan, M. Pan and R. Yuan, Au nanoparticles self-assembled onto Nafion membranes for use as methanol-blocking barriers, Electrochemistry Communications 7 (2005) 1143–1147.

[79] Z.X. Liang, T.S. Zhao and J. Prabhuram, Diphenylsilicate-incorporated Nafion® membranes for reduction of methanol crossover in direct methanol fuel cells, Journal of Membrane Science 283 (2006) 219–224.

[80] E.H. Junga, U.H. Jungb, T.H.Yanga, D.H. Peaka, D.H. Junga and S.H. Kim, Methanol crossover through Pt/Ru/Nafion composite membrane for a direct methanol fuel cell, International Journal of Hydrogen Energy 32 (2007) 903 – 907.

[81] E. Higuchi, N. Asano, K. Miyatake, H. Uchida and Masahiro Watanabe, Distribution profile of water and suppression of methanol crossover in sulfonated polyimide electrolyte membrane for direct methanol fuel cells, Electrochimica Acta 52 (2007) 5272–5280.

[82] A. Yamauchi, T. Ito and T. Yamaguchi, Low methanol crossover and high performance of DMFCs achieved with a pore-filling polymer electrolyte membrane, Journal of Power Sources 174 (2007) 170–175.

[83] R. Gosalawit, S. Chirachanchai, S. Shishatskiy and S.P. Nunes, Krytox–Montmorillonite–Nafion® nanocomposite membrane for effective methanol crossover reduction in DMFCs, Solid State Ionics 178 (2007) 1627–1635.

[84] S. Zhong, X. Cui, T. Fu and H. Na, Modification of sulfonated poly(etherether ketone) proton exchange membrane for reducing methanol crossover, Journal of Power Sources 180 (2008) 23-28.

[85] D. Wu, R. Fu, T. Xu, L. Wu and W. Yang, A novel proton-conductive membrane with reduced methanol permeability prepared from bromomethylated poly(2,6-dimethyl-1,4-phenylene oxide) (BPPO), Journal of Membrane Science 310 (2008) 522–530.

[86] V.M. Barragán and A. Heinzel, Estimation of the membrane methanol diffusion coefficient from the open circuit voltage measurements in a direct methanol fuel cell, Journal of Power Sources 104 (2002) 66-72.

[87] S.S. Sandhu, R.O. Crowther and J.P. Fellner, Prediction of methanol and water fluxes through a direct methanol fuel cell polymer electrolyte membrane, Electrochimica Acta 50 (2005) 3985-3991.

[88] M.G. Izenson and R. W. Hill, Water balance in PEM and direct methanol fuel cells, Journal of Fuel Cell Science and Technology 2 (2005) 1-8.

[89] G.Q. Lu, F.Q. Liu and C.Y. Wang, Water transport through Nafion 112 membrane in DMFCs, Electrochemical and Solid-State Letters, 8 (2005) Al-A4.

[90] F. Liu, G. Lu and C.Y. Wang, Low Crossover of Methanol and Water Through Thin Membranes in Direct Methanol Fuel Cells, Journal of the Electrochemical Society 153 (2006) A543-A553.

[91] W. Liu and C.Y. Wang, Modelling water transport in liquid feed direct methanol fuel cells, Journal of Power Sources 164 (2007) 189-195.

[92] M.H. Shi, J. Wang and Y.P. Chen, Study on water transport in PEM of a direct methanol fuel cell, Journal of Power Sources 166 (2007) 303-309.

[93] C. Xu and T.S. Zhao, In situ measurements of water crossover through the membrane for direct methanol fuel cells, Journal of Power Sources 168 (2007) 143-153.

[94] C. Xu, T.S. Zhao and Y.L. He, Effect of cathode gas diffusion layer on water transport and cell performance in direct methanol fuel cells, Journal of Power Sources 171 (2007) 268-274.

[95] C. Xu, T.S. Zhao and W.W. Wang, Modelling of water transport through the membrane electrode assembly for direct methanol fuel cells, Journal of Power Sources 178 (2008) 291-308.

[96] F. Liu and C.Y. Wang, Water and methanol crossover in direct methanol fuel cells - Effect of anode diffusion media, Electrochimica Acta 53 (2008) 5517-5522.

[97] D.H. Jung, C.H. Lee, C.S. Kim, D.R. and Shin, Performance of a direct methanol polymer electrolyte fuel cell, Journal of Power Sources 71 (1998) 169-173.

[98] K. Scott, W. M. Taama, P. Argyropoulos, Material aspects of the liquid feed direct methanol fuel cell, Journal of Applied Electrochemistry 28 (1998) 1389-1397.

[99] K. Scott, W.M. Taama, S. Kramer, P. Argyropoulos, K. Sundmacher, Limiting current behaviour of the direct methanol fuel cell, Electrochimica Acta 45 (1999) 945–957.

[100] M. Baldauf, W. and Preidel, Experimental results on the direct electrochemical oxidation of methanol in PEM fuel cells, Journal of Applied Electrochemistry 31 (2001) 781-786.

[101] J.C. Amphlett, B.A. Peppley, E. Halliop and A. Sadiq, The effect of anode flow characteristics and temperature on the performance of a direct methanol fuel cell, Journal of Power Sources 96 (2001) 204-213.

[102] S.C. Thomas, X. Ren, S. Gottesfeld, P. Zelenay, Direct methanol fuel cells: progress in cell performance and cathode research, Electrochimica Acta 47 (2002) 3741-/3748.

[103] N. Nakagawa, Y. and Xiu, Performance of a direct methanol fuel cell operated at atmospheric pressure, Journal of Power Sources 118 (2003) 248-255.

[104] J. Ge, and H. Liu, Experimental studies of a DMFC, Journal of Power Sources 142 (2005) 56-69.

[105] H. Yang, T.S. Zhao, Q. Ye, Pressure drop behaviour in the anode flow field of liquid feed direct methanol fuel cells, Journal of Power Sources 142 (2005) 117-124.

[106] A.S. Aricò, P. Cretì, V. Baglio, E. Modica and V. Antonucci, Influence of flow field design on the performance of a direct methanol fuel cell, Journal of Power Sources 91 (2000) 202-209.

[107] K. Tuber, A. Oedegaard, M. Hermann and C. Hebling, Investigation of fractal flow-fields in portable proton exchange membrane and direct methanol fuel cells, Journal of Power Sources 131 (2004) 175-181.

[108] Z. Wei, S. Wang, B. Yi, J. Liu, L. Chen, W. Zhou, W. Li and Q. Xin, Influence of electrode structure on the performance of a direct methanol fuel cell, Journal of Power Sources 106 (2002) 364-369.

[109] C. Xu, T.S. Zhao and Q. Ye, Effect of anode backing layer on the cell performance of a direct methanol fuel cell, Electrochimica Acta 51 (2006) 5524-5531.

[110] D. Cheddie, N. Munroe, Review and comparison of approaches to proton exchange membrane fuel cell modeling, Journal of Power Sources 147 (2005) 72-84.

[111] K. Z. Yao, K. Karan, K. B. McAuley, P. Oosthuizen , B. Peppley, T. Xie, A review of mathematical models for hydrogen and direct methanol polymer electrolyte membrane fuel cells, Fuel Cells (2004), 4, No. 1-2, 3-29.

[112] K. Scott, W. Taama, J. Cruickshank, Performance and modeling of a direct methanol solid polymer electrolyte fuel cell, Journal of Power Sources 65 (1997) 159-171.

[113] K. Sundmacher, K. Scott, Direct methanol polymer electrolyte fuel cell: Analysis of charge and mass transfer in the vapor-liquid-solid system, Chemical Engineering Science 54 (1999) 2927-2936.

[114] A. A. Kulikovsky, The voltage-current curve of a direct methanol fuel cell: "exact" and fitting equations, Electrochemistry Communications 4 (2002) 939-946.

[115] A. A. Kulikovsky, Analytical model of the anode side of DMFC: the effect of non-Tafel kinetics on cell performance, Electrochemistry Communications 5 (2003) 530-538.

[116] A. A. Kulikovsky, A method for analysis of DMFC performance curves, Electrochemistry Communications 5 (2003) 1030-1036.

[117] K. Scott, P. Argyropoulos, A one dimensional model of a methanol fuel cell anode, Journal of Power Sources 137 (2004) 228-238.

[118] K. Scott, P. Argyropoulos, A current distribution model of a porous fuel cell electrode, Journal of Electroanalytical Chemistry 567 (2004) 103-109.

[119] Hang Guo, Chong-fang Ma, 2D analytical model of a direct methanol fuel cell, Electrochemistry Communications 6 (2004) 306-312.

[120] B. L. García, V. A. Sethuraman, J. W. Weidner, R. E. White, Mathematical Model of a Direct Methanol Fuel Cell, Journal of Fuel Cell Science and Technology Vol.1, November 2004, 43-48.

[121] P. S. Kauranen, E. Skou, Mixed methanol oxidation/oxygen reduction currents on a carbon supported Pt catalyst, Journal of Electroanalytical Chemistry 408 (1996) 189-198.

[122] K. Sundmacher, T. Schultz, S. Zhou, K. Scott, M. Ginkel, E.D. Gilles, Dynamics of the direct methanol fuel cell (DMFC): experiments and model-based analysis, Chemical Engineering Science 56 (2001) 333-341.

[123] A. Simoglou, P. Argyropoulos, E. B. Martin, K. Scott, A. J. Morris, W. M. Taama, Dynamic modeling of the voltage response of direct methanol fuel cells and stacks Part I: Model development and validation, Chemical Engineering Science 56 (2001) 6761-6772.

[124] A. Simoglou, P. Argyropoulos, E. B. Martin, K. Scott, A. J. Morris, W. M. Taama, Dynamic modeling of the voltage response of direct methanol fuel cells and stacks Part II: Feasibility study of model-based scale-up and scale-down, Chemical Engineering Science 56 (2001) 6773-6779.

[125] P. Argyropoulos, K. Scott, A. K. Shukla, C. Jackson, A semi-empirical model of the direct methanol fuel cell performance Part I. Model development and verification, Journal of Power Sources 123 (2003) 190-199.

[126] H. Dohle, K. Wippermann, Experimental evaluation and semi-empirical modeling of U/I characteristics and methanol permeation of a direct methanol fuel cell, Journal of Power Sources 135 (2004) 152-164.

[127] K. Scott, W. Taama, J. Cruickshank, Performance of a direct methanol fuel cell, Journal of Applied Electrochemistry 28 (1998) 289-297.

[128] A. A. Kulikovsky, J. Divisek, A.A. Kornyshev, Modeling the Cathode Compartment of Polymer Electrolyte Fuel Cells: Dead and Active Reacting Zones, Journal of the Electrochemical Society 146 (11), 3981-3991 (1999).

[129] P. Argyropoulos, K. Scott, W. M. Taama, Pressure drop modeling for liquid feed direct methanol fuel cells Part 1. Model development, Chemical Engineering Journal 73 (1999) 217-227.

[130] P. Argyropoulos, K. Scott, W. M. Taama, Pressure drop modeling for liquid feed direct methanol fuel cells Part II. Model based parametric analysis, Chemical Engineering Journal 73 (1999) 229-245.

[131] K. Scott, P. Argyropoulos, K. Sundmacher, A model for the Liquid Feed Direct methanol fuel cell, Journal of Electroanalytical Chemistry 477 (1999) 97-110.

[132] P. Argyropoulos, K. Scott, W.M. Taama, One-dimensional thermal model for direct methanol fuel cell stacks Part I. Model development, Journal of Power Sources 79 (1999) 169-183.

[133] P. Argyropoulos, K. Scott, W. M. Taama, One-dimensional thermal model for direct methanol fuel cell stacks Part II. Model based parametric analysis and predicted temperature profiles, Journal of Power Sources 79 (1999) 184-198.

[134] H. Dohle, J. Divisek, R. Jung, Process engineering of the DMFC, Journal of Power Sources 86 (2000) 469-477.

[135] A. A. Kulikovsky, Two-dimensional numerical modeling of a direct methanol fuel cell, Journal of Applied Electrochemistry 30 (2000) 1005-1014.

[136] P. Argyropoulos, K. Scott, W. M. Taama, Modeling flow distribution for internally manifolded direct methanol fuel cell stacks, Chemical Engineering Technology 23 (2001) 11 985-995.

[137] J. Nordlund, G. Lindbergh, A Model for the porous Direct Methanol Fuel Cell, Journal of the Electrochemical Society 149 (9), A1107-A1113 (2002).

[138] J. P. Meyers, J. Newman, Simulation of the Direct Methanol Fuel Cell, I. Thermodynamic Framework for a Multicomponent Membrane, Journal of the Electrochemical Society 149 (6) A710-A717 (2002).

[139] J. P. Meyers, J. Newman, Simulation of the Direct Methanol Fuel Cell, III. Design and Optimization, Journal of the Electrochemical Society 149 (6) A729-A735 (2002).

[140] A. K. Shukla , C. L. Jackson , K. Scott , G. Murgia , A solid-polymer electrolyte direct methanol fuel cell with a mixed reactant and air anode, Journal of Power Sources 111 (2002) 43-51.

[141] K. T. Jeng, C. W. Chen, Modeling and simulation of a direct methanol fuel cell anode, Journal of Power Sources 112 (2002) 367-375.

[142] S. S. Sandhu, R. O. Crowther, S. C. Krishnan, J. P. Fellner, Direct methanol polymer electrolyte fuel cell modeling: reversible open-circuit voltage and species flux equations, Electrochimica Acta 48 (2003) 2295-2303.

[143] G. Murgia, L. Pisani, A. K. Shukla, K. Scott, A Numerical Model of a Liquid-Feed Solid Polymer Electrolyte DMFC and Its Experimental Validation, Journal of the Electrochemical Society 150 (9) A1231-A1245 (2003).

[144] E. Birgersson, J. Nordlund, H. Ekström, M. Vynnycky, G. Lindbergh, Reduced Two-Dimensional One-Phase Model for Analysis of the Anode of a DMFC, Journal of the Electrochemical Society 150 (10) A1368-A1376 (2003).

[145] J. Divisek, J. Fuhrmann, K. Gärtner, R. Jung, Performance Modeling of a Direct Methanol Fuel Cell, Journal of The Electrochemical Society 150 (6) A811-A825 (2003).

[146] Z. H. Wang, C. Y. Wang, Mathematical modeling of liquid-feed direct methanol fuel cell Journal of The Electrochemical Society 150 (4) A508-A519 (2003).

[147] U. Krewer, Y. Song, K. Sundmacher, V. John, R. Lübke, G. Matthies, L. Tobiska, Direct methanol fuel cell (DMFC): analysis of residence time behavior of anodic flow bed, Chemical Engineering Science 59 (2004) 119-130.

[148] E. Birgersson, J. Nordlund, C. Picard, M. Vynnycky, G. Lindbergh, Reduced Two-Phase Model for Analysis of the Anode of a DMFC, Journal of the Electrochemical Society 151 (12) A2157-A2172 (2004).

[149] P. Argyropoulos, K. Scott, W. M. Taama, Modeling pressure distribution and anode/cathode streams vapor-liquid equilibrium composition in liquid feed direct methanol fuel cells, Chemical Engineering Journal 78 (2004) 29-41.

[150] A. A. Kulikovsky, Model of the flow with bubbles in the anode channel and performance of DMFC, Electrochemistry Communications 7 (2005) 237-243.

[151] T. Schultz, K. Sundmacher, Rigorous dynamic model of a direct methanol fuel cell based on Maxwell-Stefan mass transport equations and a Flory-Huggins activity model: Formulation and experimental validation, Journal of Power Sources 145 (2005) 435-462.

[152] A. A. Kulikovsky, Comment on "A one dimensional model of a methanol fuel cell anode", Journal of Power Sources 148 (2005) 54.

[153] A. A. Kulikovsky, Bubbles in the anode channel and performance of a DMFC: Asymptotic solutions, Electrochimica Acta 51 (2006) 2003-2011.

[154] J.G. Liu, T.S. Zhao, R. Chen, C.W. Wong, The effect of methanol concentration on the performance of a passive DMFC, Electrochemistry Communications 7 (2005) 288-294.

[155] B.K. Kho, B. Bae, M.A. Scibioh, J. Lee, H.Y. Ha, On the consequences of methanol crossover in passive air-breathing direct methanol fuel cells, Journal of Power Sources 142 (2005) 50-55.

[156] J.G. Liu, T.S. Zhao, Z.X. Liang, R. Chen, Effect of membrane thickness on the performance and efficiency of passive direct methanol fuel cells, Journal of Power Sources 153 (2006) 61-67.

[157] R. Chen, T.S. Zhao, J.G. Liu, Effect of cell orientation on the performance of passive direct methanol fuel cells, Journal of Power Sources 157 (2006) 351-357.

[158] B. Bae, B.K. Kho, T.H. Lim, I.H. Oh, S.A. Hong, H.Y. Ha, Performance evaluation of passive DMFC single cells, Journal of Power Sources 158 (2006) 1256-1261.

[159] N. Nakagawa, M.A. Abdelkareem, K. Sekimoto, Control of methanol transport and separation in a DMFC with a porous support, Journal of Power Sources 160 (2006) 105-115.

[160] Y.H. Pan, Advanced air-breathing direct methanol fuel cells for portable applications, Journal of Power Sources 161 (2006) 282-289.

[161] M.A. Abdelkareem, N. Nakagawa, DMFC employing a porous plate for an efficient operation at high methanol concentrations, Journal of Power Sources 162 (2006) 114-123.

[162] H. Kim, J. Oh, J. Kim, H. Chang, Membrane electrode assembly for passive direct methanol fuel cells, Journal of Power Sources 162 (2006) 497-501.

[163] K. Song, H. Lee, H. Kim, MEA design for low water crossover in air-breathing DMFC, Electrochimica Acta 53 (2007) 637-643.

[164] G. Jewett, Z. Guo, A. Faghri, Water and air management systems for a passive direct methanol fuel cell, Journal of Power Sources 168 (2007) 434-446.

[165] P. Scharfer, W. Schabel, M. Kind, Mass transport measurements in membranes by means of in situ Raman spectroscopy- First results of methanol and water profiles in fuel cell membranes, Journal of Membrane Science 303 (2007) 37-42.

[166] R.Chen, T.S. Zhao, Mathematical modelling of a passive-feed DMFC with heat transfer effect, Journal of Power Sources 152 (2005) 122-130.

[167] J. Rice, A. Faghri, A transient, multi-phase and multi-component model of a new passive DMFC, International Journal of Heat and Mass Transfer 49 (2006) 4804-4820.

[168] V. Saarinen, O. Himanen, T. Kallio, G. Sundholm, K. Kontturi, A 3D model for the free-breathing direct methanol fuel cell: Methanol crossover aspects and validations with current distribution measurements, Journal of Power Sources 172 (2007) 805-815.

[169] R.Chen, T.S. Zhao, W.W. Yang, C. Hu, Two-dimensional two-phase thermal model for a passive direct methanol fuel cells, Journal of Power Sources 175 (2008) 276-287.

[170] T.K. Yeh, C.H. Chen, Modelling and optimizing the performance of a passive direct methanol fuel cell, Journal of Power Sources 175 (2008) 353-362.

[171] T.K. Sherwood, R.L. Pigford, C.R. Wilke, Mass Transfer, McGraw-Hill, 1975.

[172] Y.A. Çengel, Heat Transfer a Practical Approach, McGraw-Hill, 1998.

[173] Thorsten Schultz, Experimental and Model-based Analysis of the Steady-state and Dynamic Operating Behaviour of the Direct Methanol Fuel Cell (DMFC), PhD thesis, 2004.

[174] R.C. Reid, J.M. Prausnitz, T.K. Sherwood, The Properties of Gases and Liquids, McGraw-Hill, 1977.

[175] F. Liu, C.Y. Wang, Dramatic Reduction of Water Crossover in Direct Methanol Fuel Cells by Cathode Humidification, Electrochemical and Solid-State Letters 12 (6) (2009) B101.

[176] K. Yoshizawa, K. Ikezone, Y. Tasaki, Kramer D., E.H. Lehmann, C.C. Sherer, Analysis of gas diffusion layer and flow field design in a PEMFC using neutron radiography, J. Electrochemical Society 155 (2008) B223-227.

[177] Y. Wang, C.Y. Wang and K.S. Chen, Elucidating differences between carbon paper and carbon cloth in polymer electrolyte fuel cells, Electrochimica Acta 52 (2007) 3695–9375.

[178] F. Barbir, PEM Fuel Cells: Theory and Practice, Elsevier Academic Press, Oxford, 2005.

[179] Fideris: http://www.fideris.com

[180] J.S. Cowart, An experimental and modelling based investigation into the high stoichiometric flow rates required in direct methanol fuel cells, Journal of Power Sources 143 (2005) 30-35.

[181] G.B. Jung, A. Su, C.H. Tu, Y.T. Lin, F.B. Weng and S.H. Chan, Effects of cathode flow fields on direct methanol fuel cell-simulation study, Journal of Power Sources 171 (2007) 212-217.

[182] Perry, Robert H., Chilton, Cecil H., Chemical Engineers' Handbook, Fifth edition, McGraw-Hill, 1973.

Appendix A: Uncertainty analysis

Consider generically a parameter Y by a function of n measured variables (y_1, …., y_n):

$$Y = f(y_1, y_2, ..., y_n) \tag{A.1}$$

If the uncertainty of each of the measured variables is represented by δy_1, …, δy_n, one can evaluate the uncertainty of parameter Y as follows (general uncertainty analysis approach):

$$(\delta Y)^2 = \left(\frac{\partial Y}{\partial y_1}\delta y_1\right)^2 + \left(\frac{\partial Y}{\partial y_2}\delta y_2\right)^2 + ... + \left(\frac{\partial Y}{\partial y_n}\delta y_n\right)^2 \tag{A.2}$$

The evaluation of uncertainty of the parameters that affect the experimental results is described in detail in the following sections.

A.1. Methanol concentration

The methanol solutions used in the tests performed with an active and passive feed DMFC were prepared following the equation:

$$C_{final} = \frac{V_{initial}}{V_{final}} C_{initial} \tag{A.3}$$

According to the general uncertainty approach, the uncertainty of the resulting variable (C_{final}) can be calculated as follows:

$$(\delta C_{final})^2 = \left(\frac{\partial C_{final}}{\partial V_{initial}}\delta V_{initial}\right)^2 + \left(\frac{\partial C_{final}}{\partial V_{final}}\delta V_{final}\right)^2 \tag{A.4}$$

where the $\delta V_{initial}$ and δV_{final} refer to uncertainties of the corresponding measured variables. The two partial derivates are expanded in the following equations. Notice that both sides of each expanded equation were divided by the variable C_{final}.

$$\left(\frac{1}{C_{final}}\right)\frac{\partial C_{final}}{\partial V_{initial}} = \frac{1}{V_{initial}} \tag{A.5}$$

$$\left(\frac{1}{C_{final}}\right)\frac{\partial C_{final}}{\partial V_{final}} = \frac{1}{V_{final}} \tag{A.6}$$

Equation A.3 can, thus, be rewritten in the form:

$$\left(\frac{\delta C_{final}}{C_{final}}\right)^2 = \left(\frac{\delta V_{initial}}{V_{initial}}\right)^2 + \left(\frac{\delta V_{final}}{V_{final}}\right)^2 \tag{A.7}$$

A final algebraic manipulation yields an expression for the relative uncertainty of the methanol concentration:

$$\frac{\delta C_{final}}{C_{final}} = \sqrt{\left(\frac{\delta V_{initial}}{V_{initial}}\right)^2 + \left(\frac{\delta V_{final}}{V_{final}}\right)^2} \tag{A.8}$$

Regarding the active feed DMFC, all the methanol solutions prepared have the same V_{final} (2000 ml ± 0.6 ml).

Table A.1 – Values of parameters and uncertainties regarding the methanol concentration for the active feed DMFC.

Methanol concentration (M)	$V_{initial}$ (ml)	$\delta V_{initial}$ (ml)	$\frac{\delta C_{final}}{C_{final}}$ (%)
0.25	20	0.038	0.19
0.5	40	0.06	0.15
0.75	60	0.08	0.14
1	80	0.5	0.63
1.5	120	1	0.83
2	160	1	0.63
3	240	1	0.42
5	400	5	1.25

All the methanol solutions prepared, for the passive feed DMFC, have a V_{final} of 50 ml ± 0.06 ml.

Table A.2 – Values of parameters and uncertainties regarding the methanol concentration for the passive feed DMFC.

Methanol concentration (M)	$V_{initial}$ (ml)	$\delta V_{initial}$ (ml)	$\frac{\delta C_{final}}{C_{final}}$ (%)
1	2	0.01	0.51
2	4	0.03	0.76
3	6	0.03	0.51
4	8	0.04	0.51
5	10	0.02	0.23

A.2. Air flow rate

The air flow rate was set using the MTK unit and FCPower Software using a mass flow controller, so the uncertainty associated with this parameter depends on the uncertainty of the mass flow controller (δMFC), the uncertainty of the data acquisition ($\delta Data$) and the uncertainty of the measurement ($\delta Read$). According to the general uncertainty approach, and after algebraic manipulation, the uncertainty of the resulting variable (q_{air}) can be determined as follows:

$$\frac{\delta q_{air}}{q_{air}} = \sqrt{\left(\frac{\delta MFC}{q_{air}}\right)^2 + \left(\frac{\delta Data}{q_{air}}\right)^2 + \left(\frac{\delta \mathrm{Re}ad}{q_{air}}\right)^2} \tag{A.9}$$

Since the uncertainty of the data acquisition ($\delta Data$) and the measurement ($\delta Read$) are much lower than the uncertainty of the mass flow controller (δMFC), they were neglected in the calculation of the overall uncertainty. The uncertainty of the mass flow controller (δMFC) is $\pm\ 0.01\% \times range$. As already mentioned in Chapter 4 the range of the MFC is from 0 to 10 l/min.

Table A.3 – Values of parameters and uncertainties regarding the air flow rate.

q_{air} (l/min)	δMFC (l/min)	$\frac{\delta q_{CH_3OH}}{q_{CH_3OH}}$ (%)
3.6	0.2	5.56
2	0.2	10
1.5	0.2	13.33
1	0.2	20
0.75	0.2	26.68
0.5	0.2	40

A.3. Methanol flow rate

The methanol flow rate was set using the MTK unit and FCPower Software using a magnetic micropump, so the uncertainty associated with this parameter depends on the uncertainty of the micropump (δMP), the uncertainty of the data acquisition ($\delta Data$) and the uncertainty of the measurement ($\delta Read$). According to the general uncertainty approach, and after algebraic manipulation, the uncertainty of the resulting variable (q_{CH_3OH}) can be calculated as follows:

$$\frac{\delta q_{CH_3OH}}{q_{CH_3OH}} = \sqrt{\left(\frac{\delta MP}{q_{CH_3OH}}\right)^2 + \left(\frac{\delta Data}{q_{CH_3OH}}\right)^2 + \left(\frac{\delta \mathrm{Re}ad}{q_{CH_3OH}}\right)^2} \tag{A.10}$$

Since the uncertainty of the data acquisition ($\delta Data$), the uncertainty of the micropump (δMP) and the uncertainty of the measurement ($\delta Read$) are very low the overall uncertainty is near zero, so this uncertainty was neglected.

A.4. Current

The current was set using the MTK unit and FCPower Software using a loadbank system, so the uncertainty associated with this parameter depends on the uncertainty of the loadbank (δLB), the uncertainty of the data acquisition ($\delta Data$) and the uncertainty of the measurement ($\delta Read$). According to the general uncertainty approach, and after algebraic manipulation, the uncertainty of the resulting variable (I_{Cell}) can be determined as follows:

$$\frac{\delta I_{Cell}}{I_{Cell}} = \sqrt{\left(\frac{\delta LB}{I_{Cell}}\right)^2 + \left(\frac{\delta Data}{I_{Cell}}\right)^2 + \left(\frac{\delta \mathrm{Re}\,ad}{I_{Cell}}\right)^2} \tag{A.11}$$

Since the uncertainty of the data acquisition ($\delta Data$) and the measurement ($\delta Read$) are much lower than the uncertainty of the loadbank system (δLB), they were neglected in the calculation of the overall uncertainty. The uncertainty of the loadbank system (δLB) is $\pm\ 5\% \times I_{Cell}$.

Table A.4 – Values of parameters and uncertainties regarding the current.

I_{Cell} (A/cm^2)	δLB (A/cm^2)	$\frac{\delta I_{Cell}}{I_{Cell}}$ (%)
0.02	$\pm\ 5\% \times I_{Cell}$	5
0.04	$\pm\ 5\% \times I_{Cell}$	5
0.06	$\pm\ 5\% \times I_{Cell}$	5
0.08	$\pm\ 5\% \times I_{Cell}$	5
0.10	$\pm\ 5\% \times I_{Cell}$	5
0.12	$\pm\ 5\% \times I_{Cell}$	5

A.5. Potential

As already referred, all the tests were performed in the galvanostatic way. The current was set and the corresponding potential was measured by the loadbank system. It is therefore considered that we consider that the uncertainty associated with this parameter depends on the uncertainty of the data acquisition ($\delta Data$) and the uncertainty of the measurement ($\delta Read$). According to the general uncertainty approach, and after algebraic manipulation, the uncertainty of the resulting variable (E_{Cell}) can be determined from:

$$\frac{\delta E_{Cell}}{E_{Cell}} = \sqrt{\left(\frac{\delta Data}{E_{Cell}}\right)^2 + \left(\frac{\delta \mathrm{Re}\,ad}{E_{Cell}}\right)^2} \tag{A.12}$$

Since the uncertainty of the data acquisition ($\delta Data$) is much lower than the uncertainty of the measurement ($\delta Read$), it was neglected in the calculation of the overall uncertainty.

Table A.5 – Values of parameters and uncertainties regarding the potential.

E_{Cell} (V)	$\delta Read$ (V)	$\frac{\delta E_{Cell}}{E_{Cell}}$ (%)
0.1	0.0005	0.50
0.3	0.0005	0.17
0.5	0.0005	0.10
0.7	0.0005	0.07
0.9	0.0005	0.06

A.6. Power

The power density presented in the results was determined by:

$$P = I_{Cell} V_{Cell} \tag{A.13}$$

According to the general uncertainty approach, the uncertainty of the resulting variable (P) is given by:

$$(\delta P)^2 = \left(\frac{\partial P}{\partial I_{Cell}} \delta I_{Cell} \right)^2 + \left(\frac{\partial P}{\partial V_{Cell}} \delta V_{Cell} \right)^2 \tag{A.14}$$

where the δI_{cell} and δV_{Cell} refer to uncertainties of the corresponding measured variables. The two partial derivates were expanded, both sides of each expanded equation were divided by the variable P and after some algebraic manipulation of Eq. A.14 yields the following expression for the relative uncertainty of the power density.

$$\frac{\delta P}{P} = \sqrt{\left(\frac{\delta I_{Cell}}{I_{Cell}} \right)^2 + \left(\frac{\delta V_{Cell}}{V_{Cell}} \right)^2} \tag{A.15}$$

Table A.6 – Values of parameters and uncertainties regarding the fuel cell power.

P (W/cm^2)	$\frac{\delta I_{Cell}}{I_{Cell}}$	$\frac{\delta E_{Cell}}{E_{Cell}}$	$\frac{\delta P}{P}$ (%)
0.01	0.05	0.0050	5.02
0.02	0.05	0.0017	5.00
0.03	0.05	0.0010	5.00
0.04	0.05	0.0007	5.00
0.05	0.05	0.0006	5.00

A.7. Fuel Cell Temperature

As already referred in Chapter 4 the fuel cell temperature was controlled by using a digital controller (OSAKA) (Fig. 4.16) and a thermocouple type K (range 1200ºC). The uncertainty associated with the fuel cell temperature depends on the uncertainty of the thermocouple (δTC) and the uncertainty of the measurement ($\delta Read$). According to the general uncertainty approach, and after algebraic manipulation, the uncertainty of the resulting variable (T_{Cell}) can be calculated as follows:

$$\frac{\delta T_{Cell}}{T_{Cell}} = \sqrt{\left(\frac{\delta TC}{T_{Cell}}\right)^2 + \left(\frac{\delta \mathrm{Re}\,ad}{T_{Cell}}\right)^2} \tag{A.16}$$

The uncertainty of the thermocouple (δTC) is $\pm\ 0.4\% \times range$.

Table A.7 – Values of parameters and uncertainties regarding the fuel cell temperature.

T_{Cell} (ºC)	δTC (ºC)	$\delta Read$ (ºC)	$\frac{\delta T_{Cell}}{T_{Cell}}$ (%)
20	4.8	0.5	24.13
40	4.8	0.5	12.06
60	4.8	0.5	8.04
70	4.8	0.5	6.89
80	4.8	0.5	6.03

A.8. Methanol solution temperature

The methanol solution temperature was set by using the MTK unit and FCPower Software using the methanol handling system and a thermocouple type K. The

uncertainty associated with this parameter depends on the uncertainty of the methanol handling system (δMHS), the uncertainty of the data acquisition ($\delta Data$), the uncertainty of the measurement ($\delta Read$) and the uncertainty of the thermocouple (δTC). According to the general uncertainty approach, and after algebraic manipulation, the uncertainty of the resulting variable (T_{CH_3OH}) can be determined by:

$$\frac{\delta T_{CH_3OH}}{T_{CH_3OH}} = \sqrt{\left(\frac{\delta MHS}{T_{CH_3OH}}\right)^2 + \left(\frac{\delta Data}{T_{CH_3OH}}\right)^2 + \left(\frac{\delta \mathrm{Re}\,ad}{T_{CH_3OH}}\right)^2 + \left(\frac{\delta TC}{T_{CH_3OH}}\right)^2} \qquad \text{(A.17)}$$

Since the uncertainty of the data acquisition ($\delta Data$) and the measurement ($\delta Read$) are much lower than the others, they were neglected in the calculation of the overall uncertainty. The uncertainty of the methanol handling system (δMHS) is $\pm\ 5\% \times T_{CH_3OH}$.

Table A.8 – Values of parameters and uncertainties regarding the methanol solution temperature.

T_{CH_3OH} (ºC)	δMHS (ºC)	δTC (ºC)	$\frac{\delta T_{Cell}}{T_{Cell}}$ (%)
20	$\pm\ 5\% \times T_{CH_3OH}$	4.8	24.51
40	$\pm\ 5\% \times T_{CH_3OH}$	4.8	13.00
60	$\pm\ 5\% \times T_{CH_3OH}$	4.8	9.43
70	$\pm\ 5\% \times T_{CH_3OH}$	4.8	8.49
80	$\pm\ 5\% \times T_{CH_3OH}$	4.8	7.81

Appendix B: Physical Properties and Parameters

In this Chapter all the physical properties and parameters needed for model simulations can be found.

B.1. Physical properties

B.1.1. Densities

The densities of all liquid, gases and solid materials are assumed to be independent of temperature and pressure.

Table B.1 – Densities

Species j	Density, ρ_j (kg/m^3)	Reference
Water (l)	1000	[172]
Air (g)	1.186	[172]
Platinum, Pt	21450	[172]
Ruthenium, Ru	12400	[173]
Carbon (base material for carbon paper and carbon cloth)	2000	[173]
Teflon, PTFE	2190	[173]
Nafion	1970	[173]

B.1.2. Specific heat

The heat capacities, for all materials, are necessary for the heat balances. Literature data are given in the next table.

Table B.2 – Specific heat

Species j	$C_{p,j}$ (J/molK)	Reference
Liquid water (l)	75.29	[172]
Methanol (l)	80.96	[172]
Carbon dioxide (g)	$4.187\times\left(4.728+0.01754T-1.338\times10^{-5}T^{2}+4.097\times10^{-9}T^{3}\right)$	[182]
Water vapour (g)	33.58	[172]
Oxygen (g)	$4.187\times\left(6.713-8.79\times10^{-5}T+4.17\times10^{-6}T^{2}-2.544\times10^{-9}T^{3}\right)$	[182]
Air	29	[172]

B.1.3. Thermal conductivities

For liquid water and air data for different temperatures are given in the literature [182]. The thermal conductivity shows a linear increase with temperature and linear regressions yield the expressions presented.

Table B.3 – Thermal conductivities

Species j	K_j (W/mK)	Reference
Liquid water	$0.341 + 9.26\times10^{-4}T$	[182]
Air	$0.0034 + 7.6\times10^{-5}T$	[182]
Graphite	98	[178]
Aluminium	237	[178]
Rubber	0.13	[178]
Copper	401	[178]
Carbon paper untreated	1.7	[178]
Carbon cloth untreated	0.15	[178]
Teflon, PTFE	0.35	[178]
Nafion	0.43	[173]
Platinum, Pt	71	[178]
Ruthenium, Ru	117	[178]

B.1.4. Specific enthalpies

Table B.4 – Standard enthalpies of formation

Species j	H^0_j (J/mol)	Reference
Liquid water (l)	-285830	[182]
Methanol (l)	-238660	[182]
Carbon dioxide (g)	-393510	[182]
Water vapour (g)	-241820	[182]
Oxygen (g)	0	[182]

B.1.5. Gibbs free energy

Table B.5 – Standard Gibbs free energy

Species j	G^0_j (J/mol)	Reference
Liquid water (l)	-237080	[182]
Methanol (l)	-166270	[182]
Carbon dioxide (g)	-394000	[182]
Water vapour (g)	-228588	[182]
Oxygen (g)	0	[182]

B.1.6. Viscosities

Accordingly to the data [172] for air viscosity for different temperatures a nearly dependence is evident between this two parameters and a linear regression yields the expression presented above.

Table B.6 – Viscosities

Species j	μ_j (Pa.s)	Reference
Water (l)	$10^{-3} \times \exp\left(-24.700 + \frac{4209}{T} + 0.04527T - 3.376\times10^{-5}T^2\right)$	[174]
Methanol (l)	$10^{-3} \times \exp\left(-39.350 + \frac{4826}{T} + 0.10910T - 1.127\times10^{-4}T^2\right)$	[174]
Air (g)	$10^{-6} \times (4.65 + 0.0464T)$	[172]

B.1.7. Liquid molar volumes

For the calculations of the diffusion coefficients in the anode side the liquid molar volumes of water and methanol are necessary.

Table B.7 – Liquid molar volumes

Species j	V_j (J/mol)	Reference
Water (l)	18.7×10^{-6}	[174]
Methanol (l)	42.5×10^{-6}	[174]

B.1.8. Parachors

For the calculations of the diffusion coefficients in the anode side the parachors values of water and methanol are necessary.

Table B.8 – Parachors values

Species j	P ($cm^3g^{0.25}/s^{-0.5}$)	Reference
Water	51	[171]
Methanol	85.3	[171]

B.1.9. Diffusion volumes

For the calculations of the diffusion coefficients in the cathode side the diffusion volumes of water, air and oxygen are necessary.

Table B.9 – Diffusion volumes

Species j	$\sum\upsilon$ (cm^3/mol)	Reference
Water	12.7	[171]
Air	20.1	[171]
Oxygen	16.6	[171]

B.1.10. Tortuosity

Table B.10 – Tortuosity

Species j	τ	Reference
Carbon cloth	1.11	[177]
Carbon paper	2.75	[177]

B.2. Diffusion coefficients

B.2.1. Anode diffusion and Catalytic layer

The binary diffusion coefficients of the mobile species in the anode diffusion and catalytic layer are calculated using the Tyn-Calus method [174] for diffusion coefficients in liquid solutions at infinite dilution (in [m²/s]):

$$D_{ij} = 8.93\times10^{-12}\left(\frac{V_i}{V_j^{\,2}}\right)^{1/6}\times\left(\frac{P_j}{P_i}\right)^{0.6}\times\frac{T}{\mu_j} \tag{B.1}$$

Here component i is the solute and j is the solvent. The molar volumes V are in cm³/mol, the viscosities μ in cP and the temperature T in K. P is so-called parachors, which are related to the liquid surface tension, but can also be estimated from a groups contribution method developed by QUAYLE [174]. For water and methanol this method leads to parachor values presented in table B.8. According to the literature, if water is the solute, the parachor and molar volume values of water shall be doubled (water is treated as a dimer).

As the mass transport takes place within a porous matrix, effective diffusion coefficients are needed. To convert the gained values into effective coefficients, it has to be accounted for the morphology of the solid matrix represented by the tortuosity coefficient, τ [171]:

$$D_{ij}^{eff} = \frac{\varepsilon}{\tau} D_{ij} \tag{B.2}$$

where D_{ij} is the usual diffusion coefficient in a binary system and ε is the porosity.

B.2.2. Cathode diffusion and Catalytic layer

In the cathode layers it is assumed that all mobile species (oxygen, water vapour and methanol) are ideal gases. The diffusion coefficient in the cathode diffusion and catalytic layer are calculated using the Fuller, Schettler and Giddings equation [171] for diffusion coefficients in binary gas mixtures (in [cm²/s]):

$$D_{ij} = \frac{10^{-3} \times T^{1.75} \left(1/M_i + 1/M_j\right)^{1/2}}{P\left[\left(\Sigma \upsilon_i\right)^{1/3} + \left(\Sigma \upsilon_j\right)^{1/3}\right]^2} \tag{B.3}$$

Here component *i* is the solute and *j* is the solvent. The molar mass *M* is in g/mol, the pressure *P* in atm, the temperature *T* in K and the diffusion volumes $\Sigma\upsilon$ in cm^3/mol.
Like in the anode side, the mass transport takes place within a porous matrix, effective diffusion coefficients are needed. To convert the gained values into effective coefficients should be used equation (2).

B.3. Porosities of fuel cells materials

For many purposes it is necessary to know the volume fractions of several combined materials, such as the PTFE-treated carbon papers or carbon cloths used for the diffusion layers and the material forming the catalyst layers. As in the model all material balances are formulated for the free volume in the porous materials forming the respective fuel cell layers, the porosities are essencial parameters.

B.3.1. Diffusion layers

Accordingly to the description of carbon cloth and carbon paper materials supplied by E-TEK, it is possible to estimate the porosity of the untreated material.

Table B.11 – Porosities of the common materials used as gas diffusion layers.

Material	Porosity
Carbon paper	0.78
Carbon cloth	0.83

The porosity of a gas diffusion layer may be easily calculated using the following equation [178]:

$$\varepsilon = 1 - \frac{W_A}{\rho_{real} \times \delta} \tag{B.4}$$

where W_A is the areal weight in g/cm^2, ρ_{real} is the solid phase density in g/cm^3 and δ is the thickness in cm.

As the carbon paper and carbon cloth are PTFE treated the real porosity has to be calculated as a function of the PFTE content.

$$\varepsilon^{tretated} = \frac{total\ volume - carbon\ volume - PTFE\ volume}{total\ volume} \tag{B.5}$$

$$carbon\ volume = \left(1 - \varepsilon^{untreated}\right) \times total\ volume \tag{B.6}$$

$$PTFE\ volume = \left(\frac{w_{PTFE}}{1 - w_{PTFE}} \times \frac{\rho_{carbon}}{\rho_{PTFE}}\right)\left(1 - \varepsilon^{untreated}\right) \times total\ volume \tag{B.7}$$

Substituting equations (6) and (7) in (5) one gets

$$\varepsilon^{tretated} = \varepsilon^{untreated} - \frac{w_{PTFE}}{1 - w_{PTFE}} \times \frac{\rho_{carbon}}{\rho_{PTFE}}\left(1 - \varepsilon^{untreated}\right) \tag{B.8}$$

where w_{PTFE} is the PTFE mass content, normally is 0.30, $\varepsilon^{treated}$ is the porosity of the gas diffusion layer material after the treatment with PTFE and $\varepsilon^{untreated}$ the porosity of the gas diffusion layer material before the treatment with PTFE.

B.3.2. Catalytic layers

The porosity of the catalytic layer in another important parameter and it can be calculated as:

$$\varepsilon = \frac{total\ volume - catalyst\ volume}{total\ volume} \tag{B.9}$$

$$catalyst\ volume = \frac{m_{cat}}{\rho_{cat}} = \frac{A^S \times w_{cat}}{\rho_{cat}} \tag{B.10}$$

$$total\ volume = A^S \times \delta \tag{B.11}$$

Substituting equations (B.10) and (B.11) in (B.9) one gets

$$\varepsilon = \frac{\delta - \frac{w_{cat}}{\rho_{cat}}}{\delta} \tag{B.12}$$

where w_{cat} is the catalyst loading and δ is the thickness of the catalytic layer.
In the anode side the catalyst loading is a mixture between platinum and ruthenium. In this way, the density of the mixed anode catalyst can be calculated from the mass fractions of both metals and their densities.

B.4. Effective thermal conductivities

B.4.1. Diffusion layers

As the diffusion layers are porous structures, their effective thermal conductivities have to be calculated accounting for the present materials and reactants as well as their volume fractions. In table B.3 thermal conductivities of the untreated materials are presented. Using this value and the volume fractions of carbon fibres and PTFE as well as the porosity, the effective thermal conductivity can be calculated accounting for the material filling the pores and for the temperature. In the anode diffusion layer (AD) the pores are assumed to be filled with a liquid mixture, which mainly consists of water. In

the cathode diffusion layer (CD) the pores are assumed to be filled with air. The resulting expressions are:

$$K^{AD} = \left(1-\varepsilon^{untreated}\right)K_j + \left(1-\varepsilon^{treated}\right)K_{PTFE} + \varepsilon^{untreated}K_{water} \tag{B.13}$$

$$K^{CD} = \left(1-\varepsilon^{untreated}\right)K_j + \left(1-\varepsilon^{treated}\right)K_{PTFE} + \varepsilon^{untreated}K_{air} \tag{B.14}$$

where *j* is carbon paper or carbon cloth

B.4.2. Catalytic layers

Like the diffusion layers the catalytic layers are porous structures, so a similar procedure has to be done. Using the values presented in table B.3 and the porosity, the effective thermal conductivity can be calculated accounting for the material filling the pores. The resulting expressions are:

$$K^{AC} = \left(1-\varepsilon\right)K_{Pt-Ru} + \varepsilon K_{water} \tag{B.15}$$

$$K^{CC} = \left(1-\varepsilon\right)K_{Pt} + \varepsilon K_{air} \tag{B.16}$$

The thermal conductivity of the mixed anode catalyst can be calculated from the mass fractions of both metals and their thermal conductivities.

B.5. Heat transfer in finned surfaces

If we consider a fin of constant cross-sectional area, *A*, and length $\delta^{sectionII}$ that is attached to the surface with a perfect contact heat will flow from the surface to the fin by conduction and from the fin to the surrounding medium by convection with the same heat transfer coefficient, *h*. In the ideal case of zero thermal resistance or infinite thermal conductivity, the temperature of the fin will be uniform and equal to the temperature of the base T_b (T_A or T_C see Figure 3.1). The heat transfer from the fin will be maximum in this case and can be calculated by [172]

$$Q_{fin,\max} = hA_{fin}\left(T_b - T_\infty\right) \tag{B.17}$$

where T_∞ is the medium temperature (T_5 or T_{10} see Figure 3.1).

In reality, however, the temperature of the fin will drop along the fin and thus the heat transfer from the fin will be less because of the decreasing temperature difference from the fin base to the fin tip. To account for this effect on heat transfer we need to define the fin efficiency as [172]

$$\eta_{fin} = \frac{\text{Actual heat transfer rate from the fin}}{\text{Ideal heat transfer rate from the fin if the entire fin were at temperature } T_b} = \frac{Q_{fin}}{Q_{fin,\max}} \tag{B.18}$$

or

$$Q_{fin} = n_{channels}\eta_{fin}hA_{fin}\left(T_b - T_\infty\right) \tag{B.19}$$

where A_{fin} is the total surface area of the fin. If we consider the case of constant cross-section of very long fin the fin efficiency can be expressed as [172]

$$\eta_{fin} = \frac{1}{L\sqrt{\frac{hP}{KA}}} \tag{B.20}$$

were

$$A = w + e, \tag{B.21}$$

$$P = 2\times\left(w\times\delta^{\text{sec}tionII}\right) \tag{B.22}$$

and

$$A_{fin} = 2\times w\times\delta^{\text{sec}tionII} \tag{B.23}$$

The h that appears in equations (B.17), (B.19) and (B.20) is the heat transfer coefficient of water or air if is related to the anode or cathode side. The heat transfer coefficient is calculated using the set of equations presented in the next section.

B.6. Heat transfer coefficients in the anode and cathode channels

To calculate the heat transfer coefficients in the anode and cathode channels we use the correlations for forced convection inside tubes with laminar flow [172]. Therefore the hydraulic diameter is

$$D_h = \frac{4 \times A_{channel}}{P_{channel}} \tag{B.24}$$

were

$$A_{channel} = \delta^{\sec tionII} \times e \tag{B.25}$$

and

$$P_{channel} = 2\delta^{\sec tionII} + 2e \tag{B.26}$$

The maximum liquid and air velocity is

$$v_{\max}^{A} = \frac{Q^{AF}}{A_{channel} \times n_{channels}} \tag{B.27}$$

and

$$v_{\max}^{C} = \frac{Q^{CF}}{A_{channel} \times n_{channels}} \tag{B.28}$$

The maximum Reynolds number, for anode and cathode, is

$$\mathrm{Re}_{\max}^{A} = \frac{v_{\max}^{A} \times D_h \times \rho_{H_2O}}{\mu_{H_2O}} \tag{B.29}$$

and

$$\mathrm{Re}_{\max}^{C} = \frac{v_{\max}^{C} \times D_h \times \rho_{air}}{\mu_{air}} \tag{B.30}$$

For the values assumed to the anode and cathode flow rate the Reynolds number is inferior to 2300 which means laminar flow. For such flow conditions the Nusselt number as representation of the heat transfer coefficient, *h*, defined as

$$Nu = \frac{h \times D_h}{K} \tag{B.31}$$

Can be calculated from the correlation [172]

$$Nu = 1.86\left(\frac{\mathrm{Re} \times \mathrm{Pr} \times D_h}{w}\right)^{1/3} \tag{B.32}$$

The Prandtl numbers are

$$\mathrm{Pr}_{H_2O} = \frac{Cp_{H_2O,1} \times \mu_{H_2O}}{K_{H_2O}} \tag{B.33}$$

and

$$\mathrm{Pr}_{air} = \frac{Cp_{air} \times \mu_{air}}{K_{air}} \tag{B.34}$$

Appendix C: Experimental Results of an active feed DMFC

In this Chapter all the experimental results performed with the «in-house» developed active feed DMFC are presented. The results are very important and useful for evaluate the effect of different operating and design parameters on fuel cell performance and for the validation of mathematical models.

C.1. Effect of operating conditions

All the results presented in this section were obtained with a DMFC with carbon cloth type A and ELAT (E-TEK) as, respectively, anode and cathode gas diffusion layer. The catalyst loading used was 4 mg/cm^2 of Pt/Ru and Pt, respectively, at the anode and cathode side. The membrane used was Nafion 117 and a single serpentine flow field both for anode and cathode.

C.1.1. Methanol concentration

Table C.1 – Set of operating conditions used to analyse the effect of methanol concentration on the cell performance.

C_{CH_3OH} (M)	q_{CH_3OH} (ml/min)	q_{air} (l/min)	Cell temperature (ºC)
0.25	8	3.6	20
0.5			
0.75			
1			
1.5			
2			
3			
0.25	3	3.6	20
0.5			
0.75			
1			
1.5			
2			
3			
5			
0.25	3	1	20
0.5			
0.75			
1			
1.5			
2			
3			

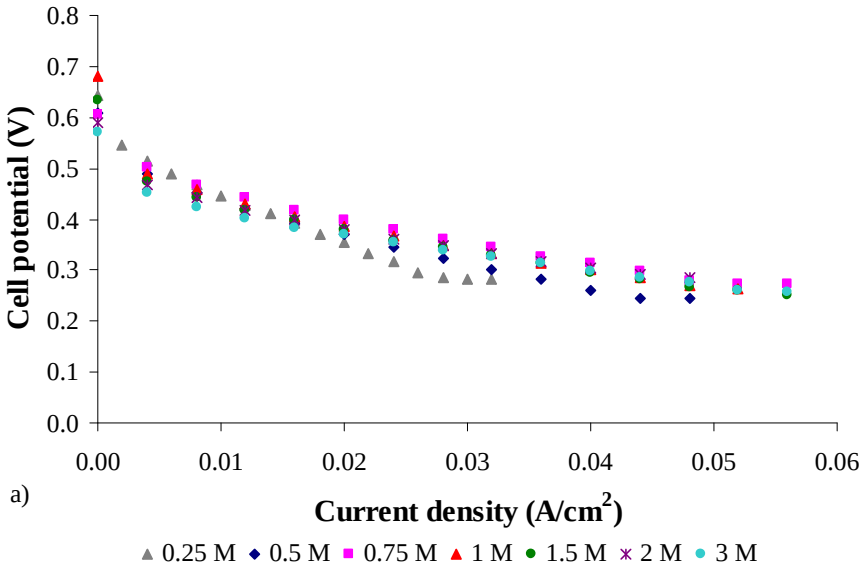

Figure C.1 – Effect of methanol concentration on a) cell performance. Operating conditions: methanol flow rate 8 ml/min and air flow rate 3.6 l/min.

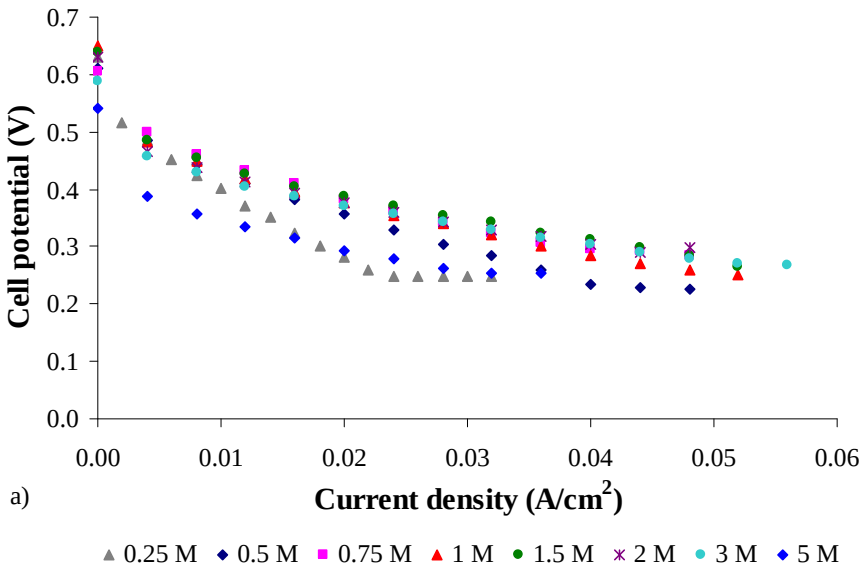

Figure C.2 – Effect of methanol concentration on a) cell performance. Operating conditions: methanol flow rate 3 ml/min and air flow rate 3.6 l/min.

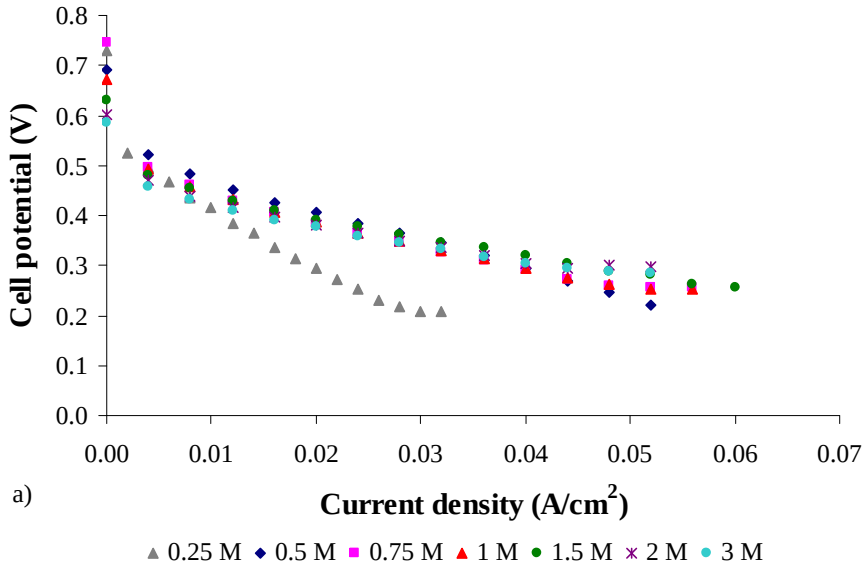

Figure C.3 – Effect of methanol concentration on a) cell performance. Operating conditions: methanol flow rate 3 ml/min and air flow rate 1 l/min.

C.1.2. Fuel cell temperature

Table C.2 – Set of operating conditions used to analyse the effect of cell temperature on the cell performance.

C_{CH_3OH} (M)	q_{CH_3OH} (ml/min)	q_{air} (l/min)	Cell temperature (ºC)
0.75	8	3.6	20
			40
			60
			70
			80
0.75	3	3.6	20
			40
			60
			70
			80
0.75	3	1	20
			40
			60
			70
			80

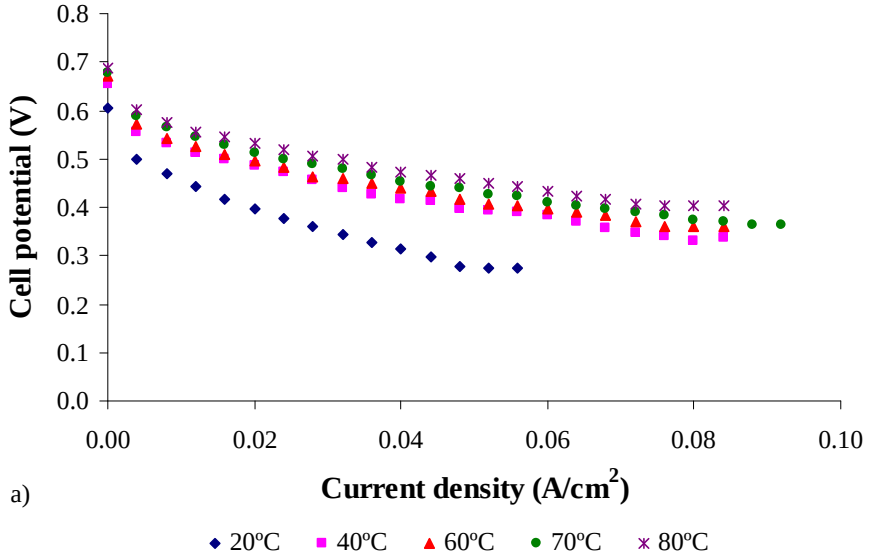

a)

Figure C.4 – Effect of fuel cell temperature on a) cell performance. Operating conditions: methanol flow rate 8 ml/min and air flow rate 3.6 l/min.

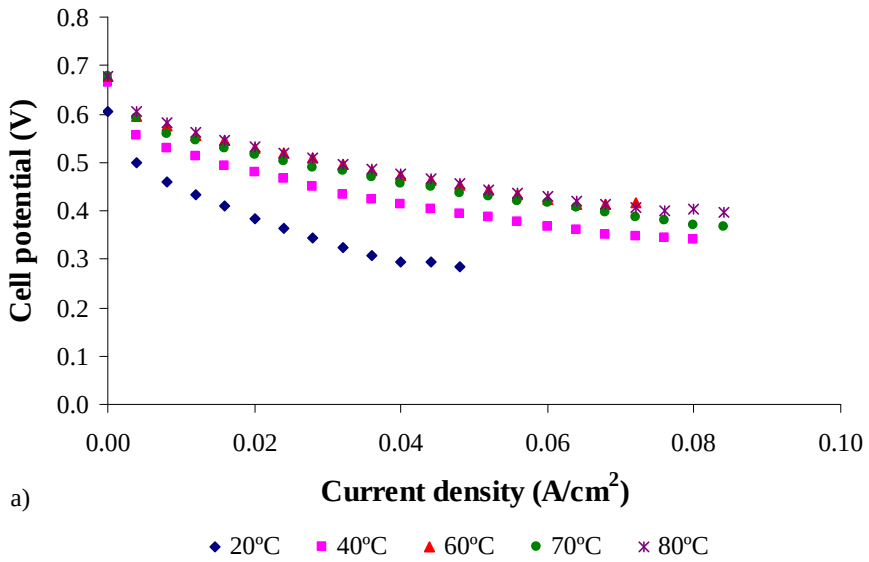

a)

Figure C.5 – Effect of fuel cell temperature on a) cell performance. Operating conditions: methanol flow rate 3 ml/min and air flow rate 3.6 l/min.

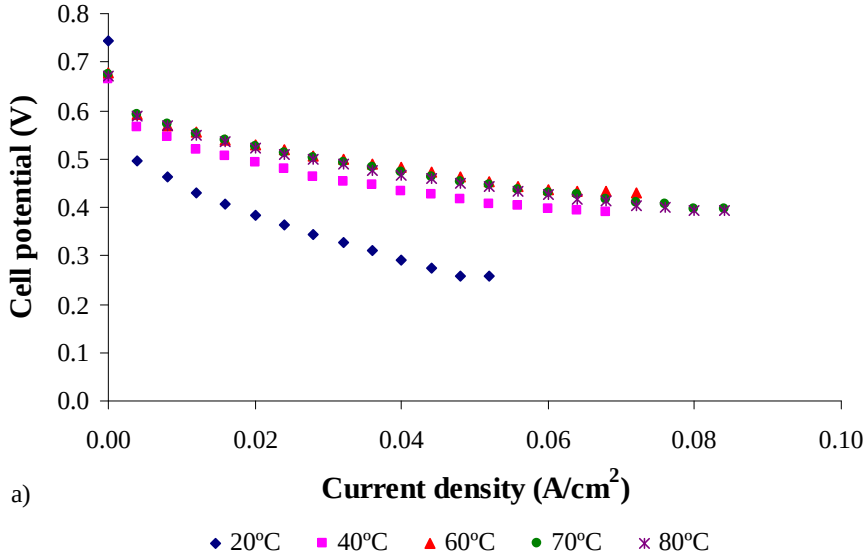

a)

Figure C.6 – Effect of fuel cell temperature on a) cell performance. Operating conditions: methanol flow rate 3 ml/min and air flow rate 1 l/min.

C.1.3. Methanol flow rate

Table C.3 – Set of operating conditions used to analyse the effect of methanol flow rate on the cell performance.

C_{CH_3OH} (M)	q_{CH_3OH} (ml/min)	q_{air} (l/min)	Cell temperature (ºC)
0.25	20	3.6	20
	16		
	14		
	12		
	10		
	8		
	3		
0.75	20	3.6	20
	16		
	14		
	12		
	10		
	8		
	3		
0.75	10	1	20
	8		
	3		

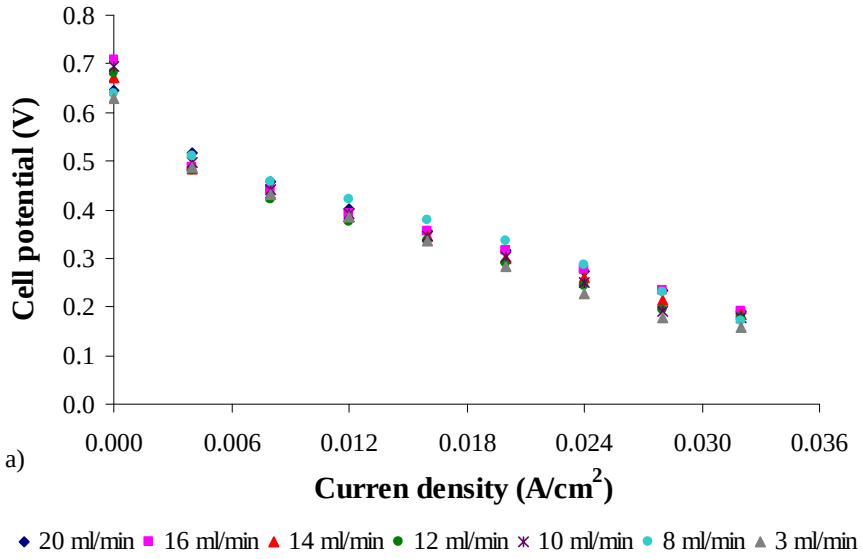

Figure C.7 – Effect of methanol flow rate on a) cell performance. Operating conditions: methanol concentration 0.25M and air flow rate 3.6 l/min.

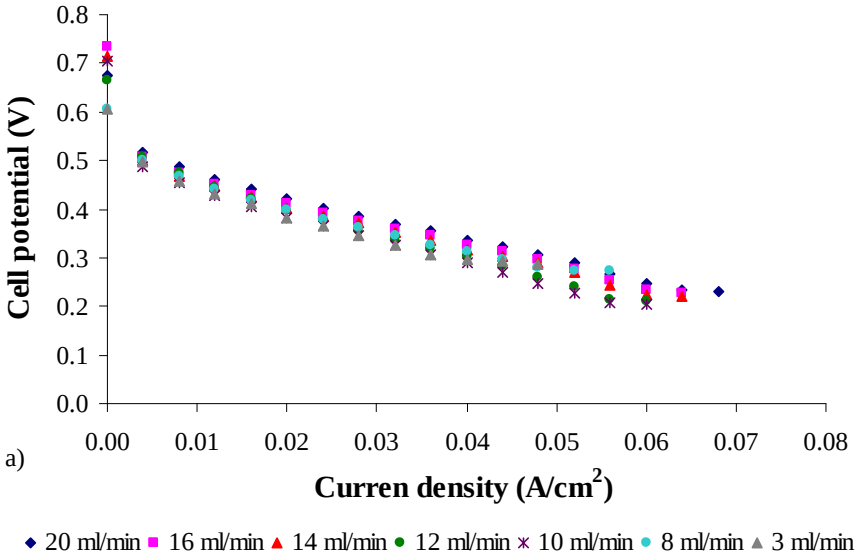

Figure C.8– Effect of methanol flow rate on a) cell performance. Operating conditions: methanol concentration 0.75M and air flow rate 3.6 l/min.

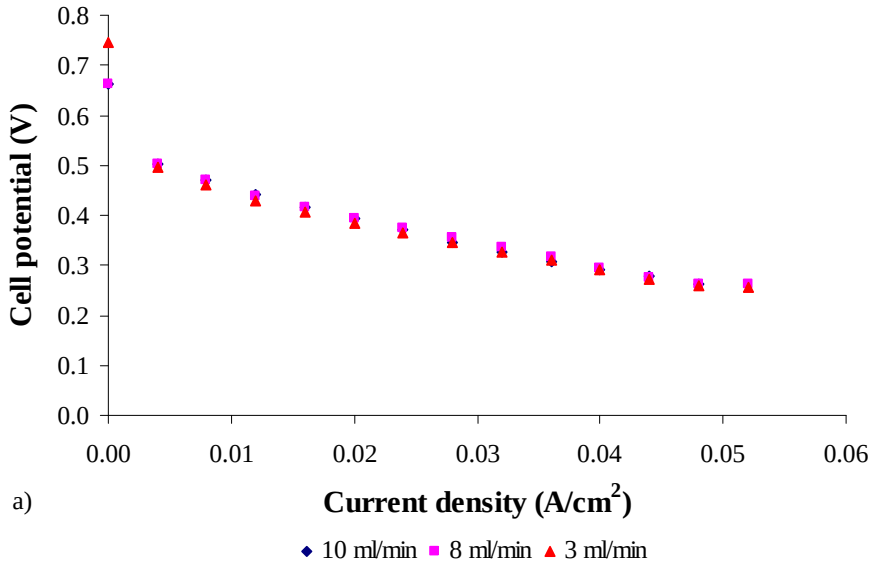

Figure C.9 – Effect of methanol flow rate on a) cell performance. Operating conditions: methanol concentration 0.75M and air flow rate 1 l/min.

C.1.4. Air flow rate

Table C.4 – Set of operating conditions used to analyse the effect of air flow rate on the cell performance.

C_{CH_3OH} (M)	q_{CH_3OH} (ml/min)	q_{air} (l/min)	Cell temperature (ºC)
0.25	8	3.6	20
		2	
		1	
		0.75	
		0.5	
0.75	8	3.6	20
		2	
		1.5	
		1	
0.75	3	3.6	20
		2	
		1	
		0.75	
		0.5	

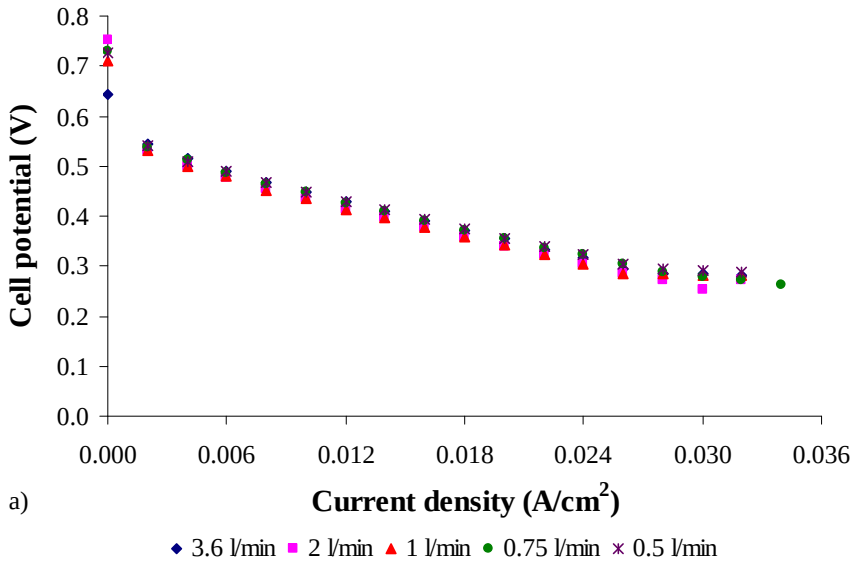

Figure C.10 – Effect of air flow rate on a) cell performance. Operating conditions: methanol concentration 0.25M and methanol flow rate 8 ml/min.

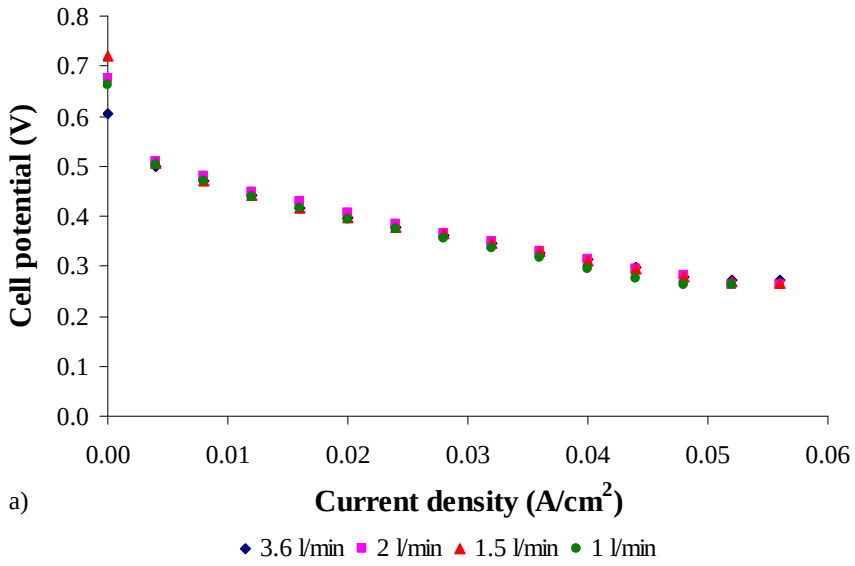

Figure C.11 – Effect of air flow rate on a) cell performance. Operating conditions: methanol concentration 0.75M and methanol flow rate 8 ml/min.

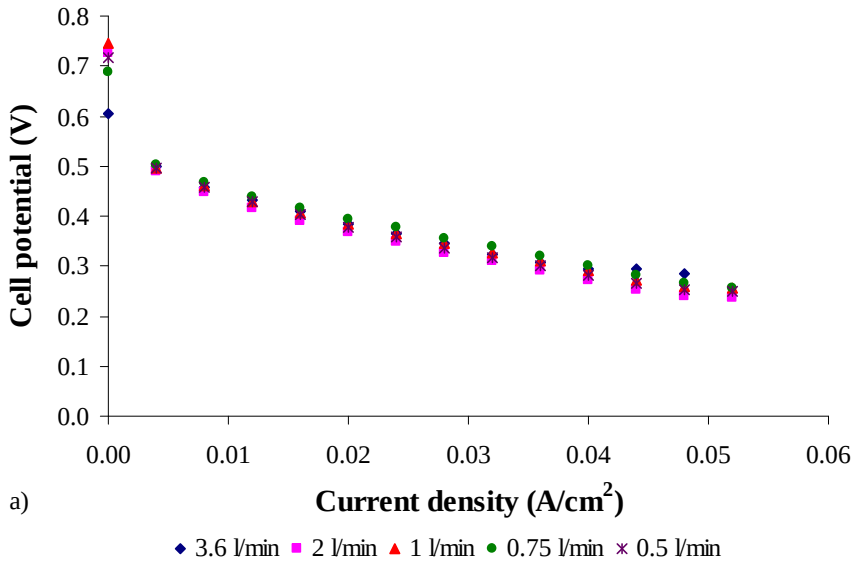

Figure C.12 – Effect of air flow rate on a) cell performance. Operating conditions: methanol concentration 0.75M and methanol flow rate 3 ml/min.

C.2. Effect of design parameters

In this section is presented a systematic study done in order to elucidate the effect of the design parameters on the fuel cell performance. The set of operating conditions used is presented in the table C.5.

Table C.5 – Set of operating conditions used to analyse the effect of design parameters on the cell performance.

C_{CH_3OH} (M)	q_{CH_3OH} (ml/min)	q_{air} (l/min)	Cell temperature (ºC)
0.75	20	3.6	20
	8	3.6	
	8	1	
	3	3.6	
	8	3.6	60
	3	3.6	
	3	1	
2	8	3.6	20
	3	3.6	
	3	1	
5	3	3.6	20

C.2.1. Anode diffusion layer material

Table C.6 – Set of design parameters used to analyse the effect of the diffusion layer material on the cell performance.

Diffusion layer	Anode	Carbon cloth or carbon paper
	Cathode	ELAT
Catalyst loading	Anode	4 mg/cm^2 Pt/Ru
	Cathode	4 mg/cm^2 Pt
Flow field design	Anode	Serpentine
	Cathode	Serpentine
Membrane		Nafion 117 or 212

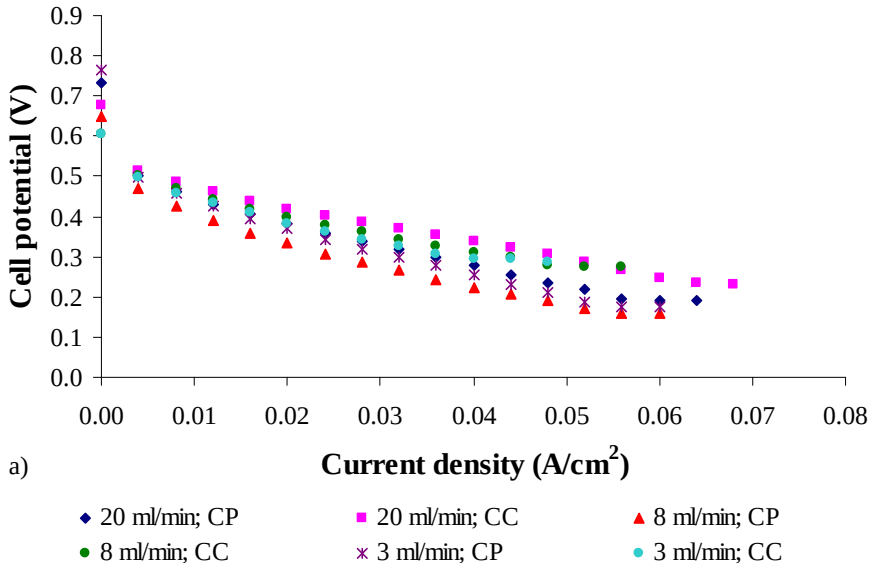

Figure C.13– Effect of anode diffusion layer material on a) cell performance. Operating conditions: methanol concentration 0.75M, air flow rate 3.6 l/min and cell temperature 20°C. Design parameters: Nafion117.

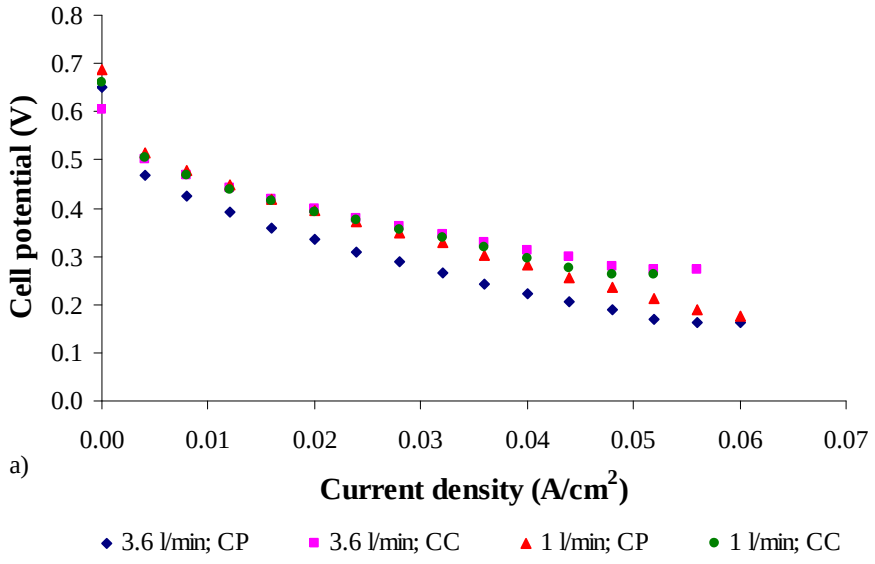

Figure C.14 – Effect of anode diffusion layer material on a) cell performance. Operating conditions: methanol concentration 0.75M, methanol flow rate 8 ml/min and cell temperature 20ºC. Design parameters: Nafion117.

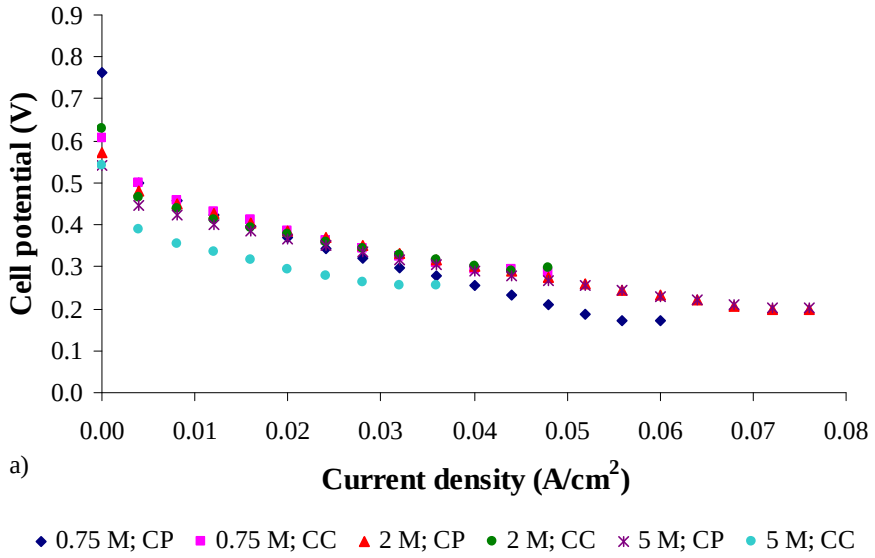

Figure C.15 – Effect of anode diffusion layer material on a) cell performance. Operating conditions: methanol flow rate 3 ml/min, air flow rate 3.6 l/min and cell temperature 20ºC. Design parameters: Nafion117.

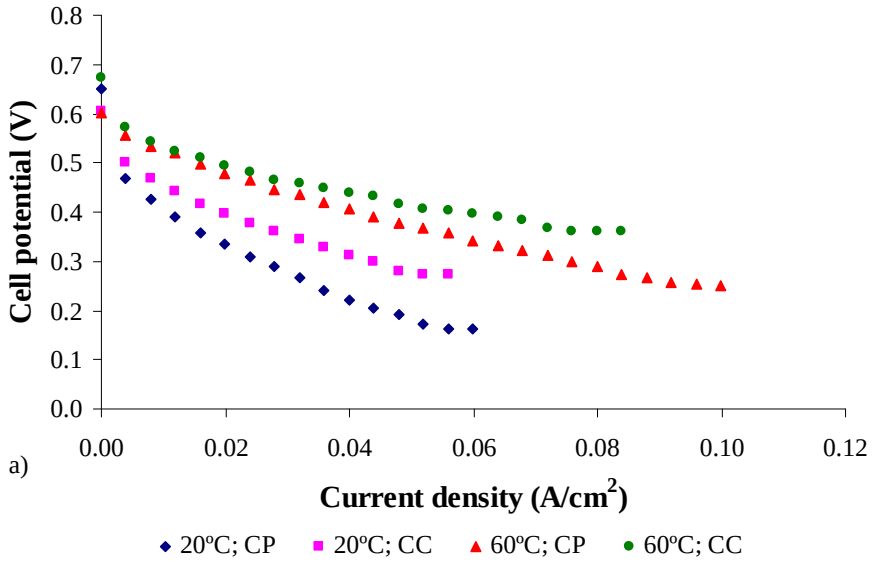

Figure C.16 – Effect of anode diffusion layer material on a) cell performance. Operating conditions: methanol concentration 0.75M, methanol flow rate 8 ml/min and air flow rate 3.6 l/min. Design parameters: Nafion117.

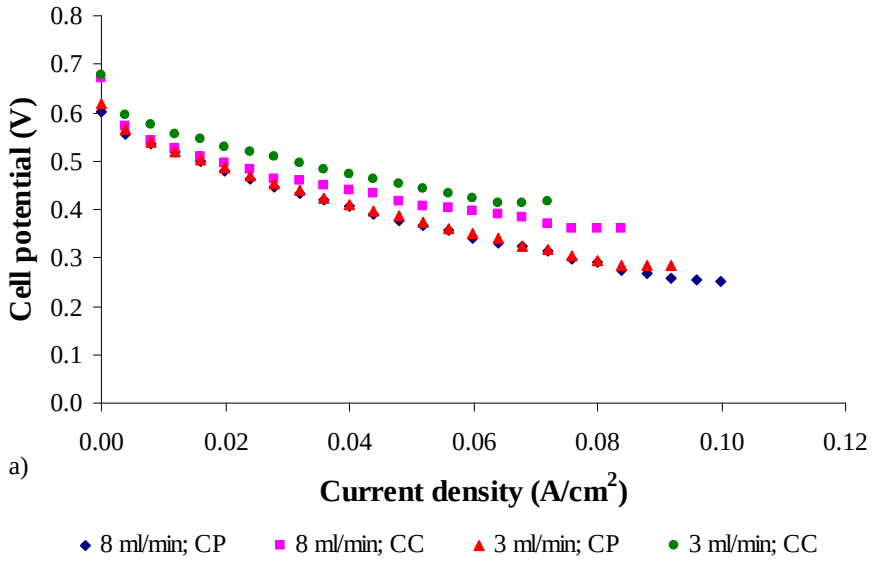

Figure C.17 – Effect of anode diffusion layer material on a) cell performance. Operating conditions: methanol concentration 0.75M, air flow rate 3.6 l/min and cell temperature 60ºC. Design parameters: Nafion117.

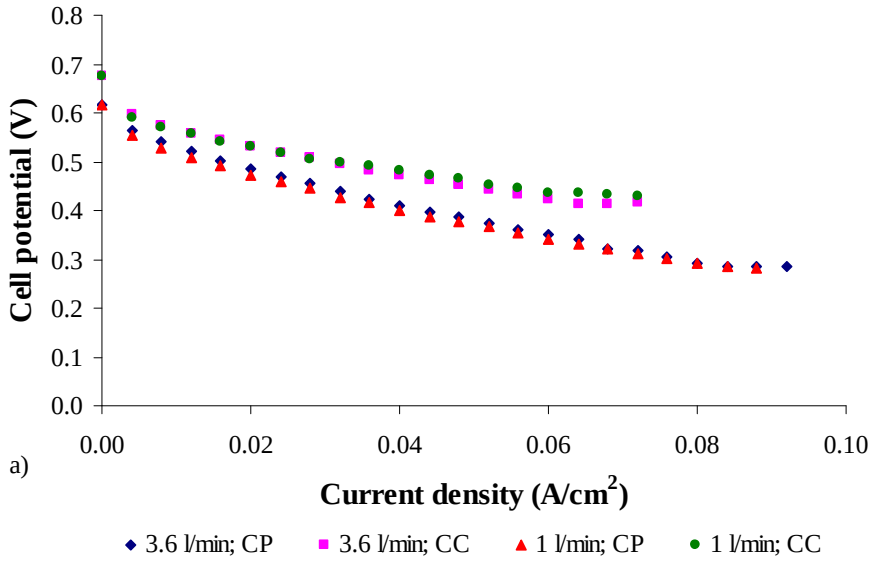

Figure C.18 – Effect of anode diffusion layer material on a) cell performance. Operating conditions: methanol concentration 0.75M, methanol flow rate 3 ml/min and cell temperature 60ºC. Design parameters: Nafion117.

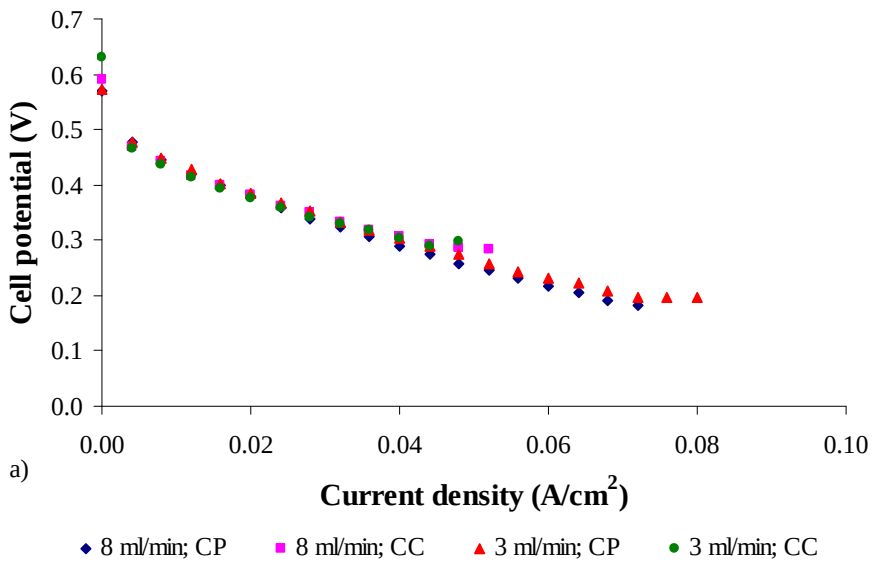

Figure C.19 – Effect of anode diffusion layer material on a) cell performance. Operating conditions: methanol concentration 2M, air flow rate 3.6 l/min and cell temperature 20ºC. Design parameters: Nafion117.

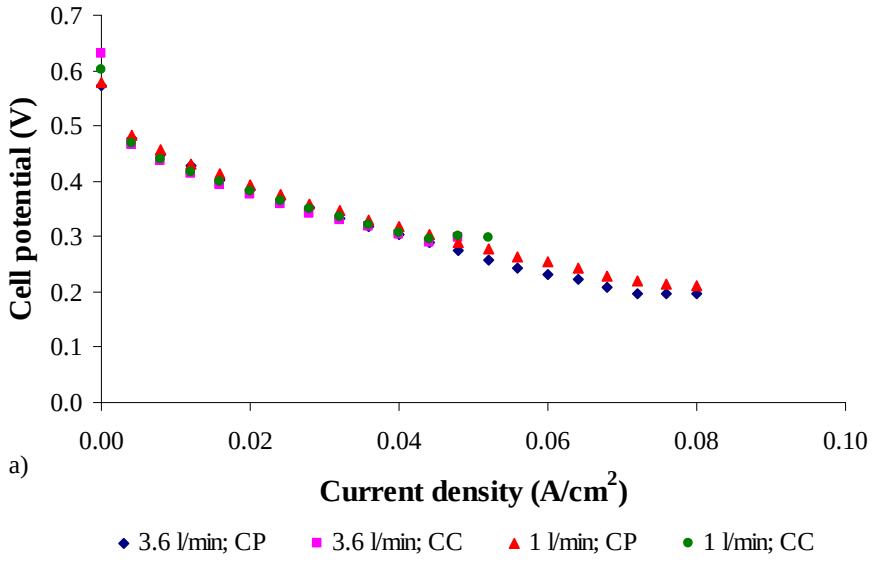

Figure C.20 – Effect of anode diffusion layer material on a) cell performance. Operating conditions: methanol concentration 2M, methanol flow rate 3 ml/min and cell temperature 20ºC. Design parameters: Nafion117.

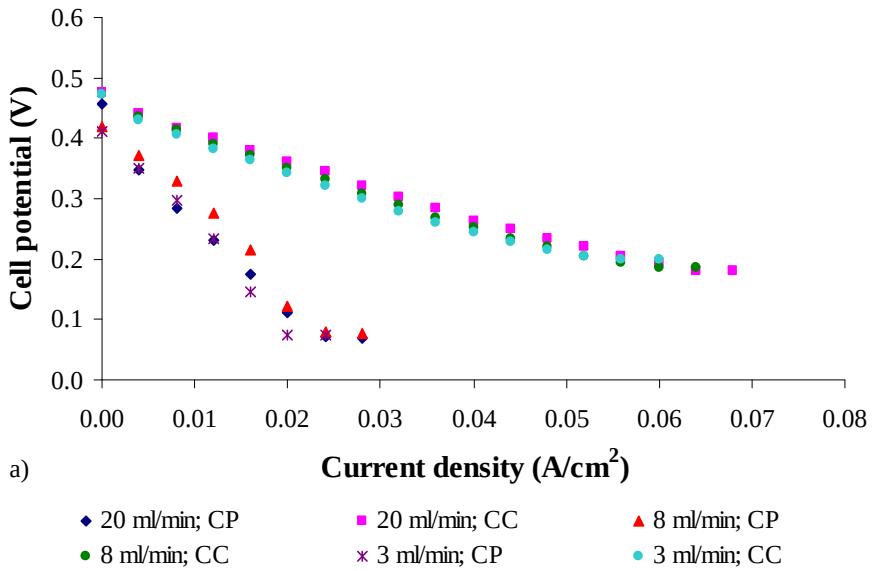

Figure C.21 – Effect of anode diffusion layer material on a) cell performance. Operating conditions: methanol concentration 0.75M, air flow rate 3.6 l/min and cell temperature 20ºC. Design parameters: Nafion212.

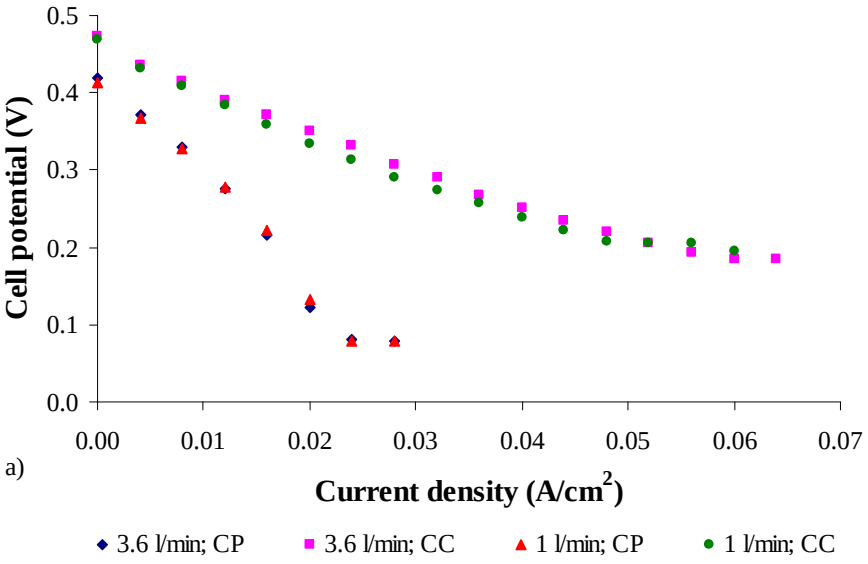

Figure C.22 – Effect of anode diffusion layer material on a) cell performance. Operating conditions: methanol concentration 0.75M, methanol flow rate 8 ml/min and cell temperature 20ºC. Design parameters: Nafion212.

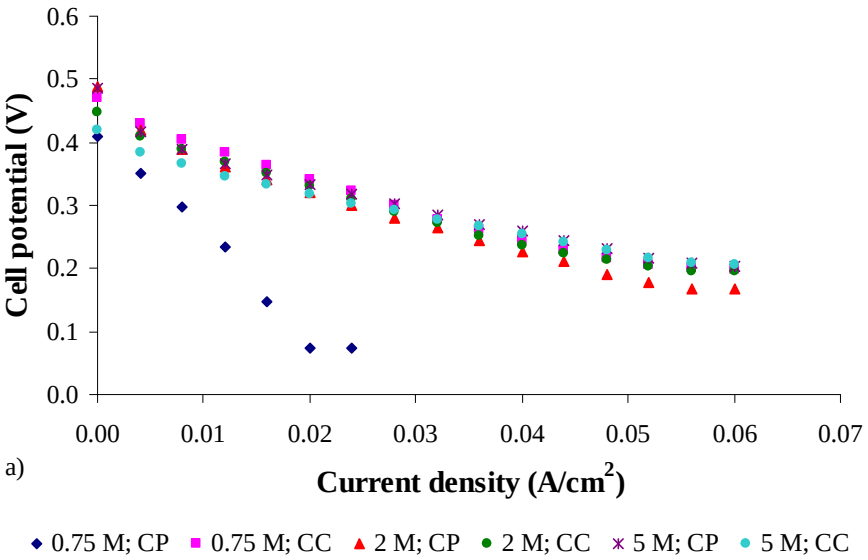

Figure C.23 – Effect of anode diffusion layer material on a) cell performance. Operating conditions: methanol flow rate 3 ml/min, air flow rate 3.6 l/min and cell temperature 20ºC. Design parameters: Nafion117.

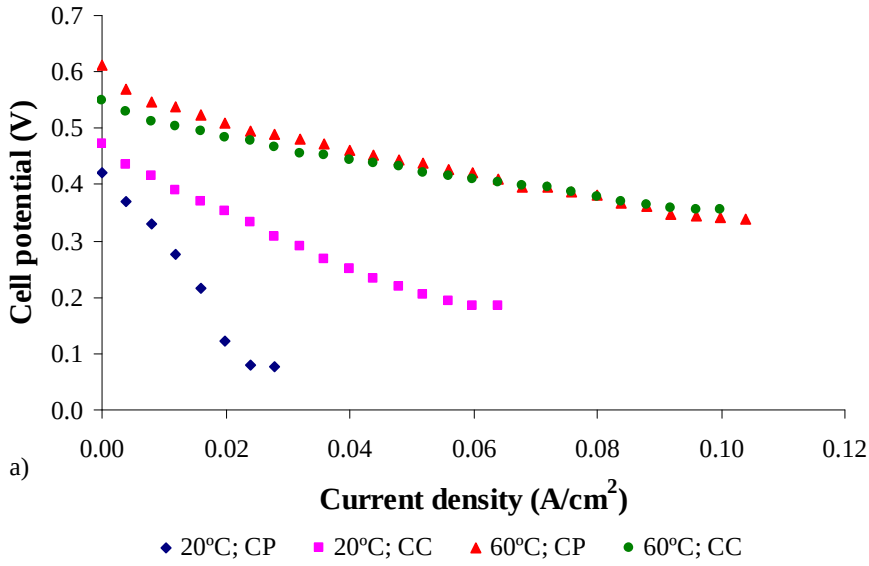

Figure C.24 – Effect of anode diffusion layer material on a) cell performance. Operating conditions: methanol concentration 0.75M, methanol flow rate 8 ml/min and air flow rate 3.6 l/min. Design parameters: Nafion212.

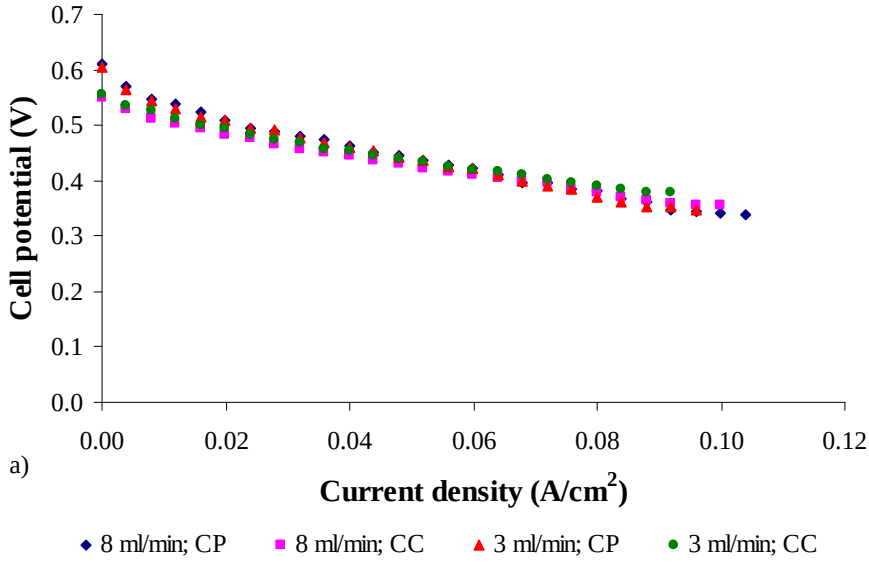

Figure C.25 – Effect of anode diffusion layer material on a) cell performance. Operating conditions: methanol concentration 0.75M, air flow rate 3.6 l/min and cell temperature 60ºC. Design parameters: Nafion212.

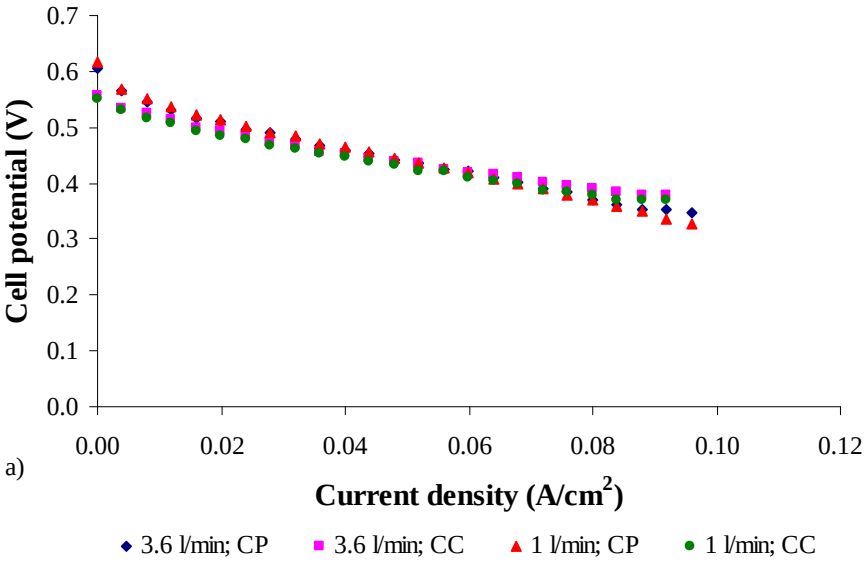

Figure C.26– Effect of anode diffusion layer material on a) cell performance. Operating conditions: methanol concentration 0.75M, methanol flow rate 3 ml/min and cell temperature 60ºC. Design parameters: Nafion212.

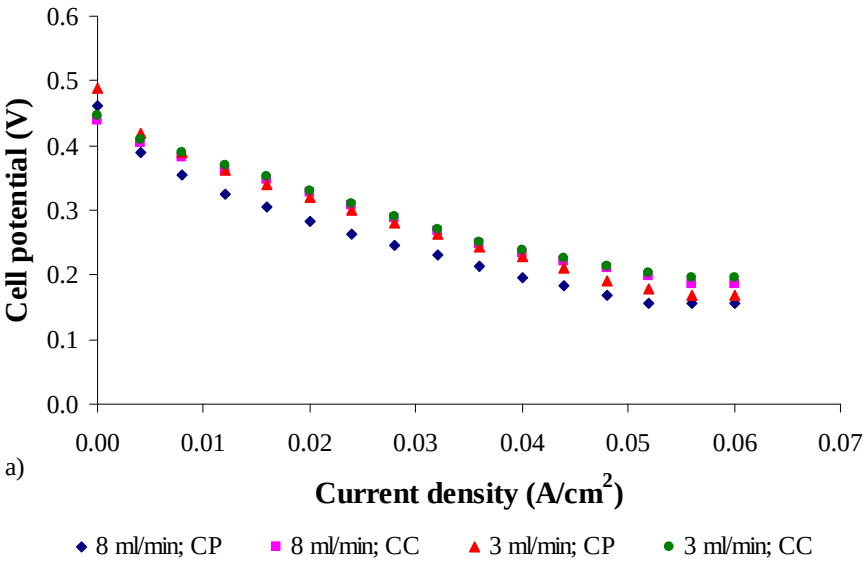

Figure C.27 – Effect of anode diffusion layer material on a) cell performance. Operating conditions: methanol concentration 2M, air flow rate 3.6 l/min and cell temperature 20ºC. Design parameters: Nafion212.

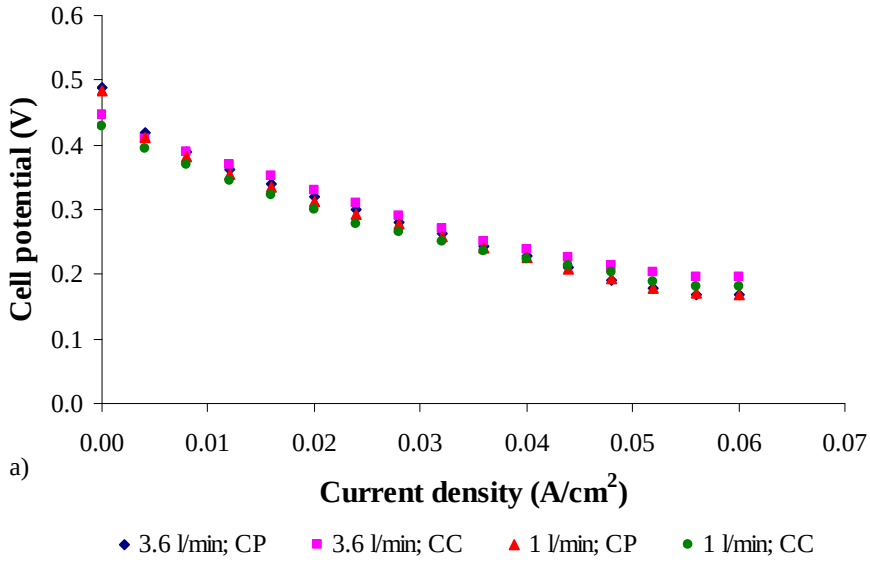

Figure C.28 – Effect of anode diffusion layer material on a) cell performance. Operating conditions: methanol concentration 2M, methanol flow rate 3 ml/min and cell temperature 20ºC. Design parameters: Nafion212.

C.2.2. Cathode diffusion layer material

Table C.7 – Set of design parameters used to analyse the effect of the diffusion layer material on the cell performance.

Diffusion layer	Anode	Carbon cloth
	Cathode	ELAT, carbon cloth or carbon paper
Catalyst loading	Anode	4 mg/cm^2 Pt/Ru
	Cathode	4 mg/cm^2 Pt
Flow field design	Anode	Serpentine
	Cathode	Serpentine
Membrane		Nafion 117 or 212

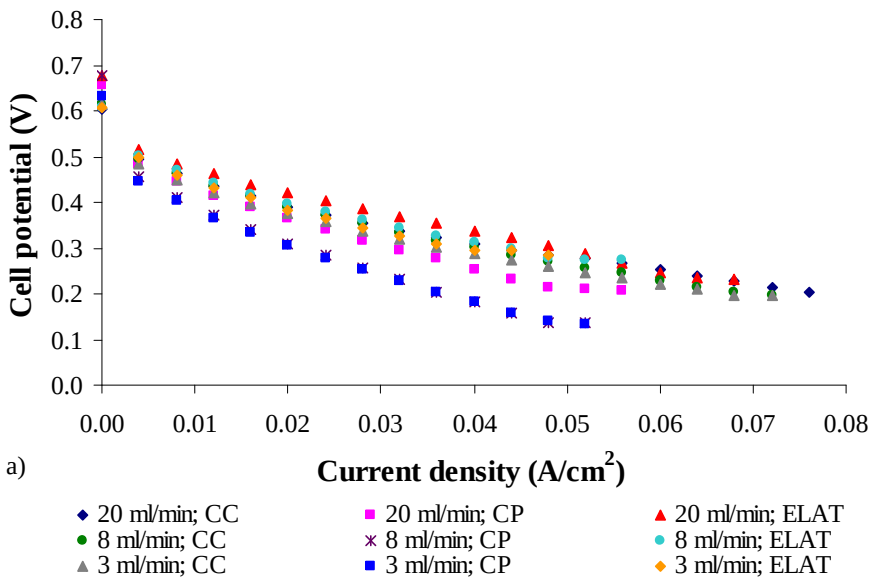

Figure C.29 – Effect of cathode diffusion layer material on a) cell performance. Operating conditions: methanol concentration 0.75M, air flow rate 3.6 l/min and cell temperature 20ºC. Design parameters: Nafion117.

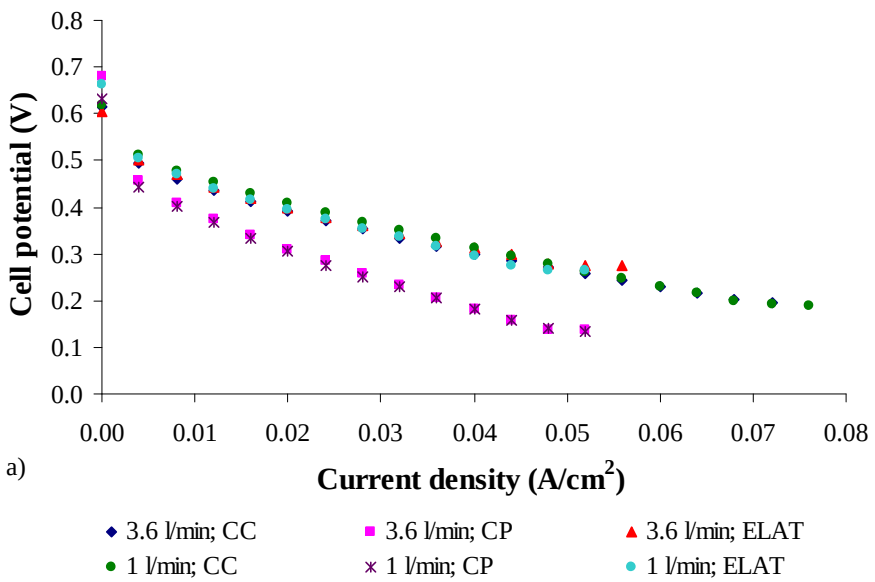

Figure C.30 – Effect of cathode diffusion layer material on a) cell performance. Operating conditions: methanol concentration 0.75M, methanol flow rate 8 ml/min and cell temperature 20ºC. Design parameters: Nafion117.

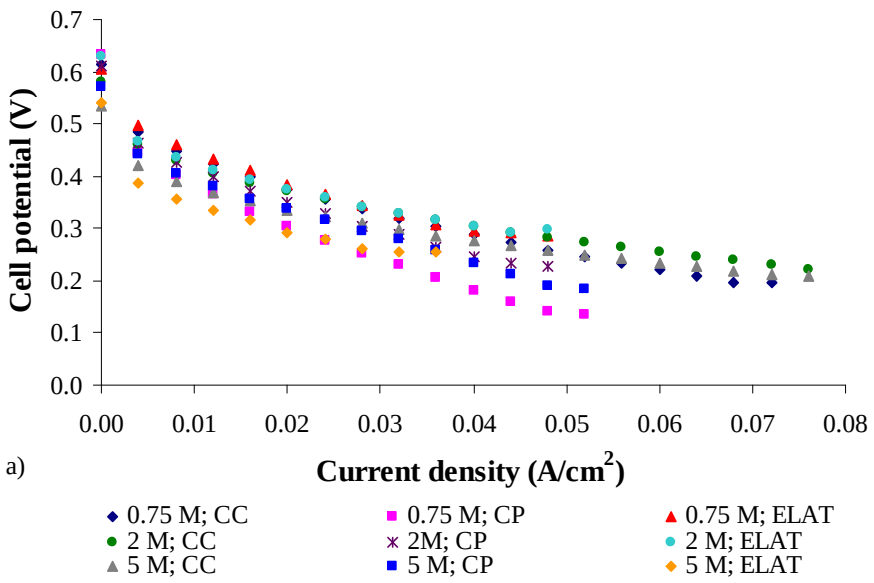

Figure C.31 – Effect of cathode diffusion layer material on a) cell performance. Operating conditions: air flow rate 3.6 l/min, methanol flow rate 3 ml/min and cell temperature 20ºC. Design parameters: Nafion117.

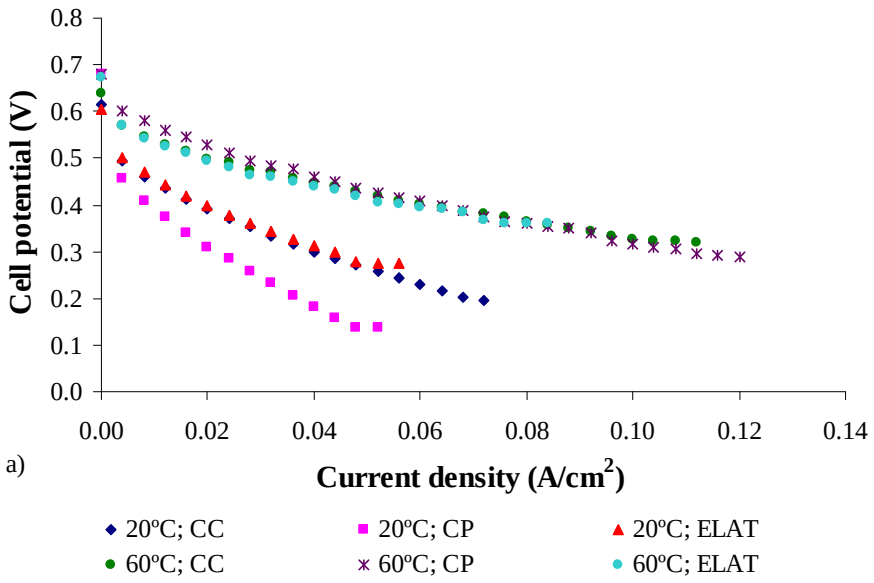

Figure C.32– Effect of cathode diffusion layer material on a) cell performance. Operating conditions: methanol concentration 0.75M, methanol flow rate 8 ml/min and air flow rate 3.6 l/min. Design parameters: Nafion117.

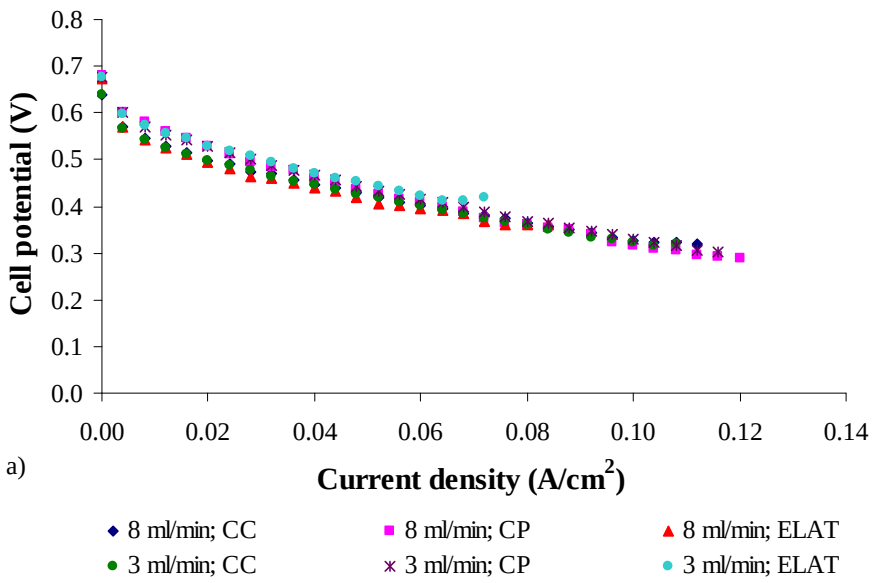

Figure C.33 – Effect of cathode diffusion layer material on a) cell performance. Operating conditions: methanol concentration 0.75M, air flow rate 3.6 l/min and cell temperature 60ºC. Design parameters: Nafion117.

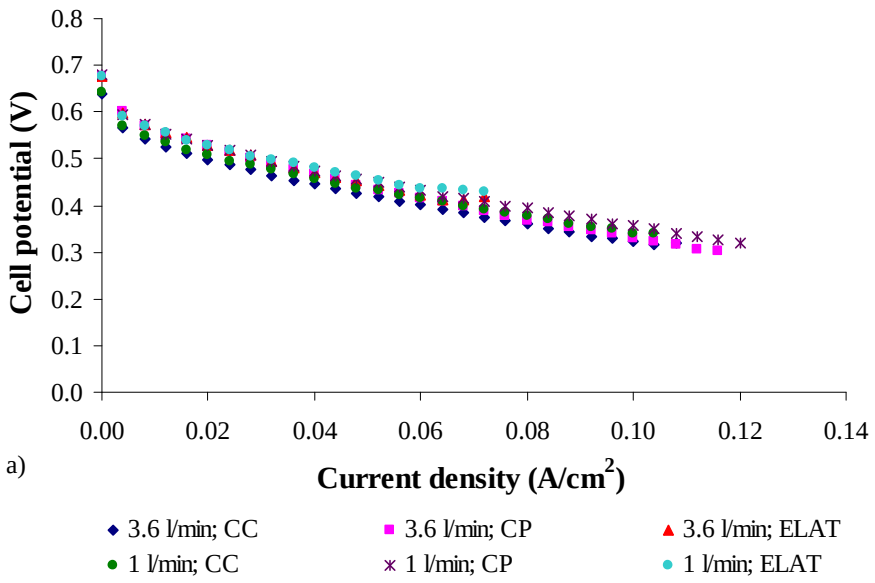

Figure C.34 – Effect of cathode diffusion layer material on a) cell performance. Operating conditions: methanol concentration 0.75M, methanol flow rate 3 ml/min and cell temperature 60ºC. Design parameters: Nafion117.

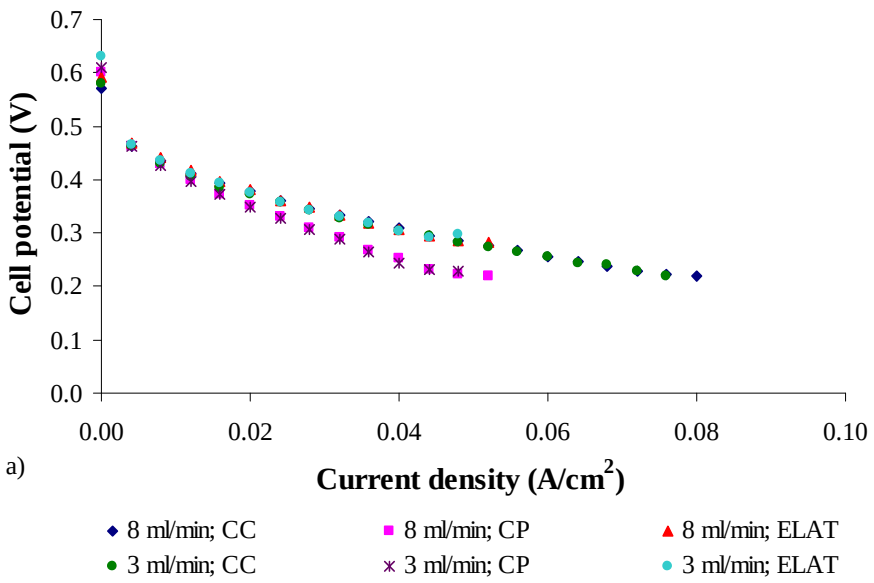

Figure C.35 – Effect of cathode diffusion layer material on a) cell performance. Operating conditions: methanol concentration 2M, air flow rate 3.6 l/min and cell temperature 20ºC. Design parameters: Nafion117.

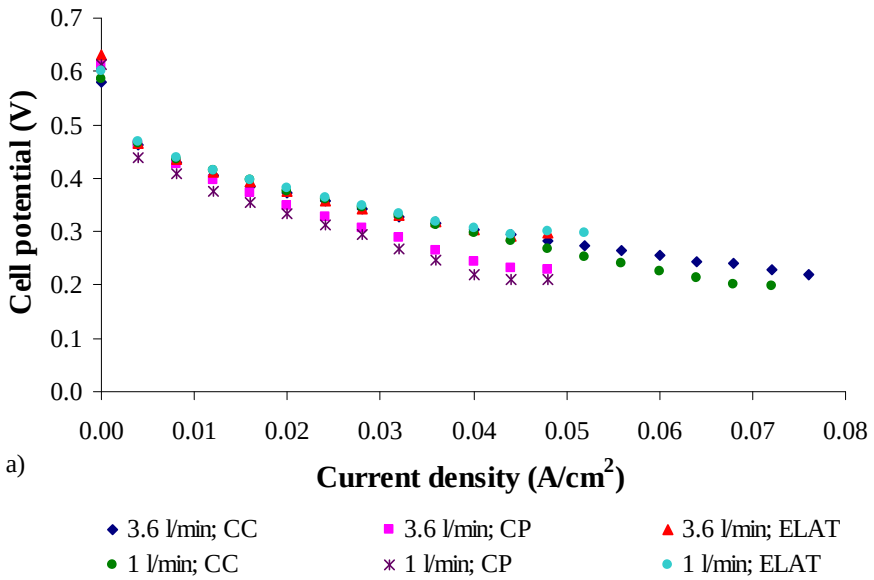

Figure C.36 – Effect of cathode diffusion layer material on a) cell performance. Operating conditions: methanol concentration 2M, methanol flow rate 3 ml/min and cell temperature 20ºC. Design parameters: Nafion117.

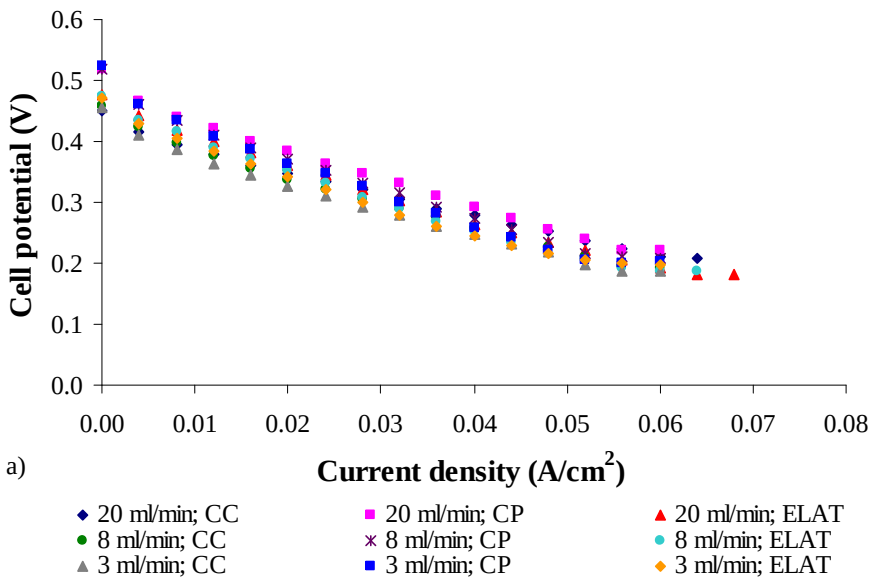

Figure C.37 – Effect of cathode diffusion layer material on a) cell performance. Operating conditions: methanol concentration 0.75M, air flow rate 3.6 l/min and cell temperature 20ºC. Design parameters: Nafion212.

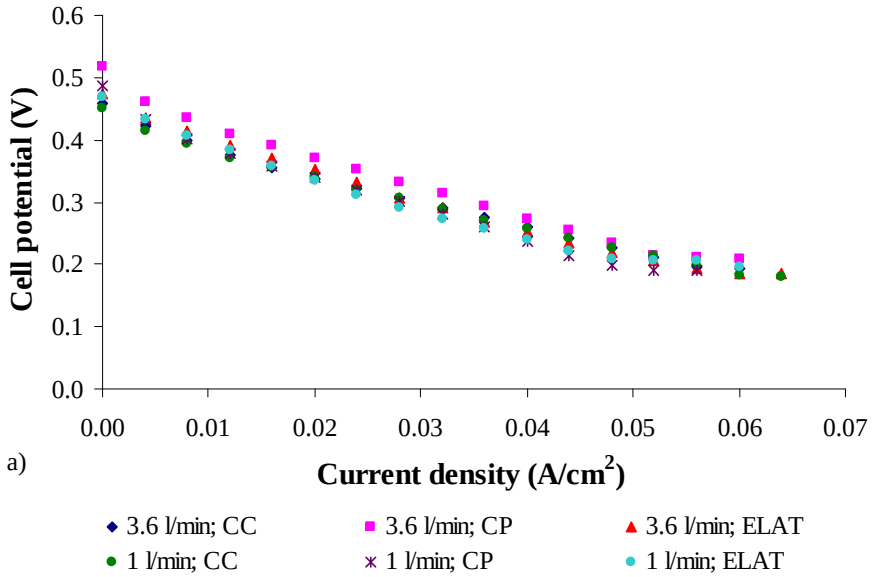

Figure C.38 – Effect of cathode diffusion layer material on a) cell performance. Operating conditions: methanol concentration 0.75M, methanol flow rate 8 ml/min and cell temperature 20ºC. Design parameters: Nafion212.

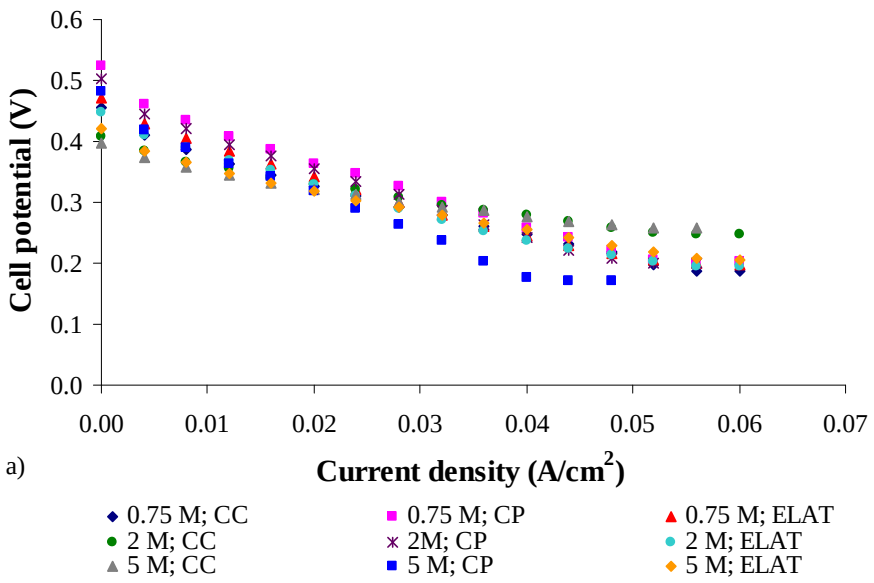

Figure C.39– Effect of cathode diffusion layer material on a) cell performance. Operating conditions: air flow rate 3.6 l/min, methanol flow rate 3 ml/min and cell temperature 20ºC. Design parameters: Nafion212.

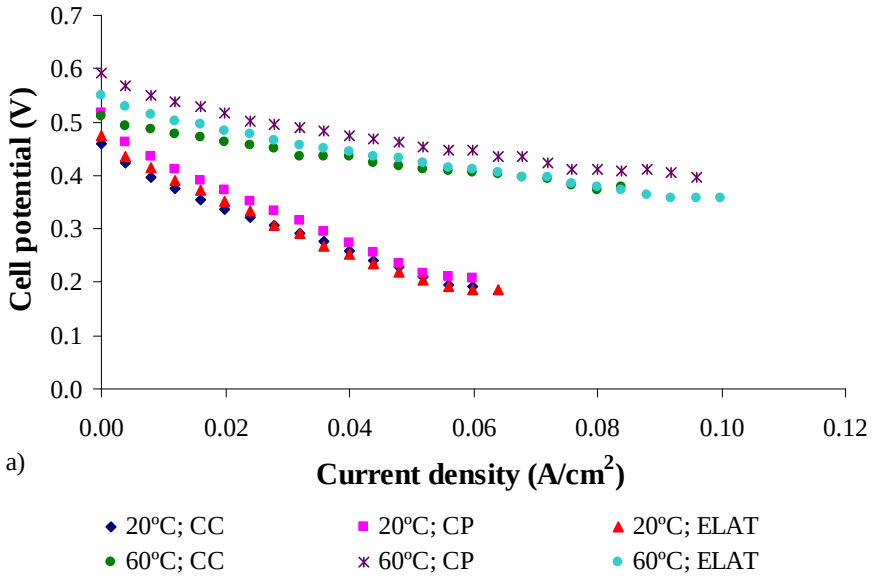

Figure C.40 – Effect of cathode diffusion layer material on a) cell performance and b) power. Operating conditions: methanol concentration 0.75M, methanol flow rate 8 ml/min and air flow rate 3.6 l/min. Design parameters: Nafion212.

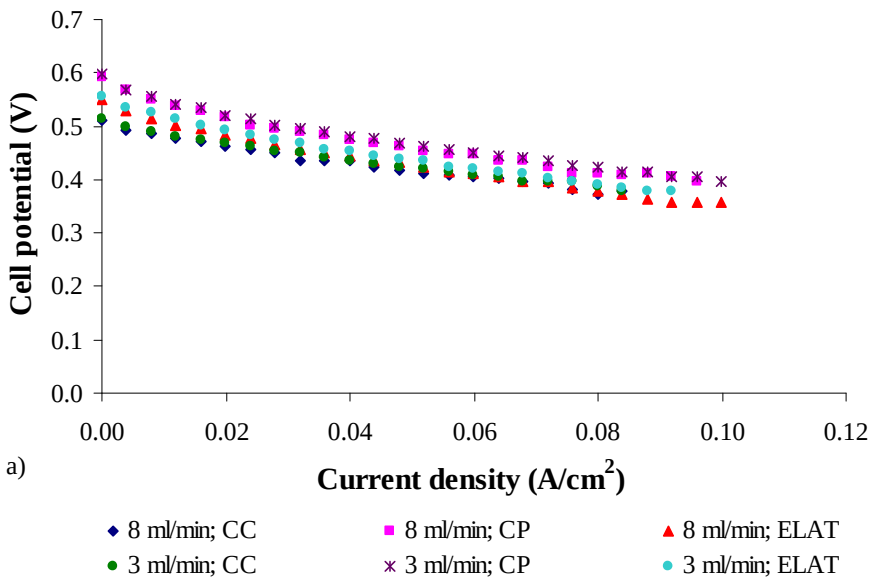

Figure C.41 – Effect of cathode diffusion layer material on a) cell performance and b) power. Operating conditions: methanol concentration 0.75M, air flow rate 3.6 l/min and cell temperature 60ºC. Design parameters: Nafion212.

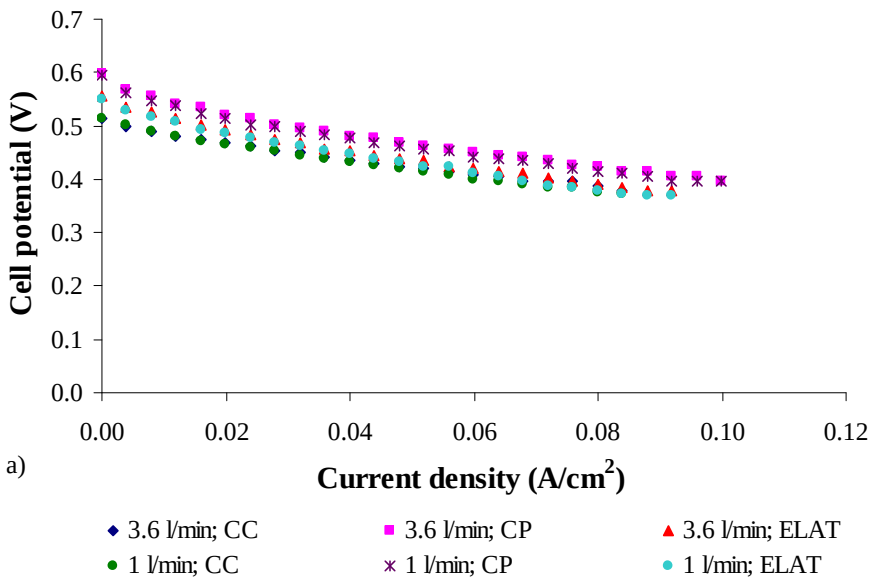

Figure C.42 – Effect of cathode diffusion layer material on a) cell performance and b) power. Operating conditions: methanol concentration 0.75M, methanol flow rate 3 ml/min and cell temperature 60ºC. Design parameters: Nafion212.

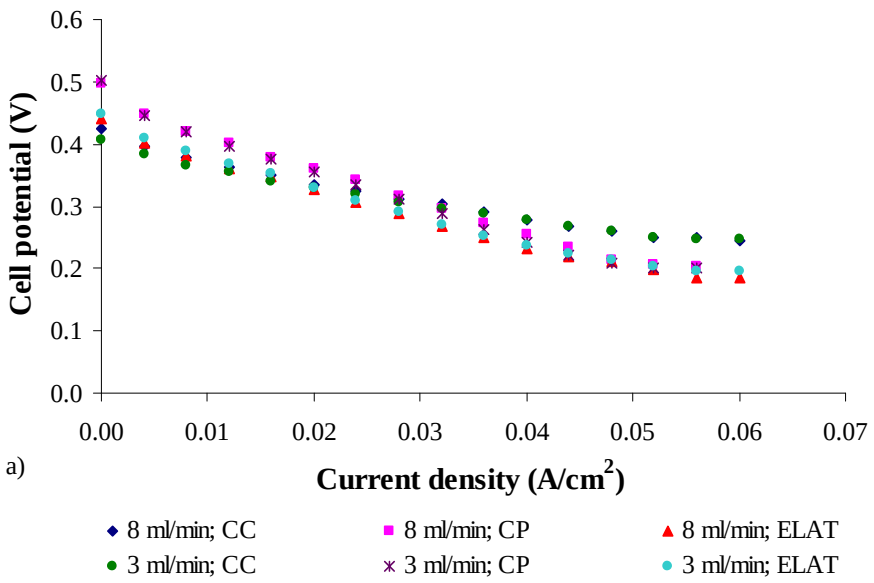

Figure C.43 – Effect of cathode diffusion layer material on a) cell performance and b) power. Operating conditions: methanol concentration 2M, air flow rate 3.6 l/min and cell temperature 20ºC. Design parameters: Nafion212.

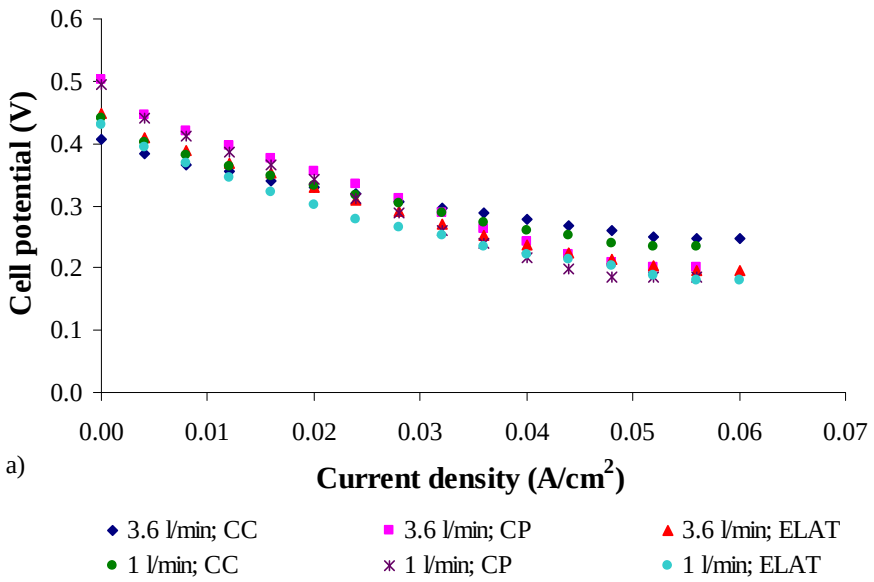

Figure C.44– Effect of cathode diffusion layer material on a) cell performance and b) power. Operating conditions: methanol concentration 2M, methanol flow rate 3 ml/min and cell temperature 20ºC. Design parameters: Nafion212.

C.2.3. Effect of membrane thickness

Table C.8 – Set of design parameters used to analyse the effect of the membrane thickness on the cell performance.

Diffusion layer	Anode	Carbon cloth type A
	Cathode	Carbon cloth type A
Catalyst loading	Anode	4 mg/cm^2 Pt/Ru
	Cathode	4 mg/cm^2 Pt
Flow field design	Anode	Serpentine
	Cathode	Serpentine
Membrane		Nafion 117, 115 or 212

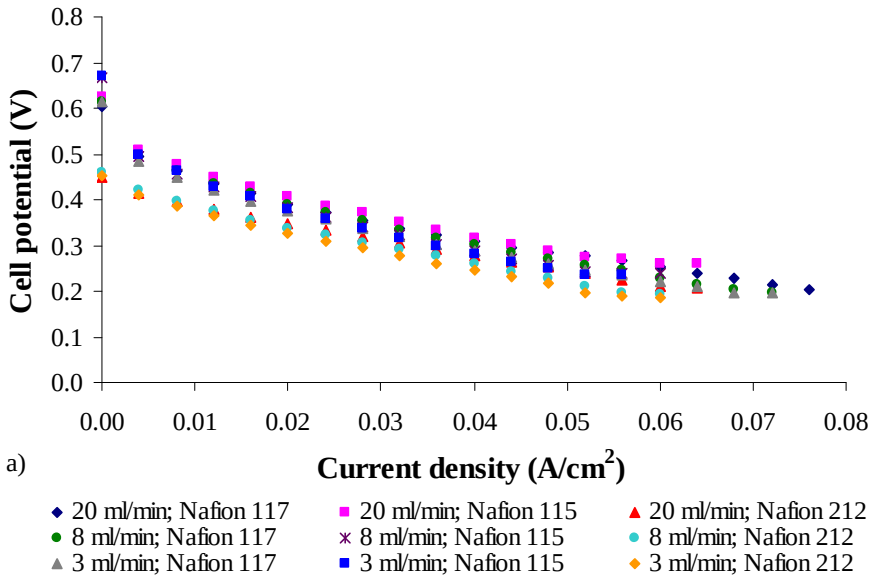

Figure C.45 – Effect of membrane thickness on a) cell performance and b) power. Operating conditions: methanol concentration 0.75M, air flow rate 3.6 l/min and cell temperature 20ºC.

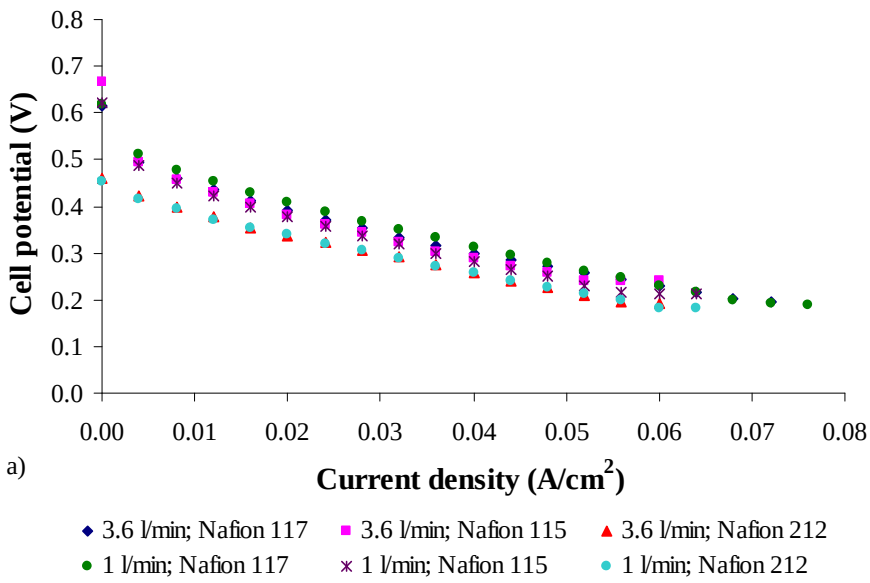

Figure C.46 – Effect of membrane thickness on a) cell performance and b) power. Operating conditions: methanol concentration 0.75M, methanol flow rate 8 ml/min and cell temperature 20ºC.

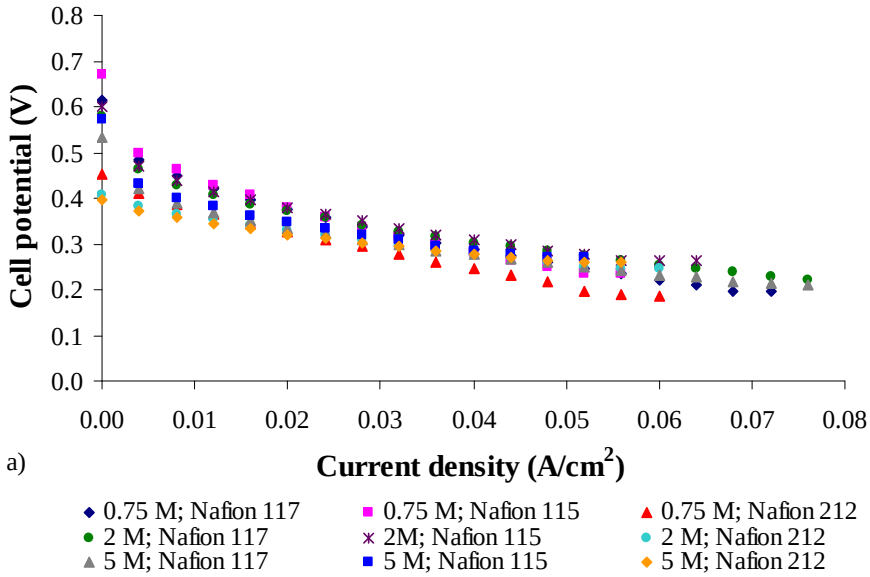

Figure C.47 – Effect of membrane thickness on a) cell performance and b) power. Operating conditions: air flow rate 3.6 l/min, methanol flow rate 3 ml/min and cell temperature 20ºC.

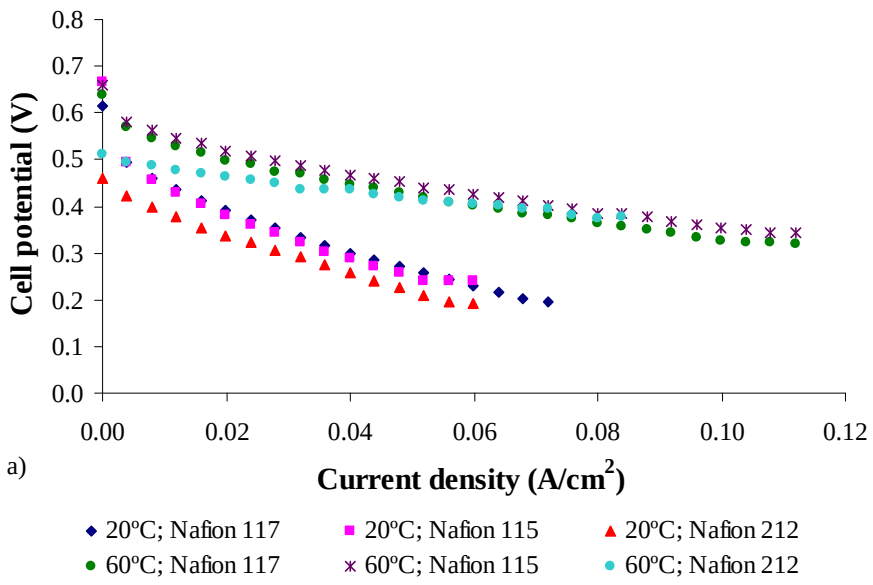

Figure C.48 – Effect of membrane thickness on a) cell performance and b) power. Operating conditions: methanol concentration 0.75M, methanol flow rate 8 ml/min and air flow rate 3.6 l/min.

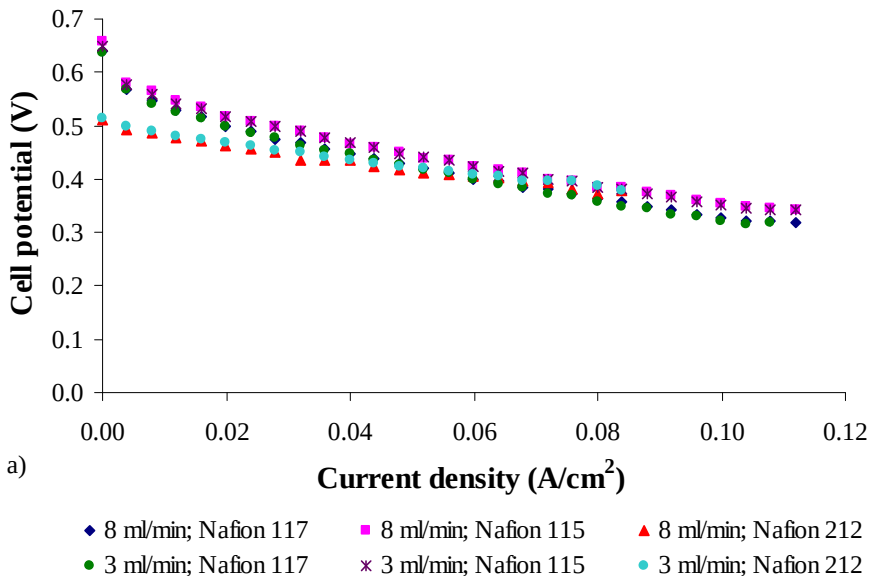

Figure C.49 – Effect of membrane thickness on a) cell performance and b) power. Operating conditions: methanol concentration 0.75M, air flow rate 3.6 l/min and cell temperature 60ºC.

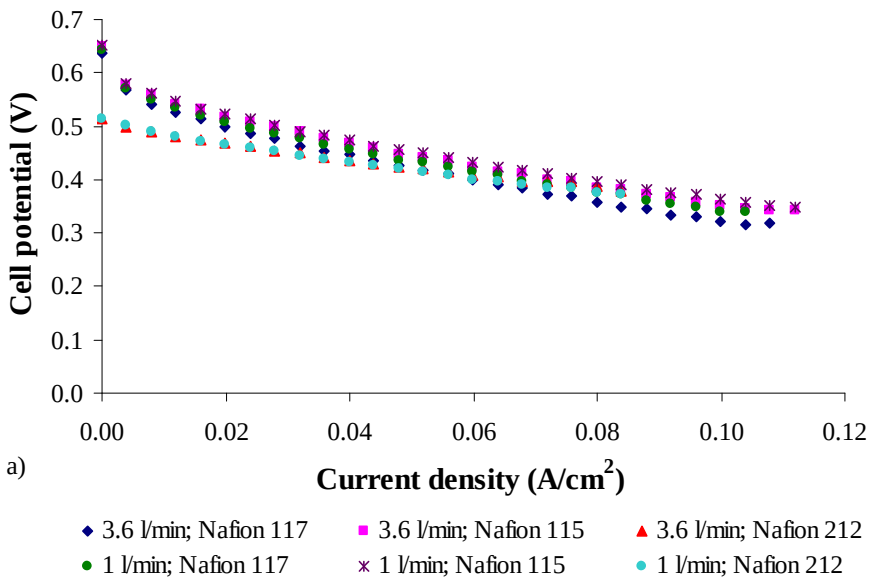

Figure C.50 – Effect of membrane thickness on a) cell performance and b) power. Operating conditions: methanol concentration 0.75M, methanol flow rate 3 ml/min and cell temperature 60ºC.

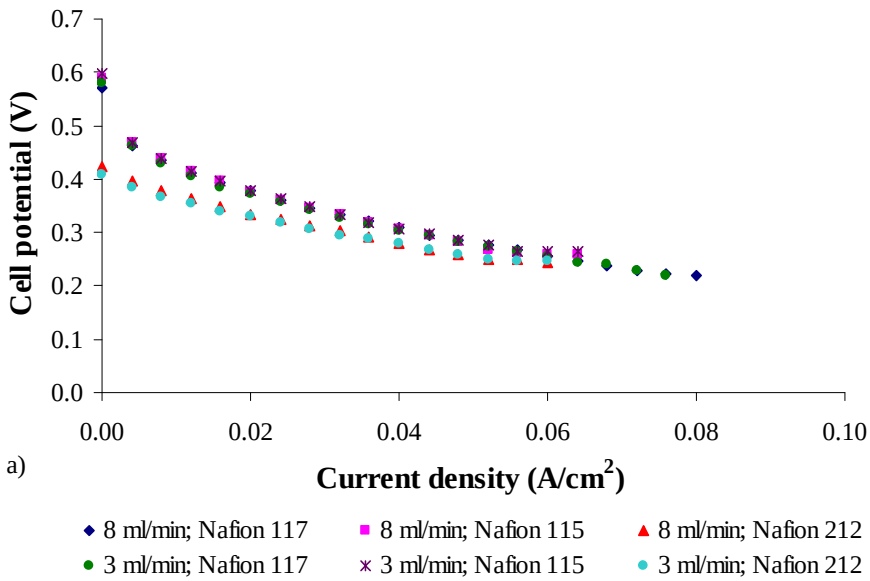

Figure C.51– Effect of membrane thickness on a) cell performance and b) power. Operating conditions: methanol concentration 2M, air flow rate 3.6 l/min and cell temperature 20ºC.

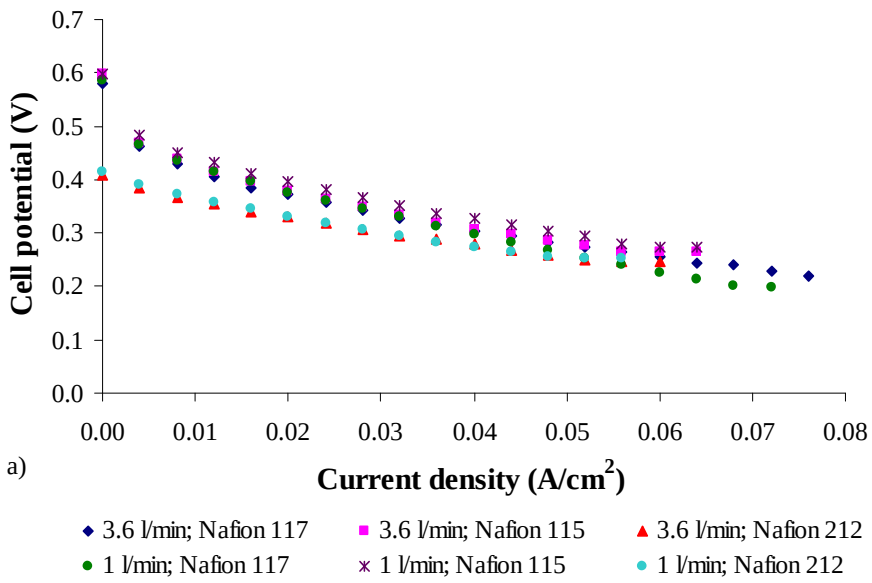

Figure C.52 – Effect of membrane thickness on a) cell performance and b) power. Operating conditions: methanol concentration 2M, methanol flow rate 3 ml/min and cell temperature 20ºC.

C.2.4. Effect of catalyst loading

Table C.9 – Set of design parameters used to analyse the effect of the catalyst loading on the cell performance.

Diffusion layer	Anode	Carbon cloth type A
	Cathode	Carbon cloth type A
Catalyst loading	Anode	4 mg/cm^2 or 8 mg/cm^2 Pt/Ru
	Cathode	4 mg/cm^2 or 8 mg/cm^2 Pt
Flow field design	Anode	Serpentine
	Cathode	Serpentine
Membrane		Nafion 117

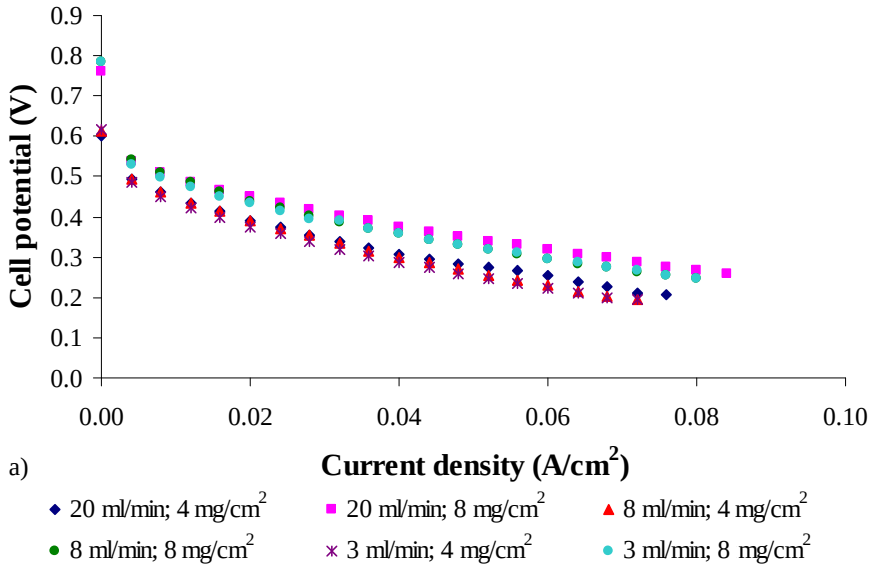

Figure C.53 – Effect of catalyst loading on a) cell performance and b) power. Operating conditions: methanol concentration 0.75M, air flow rate 3.6 l/min and cell temperature 20ºC.

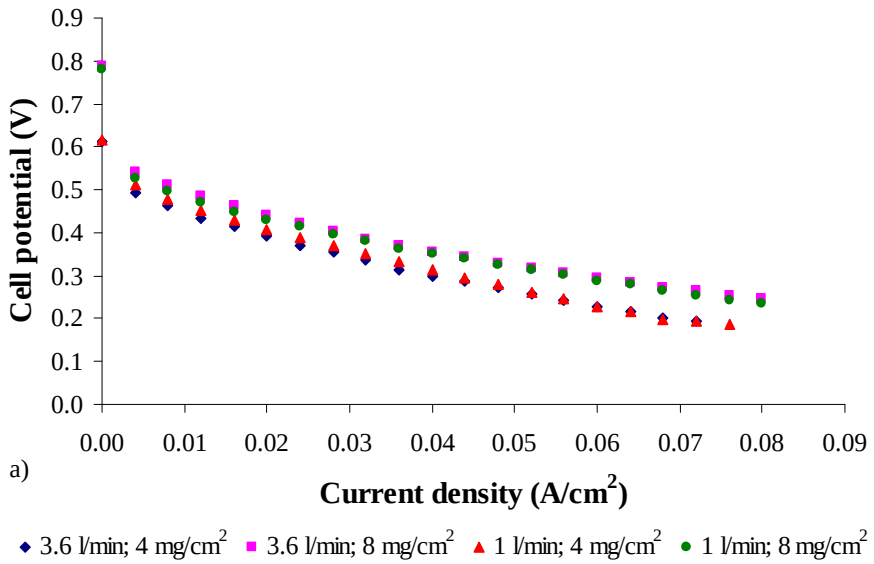

Figure C.54– Effect of catalyst loading on a) cell performance and b) power. Operating conditions: methanol concentration 0.75M, methanol flow rate 8 ml/min and cell temperature 20ºC.

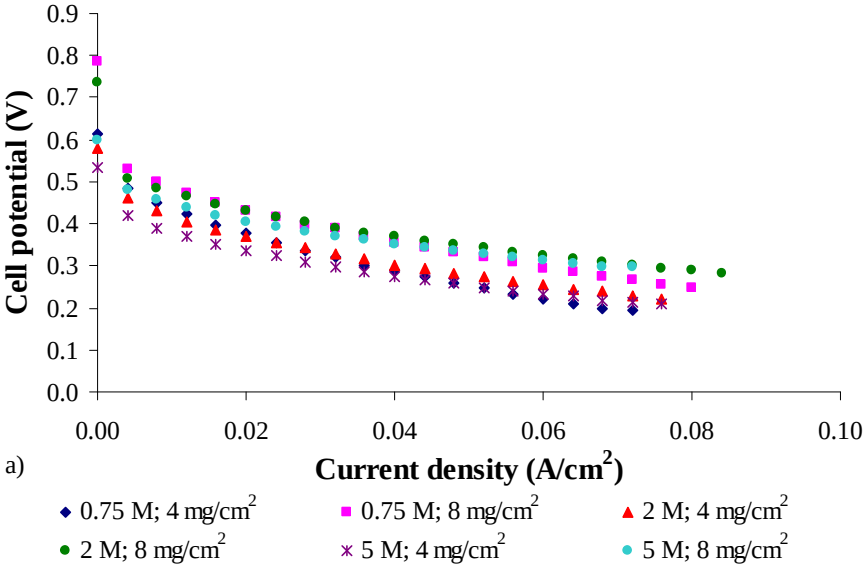

Figure C.55 – Effect of catalyst loading on a) cell performance and b) power. Operating conditions: air flow rate 3.6 l/min, methanol flow rate 3 ml/min and cell temperature 20ºC.

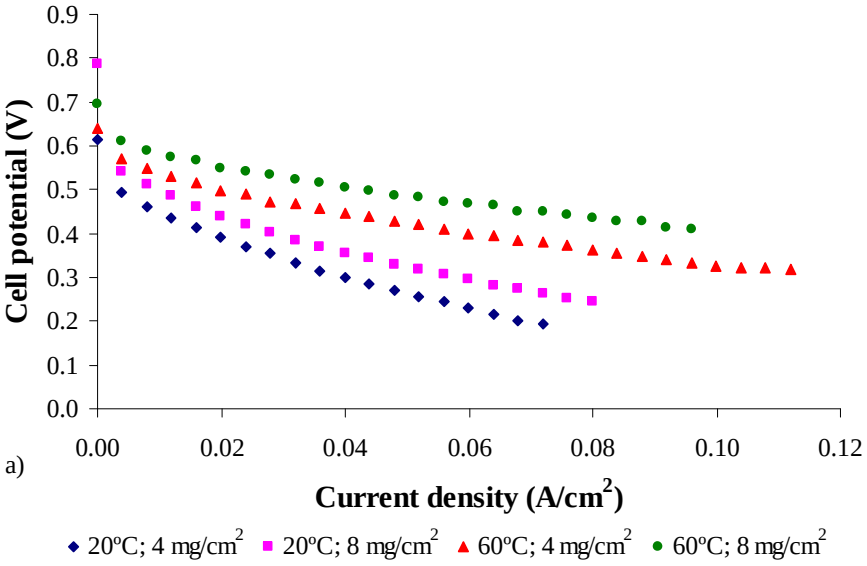

Figure C.56– Effect of catalyst loading on a) cell performance and b) power. Operating conditions: methanol concentration 0.75M, methanol flow rate 8 ml/min and air flow rate 3.6 l/min.

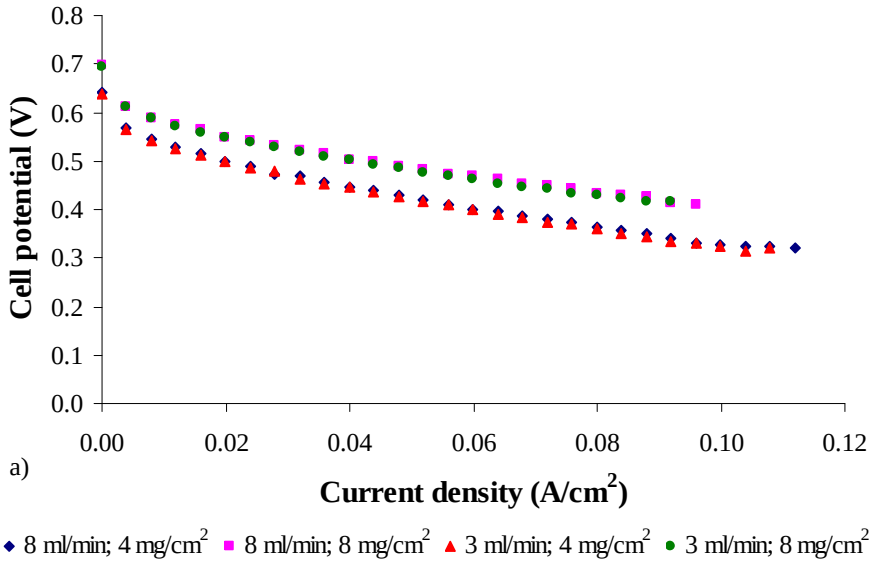

Figure C.57– Effect of catalyst loading on a) cell performance and b) power. Operating conditions: methanol concentration 0.75M, air flow rate 3.6 l/min and cell temperature 60ºC.

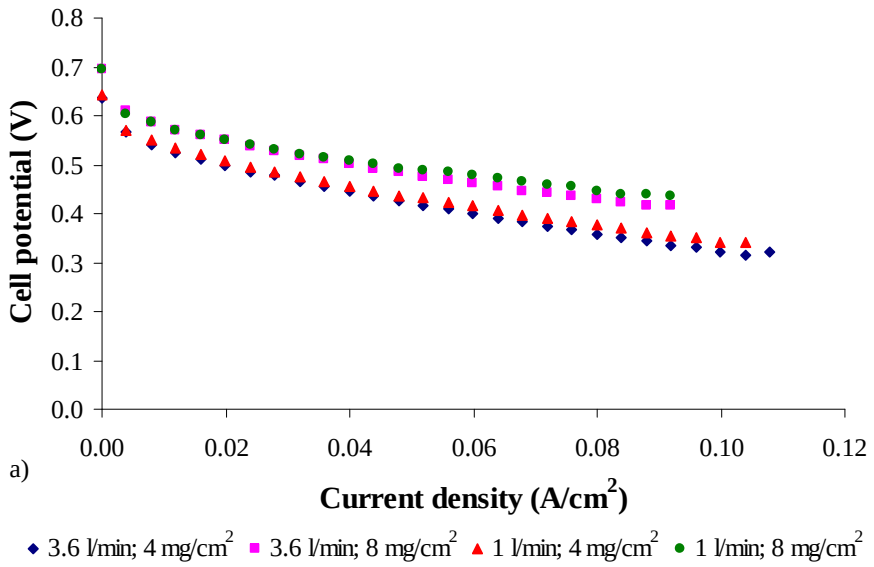

Figure C.58 – Effect of catalyst loading on a) cell performance and b) power. Operating conditions: methanol concentration 0.75M, methanol flow rate 3 ml/min and cell temperature 60ºC.

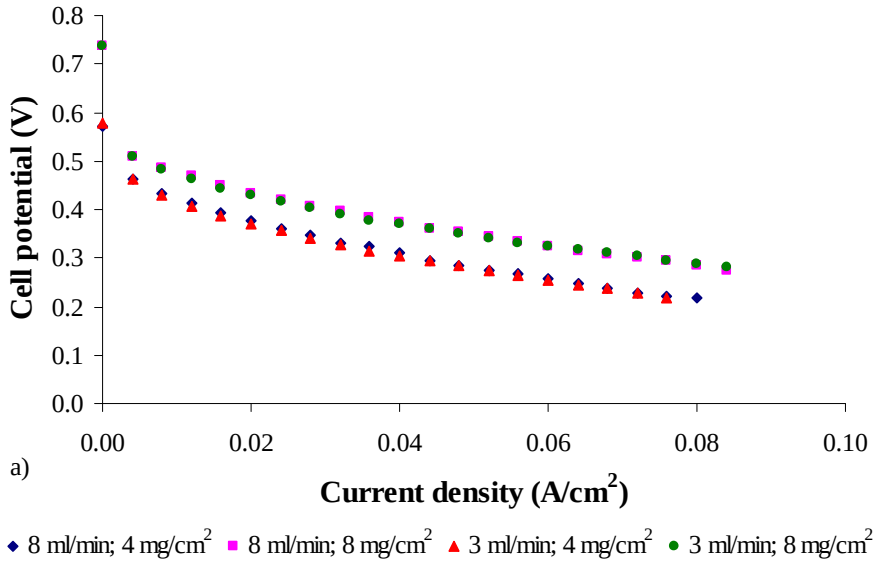

Figure C.59 – Effect of catalyst loading on a) cell performance and b) power. Operating conditions: methanol concentration 2M, air flow rate 3.6 l/min and cell temperature 20ºC.

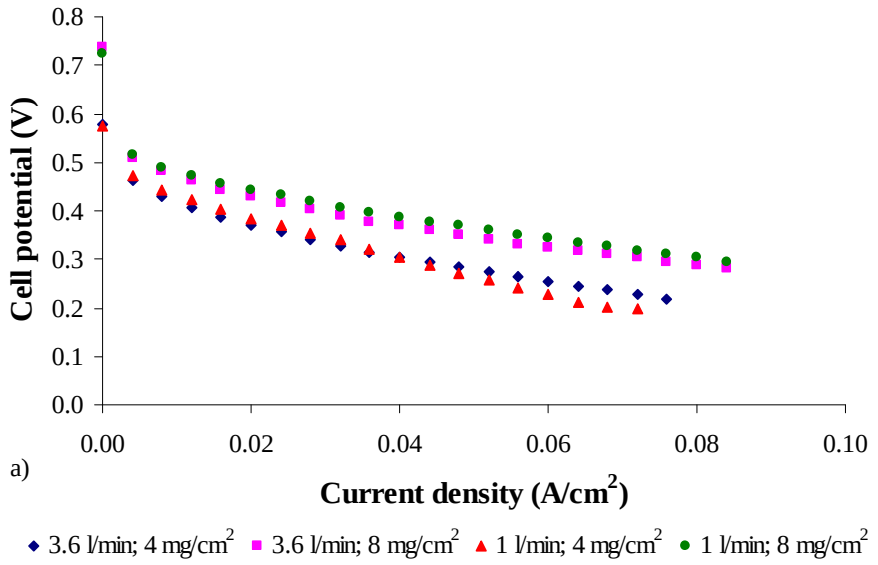

Figure C.60 – Effect of catalyst loading on a) cell performance and b) power. Operating conditions: methanol concentration 2M, methanol flow rate 3 ml/min and cell temperature 20ºC.

C.2.5. Effect of anode flow field

Table C.10 – Set of design parameters used to analyse the effect of the anode flow field on the cell performance.

Diffusion layer	Anode	Carbon cloth type A
	Cathode	Carbon cloth type A
Catalyst loading	Anode	4 mg/cm^2 Pt/Ru
	Cathode	4 mg/cm^2 Pt
Flow field design	Anode	Serpentine, multi-serpentine or mixed
	Cathode	Serpentine
Membrane		Nafion 117

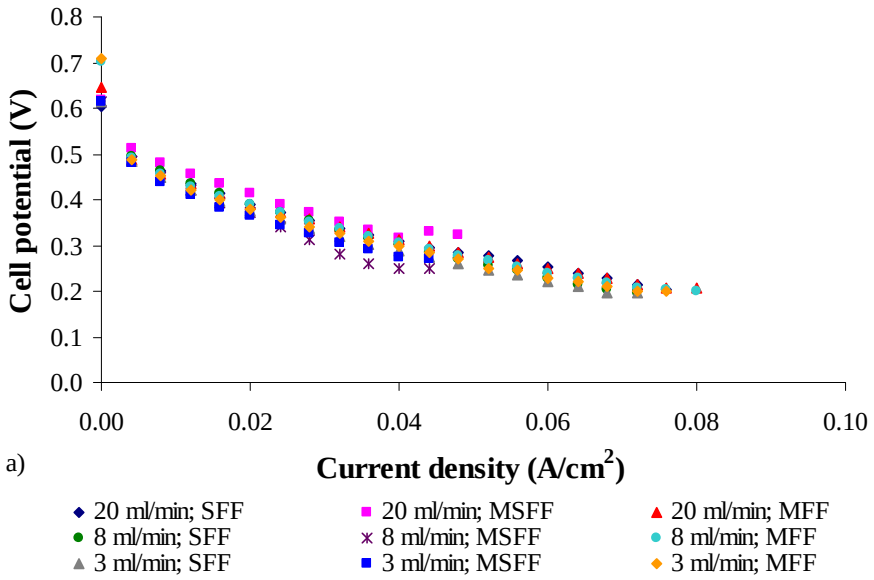

Figure C.61 – Effect of anode flow field design on a) cell performance and b) power. Operating conditions: methanol concentration 0.75M, air flow rate 3.6 l/min and cell temperature 20ºC.

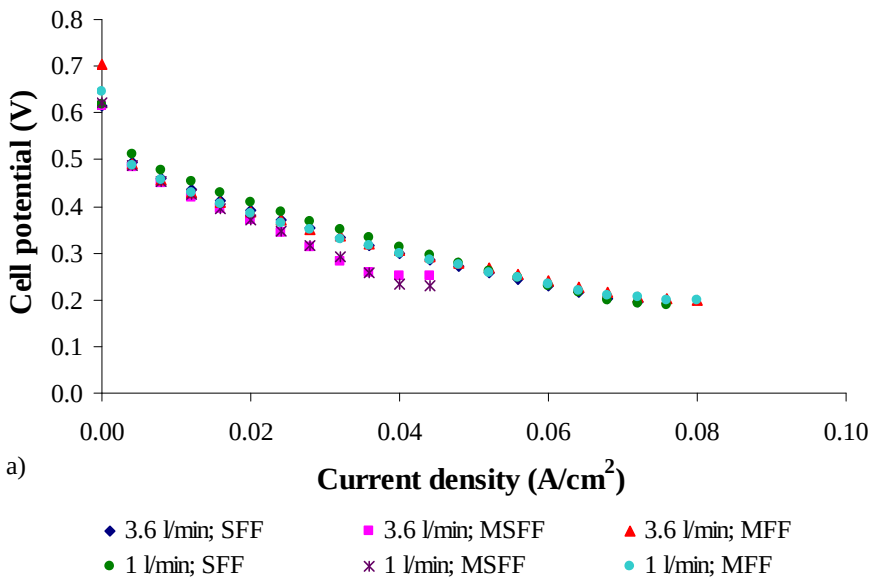

Figure C.62 – Effect of anode flow field design on a) cell performance and b) power. Operating conditions: methanol concentration 0.75M, methanol flow rate 8 ml/min and cell temperature 20ºC.

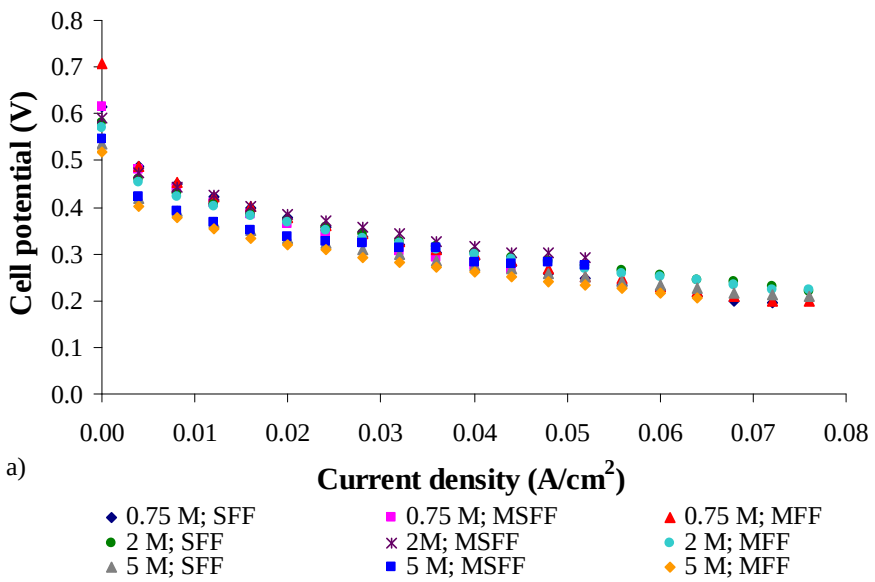

Figure C.63 – Effect of anode flow field design on a) cell performance and b) power. Operating conditions: air flow rate 3.6 l/min, methanol flow rate 3 ml/min and cell temperature 20ºC.

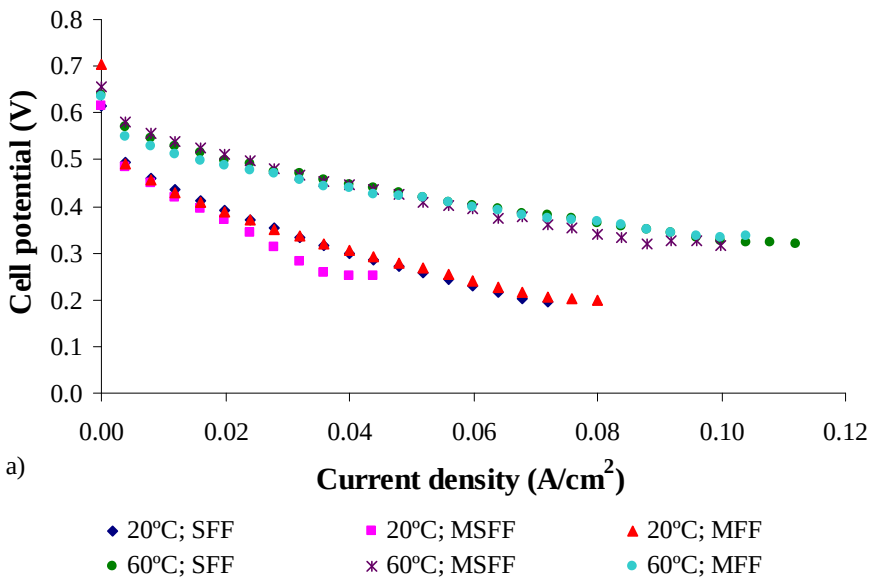

Figure C.64 – Effect of anode flow field design on a) cell performance and b) power. Operating conditions: methanol concentration 0.75M, methanol flow rate 8 ml/min and air flow rate 3.6 l/min.

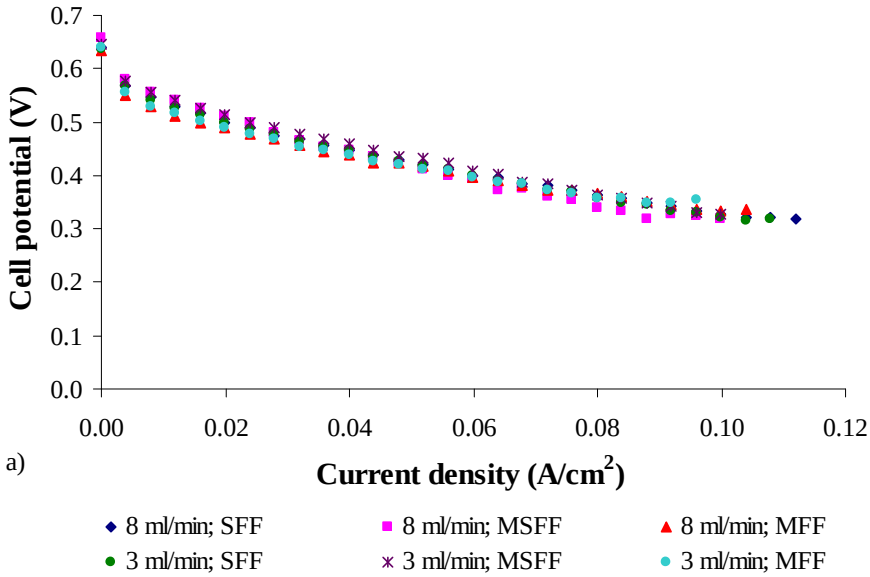

Figure C.65 – Effect of anode flow field design on a) cell performance and b) power. Operating conditions: methanol concentration 0.75M, air flow rate 3.6 l/min and cell temperature 60ºC.

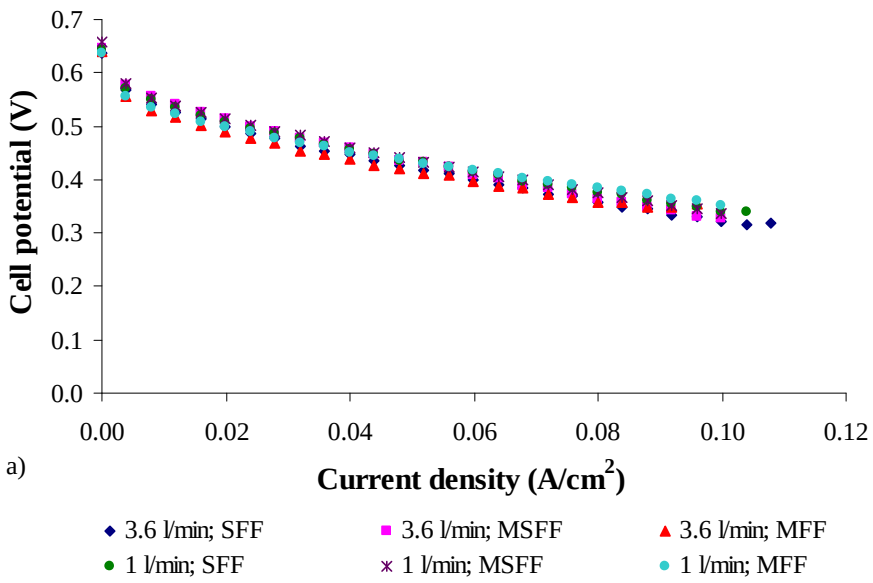

Figure C.66 – Effect of anode flow field design on a) cell performance and b) power. Operating conditions: methanol concentration 0.75M, methanol flow rate 3 ml/min and cell temperature 60ºC.

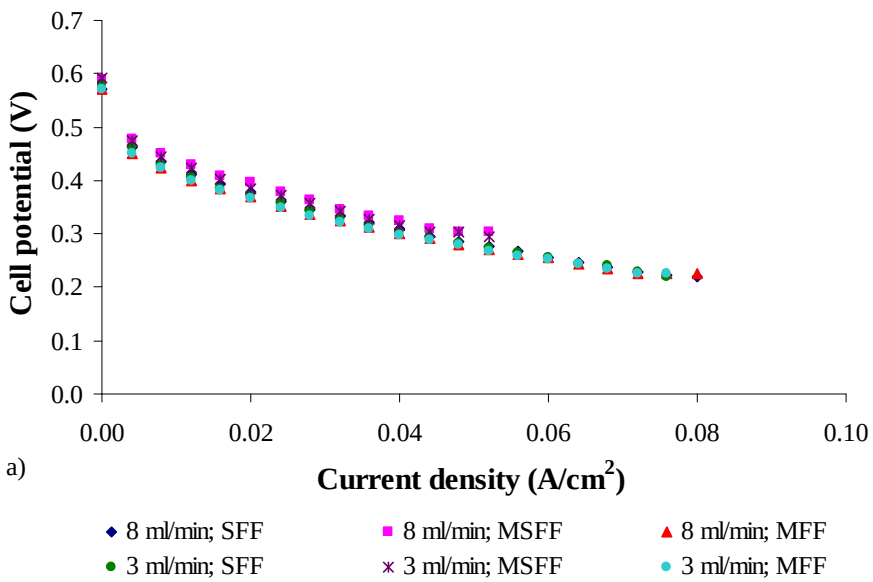

Figure C.67 – Effect of anode flow field design on a) cell performance and b) power. Operating conditions: methanol concentration 2M, air flow rate 3.6 l/min and cell temperature 20ºC.

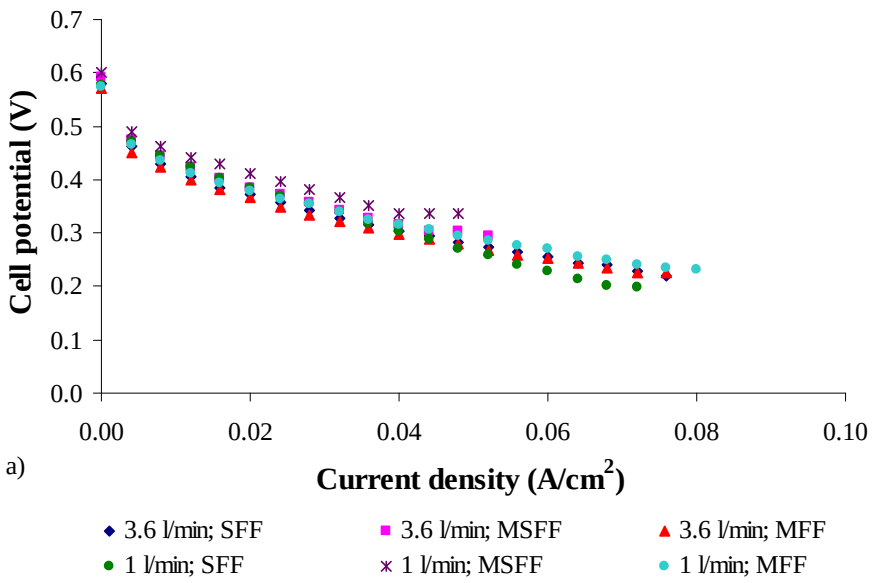

Figure C.68 – Effect of anode flow field design on a) cell performance and b) power. Operating conditions: methanol concentration 2M, methanol flow rate 3 ml/min and cell temperature 20ºC.

C.2.6. Effect of cathode flow field

Table C.11 – Set of design parameters used to analyse the effect of the cathode flow field on the cell performance.

Diffusion layer	Anode	Carbon cloth type A
	Cathode	Carbon cloth type A
Catalyst loading	Anode	4 mg/cm^2 Pt/Ru
	Cathode	4 mg/cm^2 Pt
Flow field design	Anode	Serpentine
	Cathode	Serpentine, multi-serpentine or mixed
Membrane		Nafion 117

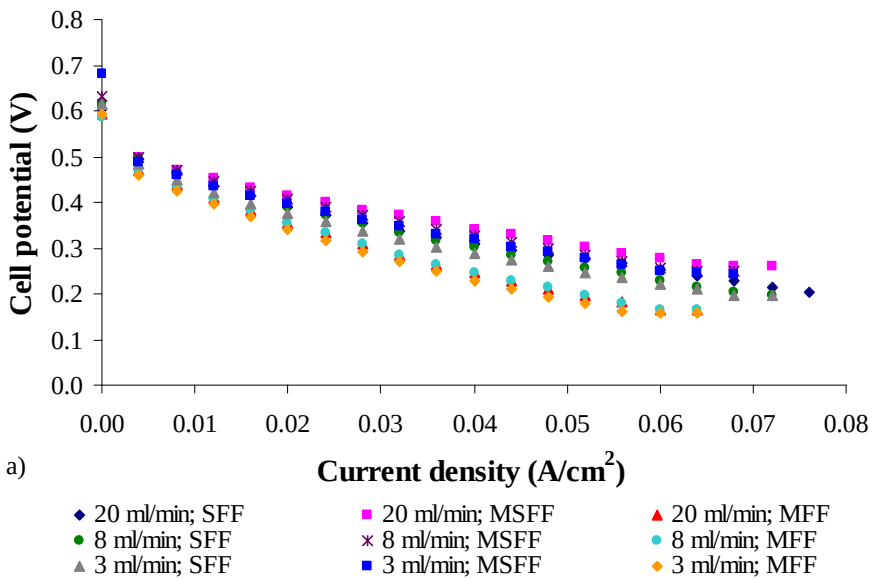

Figure C.69 – Effect of cathode flow field design on a) cell performance and b) power. Operating conditions: methanol concentration 0.75M, air flow rate 3.6 l/min and cell temperature 20ºC.

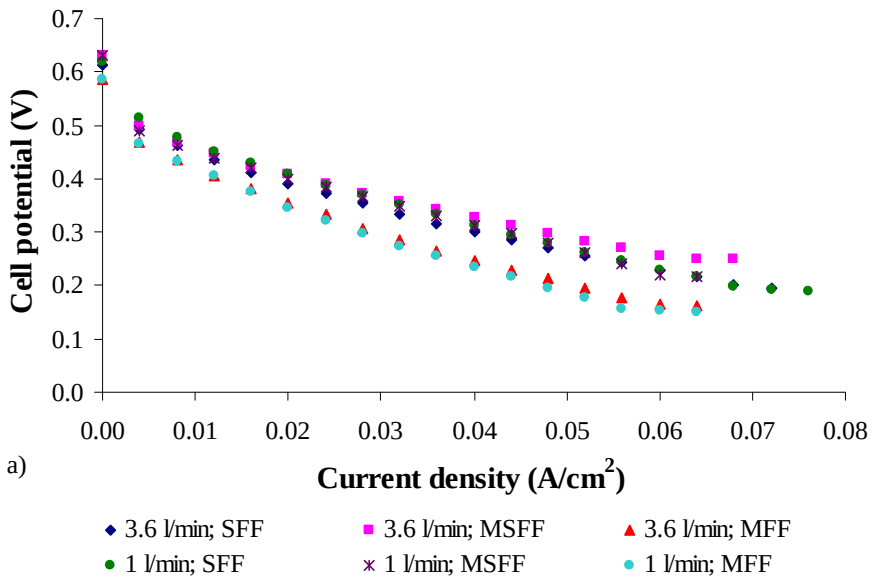

Figure C.70 – Effect of cathode flow field design on a) cell performance and b) power. Operating conditions: methanol concentration 0.75M, methanol flow rate 8 ml/min and cell temperature 20ºC.

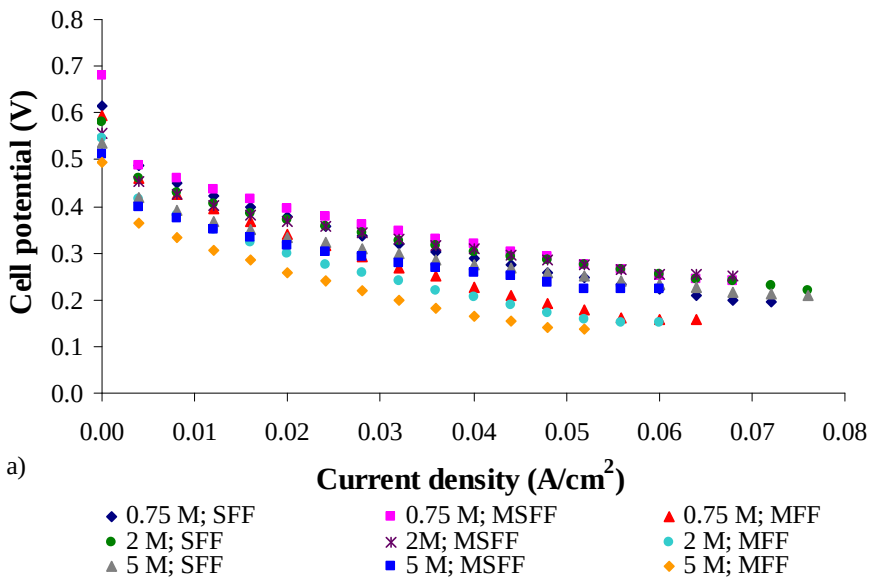

Figure C.71 – Effect of cathode flow field design on a) cell performance and b) power. Operating conditions: air flow rate 3.6 l/min, methanol flow rate 3 ml/min and cell temperature 20ºC.

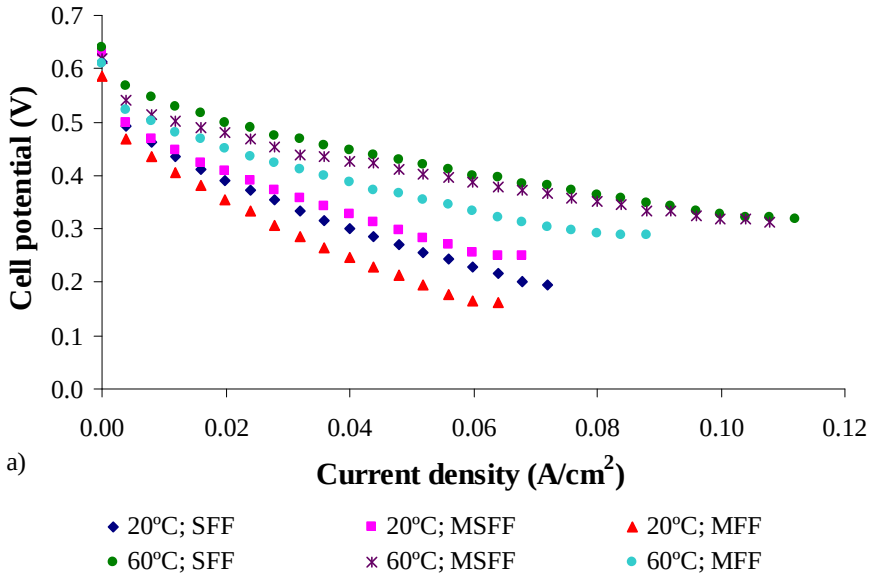

Figure C.72 – Effect of cathode flow field design on a) cell performance and b) power. Operating conditions: methanol concentration 0.75M, methanol flow rate 8 ml/min and air flow rate 3.6 l/min.

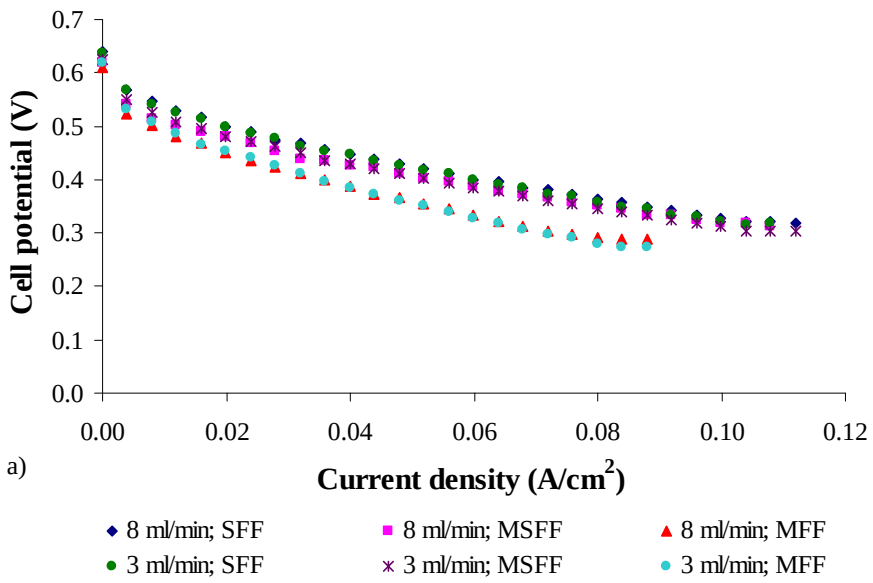

Figure C.73 – Effect of cathode flow field design on a) cell performance and b) power. Operating conditions: methanol concentration 0.75M, air flow rate 3.6 l/min and cell temperature 60ºC.

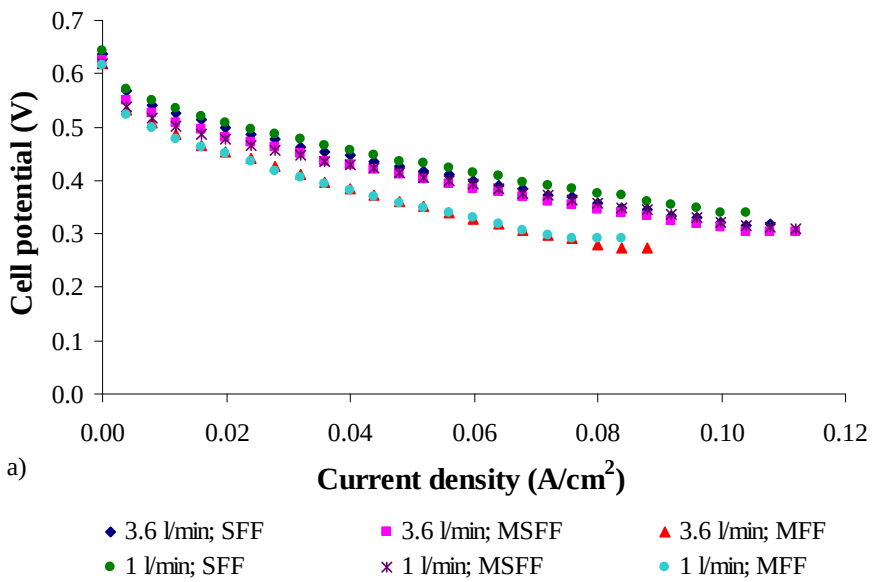

Figure C.74 – Effect of cathode flow field design on a) cell performance and b) power. Operating conditions: methanol concentration 0.75M, methanol flow rate 3 ml/min and cell temperature 60ºC

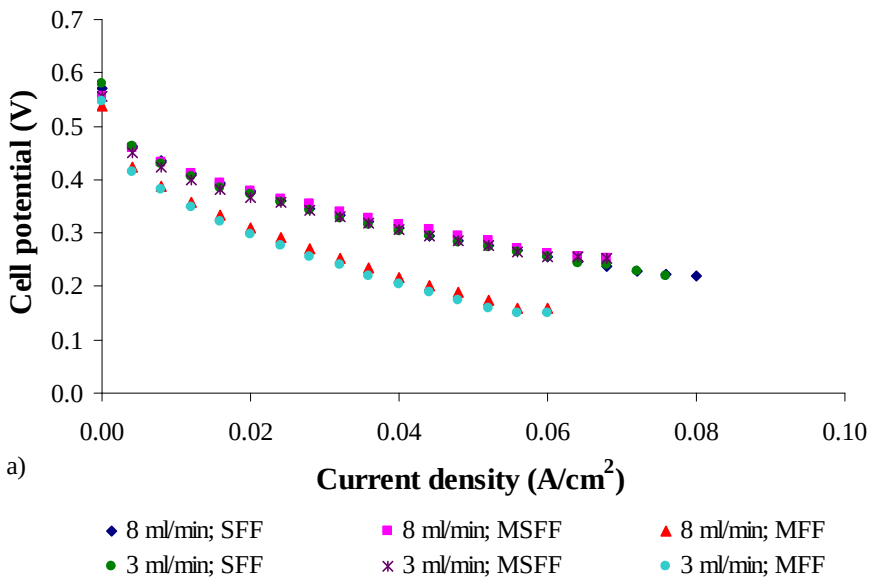

Figure C.75 – Effect of cathode flow field design on a) cell performance and b) power. Operating conditions: methanol concentration 2M, air flow rate 3.6 l/min and cell temperature 20ºC.

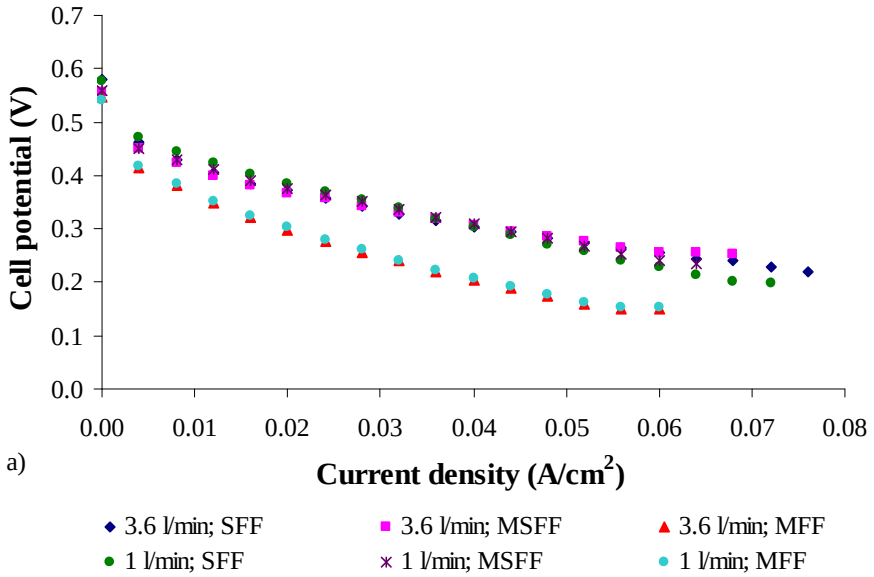

Figure C.76 – Effect of cathode flow field design on a) cell performance and b) power. Operating conditions: methanol concentration 2M, methanol flow rate 3 ml/min and cell temperature 20ºC.